Comparison of Shaft Position Estimation and Correction Techniques for Sensorless Control of Surface Mounted PM Synchronous Motors

Ming Chuan Huang

Ph.D. Thesis

Wolfson Centre for Magnetics
Cardiff School of Engineering
Cardiff University

27th November, 2009

ProQuest LLC
789 East Eisenhower Parkway
P.O. Box 1346
Ann Arbor, MI 48106-1346

DECLARATION

This work has not previously been accepted in substance for any degree and is not concurrently submitted in candidature for any degree.

Signed.....M C Huang 黃明偉.....(candidate)

Date.....3rd December 2009.....

STATEMENT 1

This thesis is being submitted in partial fulfilment of the requirements for the degree of PhD

Signed.....M C Huang 黃明偉.....(candidate)

Date.....3rd December 2009.....

STATEMENT 2

This thesis is the result of my own independent work/investigation, except where otherwise stated. Other sources are acknowledged by explicit references.

Signed.....M C Huang 黃明偉.....(candidate)

Date.....3rd December 2009.....

STATEMENT 3

I hereby give consent for my thesis, if accepted, to be available for photocopying and for interlibrary load, and for the title and summary to be made available to outside organisations.

Signed.....M C Huang 黃明偉.....(candidate)

Date.....3rd December 2009.....

SUMMARY

This thesis is a detailed study of how two error correction schemes affect the precision of shaft position estimation in state-observer techniques for sensorless control surface-mounted Permanent Magnet Synchronous Motors (PMSM), variance correction and variable PI regulation. A novel sensorless estimation technique based on Linear Kalman Filter (LKF) through constant variance correction is proposed and compared with the conventional Flux Linkage Observer (FLO) method and other state-estimation sensorless control techniques namely, Extended Kalman Filter (EKF), variable variance correction, Single Dimension Luenberger (SDL) observer and Full-Order Luenberger (FOLU) observer both through variable PI regulation. These five sensorless control techniques for PMSM are successfully implemented in the same lab-based hardware platform, i.e. full digital float-point-type DSP control inverter-fed PMSM system. Experiments are reported on each sensorless method covering position estimation, speed response, self-startup and load behaviour.

Intensive analysis has also been carried out on the impact of error correction of estimated position on the steady/dynamic PMSM characteristics with different sensorless approaches. The experiment demonstrates that the novel Linear Kalman Filter can achieve the minimum average position estimation error throughout the electrical cycle of the five sensorless estimation techniques during no load operation at rated speed and also makes PMSM capable of self-startup for any initial rotor position except the dead area.

A speed response experiment for LKF shows that individual speed estimation can be extracted directly from LKF state estimation for sensorless control PMSM. Experiments on the five sensorless methods proves that position error correction scheme is the dominating factor for state estimation sensorless control PMSM and better dynamic/steady control performance can be achieved using a variance correction scheme applied in EKF/LKF than with variable PI regulation applied in SDL/FOLU. The thesis also concludes that the novel Linear Kalman Filter is an optimised cost-effective sensorless estimation method for the PMSM drive industry compared with classic and Flux Linkage observers/Extended Kalman Filters.

ACKNOWLEDGEMENTS

I would like to thank staff and students at the Wolfson Centre for Magnetics for support, especially my supervisors **Prof. Anthony J. Moses** and **Dr Fatih E. Anayi** for their guidance and patience.

In addition, I would like to give a special thank to my wife, **Hong-yue Wang,** for her encouragement and understanding and all my family and friends who have supported me throughout.

This work was made possible through the gratefully received financial support of scholarships from the Wolfson Centre for Magnetics and the School of Engineering and at Cardiff University.

CONTENTS

FIGURES

TABLES

CONFERENCE PUBLICATIONS

1. M. C. Huang, A. J. Moses, F. Anayi, "The Comparison of Sensorless Estimation Techniques for PMSM between Extended Kalman Filter and Flux Linkage Observer", *Twenty-First Annual IEEE Applied Power Electronics Conference and Exposition, 2006(APEC '06),* March 19~23, 2006, on Page(s):654-659, Dallas, USA;
2. M. C. Huang, A. J. Moses, F. Anayi, X. G. Yao, "Linear Kalman filter (LKF) sensorless control for permanent magnet synchronous motor based on orthogonal output linear model", *International Symposium on Power Electronics, Electrical Drives, Automation and Motion (SPEEDAM 2006)*, 23~26 May, 2006, on Page(s):1381 – 1386, Taormina, Italy.
3. M. C. Huang, A. J. Moses, F. Anayi, X. G. Yao ," Reduced-Order Linear Kalman Filter (RLKF) Theory in Application of Sensorless Control for Permanent Magnet Synchronous Motor(PMSM)", *the 1st IEEE Conference on Industrial Electronics and Applications (ICIEA 2006),* May 24~26, 2006, on Page(s):928-933,Singapour.
4. M. C. Huang, A. J. Moses, F. Anayi, Juan Sagarduy, "Two Reduced-order Stochastic State Observer Comparison &Investigation based on LKF and SDL", *37th IEEE Power Electronics Society Conference(PESC2006),* June 18~22, 2006, on Page(s): 1484-1489, Jeju, South Korea.
5. M. C. Huang, A.J Moses, F. Anayi, "Position Calibration technology Comparison for Sensorless Controlled PMSM based on Stochastic Variance and Angle Correction", *12th International Power Electronics and Motion Control Conference (EPE-PEMC 2006)* , August 30, September, Aug. 2006 on Page(s): 1301 – 1306, Portoroz, Slovenia.
6. Huang M.C., Moses A.J., Anayi F., Yao X.G., "Shaft Position Correction Scheme Comparison for Sensorless Control PMSM based on Space State-Estimation between α-β coordinate and Angle Calibration in d-q coordinate for Sensorless Control PMSM based on Space State-estimation", *32nd IEEE Annual Conference on Industrial Electronics, IECON 2006*, on Page(s): 1469 – 1474 in Paris, France.
7. Ming Chuan Huang; A. J. Moses,; F. J. Anayi, "Shaft Position Correction Scheme Comparison for Sensorless Control of a PMSM Based on State-Space

Estimation between Variance Adjustment and Angle PI Regulation", *Industry Applications Society Annual Meeting, 2008, IAS '08,. IEEE* 5-9 Oct. 2008 Page(s):1 - 8;

CHAPTER 1. INTRODUCTION

1.1 A Brief History of PM Motors

1.1.1 Impact of PM material in the motor industry

The application of Permanent Magnet (PM) materials for energy conversion was reported with the first electric motor invented by Faraday [1·23] in 1821. Early in the 19th century, the main type of PM material was natural magnetite ($F_{e3}O_4$), whose magnet energy density is low resulting in large motors.. Due to rapid rising demand for electric machines and the invention of dc machines, many new PM materials appeared including carbon steel, tungsten steel (max. energy product 2.7 kJ/m^3), cobalt steel (max. energy product 7.2 kJ/m^3), AlNiCo (max. energy product 85 kJ/m^3) [1·24] and ferrites (40 kJ/m^3) [1·25]. The magnetic performance of these new PM materials was capitalised on in various micro and small motors for field excitation. After samarium-cobalt magnets in the 1970's [1·26] and neodymium-iron-boron magnet in the1980's [1·27] were discovered and developed the outstanding high coercive force, remanence, maximum energy product and linear demagnetization curve particularly matched the motor requirement.

Rare earth materials shown in Fig.1·1 have been developed for 3 decades: The first generation is samarium cobalt (RC_{O5}) found by Strnat in 1963 [1·28], its maximum energy product can reach 199 kJ/m^3 [1·31]. The second generation of rare earth PM material (R_2C_{O17}) was developed in 1973 [1·29], its maximum energy product can reach 258 kJ/m^3 [1·31]. The third generation of rare earth PM material (NdFeB) was developed in 1983 [1·29], its maximum energy product can be 430 kJ/m^3 [1·27].

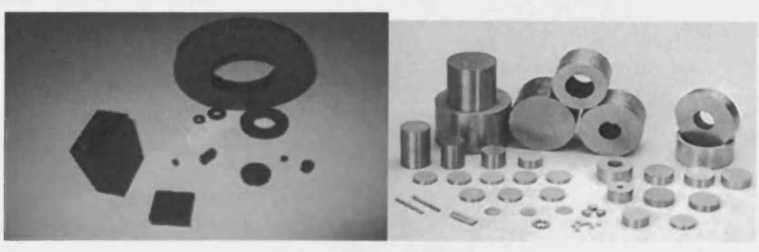

(a) (b)

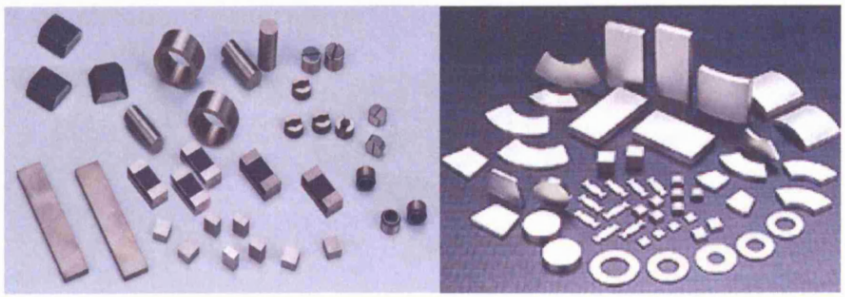

(c) (d)

Fig. 1·1 (a) Ferrite[1·32], (b) samarium cobalt[1·33], (c) Al-Ni-Co[1·33], (d) Nd-Fe-B[1·33]

1.1.2 History of PM motors

Research and development of PM motors can be categorized into 3 stages:

1. In the late 1960s and early 1970s, the price of the rare earths was high, so their application was limited to aircraft and space applications.
2. Since the cost of NdFeB was dropped in the 1980s, the focus of research and development was diverted to its application in industrial and domestic motors. The performance of NdFeB combined with more advanced power electronics devices and microcomputer control techniques saw conventional synchronous motors with DC field excitation replaced by rare earth PM excited synchronous motors.
3. Since the 1990s, with the improved thermal stability and corrosion resistance of NdFeB PM material and falling price, PM motors have become mature. Currently PM motors are found in a wide range of applications including industrial drives, domestic appliances and automotive [1·57]. The diameter of the smallest PM motor is around 0.8 mm while the defence. PM motors are developing towards high power performance. Power capacity for PM motors reach can 1000 kW [1·35] with peak speed over 300 krpm [1·34], minimum speed can be lower than 0.01rev [1·58].

1.1.3 Applications of PM motors

1.1.3.1 PM synchronous generators

(a) (b) (c)

Fig. 1·2 (a) Low speed permanent magnet generator, (b) medium speed permanent magnet generator, (c) high speed permanent magnet generator [1·22]

Without the coils on the rotor and external power supply for DC field excitation, PM synchronous generators shown in Fig. 1·2 and 1·3 become brushless eliminating the commutator and the structure is simplified so the operation is more reliable. Rare earth materials applied for field excitation can increase the flux density and increase the top speed. The size and weight are reduced so the power-to-weight ratio is increased. At present, PM generators such as those shown in Fig. 1·2 and 1·3 [1·22] find application in power stations and wind turbines.

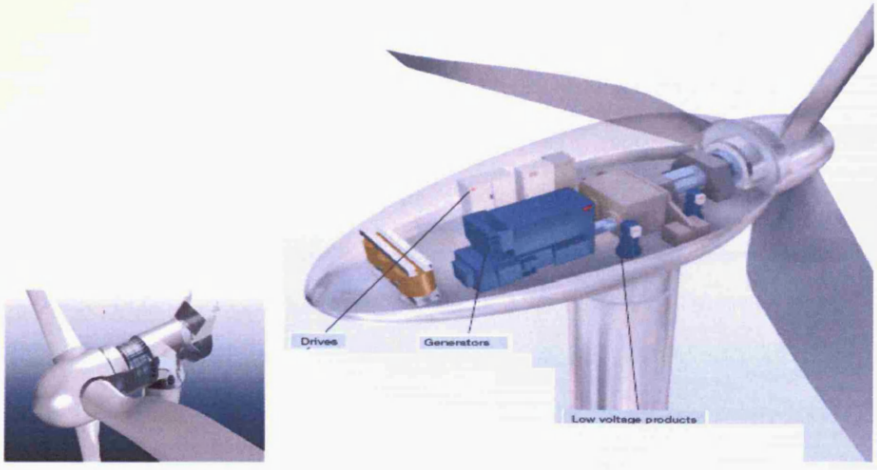

Fig. 1·3 Permanent magnet generators applied in wind power [1·22]

Contemporary air and spaceflight reveals that every kilogram of equipment needs about 15~20 kg mass to support during high-speed flight [1·39] which means that a high power-to-weight ratio is required for actuation devices. High-speed PM synchronous generators for aircraft are capable of increasing the power-to-weight ratio

by up to 20kw/kg [1·41]. PM synchronous generators can thereby be suitable in other applications requiring high reliability and power-to-weight ratio. Present aeroplane and spaceflight generators are reported to use rare earth cobalt alloys [1·37-38]. The classic products are 150 kVA, 14 poles, 12k~21 krpm and 100 kVA 60 krpm rare-earth samarium cobalt PM synchronous VSCF Starter Generators [1·40]. Fig. 1·4 shows PM motors applied in a Thales high pressure starter/generator [1·37] and a fan shaft generator [1·38] for the Rolls-Royce Trent 800 turbine engine [1·36].

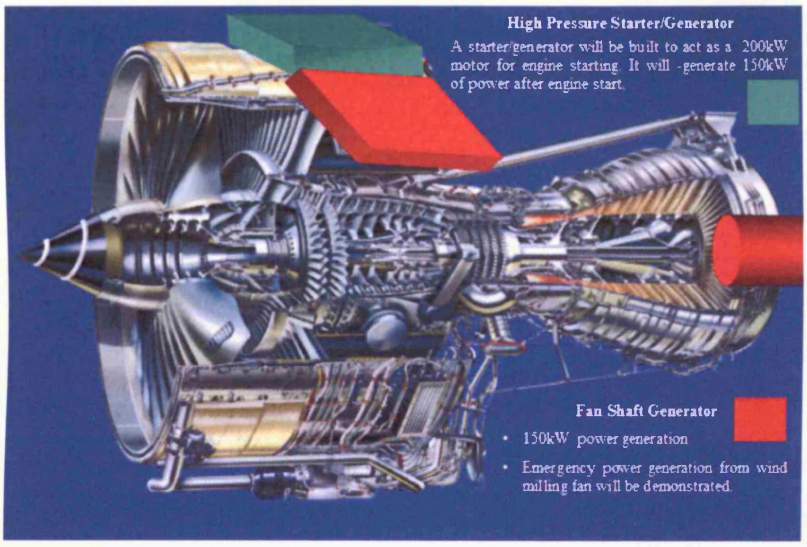

Fig. 1·4 PM generator for high pressure starter/generator used in an aircraft engine [1·36-38]

Rare-earth PM generators have been used for the pilot exciter supply for turbine generators. Fig.1·5 illustrates a PM generator employed in a KATO PMG pilot exciter [1·42] which shares the shaft with a brushless synchronous main generator. The field exciter of the main synchronous generator is fed and regulated by the voltage regulator which is powered by a pilot exciter. PM generators, such as pilot exciters, are found widely in power plants. For example, a 75 kVA, 3000 r/min rare-earth cobalt PM generator [1·39] has a voltage adjustment rate of only 9.8 %[1·39] and sinusoidal distortion rate of 0.7% [1·39] for linear voltage waveform on no-load. The cobalt content is only 50% of that of an AlNiCo PM generator with the same specification.

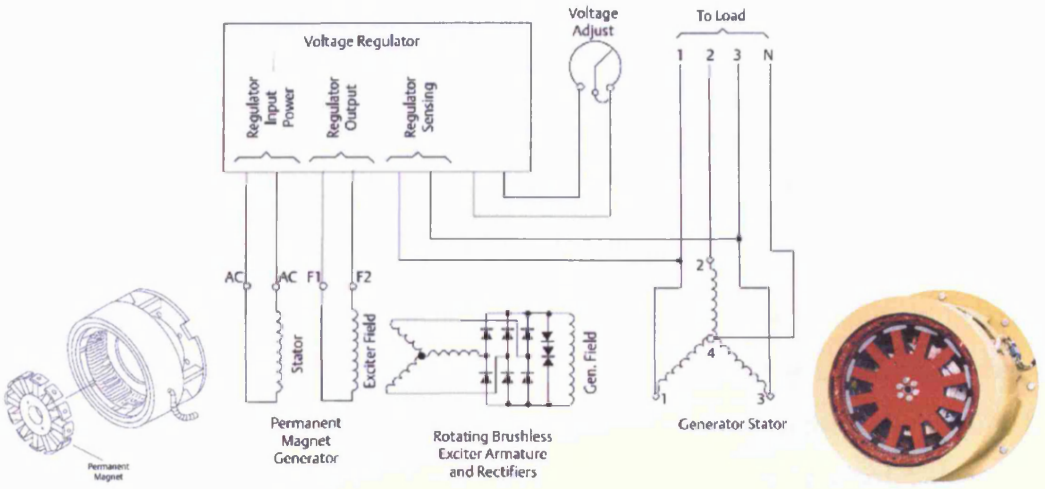

Fig. 1·5 PM generator pilot exciter by KATO Engineering Inc.[1·42]

Low speed hydraulic generators driven by water turbines employ permanent magnet generators as pilot exciter. Fig.1·6 shows a permanent magnet generator used to supply the field exciter on the rotor of a large hydroelectric generator [1·43].

Permanent magnets are found in small hydraulic generators and small gas turbine generators. However, the application range is limited since the field can hardly be regulated to control output voltage and power factor.

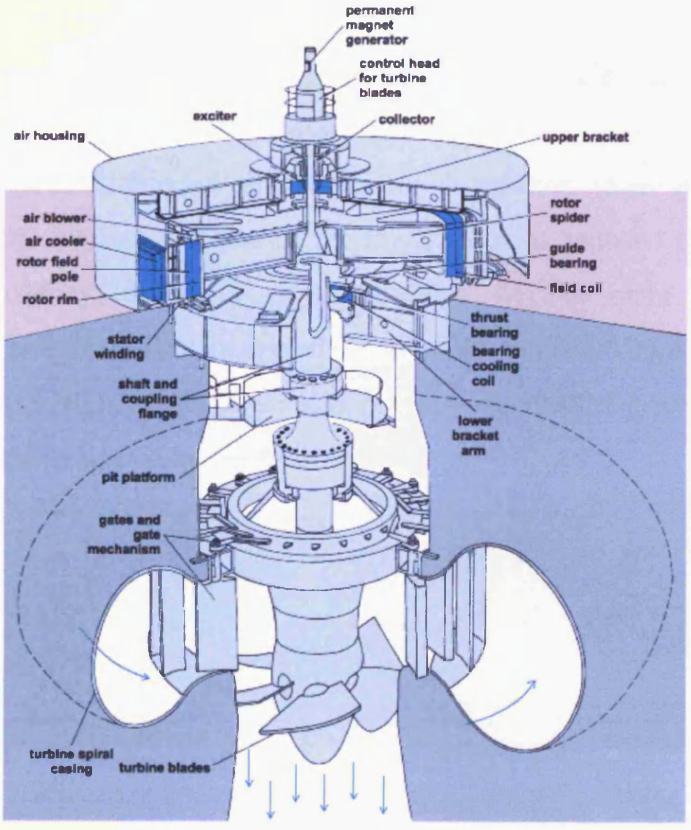

Fig. 1·6 Large hydroelectric generator by Westinghouse Electric Corp. [1·43]

1.1.3.2 PM synchronous motors

Compared with induction motors, PM synchronous motors don't need a reactive excitation current so their power factors can reach unity. The loss due to the current flowing through stator resistance is significantly reduced. Total loss is reduced, as a consequence both the fan size and its windage loss decrease. Therefore the efficiency of PM synchronous motors can be 2~8% higher than that of induction motors [1·39]. PM synchronous motors can obtain high efficiency and power factor in the range between 25% and 120% at rated load [1·39]. PM synchronous motors occasionally require cage windings set on the rotor, which enables them to start up directly at a fixed frequency and voltage.

1.1.3.3 Brushless AC and DC motors

With the rapid development of power electronics, more inverters and AC motors are employed in AC variable speed systems. The speed of AC synchronous motors is proportional to the inverter frequency during steady operation so this inherent feature enables them to be used directly in open-loop variable speed systems, especially multi-motor drives fed by a power converter operating with synchronised steps. Then the drive system can benefit from not only a simplified structure but also brushless operation. A PMSM can be started by increasing the frequency of the converter gradually. The rotor need not have cage windings. For example, Fig.1·7(c) shows a 30 MW, 130 rpm, low speed PM synchronous motor fed by a 6 phase converter employed in the Siemens-Schottel podded diesel-electric propulsion (SSP propulsor) [1·44]. Compared with DC motors, the size of the drive motor is reduced by 60% while the total loss is reduced by 20% [1·44]. It is claimed [1·44] that more than 10% energy saving from SSP propulsor directly drived by a PMSM can be guaranteed over a classic diesel-direct drive system. Fig.1·7 (a) and (b) show a PMSM-driven SSP propulsor applied in two commercial vessels.

(a) (b)

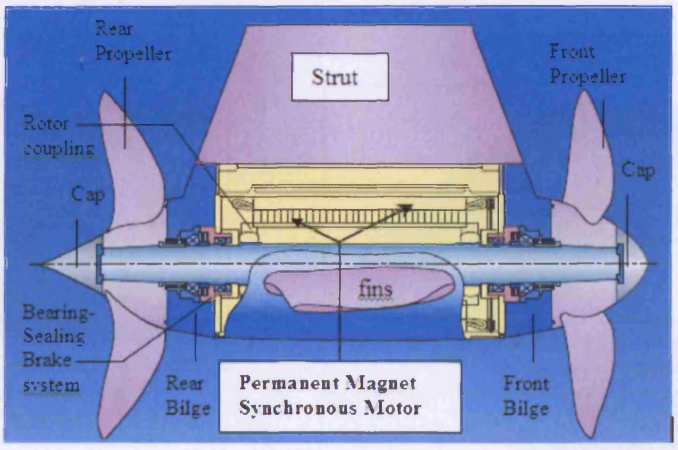

(c)

Fig. 1·7 (a) Two RoRo ferries for TT-Line, two units SSP10 in each vessel, (b) Two chemical product tankers for DansØ Tank Rederi AB, one unit SSP7 each tanker, (c) Ship propulsion systems —SSP Propulsor (Siemens Schottel Propulsor) employing PM motors [1·44]

A PM synchronous motor fed by a converter through a rotor position close-loop control system is not only capable of good speed adjustment but also operates in the brushless mode. There are two types of such servo motors: one is the brushless DC servo motor whose back-emf waveform and supply current are trapezoidal; the other is the brushless AC servo motor whose back-emf waveform and supply current are sinusoidal. For example, a 12.6 KW, 9000 rpm, rare earth brushless DC PM motor, applied in the lifting aileron of space shuttle [1·58], has an efficiency of 95% while its weigh is only 7.65 kg [1·58]. Fig.1·8 also illustrates a 25 KW three phase brushless DC permanent magnet motor [1·59] employed in a LIEBHERR Electro-Mechanical Actuation (EMA) for an aircraft high-lift system [1·45].

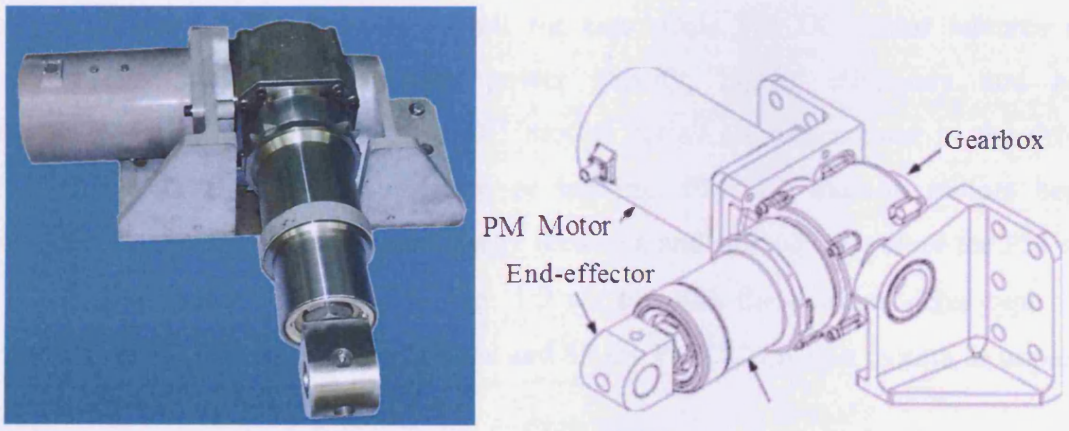

Fig. 1·8 LIEBHERR Electro-Mechanical Actuation (EMA) for aircraft high-lift systems [1·45, 59]

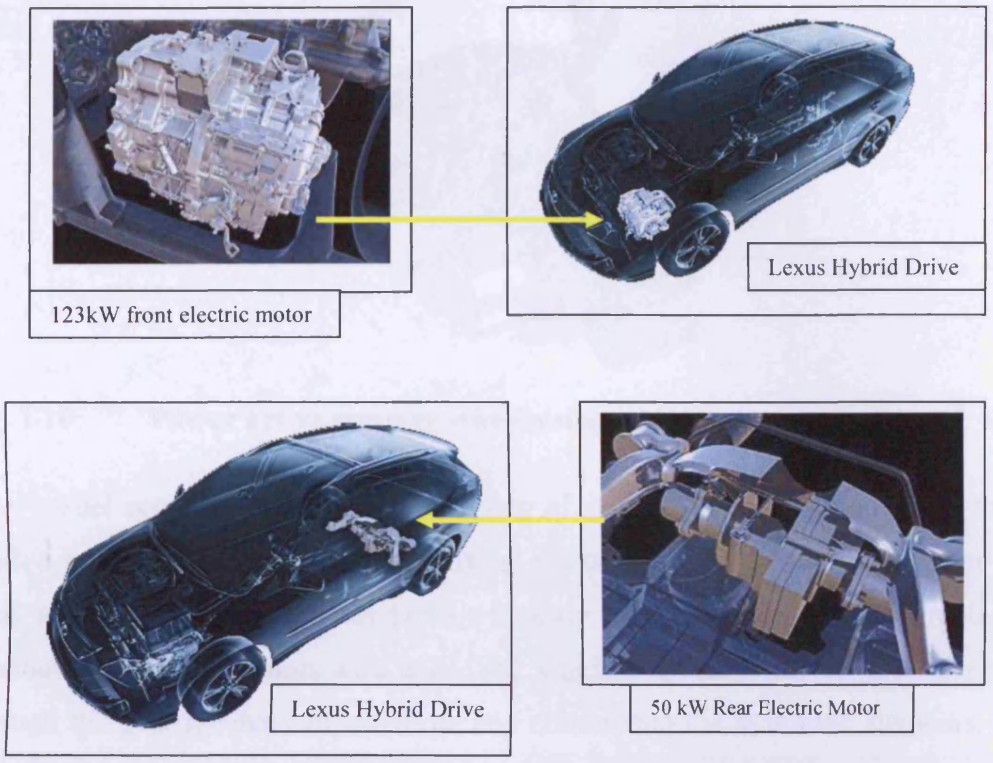

Fig. 1·9 Four-Wheel Drive in Lexus Hybrid Car Rexus employing 123 kw&50 kw PM motor for front & rear drive [1·46]

The Electric Vehicle (EV) or Hybrid Electric Vehicle (HEV) driven by electric motors are main transportation of the future. Many automotive manufactures have released commercial hybrid cars: Lexus RX450H [1·46], Toyota Prius [1·60], Ford Fusion Hybrid[1·60], etc. Currently 2nd generation HEVs have appeared on the market [1·62]. Brushless PM DC traction motors powered by storage batteries and fuel-efficient gas engines power HEVs.

Space for the drive is a limit for cars while PM DC motor features many advantages: compact size, high power density, higher efficiency and higher torque/weight rate. Brushless PM DC motors act as motor/generator in the drive of EV/HEVs. In the case of coasting or braking, PM DC traction motors become generators to charge batteries for energy feedback and storage. Therefore the PM motor is the first choice for EV/HEV. Fig. 1·9 shows that the 4-wheel drive type Lexus Hybrid car RX450 adopts two 123 kw and 50 kw PM DC traction motors to implement front and rear drives [1·46].

Fig. 1·10 Power active steering wheel using PM synchronous motor [1·47]

Fuel economy and reduced emission of vehicles require not only that the main motive power is replaced fully/partially by electricity but also auxiliary power system such as active steering wheels [1·63]. Electric power assisted steering replaces the traditional hydraulic pump with a PMSM which eventually drives the steering rack through the gear mechanism, consequently eliminating the hydraulic elements. Figure. 1·10 shows a 12V, DC 0.75 kw, three phase, permanent magnet synchronous motor employed in electric power assist steering [1·47]. It is reported [1·64] that electric power assisted steering can improve the fuel economy by up to 4%. On the contrary, the traditional hydraulic steering can produce about 1.5 kW active load on the vehicle only one third of which is actually transferred as mechanical assistance at the steering shaft [1·65].

Fig. 1·11 Brushless PM DC Drive compressor with a Daikin Variable Refrigerant Volume (VRV) System [1·48]

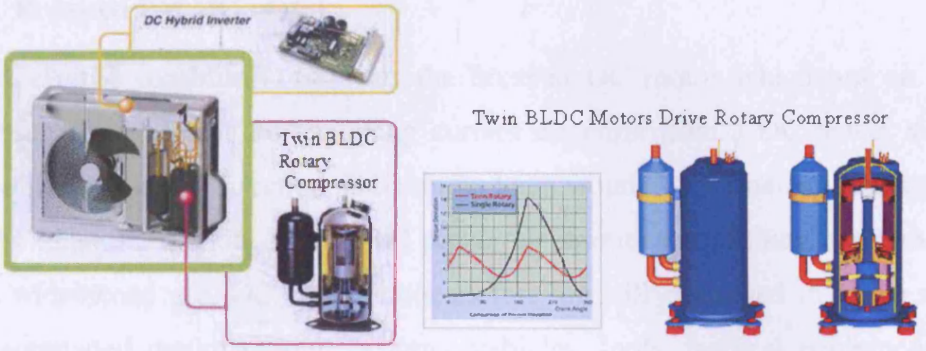

Fig. 1·12 Twin rotary compressor in Toshiba air conditioner using double brushless DC PM motors [1·49]

PM DC motors are found in domestic appliance. It is reported [1·48] that one third of electricity can be saved by use of variable speed air conditioners. Brushless DC PM motors can significantly increase efficiency compared to PM synchronous motors. Fig.1·11 shows a brushless PM DC motor employed in the Daikin Variable Refrigerant Volume (VRV) air conditioner system [1·48]. Fig.1·12 shows two brushless DC PM motors employed in a Toshiba twin rotary compressor for air conditioners [1·49].

Other house-hold domestic appliances such as refrigerators and washing machines use brushless PM motors. For example, the direct-drive PM motor (DDPM) drive system [1·66] can couple the rotor shaft of a PM DC motor to the basket/drum of a washing machine without any belt, gearbox, pulleys or wheels. Domestic washing machines require a maximum torque during quick start up on load, low full torque and high constant power during the washing spinning processes [1·66]. Therefore, the brushless PM DC motor in a DDPM system for washing machines employs field oriented PWM control strategy by a sinusoidal inverter [1·67]. Figure.1·13 shows a brushless DC PM motor used in a NEC DDPM washing machine drive system [1·50].

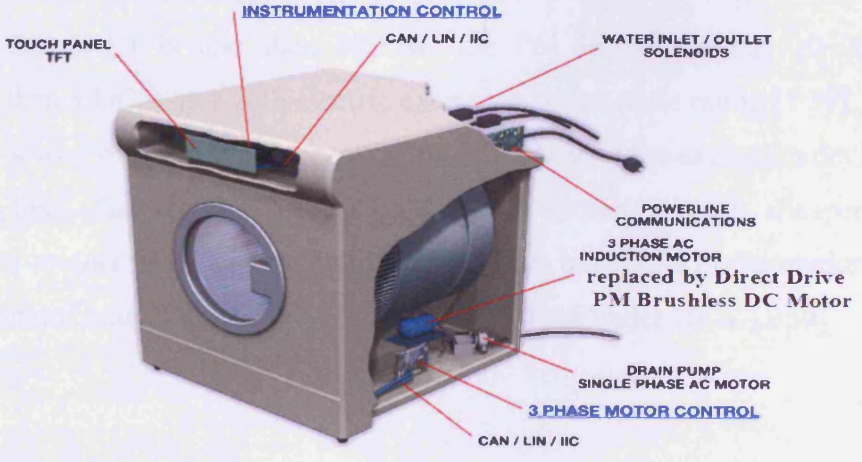

Fig. 1·13 Brushless DC PM motor drive in a washing machine [1·50]

1.1.3.4 Brushed PM DC motors

The first electric machine [1·68] was the brushed DC motor which has an internal carbon brush commutator for switching current direction from a DC power supply to obtain constant rotating direction. DC motors have wound or permanent magnet stators for field excitation. Although advanced power electronics are pushing brushless motor towards widespread use, DC commutator motors are still employed in office machine drives, automated manufacturing systems, vehicles, tools, medical equipment, home appliances, etc since they have many advantages such as relatively cheap manufacture, small size, ruggedness and simple structure.

Fig. 1·14 Thales High voltage DC engine embedded starter/generators for a future power optimised aircraft [1·45][1·69~71]

Compact high power PM DC commutator motors without field coils retain the linear electro-mechanical characteristics of speed-voltage and torque-current while the excitation winding loss is eliminated. Fig. 1·14 shows a PM DC commutator motor employed in the Thales embedded starter/generator [1·45] [1·69~71].

If the power is less than 300 W, the PM DC motor has 10~20% higher efficiency than a DC motor with electric excitation of the same rating [1·39]. The lower the motor power, the higher is the proportion of the size of the excitation device and the excitation loss. The ferrite PM DC commutator motor is much cheaper than DC commutator motors with field excitation. PM motors have 92% of the market for micro DC commutator motors under 500 W and, 99% of those under 10 W [1·39].

1.1.4 Status and Trends for PM servo motors

1.1.4.1 PM servo motor in mechatronics

Mechatronics products are essentially optimised systems which combine precision machinery techniques with other techniques such as software, computer techniques, power electronics, sensors and automation [1·97].

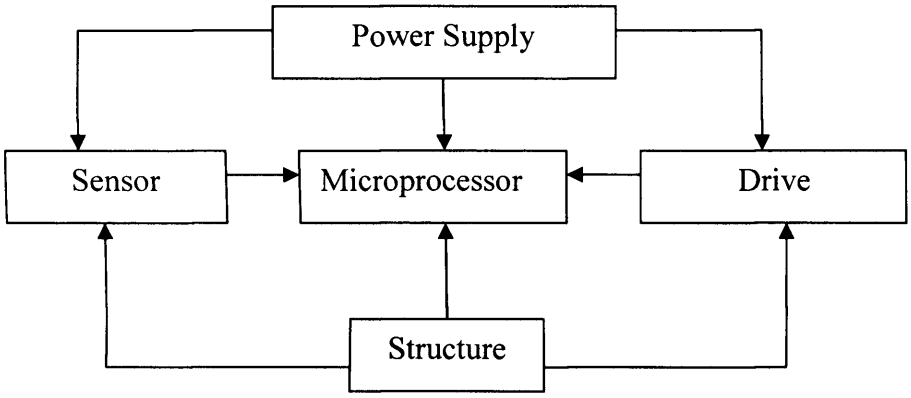

Fig. 1·15 Modern mechatronics system structure.

A classic mechatronics product consists of a sensor, microprocessor, drive, power supply and structural elements as shown in fig.1·15. The drive such as a PM servo motors is the important part of a mechatronic product. The electrical servo drive is monitored by the processor, and it will respond and take action to execute instructions given by the processor, producing enough force and torque to subsequently move the driven mechanical structure to attain the desired speed and acceleration.

PM servo drives are supposed to amplify a reference signal and adjust the transferred power according to the commands from the processor. The servo system mainly consists of three components, the processor, the power electronics and the motor.

Generally a PM servo motor has the following features:

- Minimal size and mass.
- Control functions implemented by software.
- Flexible design.
- Energy efficient.
- Safe and reliable.

1.1.4.2 Servo drive technology in industrial robotics and manufacture

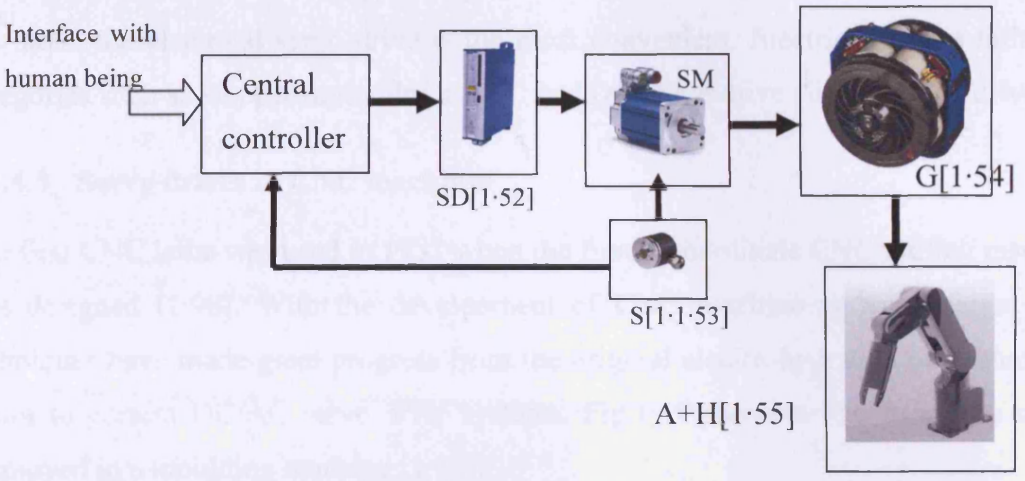

Fig. 1·16 Servo drive industrial system

The classical application for mechatronic products is industrial robotics. The industrial robot is an important part of a production line. The basic structure of a robot system is shown in fig.1·16. Its core is the central controller, which schedules sequential control, stores instructions and send out executive instructions to servo motion drives. To control precise rapid motion, the central controller is required to execute complex coordination transformation algorithms. The speed instruction of the mechanical arm is compared with the actual speed signal from a measurement and the difference signal is sent to the input of the servo amplifier. After power amplification, the amplified signal controls the torque and angular velocity of servo motors to position the mechanical arms smoothly and rapidly.

Rare-earth PM DC and AC servo motors are the first choice for industrial robot drives. Shaft position sensors used in industrial robots are generally installed at the non-load shaft end of a servo motor for measuring angular velocity and position. Therefore, the axes coupled with drives in industrial robots can be separately controlled with respect to the speed and position. The requirements from industrial robots are as follow:

1. The servo drive system should produce sufficient output torque and power,
2. The servo drive system should be able to make repetitive actions such as start-up, braking and switching directions,
3. The servo drive system should conveniently receive instructions from the central controller to implement torque and speed/position contro,;
4. The servo drive system must be stable and have a fast response.
5. The inertia of moving components should be as small as possible,

6. The servo drive system should be small in volume and weight.

Industrial drive has three types of power sources, namely, electrical, air and oil. Of the three, the electrical servo drive is the most convenient. Electrical servos falls into categories such as stepper motor drives, AC and DC servo drives linear motor drive, etc.

1.1.4.3 Servo drives in CNC machines

The first CNC lathe was used in 1953 when the first 3-coordinate CNC milling machine was designed [1·98]. With the development of CNC machine systems, servo drive techniques have made great progress from the original electro-hydraulic pulse and step motor to current DC/AC servo drive systems. Fig.1·17 shows a PM AC servo motor employed in a moulding machine [1·56].

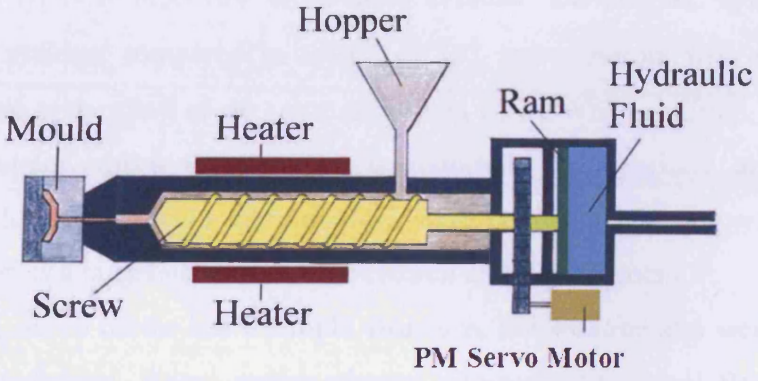

Fig. 1.17 PM servo motor application in a moulding machine [1·56]

CNC systems can store auxiliary machining programs to execute the various interpolation algorithms for real-time control and control instructions are sent to servo drives for the positioning of coordinate shaft axes. Servo drives can receive control commands, and adjust the motor speed smoothly and implement precise positioning.

The CNC machine system has the following requirements for the servo drive system:

1. A speed range over the ratio of 10000:1 for machining at low speed and reciprocation movement in high speed
2. High torque for acceleration and deceleration, for heavy cutting and rapid movement requiring the servo motor to produce high torque
3. Servo drive systems should make a fast response to give good dynamic capability of tracking, eliminating the load disturbance to motor speed
4. The inertia of the servo motor rotor should be as small as possible to improve the acceleration and deceleration performance of the servo system.

5. From low to high speed, the operation of a servo motor should remain smooth, the torque ripple should be as small as possible, severe pulsating and acoustic noise should not be generated during rotating motion
6. The servo motor should be safe and reliable with little maintenance needed. It may be required to work in hazardous environments
7. The interface with CNC machines should be easily accessed.

The load inertia and torque delivered at the shaft of a servo motor often vary with the change of the motion of the load. Generally, the CNC machine demands highly precise dynamic and statistic control, wide speed range and positioning precision.

1.1.5 Types of servo motors

There are two types of electrical servo drive systems; DC and AC synchronous and asynchronous systems compared in table 1·1. DC servo motors with speed/position sensors installed at the shaft of the rotor are driven by a PWM amplifier. However, due to the commutator, more maintenance is required, and sparking also limits the applications. Elimination of the commutator, while keeping the same performance as a DC servo motor, is a target of servo drive research and development.

The AC servo motor has a simple structure, low volume and weight, and does not need a commutator. Power semiconductor inverters and control flexibility of the microprocessor provides the possibility of eliminating the mechanical commutator.

Table 1·1 Comparison between DC Servo motor and AC Servo motor

Type / Content	PM synchronous AC servo motor	Asynchronous AC servo motor	DC servo motor
Structure	Simple	Simple	Complex due to brush and Commutator
Commutator	Inverter	Inverter	No
Max torque limit	Demagnetizing PM	No special requirement	Spark from commutating and demagnetizing PM
Thermal dissipation	Stator winding	Stator winding and rotor squirrel cage	Rotor

High speed	Easy	Easy	Difficult
High power	A little difficult	Easy	Difficult
brake	Easy	Difficult	Easy
Control algorithm	Complex	Complex	Simple
Flux generation	PM	Secondary	PM
Induced voltage	Armature induction voltage	Secondary resistance voltage	Armature induction voltage
Environment adaptation	Good	Good	Limited by spark
maintenance	No	No	Necessary

There are two types of AC servo motor: squirrel cage asynchronous and PM synchronous servo motors. The asynchronous AC servo system employs space vector transformation strategy for motor control. In order to imitate DC servo motor control, the stator current of the asynchronous servo motor is decomposed into two parts: excitation and torque. The excitation component of the stator current is aligned with the rotor flux; the torque component is orthogonal to the rotor flux. Due to complex calculations for the space vector transformation, asynchronous AC servo systems have poor performance at low speed and the asynchronous motors easily overheats.

Position signals are used to control the armature current of synchronous servo motors in phase angular steps, the armature current needs to be orthogonal to the rotor flux in vector space to generate the optimum torque. The flux of the synchronous servo motor is generated by the PM rotor and is supposed to be constant. This feature is similar to the DC servo motor. The torque is proportional to the stator current. However, if the stator current is not orthogonal with the rotor flux, the magnetic field in the air gap increases or decreases resulting in a change in operating conditions.

1.1.6 Introduction to the PM synchronous motor and servo drive systems

Synchronous AC servo motors with PM rotors have wider applications than squirrel cage asynchronous AC servo motors in the low/middle power level. The main reason is that the performance of PM material has improved continuously while its price has dropped and the vector control algorithm for the PM synchronous motor is simpler to implement than with the asynchronous AC servo motor.

The PM synchronous servo system consists of the following components:

1 ***PM synchronous servo motor:*** **This** consists of the stator and rotor. The rotor has surface-mounted magnets or they are embedded deeply inside. The PM body in the rotor can employ hard ferrite or NdFeB magnets. The three phase armature windings installed in the stator core are connected to the converter. The stator core is directly exposed in the external environment through the housing which dissipates heat.

2 ***Speed and position sensor:*** This is installed at the non-load end of rotor shaft. Encoders are required for precise position control. For PM synchronous servo motors, further sensors for rotor poles need to be mounted. The pole position is measured to carry out control of the armature current. Practically the rotor angular velocity, pole position and shaft position can be measured by a single optical encoder or tachometer. At least two functions of three can be completed by one sensor. Single sensor usage for multiple functions can reduce the size of the motor drive system in the axis direction and simplify control and installation.

3 ***Power converter and PWM strategy:*** A power converter consists of a rectifier and an inverter. The rectifier is used to commutate single/3 phase AC input current into DC pulsating current, which is filtered and smoothed by a DC link capacitor and fed into the inverter as the DC input voltage. The inverter is used to transform the DC input voltage into AC voltage with variable frequency and amplitude by PWM trigger signals. The AC PWM output voltage is fed to the stator armature of the servo motor. PWM trigger signals are generated by the microprocessor and software to switch power semiconductors at variable frequency and it generates AC sinusoidal armature current.

4 ***Speed and current controller:*** The speed controller employs a Proportion Integration (PI) regulator to give out the current/voltage reference instruction. A speed controller is used to stabilize the angular velocity and prevent it from oscillating. For position control, a speed loop is required to have rapid response to speed instruction, and remain stable during any disturbance.

The current loop acts as the inner loop relative to an outer speed loop in the space vector loop control PM synchronous drive system. The inner current loop synthesizes current instruction and feedback signals to tune the phase and amplitude of the current in the armature winding for controlling current and flux vectors or for high speed field-

weakening control. The current controller generally employs a PI regulator to implement faster response.

Speed instructions and measurements are compared at the input port of the speed controller to generate current instructions. The DC current instructions from the output port of the speed controller have to be transformed into equivalent AC current instructions. The phase of the AC current is determined by the position of the rotor poles while the frequency of the current instruction is decided by the angular velocity of the rotor. The transformed AC current instructions can generate the AC current whose vector is orthogonal to the rotor flux in space, thus space vector control can implement torque control similar to the DC servo motor. The position information is measured by a position sensor and passed into a microprocessor which executes the coordinate transformation based on DC current instruction and position to calculate instantaneous AC current or voltage reference/instruction by space vector strategy.

Instantaneous AC current instruction can be compared with the measured current to generate the control error which is sent into the current controller. The fast track of the current controller can generate the sinusoidal current with a similar waveform to the AC current instruction and higher amplitude in the stator winding for implementing the speed requirement. The AC current can generate electromagnetic torque through the reaction with the PM body to make the rotor move.

1.1.7 Research activity into sensorless control

Space vector field-oriented control PM Synchronous motors (PMSM) require the detected angular position of the rotor pole to calculate trigonometric functions for coordination transformation. Commercial servo drives based on PM synchronous motors generally employ position sensors to measure the angular position of the rotor pole. The added position sensors reduce the reliability of the mechanical structure and the cost is increased.

Sensorless control PM synchronous motors calculate the angular position of the rotor pole through electrical quantities such as DC–link voltage and current in the winding. Sensorless control synchronous motor techniques were explored as self-commutated synchronous motor without a shaft position initially by Plunkett [1·100] in the late 1970's and Davoine [1·2] in the early 1980's. The term "Sensorless" was used to describe the synchronous motor control without a shaft position by Iizuka [1·99].
There are three kinds of sensorless control PMSM methods. One method is to measure speed-dependent variables such as back-EMF, flux linkage or its 3rd harmonic

[1·1,2,3,99,101~105,]. In order to obtain the back-EMF/flux linkage, direct access to machine terminals for armature current and voltage is usually required. Plunkett and Turnbull [1·100] used the terminal voltage and AC line current to extract the sine of the phase angle through calculating flux linkage for synchronous motor operation without shaft position and subsequently employing a hybrid controller based on mixed signal hardware to implement it, although the test was subject to obsolete mixed analogue/digital circuitry. Davoine and Perret [1·2] also employed a similar EMF-detection circuit to replace shaft position for synchronous motor commutation. Iizuka [1·99] further used a terminal voltage sensing circuit by low pass filters and voltage comparators to obtain the back-EMF of a synchronous motor. The improved EMF detection circuit was applied in sensorless control brushless PM DC motor by Ogasawara [1·3].

Since high speed DSP has been used in motor control, the back-EMF algorithm is alternatively implemented digitally. The subsequent issue is the various errors, for example, a DC thermal drift, measurement offset, etc. Wu [1·103] considered the issue of the integration error and employed a mixed solution combining the analogue integrator with a microcontroller to complete back EMF type position estimation. Instead of the DC link voltage, line-to-line voltage and current are measured to deduce back-EMF. To eliminate noise amplified by the integration, a digital low pass filter was implemented by a microcontroller. Regarding DC drift of flux linkage, the real and imaginary components are modified by adding the measured average drift quantity before the real and imaginary values are used to induce the rotor position. The experiment [1·103] showed that the compensation for DC drift effectively reduces the oscillating position error.

The error of EMF-based estimated position is linked with that of flux linkage. The direct correction flux linkage can effectively reduce the error of estimated position. For example, Ertugrul and Acarnley [1·4] built up a three phase PMSM model in an a-b-c coordination frame to detect 3 individual phase flux linkages by integration. However, two additional current loops are employed to correct the errors, the outer current loop is used to correct the initial position estimation from the extrapolation of former estimated position. The inner current loop is used to correct the measured flux linkage by the updated predicted position. Eventually double current loop correction gives very smooth flux linkage waveforms.

Kim [1·105] tried to solve the issue from the voltage/current waveform. The estimated position and speed can be extracted in the transient state such as speed

fluctuation or sudden load variation when the PMSM is modelled in the d-q reference frame. Moreover the position error can be predicted by the error-track equation provided by a specific model at every step. The experiment by the approach [1·105] can make PMSM operate at the lowest speed of 50 rpm, however, this approach also requires line-to-line current measurement. The back-EMF method is also adapted for sensorless, trapezoidal-EMF, PM motors. Moreira [1·101] used the summation of three phase voltages to extract third harmonic components of the back-EMF so the sinusoidal third harmonic component could be treated by the back-EMF method to get the rotor position. Terminal voltage detection for back-EMF detection may introduce noise and reduce system reliability.

The back-EMF method for sensorless control PM motors hardly works at very low speed or at standstill when the back-EMF is too weak. The integration error needs to be compensated for during the position extracting process. The differential extraction method was alternatively considered [1·10]. Ying [1·10] calculated the incremental values of flux linkages and back-EMF functions from three phase voltages and currents to derive the rotor position increments which were further used to induce rotor position. Its implementation by the help of DSP and Phase-Locked Loop (PLL) can enable the PMSM to accelerate from standstill. However, the measurement of phase voltages replies on the neutral point of the three phase motor. Only the DC link voltage is convenient for detection in sensorless control.

Due to low computation load and memory requirements for implementation, back-EMF detection for sensorless control PMSM is suitably used for servo drives in medium and high speed ranges if self-start up is not required so the back-EMF method is able to obtain high estimation accuracy relative to other methods. For example, Shen [1·102] used full-digital implementation of direct flux linkage estimations to make the maximum estimation error 4.5 electrical degree, which shows that back-EMF method is capable of obtaining sufficient accuracy for most vector control servo drives.

The application of back EMF-based sensorless estimation is mainly limited in arbitrary self starting and at low speed because of the low amplitude of back-EMF. Ribeiro and Harke [1·104] concluded that sensorless estimation for PMSM based on back-EMF must operate at higher speed than the stability limit if the track command and disturbance rejection need to be maintained.

Currently the main interest for sensorless control PMSM is in observer-based estimation or signal carrier injection estimation which can overcome the drawbacks at low speed or arbitrary start up. Techniques used in back-EMF estimation such as low

pass filter are still employed in sensorless estimation such as observers or signal injection for PMSMs.

The second method is observer-based state estimation [1·5,6] in which the position and speed information along with other variables in the PMSM model can be derived from digital differentiation using measured voltages and currents. The position estimation method by a state observer is the most popular sensorless method, even currently facing competition from the high frequency carrier-signal injection method. The state observer estimation is essentially the differential solution to a multi-order dynamic PMSM model. The state/vector in the observer model consists of more than one variables including rotor position, speed or other variables from the PMSM model. A state observer estimation for sensorless control PMSM is always accompanied by the error correction scheme which makes the observer-based sensorless estimation feature a strong ability for self start-up from an arbitrary position. The state observer for sensorless control requires a dynamic math model for PMSM where the derivative of the system state is expressed by the linear or nonlinear relationship between the system state and input state.

The observer controlled PMSM was studied [1·5] before DSP was employed to implement digital state control. Jones [1·5] investigated the nonlinear identity state observer to estimate the electrical/mechanical quantities for PMSM by simulation. The d-q transformed model [1·5] is driven by voltage and innovation. The simulation [1·5] showed that the error of state in the observer can converge rapidly in one electrical cycle and is robust for large disturbance.

More advanced state observers have started to be used in observer-based sensorless controlled PMSMs. The most representative state observer for sensorless controlled PMSM is the Extended Kalman Filter (EKF) [1·6,12,16,106,107]. Dhaouadi et al. [1·6] first used the EKF observer to implement rotor position and speed estimation for sensorless control PMSMs and 4-order nonlinear dynamic PMSM models [1·6]. The recursive state expressions are composed of 16 single-order equations and contain four types of vectors for system states and corresponding covariance states respectively in prediction and filtering stages, thus a 16-bit 25 Khz fixed-point DSP [1·6] has to be employed to deal with the heavy computation load and successfully complete the rotor and speed estimation for PMSMs. Covariance-based correction gives EKF-based sensorless controlled PMSMs satisfactory self start from arbitrary positions. Its result suggested that the initial matrices for system noise, measurement noise and covariance

state are better set by the diagonal matrices due to the lack of sufficient statistical data to evaluate off-diagonal terms.

In spite of success of the first EKF-based sensorless controlled PMSM, the EKF observer [1·6] is characterized by heavy computation requirement, high parameter sensitivity and random initial condition. Bolognani [1·16] improved the nonlinear PMSM model for the EKF observer under the infinite inertia hypothesis which eliminates any mechanical load parameters. The initial matrices for measurement and system noise follow the diagonal pattern [1·6] and their selection depends on optimised trade-off between filter stability and convergence time by trial-and-error. The improved EKF observer was implemented in full-digital control drive by float-point DSP. The experimental results [1·16] show the estimated rotor position has satisfactory linearity and corresponds with the actual position. It is also recognised [1·16] that the infinite inertia hypothesis generates a steady-state error, which makes the derivative of the estimated position more reliable than the estimated speed. The 4×4 element of the initial covariance matrices is found to affect the convergence speed in two aspects: a sufficiently high value helps to remedy the wrong convergence while a small value might avoid slow convergence. The minimum speed by the EKF observer can drop to 40 rad/s [1·16].

The EKF observer under infinite inertia continued to be studied over wide speed range at full torque [1·106]. The reference space vector modulating signal replaces the measured voltage and a leading component is added for delay compensation. A dedicated algorithm [1·16] for start up is used in the EKF observer to correct the misconvergence. The transient direct-axis current pulse was used to solve the locked rotor from start up and a d-current reference equation from the trial-and-error experiment was given [1·16].

To counter measure the flux linkage error, a closed-loop on-line tuning procedure by low pass filter and absolute block was used [1·16] to make a EKF observer robust to electromagnetic parameter variation. The load experiment [1·16] showed that the EKF-based sensorless controlled PMSM was able to deliver rated torque from rated speed (419 rad/s) to 35rad/s, a speed range ratio of 1:12. The EKF observer has been recognised [1·6, 16] to be an optimal estimator of the least-square error of the the dynamic nonlinear PMSM system. However, it is difficult to design and tune the covariance matrices as a standard procedure.

An alternative method was investigated [1·107] to find the optimal initial matrices settings for EKF-based sensorless controlled PMSMs. The investigation into

both motor control and electromechanical design [1·107] revealed that suitable normalization can give a PMSM with isotropic parameters varying over a narrow range regardless of motor size. The novel procedure features the combined normalization of both the controlled PMSM model and the EKF algorithm. It was also validated that the normalized covariance matrices could roughly fit most standard PMSM drives [1·107].

The EKF-based sensorless estimation for surface-mounted PMSMs is not straightforwardly applicable to IPMSMs due to both PM and reluctance torques existing in the IPMSM [1·12]. Most EKF-based sensorless estimation methods for PMSMs [1·6,16,106,107] are applied only for the surface-mounted PMSM with an isotropic rotor. The variables in the system state of the EKF observer are not limited to position, speed, voltage and current. Any variables such as stator or rotor flux from the PMSM model can be chosen as state variables to estimate rotor position/speed indirectly. Model Reference Adaptive Control (MRAC), the Extended Kalman filter (EKF), and other sensorless control schemes based on the application of sophisticated identification procedures can enable low and zero-speed operation but are too complex and expensive to be used in practical systems.

Since the full-order state [1·108] used nonlinear techniques to design a second-order observer, two new constructed variables are estimated instead of phase voltage and current. The rotor position and speed are eventually derived from the two variables. The simulation reveals [1·108] that the position and speed errors can converge soon to zero at low speed and the estimated position is not sensitive to uncertainties in mechanical parameters and torque disturbance. As in [1·5] it was concluded that the nonlinear observer is more sensitive to electrical parameters [1·108].

Although the reduced-order observer for position estimation is implemented through less digital Euler integration by microprocessor, it doesn't mean that the rotor/speed can be estimated directly without any computation cost. The state observer [1·108] consequently relies on a nonlinear structure such as an arctangent function or root square to calculate position/speed. Therefore the desired state observer estimates the variables directly by digital Euler integration [1·109].

To exhibit the ability of the state observer for a sensorless PMSM, Snary et al. [1·109] adopted the same full order d-q dynamic nonlinear PMSM model as the literature [1·110-112] to construct the state observer. A similar approach is employed to linearize the d-q PMSM model by defining the voltage and the coupled variables as new variables. The principle of observer design is to assign eigen values of the observer for the state error to converge faster than PMSM electrical dynamics.The subsequent

observer gain matrix was produced by assigned eigen values. The state of the observer [1·109] excludes the rotor position as a variable but includes angular velocity. The rotor position is extracted from the integration of speed and the error-correction mechanism is adopted from the corrective scheme by Matsui [1·113]. The d-axis voltage error in sensorless control PM motors is approximately proportional to the error in rotor position. The asymptote observer was consequently mathematically implemented to estimate the rotor position through a matrix converter fed PMSM [1·109]. The experiment [1·109] showed that the steady-state position error under load is 0.25 rad/s if the load torque state is included in the observer. It is also recognised [1·109] that low power operation at 6% full load torque is poor because the performance is reliant on the phase current measurement with low amplitude. The asymptotic observer requires the additional error-correction scheme, and only an approximate linearized structure is assigned with eigenvalues, thus not all desired variables apart from speed can converge. To make all desired variables converge, a nonlinear observer had to be validated in a sensorless controlled PMSM. Zhu and Kaddouri used elaborately implemented the rotor/speed estimation through a nonlinear observer for sensorless controlled PMSM [1·114]. The proposed structure solely requires line current measurement. The nonlinear observer is derived by new (y, z) coordinates changes while the variables for rotor angle and speed are extracted respectively by nonlinear functions, Moreover, the nonlinear observer gain matrix has to be a nonlinear function of the state variables. An additional nonlinear controller is designed by the linearization similar to the approach in the literature [1·109-112].

The speed regulation law of the nonlinear controller adopts PI regulators driven by the position, speed and current errors to generate the d/q-axis voltage obtained without measurement. The nonlinear gain matrix and nonlinear PI regulator coefficients must be calculated by simulation. The consequent test [1·114] shows that the speed quickly converges to the reference and recovers from the load torque disturbance. Meanwhile, it was found [1·114] that the speed regulation performed poor during the speed reference transition at low load. The open-loop start-up[1·114] implied that the transient speed command can't be applied on heavy load.

Angelo and Bossio [1·115] employed a reduced-order observer to estimate the induced EMF and load torque first and then the rotor position and speed were indirectly derived through the relationship with torque and EMF for closed-loop control. The experiment for the load observer [1·115] shows that minimum torque ripple and copper loss were produced during the sensorless operation. The design for the asymptotic type

of state observers commonly features high exponentially convergent rates for the error of estimated state. State feedback linearization [1·109~114] is the sole solution to treat the nonlinear PMSM model. Other solutions [1·116] were tried to separate the coupled variables in nonlinear PMSM models. For example, Lian and Chiang [1·116] used the Takagi-Sugeno fuzzy model to replace the conventional nonlinear PMSM model. It was concluded [1·116] that the control gain and observer gain can be separately designed in the Takagi-Sugeno fuzzy model of the membership function satisfying Lipschitz–like condition. The control gains were calculated based on linear matrix inequalities method by offline MATLAB simulation, afterwards, a state observer was designed to estimate the rotor position and speed. The experiment [1·116] showed that the fuzzy-model observer implemented the sensorless controlled PMSM and obtained the rapid transient speed response. The test result [1·116] shown that the measured position error shown to be less than 0.0125 rad/s and the speed error is within 2-3 rad/s for sinusoidal reference and 0.3 rad/s for low speed reference. The appropriately linearized PMSM model can improve the rotor/speed estimation for sensorless operation, contemporary control theory such as fuzzy control decoupled the nonlinear terms of PMSM model only by a new mathematical approach to decouple the nonlinear PMSM while keeping the classic PMSM math model. For example, Nesimi and Acarnley [1·11] proposed an observer based on the classic PMSM math model in the ABC coordinate frame with flux linkage and equivalent phase inductance as new defined variables. The introduced new flux linkage refers to flux linkage by the rotor PM body from the view of state phase windings while new equivalent inductance refers to the difference between self and mutual inductance. These two newly defined variables transform the nonlinear PMSM dynamic model into a linear magnetically decoupled model with a diagonal coefficient matrix.

The discrete rectangular integration on the linearized model is used to estimate the total flux linkage, and the estimated flux linkages are combined with magnet flux linkage at the position predicted previously to extrapolate the estimated current through a second-order polynomial curve since the magnet flux linkages are obtained by measuring back EMF in the individual test. The estimated line current can be used to derive the estimated position error by the partial derivative and relationship between the ideal back EMF and rotor angle. Eventually the average position error for three phases is used to produce a single correction for initial rotor position. The structure of the observer [1·116] is actually the three-level error cascade loop control system for line current error, flux linkage error and position error.

The state observer was implemented to estimate the rotor position in sensorless control PMSMs. The experiments [1·116] shown that the estimated rotor position agreed well with the actual one for both rectangular current-excited and sine wave current-excited drives. Moreover, the state observer can overcome the initial rotor estimation error to implement self start up due to strong correction. The state observer [1·11,115] essentially introduces back EMF measurement into the state observer, making most use of the relationship between EMF and rotor position. The drawback is that state observers are heavily dependent on the electrical parameters; thus the performance of the rotor position estimation will deteriorate as the motor parameters vary with thermal and operational condition. Such problem can be overcome to some degree by using on-line adaptive tuning [1·117,118], but on-line tuning intensifies computation from the microprocessors. Moreover, the observer-based method suffers from low frequency problems since the signal-to-noise ratio of the sensed voltage is poor at low frequencies and measurement of voltage and current is subject to the maximum precision of the A/D converter. However, compared with solely back-EMF detection, the state observer-based rotor position estimation scheme has a comprehensive performance in detecting more electrical parameters including load torque and error-correction capability to implement the self start up from almost arbitrary positions. Hence the state observer is a very strong candidate for the sensorless scheme in the medium to high speed range.

The back-EMF detection and state observer both are susceptible to poor behaviour when the speed is very low or zero. Therefore a third method is introduced to detect the rotor position based on spatial saliency by high frequency signal carrier signal injection. Instead of a parameter-sensitive observer, the position/speed information is extracted from the response of the high frequency excitation applied to the PM motor. Rotor position detection techniques based on phase inductance evaluation, originally named as the indirect flux detection by Online Reactance Measurement (INFORM) method [1·5,18], give reliable low and zero speed operation in machines with self or induced anisotropy. However, the INFORM-type sensorless techniques generally give a discrete position detection in a specific limited speed range and need to be complemented by a state observer for medium and high speeds.

Usually, special high frequency signals are injected into the motor stator windings with normal digital signal processing techniques such as DSP to obtain the position information except in the special case of specific function hardware implementation without CPU [1·7]. Besides, the operational PWM voltage applied in

PM motor also generates additional current signal to detect the rotor information. For example, Ogasawara and Akagi [1·8] employed a operating PWM voltage to generate the current harmonics as an additional signal which can be used to estimate the inductance matrix of an interior PM motor containing rotor position information. Wang and Xu [1·9] developed a similar rotor position estimation to measure current change from the voltage vector for a PM motor with or without saliency.

Since the high frequency excitation is independent of the motor speed, high frequency injection methods can be used at low speed and at standstill. However, the high frequency injection method may cause some undesirable side effects such as a torque oscillation and harmonic losses. Different types of carrier signal are used in the signal injection method. For example, Schrödl and Stefan [1·13] proposed a periodic burst signal injection method. Jansen and Lorenz [1·18] employed high frequency rotating signal injection and Ha and Sul [1·81] used a high frequency fluctuating signal injection method.

Inductance variation also can be used to detect rotor initial position by injecting specific PWM signals for PM motors [1·15]. For example, [1·15] proposes an initial rotor position detection method for a salient PM motor at standstill to make the rotor avoid temporary reverse rotation from start up failure. The approach is based on the saturation principle of a salient PMSM where the angle between current and magnet axis affects the saturation level. Rotor position detection also requires the excitation of a proper sequence of voltage pulses and the peak values measurement of the resulting current.

The specific PWM signal not only can generate the steady response for saturation-based rotor position detection [1·15] but also the transient response for observer-based sensorless schemes. For example, Vladan and Stankovic [1·17] used the inherent high-frequency content of PWM excitation to measure position-dependent inductance parameters through least-squares parameter estimation by a nonlinear observer. Accordingly the modified PWM scheme using all six nonzero vectors in each PWM period had to be employed to generate the additional harmonic for exterminating parameters. The method [1·15,17] relies on position dependence of motor inductances due to magnetic saliency. It usually involves injection of an auxiliary signal to probe the motor electrical subsystem, and use the response to such excitation to estimate the position [1·18-23]. The inductance variation is not the only feature of a salient PMSM for signal injection-based rotor estimation methods, the cross coupling from a spatial saliency [1·7] can be utilized to estimate the rotor position of interior PMSM. Corley and Lorenz [1·7] intentionally build up the d-q PMSM model in the rotor reference

frame to implement the decoupling of d- and q-axis flux. Carrier-frequency voltage was applied to generate the desired decoupled flux and resulting high frequency current with amplitude modulated by the error between actual and estimated rotor position, the resultant current is similar to that in a resolver and Resolver-To-Digital Converter (RTDC). The experiment [1·7] implemented by specific hardware show good tracking ability for position estimation at speeds down to 4.6 rpm and up to 5000 rpm. The carrier-signal injection method by Corley and Lorenz [1·7] relies on high frequency saliency of the PMSM rotor. Jansen and Lorenz [1·18] reported a similar method with a lower injection signal frequency to complete carrier-signal rotor estimation for a salient PMSM with a sinusoidal variation in the inductance.

Unlike the high frequency carrier-signal injection method, the PWM or other type signal injection position detection method is usually used only for the initial rotor position detection in the low or zero speed range. Hence linking it with other sensorless methods is a practical solution for full speed range operation. The cooperation scheme between PWM signal injection at start up and back-EMF/a state observer at rotation has been reported [1·19, 20] which use interior PM motor saliency at start up and switch to state observer-based or back-EMF-based algorithms at higher speeds. Due to disturbance from the injected signal, the estimated initial rotor position suffers from various errors [1·19, 21] so it is necessary to use error-correction state observer to improve the estimation. Schroedl and Weinmeier [1·21] also combine the two position sensing principles to implement sensorless control over the full speed range. The approach used carrier-signal injection (INFORM method) for position estimation at low speed then switches to the back-EMF method at higher speeds. A Kalman filter is used to estimate the mechanical variables and load torque to improve the accuracy of position estimation.

The rotor saliency of PMSMs affects the magnitude of the stator carrier current modulated by injecting a high frequency voltage into zero-speed signal. Bianchi and Bolognani [1·72] investigated the INFORM-like sensorless controlled inset PMSM which is similar to SPMSM except for the iron tooth between each pair of adjacent magnets and concluded that INFORM-like sensorless detection for inset PMSM for low and zero speed can produce better performance than that for IPMSM because inset PMSMs have the larger rotor flux path whose saturation can be weakened. On the contrary, [1·72] reported that the saturation in the magnet path of a rotor from IPMSM easily occurs with the current increasing. [1·72] implies that the signal injection based

sensorless method at zero and low speed is effective under high current or load when saturation of the rotor can be avoided or decreased.

Carrier-signal injection-based sensorless control methods need the high frequency carrier-signal voltage injected into stator windings, and then the resultant negative-sequence carrier-signal current and zero-sequence components can be used to track the spatial location of asymmetries from the rotor saliency. García and Briz [1·73] analyzed the accuracy and the bandwidth of the position estimation. Either wye-connected AC motors or delta-connected ones under the control of carrier-signal injection such as INFORM can produce the interaction between carrier-signal injection voltage and saliency, and both the negative-sequence carrier-signal current and zero-sequence carrier-signal voltage from the interaction can be used to derive angular position of rotor saliency.

The effect on overall position estimation by the total harmonic distortion (THD) of negative-sequence carrier-signal current and zero sequence carrier-signal voltage taking the decoupling of secondary saliencies and other noise into account has been investigated [1·73]. The variation trend for the THD of the negative-sequence carrier-signal current with frequency increasing is opposite to that of the zero-sequence carrier-signal voltage. The error in decoupling plays the major role on the THD. The carrier signals contain two types of disturbing components, colour noise and white noise. The first is related to specific frequency and is caused by incorrectly decoupled secondary saliencies while the second exists in measured signal. It is found [1·73] that the estimation accuracy can be more severely affected by the rotor saturation induced from a single secondary saliency than multiple noise. The sources for THD of the resultant carrier-signal current/voltage are errors in the injected carrier-signal voltage and measurement. Although increasing the magnitude of carrier-signal injection voltage can mitigate a given amount of distortion, a series of drawbacks such as loss and vibration will be brought into practical operation. Whereas [1·73] recommends alternatively to increase the carrier frequencies which is subject to inverter switching frequency and microprocessor capability.

Further analysis [1·73] targeted three factors for THD of carrier-signal injection voltage, i.e., nonlinear behaviour of the inverter, PWM strategy and the current regulator reaction to the negative-sequence carrier-signal current. PWM strategy is classified into two categories, symmetric regularly sampled PWM and asymmetric regularly sampled PWM. It is found [1·73] that they both can produce a component of that frequency which is near to the negative-sequence carrier signal frequency and

would coincide and resonate with carrier signals. It is pointed out [1·73] that the asymmetric triangle wave from PWM would enhance the magnitude of the resonant component in the injected carrier-signal voltage more than that by a symmetric wave. The resonant component produced by PWM strategy causes THD to increase significantly with the carrier frequency. The current regulators during the carrier-signal injection operation attempt to compensate for the fundamental current by adding terms to the voltage command, these terms contributes to the THD significantly. When torque step-like commands cause a fast transient response in the current regulator output voltage, the frequency portions of the transients might coincide with the negative-sequence carrier-signal frequency to form THD also. In order to reduce the current regulator interference with the carrier signals, it is advised to separate the carrier frequency from the current regulator bandwidth and used band-rejection filters in the current feedback path to decrease the magnitude of the harmonic components the from carrier signals [1·73].

THD of the resultant carrier signals are reported [1·73] to be affected by the measurement of carrier signals also. The sensor and A/D converter for phase current measurement can also be used to detect the negative-sequence carrier-signal current while the zero-sequence carrier-signal voltage measurement has to employ additional sensors and A/D converters though motor terminals and the neutral point. However, the full range of current sensors and A/D converters are not able to be completely used to measure negative-sequence carrier-signal current since a considerably large part of the A/D converter input is used to scale the current sensor range for over-current. Conversely, the full range of voltage sensors and A/D converters is capable of measuring zero-sequence carrier-signal voltage. Therefore, [1·73] concludes that zero-sequence carrier-signal voltage with better scale of measurement can improve the signal-to-noise ratio, and negative-sequence carrier-signal current scaling can produce a low signal-to-noise ratio with the carrier frequency increased.

The influence of the A/D converter bits number on THD of carrier signal has been investigated and it was found that A/D converters with bits number less 10 are not able to establish stable carrier-signal injection sensorless control due to high THD generated [1·73]. Furthermore, over 10-bit A/D converters are able to obtain similar small THD of carrier signals which satisfy the essential criteria for sensorless operation. The frequency spectrum analysis [1·73] shows that the bandwidth for the case of zero-sequence carrier-signal voltage can be more easily used to isolate the frequency of

carrier signals related to the saliency from measured signals than that of the negative-sequence carrier-signal current.

Ideal sensorless control PMSM should be able to detect not only the initial rotor position but also the magnet polarity. However, most of high frequency carrier-signal injection sensorless methods can detect the axis of the magnets but not the polarity. If the north-south poles need to be identified, the pilot voltage will be injected into the stator winding and the responding current is utilized to decide the polarity through the magnetic saturation. Ostlund and Brokemper [1·19] explored initial rotor position detection and N-S identification by applying voltage pulses to attract the rotor by 360°. One drawback from such detection is that the accuracy is decided by the angle step length. The second is that the method [1·19] requires pre-alignment of the rotor before the voltage pulses are injected. The pre-alignment of the rotor cannot implement N-S detection at an arbitrary rotor position.

Hu and Liu [1·73] improved the initial N-S identification method by Ostlund [1·19]. Although high frequency carrier signal injection is employed first to get an accurate initial rotor position angle, the subsequent voltage pulses are injected to align the rotor to the identified angular position referring to the initial rotor position identified by carrier signal injection. The approach by Hu [1·73] overcomes previous pre-alignment drawbacks [1·19] about and is able to predict N-S polarity. Considering the fact that the PMSMs with some rotor saliency are commonly designed to produce little eddy current effect, the approach by Hu [1·73] specifically chose a synchronous motor with damping windings as an equivalent PMSM with an eddy current effect. Hence, the mathematical mode for a PMSM with eddy current effect regards the eddy current as the extra current circulating through a pair of short-circuited coil along d and q axes, which is similar to the literature [1·74,75].

For an approximate PMSM with short-circuited coils on the rotor in [1·73], the conventional high frequency carrier signal is required to contain the eddy current compensation before being superimposed on the fundamental excitation voltage. Then the initial rotor position can be extracted by a signal demodulator from the carrier signal response current. Aihara [1·76], Wang [1·77] and Ortega [1·78] discuss the identification N-S polarity based on magnetic saturation effects, the flux increment is commonly in direct proportion to the current increment if the magnetic path is not saturated; however, the excessive increment in current can cause a smaller increment in flux when the magnetic path is saturated, so the previous methods [1·76-78] apply the stator voltage excitation in the same polarity as that of the rotor PM to confirm the

saturation and the stator voltage excitation is applied in the opposite polarity as that of the rotor PM to confirm non-saturation. The core saturation nonlinearity can determine different magnitudes of current increment caused by the same voltage excitation. Hu [1·73] also follows and improved the previous method [1·76, 77, 78]. After the axis of the initial arbitrary rotor position is decided by the carrier-signal injection method, a pair of "+" and "-" pilot voltage are injected with same magnitude according to the axis direction of the rotor PM. Then the magnitudes of responding current increments are compared to identify N-S polarity. In order to determine out which phase winding is closest to the rotor axis, the excitation voltage is based on Space Vector PWM and the sensed 3-phase currents are transformed into synchronous reference frame before obtaining the polarity information.

It is reported [1·79] that back-EMF-based sensorless estimation methods for PMSM are capable of working at above 3% nominal speed, conversely the high frequency carrier-signal injection method can make PMSMs operate below 3% of nominal speed including zero speed. The rotor position detection at standstill by previous carrier-signal methods utilizes the anisotropic characteristics of PM rotors which comes from two different sources, the saliency of the interior PM motor and saturation in surface-mounted PM motors.

The anisotropic magnetic structure of the rotor contributes to the induced carrier-signal current, which need to be extracted from the fundamental frequency current. Generally the angular orientation in space of the rotor is calculated from the differences in amplitude and phase angle between carrier current and voltage. The exploration of relationships between the carrier-signal current and voltage require not only the preferable effect of anisotropic properties of the rotor to be considered but also the adverse effect of the delays and the nonlinear distortion yielded by the PWM inverter.

It is difficult to eliminate the distortion introduced by PWM inverters from the carrier current containing the anisotropic information. Currently two types of carrier signals have been employed by INFORM-based sensorless estimation. One type is a revolving carrier signal [1·7, 19, 80] which is generated by a rotating high frequency carrier-signal voltage vector. The second type is an alternating signal by [1·20, 81] which makes reaction in a specific time-variant spatial direction. Neither type of carrier signal method is required to implement smooth start without producing electromagnetic torque in the initial rotor position detection.

The carrier signal injection method by Corley [1·7], Ostlund [1·19] or Jeong [1·80] can identify the magnetization axis through analyzing the negative sequence component of the carrier current. The carrier current must be high enough to change the saturation of the stator core when the rotating carrier vector is aligned with the rotor magnetization axis to produce the second harmonic component in the carrier current. Also it suffers from low sensitivity. The second method for initial rotor position detection by oscillating carrier in time-varying spatial orientation [1·81,20] can also work well through changing the saturation when the direction of the carrier current coincides with the magnet field Ha [1·81] exploited the magnet polarity through analysing second order current harmonic component. Haque [1·82] alternatively injected a series of carrier signal voltages with different amplitudes to survey the oscillating field rotating along the circumference of air gap. The oscillating field generated by the carrier signal voltage would align with the d-axis to produce the maximum and minimum values, obviously the maximum one corresponds to direction of the positive axis.

The oscillating carrier signal method also meets the problems such as inaccuracy in measurement, periodic rotor error caused by dead time, excessive torque oscillating over fundamental frequency, low signal-to-noise ratio, low sensitivity to the anisotropic structure and parameter dependence of carrier-signal types. To address these issues, Holtz [1·79] continues the work of Linke [1·83, 84] to investigate a two-phase equivalent orthogonal PMSM model, which consists of excitation and detection windings. The model by Holtz benefits from no magnetic coupling between orthogonal phases. The permanent magnetic rotor is defined to saturate the stator core locally and exhibit a magnetic anisotropy by a partial enlarged air gap, a new defined variable. As the flux density by the new excitation phase is also introduced by Holtz [1·79] to detect the rotor position, the specific excitation flux density is an independent field component small enough not to change the core saturation.

Holtz [1·79] concluded that the amplitude of the induced current in the detection winding is proportional to the displacement angle, provided the excitation current and its induced flux distribution is time-varying. Subsequently a coordination transformation is employed by Holtz to convert the specific excitation winding into a 3-phase reference frame rotating synchronously with the rotor. The carrier-signal voltage injection in the spatial north pole direction of the PM rotor generates a corresponding spatial excitation flux density and carrier current both dependent on the anisotropic condition. This is because the spatial excitation magnetic flux is attracted by adjacent

region of low magnetic resistance while the carrier current vector is attracted by similar regions of low inductance. To minimize the phase displacement between carrier voltage and current created by the spatial deviation between the respective vectors, Holtz [1·79] employed a superimposed control loop to manipulate the injection angle whose error with the phase displacement finally converges.

Compared with existing methods, both the position information and the reference signal are affected by the delays and nonlinear distortions of the inverter since the carrier current is used as the reference instead of the injected voltage. The benefit of new rotor position estimation is that there is no disturbance in position information. The experiment by Holtz [1·79] demonstrates the carrier-signal method based on the new model has high sensitivity, position accuracy and low signal-to-noise ratio. Also it can work on surface-mounted PMSMs with weak anisotropic properties.

Teske [1·86], Guerrero [1·87] and Choi [1·88] report that Zero Current Clamping (ZCC) exists during the zero and low speed operation of high frequency carrier signal injection sensorless estimation. The cause is that the phase current has multiple zero-crossings due to high frequency signal force when the fundamental phase current is close to zero. [1·86~88] find that ZCC can easily cause disturbance and generate position error ripple. The speed/current control bandwidth and dynamic response of torque are thus limited by the ZCC effect. The field orientation might be lost finally because of ZCC effect. To address this issue, Teske [1·86] employed a look-up table of phase current and rotor position measured by test. Choi [1·88] used a correction scheme through ZCC modelling for a periodic HF carrier signal in a stationary reference frame to compensate for the disturbance and error ripple. Meanwhile, Kwon [1·89] was aware of essential modelling for voltage distortion for cancelling the ZCC effect in the pulsating HF carrier signal injection estimation. Thus the related distortion factor around the zero-crossing event for the fundamental current is defined as a distortion factor.

Previous work [1·86~89] about cancelling the ZCC effect shares the same drawback. Many offline tests are required to pre-act. These offline data commonly work well on single specific types of motor. If the targets are changed numerous iterative offline remedies are required. To overcome these common drawbacks, Choi [1·85] proposed a pulsating HF carrier signal injection-based axis switching (IAS) rotor estimation which is able to minimize the ZCC effect for SMPMSMs. When the specific pulsating carrier-signal voltage is injected into the stator windings of a PMSM, an amplitude-modulated trajectory with alternating magnitude from zero to maximum is

formed as the envelope of the HF carrier-signal current in the stationary reference frame. The phase angle of the carrier current with respect to load situation can be tuned to avoid multiple zero-crossings of the HF carrier-signal current. The IAS carrier-signal estimation method by Choi [1·85] requires the injected carrier signal voltage vector oriented to d-axis and carrier current to be limited at the nonzero value under no load. When the load is applied, the injected carrier-signal voltage vector is required to be switched to the q-axis, so the carrier-signal current can become zero.

The IAS carrier-signal injection estimation scheme can generate zero magnitude of HF carrier current at every cross-zero point. Choi [1·85] demonstrated that the IAS injection estimation can obtain the minimum ZCC effect in the zero-cross regions and concluded that the IAS carrier-signal injection method for sensorless control SMPMSM can avoid immense offline test work be independent of motor saturation properties.

Acarnley [1·91] explain that HF carrier-signal injection rotor estimation for PMSM can track the position-depend magnetic asymmetries from the rotor saliency by the active carrier signal means in the zero-and-low speed range. Previous works by Bianchi [1·72, 93] and Guglielmi [1·92] recognised that the major source of the estimation error for the carrier signal injection method is saturation. To address the issue of saturation, both adopted a nonlinear model to measure and decouple the cross-coupling effect between d-axis and q-axis related to the fundamental current in the rotational frame. Besides, Garcia [1·119] further points out the additional sources for estimation error in carrier signal estimation such as harmonics emitted by the inverters, nonsinusoidal distribution around the air gap and the distortion of high injection frequency. He concluded that these additional sources cause secondary saliencies in carrier-signal saliency-track position estimation.

To analysis the effects of saturation and secondary saliencies, Reigosa [1·90] compared two types of carrier voltage/current and inductance models in a rotational coordination frame with cross-coupling effect between d-axis and q-axis. He found that a new carrier-signal cross-saturation current is generated. Such cross-saturation effects caused by cross-saturation inductance not only produce a variation of the saliency ratio but also cause a phase difference between the estimated and real position of saliency. If the saliency ratio becomes small zero, Guglielmi [1·92] and Bianchi [1·93] found that carrier-signal saliency-track rotor estimation will be limited in the sensorless application and the working point of the sensorless controlled PMSMs will be changed accordingly.

The phase difference between the estimated and real saliency has a negative error as a systematic noise in the carrier-signal estimated position. To take the

secondary saliency into account, Reigosa [1·90] employed additional spectral harmonics to model the resultant carrier signal current. Because the secondary components in the carrier-signal current features the same spatial harmonic order as the tracked dominant saliency, a steady-state angular error between the estimated and real rotor position will be generated.

The effects of cross-saturation and secondary saliencies need to be decoupled to then be compensated by an online look-up table obtained by the offline measurement and manipulation. Reigosa [1·90] used the adaptive network to build up the learned nonlinear relationship between the negative-sequence tracked components and the real one for online lookup compensation. Each type of secondary saliency is modeled as a single sinusoidal saliency through a fictitious carrier voltage which is used to predict and decouple the secondary saturation-induced saliencies.

The adaptation process has two steps. First, the mean transient impedance by positive-sequence current and carrier voltage command is measured then the second step is to measure the differential impedance by the gradient descent. The follow-up process after the adaption is to incorporate the mean and differential transient impedances directly into an inverse model to decouple the secondary components of the negative-sequence carrier-signal current. Finally the rotor position can be derived from the resultant signals obtained by subtracting the output of the inverse model from the negative-sequence carrier-signal current.

Cross-coupling between d-axis and q-axis of PMSM would cause the cross saturation for carrier signal injection controlled PMSM. Stumberger [1·94] used finite element analysis and measurement to find that the cross-coupling between d-axis and q-axis would generate the mutual inductance between d-axis and q-axis by cross-saturation especially for carrier-signal injection controlled interior permanent magnetic motors. Silva [1·95] also concluded that the equivalent mutual inductance between α-axis and β-axis would generate the rotor estimation error as a saliency offset. To eliminate the estimated rotor error, Silva followed the conventional assumption in the carrier signal injection method to compensate the error by the premeasured rotor error based on measured d-axis/q-axis self-inductances.

The conventional assumption in the carrier-signal injection model is that the high frequency components in the q-axis current is forced to zero. Li and Zhu [1·96] built up an optimal relationship between d-axis and q-axis current by finite element analysis. The ratio of mutual inductance to q-axis self inductance is introduced to define the cross coupling factor which is either calculated by finite element analysis or measured. The

cross coupling factor is used to determine the estimated rotor error in the new carrier signal injection PMSM model accounting for cross-coupling. The optimal cross coupling factor must be measured by the practical operation of PMSM based on real position sensing validated by finite element analysis. The experiment showed that the improved carrier-signal injection method with optimal cross-coupling is able to reduce the estimated rotor error by up to 10 elec° [1·96]. This improved method revealed that finite element analysis can be employed to find the optimised mutual inductance between d-axis and q-axis for reducing the estimated position error.

1.2 Definition of Research Problem

The state-estimate sensorless controlled PMSMs are essentially divided into two types.First, state covariance correction such as the Kalman filter, reduced Kalman filter or Linear Kalman Filter and variable PI regulators such as Luenberger or reduced order state feedback. State estimation correction not only enables sensorless control of PMSM self-start but also makes the position estimation. The main concern is to choose the best cost-effective state estimation sensorless scheme. Computation load or comprehensive characterisation must be considered. This thesis focuses on comparison of state estimation sensorless control of PMSMs. Furthermore, a new Linear Kalman filter technique is proposed to overcome the drawbacks of current methods.

1.3 References

[1·1] P.Vas, "Sensorless vector and direct torque control" New York: *Oxford University Press,* 1998

[1·2] Jacques.Davoine, Robert.Perret, Hoang.Le-Huy, "Operation of a self-controlled synchronous motor without a shaft position sensor," IEEE Trans. on Ind. Appl., Vol.19, No.2, 1983, 217-222

[1·3] S.Ogasawara, H.Akagi, "An Approach to position sensorless drive for brushless DC Motors," IEEE Trans. on Ind. Appl.,Vol. 27, No.5, 1991, 928-933

[1·4] N.Ertugrul, P.P.Acarnley, "A new algorithm for sensorless operation of permanent magnet motors," IEEE Trans. on Ind. Appl., Vol.30, No.1, 1994, 126-133

[1·5] L.A.Jones, J.H.Lang, "A state observer for the permanent-magnet synchronous motor," IEEE Trans. on Ind. Appl., Vol. 30, No. 3, 1989, 374-382

[1·6] R.Dhaouadi, N.Mohan, L.Norum, "Design and implementation of an extended Kalman Filter for the state estimation of a permanent magnet synchronous motor," IEEE Transactions on Power Electronics, Vol.6, Issue 3, Jul 1991, 491-497

[1·7] M.J.Corley, R.D.Lorenz,, "Rotor position and velocity estimation for a salient-pole permanent magnet synchronous machine at standstill and high speeds," IEEE Trans. on Ind. Appl., Vol.34, No. 4, 1998, 84-789

[1·8] S.Ogasawara, H.Akagi, "Implementation and position control performance of a position-sensorless IPM motor drive system based on magnetic saliency," IEEE Trans. on Ind. Appl., Vol.34 (4), 1998, 806-812

[1·9] Chuanyang.Wang, Longya.Xu, "A novel approach of rotor position detection for PM machines based on conventional PWM algorithms", National Aerospace and Electronics Conference 2000, NAECON 2000, Proc. of the IEEE 2000, Vol.1 (1) 2000, 547 – 553

[1·10] Ying.Li, N.Ertugrul, "A novel ,robust DSP-Based indirect rotor position estimation for permanent magnet AC motors without rotor saliency", IEEE Transactions on Power Electronics, Vol. 18, Issue 2, Mar 2003, 539 – 546

[1·11] N.Ertugrul, P.P.Acarnley, "Indirect rotor position sensing in real time for brushless permanent magnet motor drives", IEEE Trans. on Power Electronics, Vol. 13, Issue 4, Jul 1998, 608 – 616

[1·12] S.Bolognani, L.Tubiana, M.Zigliotto, "EKF-based sensorless IPM synchronous motor drive for flux-weakening applications", IEEE Transactions on Industrial Applications,Vol.39, Issue 3, May-June 2003, 768 – 775

[1·13] M. Schrödl, T. Stefan, "New rotor position detector for permanent magnet synchronous machine using the INFORM method", Eur. Trans. Elect. Power Eng., Vol.1, No.1, 1991, 47-53

[1·14] M.Schroedl, "Sensorless control of ac machines at low speed and standstill based on the INFORM method", Industry Applications Conference, 1996, Thirty-First IAS Annual Meeting IAS'96 IEEE Publication, Vol. 1, 6-10 Oct 1996, 270-277

[1·15] Marco.Tursini, R.Petrella, F.Parasiliti, "Initial rotor position estimation method for PM motors", IEEE Trans. on Ind. Appls., Vol. 39, (6), Nov.-Dec. 2003, 1630 – 1640

[1·16] S.Bolognani, R.Oboe, M.Zigliotto,, "Sensorless full-digital PMSM drive with EKF estimation of speed and rotor position", IEEE Trans. on Industrial Electronics, Vol. 46, Issue1, Feb 1999, 184 – 1919

[1·17] Vladan.Petrovic, A.M.Stankovic, V.Blasko, "Position estimation in salient PM synchronous motors based on PWM excitation transients", IEEE Transactions on Industrial Applications, Vol. 39, Issue 3, May-June 2003, 835 – 843

[1·18] P.L.Jansen, R.D.Lorenz, "Transducerless position and velocity estimation in induction and salient AC machines", IEEE Trans. on Industrial Applications, Vol. 31, Issue (2), Mar/Apr 1995, 240 – 247

[1·19] S.Ostlund, M. Brokemper, "Sensorless rotor –position detection from zero to rated speed for an integrated PM synchronous motor drive", IEEE Transactions on Industrial Applications, Vol. 32, Issue 5, Sep/Oct 1996, 1158 – 1165

[1·20] T.Aihara et al.,"Sensorless torque control of salient-pole synchronous motor at zero-speed operation", IEEE Trans. on Power Electronics, Vol.14, Issue 1,Jan 1999, 202 – 208

[1·21] M.Schroedl, P.Weinmeier, "Sensorless control of reluctance machines at arbitrary operating conditions including standstill", IEEE Transactions on Power Electronics,
Vol.9, Issue 2, Mar 1994, 225 – 231

[1·22] http://www.abb.co.uk/product/us/9AAC100348.aspx?country=GB

[1·23] http://en.wikipedia.org/wiki/Electric_motor;

[1·24] http://en.wikipedia.org/wiki/Alnico#cite_note-2

[1·25] Peter.Campbell, (1996), Permanent magnet materials and their application, UK: Cambridge University Press, pp. 35-38, ISBN 0521566886

[1·26] http://en.wikipedia.org/wiki/Samarium%E2%80%93cobalt_magnet;

[1·27] http://en.wikipedia.org/wiki/Neodymium-Iron-Boron

[1·28] B.D.Cullity, C. D. Graham (2008), Introduction to Magnetic Materials, Wiley-IEEE, pp. 489, ISBN 0471477419

[1·29] E.d.T.d.Lacheisserie et al., Magnetism: Materials and Applications, Springer, pp.11

[1·30] http://en.wikipedia.org/wiki/Neodymium_magnet

[1·31] http://en.wikipedia.org/wiki/Samarium%E2%80%93cobalt_magnet

[1·32] http://lihe-china.chinese-suppliers.com/a_anisotropic_ferrite.htm

[1·33] http://www.magnetmaterialyl.com/

[1·34] C. Zwyssig et al., "An ultra-high-speed, 500000 rpm, 1 kW electrical drive system", Power Conversion Conference - Nagoya, 2007. PCC '07, 2-5 April 2007, 1577 - 1583

[1·35] http://njsupermann.en.made-in-china.com/product/qMWElTxrYIhw/China-Wind-Turbine-Vertical-Horizontal-Permanent-Magnet-Generator-Alternator-0-1-1000 kw

[1·36] http://www.rolls-royce.com/Images/brochure_Trent800_tcm92-5720

[1·37] Thales starter-generator integrated on Hispano-Suiza's POA test rig, http://www.thalesgroup.com/assets/0/249/250/3b064b3c-580a-4d99-bc44-8b10ef77b841

[1·38] Tadashi.Sawata, "Development and initial test results of the fan shaft driven generator", UK Magnetics Society Seminar for Electrical Drive Systems for the More Electric Aircraft,14 April 2005

[1·39] Renyuan.Tang, Beijing. Modern Permanent Magnet Machines-theory and design, China Machine Press, 1994

[1·40] General Electric Company, "150 Kva samarium cobalt VSCF starter/generator electrical system, Final Technical Report", 1979

[1·41] Andrew R. Druzsba, Advanced high-power generator for airborne applications Airesearch Mfg. Co. TORRANCE CA, Tech. Report, AFWAL-80-2130, Dec. '80, 76

[1·42] Kato Engineering: PMG pilot exciter, http://www.kato-eng.com/

[1·43] http://www.answers.com/topic/hydroelectric-generator

[1·44] The SSP Propulsor--An Ingenious Podded Drive System http://www.schottel.de/pdf_data/eng_SSP

[1·45] Power Optimised Aircraft(POA) 2006, "POA Lester Faleiro E.6 Presentation", http://www.dglr.de/veranstaltungen/extern/aerodays2006/sessions/E_Sessions/E6/E61df

[1·46] www.lexus.co.uk/hybrid/

[1·47] "The active steering wheel", www.conekt.net/docs/ASWS%20Leaflet%20V4.0.pdf

[1·48] http://www.daikinac.com/commercial/productsFeatures.asp?sec=products&page=7;

[1·49] www.toshiba-aircon.in.th/inverter.html

[1·50] http://www.eu.necel.com/applications/industrial/01_motor_control/010_domestic_appliances/010_white_goods/010_washing_machine/index.html

[1·52] http://www.heason.com/catalogue/82/servostar-600.html

[1·53] "Encoder Solutions for the Wind Power Industry", http://www.globalencoder.ca/download.php?id=8&type=bro&PHPSESSID=c7f8d31726d832d9fe46be1f9bc79e11

[1·54] http://www.utxchange.com/K%20B%20Retarder.html

[1·55] http://www.ece.uvic.ca/~ece499/2004a/group08/

[1·56] http://en.wikipedia.org/wiki/Injection_molding

[1·57] http://www.automation.siemens.com/doconweb/pdf/840C_1101_E/IBN_LI.pdf?p=1

[1·58] "Commercialization of High-Resolution, Ultra-small PM-Type Stepping Motors", http://www.minebea.co.jp/english/press/2009/1184420_3755.html

[1·58] "Chpt. 27 Flight Controls", www.extraaircraft.com/Tech-Manuals/MM400/27r11

[1·59] K.Atallah et al., "Comparison of electrical drive technologies for aircraft flight control surface actuation", 19th Int. Conf. on Elec. Machines and Drives, 1999, Canterbury, 159 – 163

[1·60] http://en.wikipedia.org/wiki/List_of_hybrid_vehicles#2009

[1·62] http://en.wikipedia.org/wiki/Hybrid_electric_vehicle#cite_note-3

[1·63] "Active steering wheel", www.conekt.net

[1·64] B.S.Bhangu,C.M.Bingham, GA-tuning of nonlinear observers for sensorless control of automotive power steering IPMSMs, IEEE Conference on Vehicle Power and Propulsion, 7-9 Sept. 2005, 772 – 77

[1·65] Electric Steering Systems – E-SteerTM electric power steering. Delphi

[1·66] C.Song, Z.Zheng, X.Longya, "Sliding-mode sensorless control of direct-drive PM synchronous motors for washing machine applications", IEEE Transactions on Industrial Applications,Vol.45, Issue 2, March-April 2009, 582 – 590

[1·67] Huangsheng.Xu;Z.Zhang; H.Layne, "Sensorless direct field oriented control of three-phase induction motors based on "sliding mode" for washing machine drive applications", Fourtieth IAS Annual Meeting, 2005, Vol.1, 2-6 Oct. 77 - 83

[1·68] H. Beaty and J. Kirtley, Elec. Motor Handbook, McGraw-Hill Professional, 1998

[1·69] "More-electric aircraft", Conference reports From: Aircraft Engineering and Aerospace Technology, 2005, Volume 77, Issue 1

[1·70] "Thales Presentation", Dornier 328 Operator's Conference 2006-Aerospace, Munich,December13-4,2006,http://www.328support.de/opscon/presentations/supplier-presentations/5_Thales-Presentation

[1·71] "Thales Presentation", Dornier328 Operator's Conference 2008, Electrical Systems –Power Generatio, Palma De Mallorca, June3-5 2008, http://www.328support.de/ops

con/presentations08/Thales

[1·72] N.Bianchi, S.Bolognani, Jang.Ji-Hoon Sul.Seung-Ki , "Advantages of inset PM machines for zero-speed sensorless position detection", IEEE Transactions on Industrial Applications,Volume 44, Issue 4, July-Aug. 2008, 1190 – 1198

[1·73] Jiangang.Hu, Jingbo.Liu, Longya.Xu, "Eddy current effects on rotor position estimation and magnetic pole identification of PMSM at zero and low speeds", IEEE Transactions on Power Electronics, Vol. 23, Issue 5, Sept. 2008, 2565 - 2575

[1·74] L. Xu et al., "Vector control of a synchronous reluctance motor including saturation and iron losses," IEEE Trans. on Ind. Appl.., vol. 27, (5), Sep./Oct. 1991, 977–985

[1·75] I. Boldea and S. A. Nassar, "Unified treatment of core losses and saturation in orthogonal-axis model of electric machines," IEE Proceedings on Electric Power, vol. 134, no. 2, Nov. 1987, 355–363

[1·76] T. Aihara, A. Toba, T. Yanase, A. Mashimo, and K. Endo, "Sensorless torque control of salient-pole synchronous motor at zero-speed operation," IEEE Transactions Power Electronics, vol. 14, no. 1, Jan.1999, 202–208

[1·77] C. Wang and L. Xu, "A novel approach for sensorless control of PM machines down to zero speed without signal injection or special PWM technique," IEEE Transactions on Power Electronics, vol. 19, no. 6, Nov. 2004,1601–1607

[1·78] C. Ortega et al., "Sensorless direct torque control of a surface mounted PMSM using high frequency injection", IEEE Int. Symposium on Ind. Electronics, Jul. 9–13, 2006, vol. 3, 2332–2337

[1·79] Joachim.Holtz, "Initial rotor polarity detection and sensorless control of PM synchronous machines", 41st Annual Meeting of IEEE Industrial Applications Conference, Vol. 4, 8-12 Oct. 2006, 2040 – 2047

[1·80] Y.-S. Jeong, R. D. Lorenz, T. M. Jahns and S.-K. Sul, "Initial rotor position estimation of an interior permanent magnet synchronous machine using carrier-Frequency Injection Methods," IEEE Transaction on Industrial Applications, Vol. 41, No. 1, Jan./Feb.2005, 38-45

[1·81] J.-I. Ha and S.-K. Sul, "Sensorless field-oriented control of an induction machine by high-frequency signal injection", IEEE Transactions on Industrial Application., Vol. 35, No. 1, Jan/Feb. 1999, 45-51

[1·82] M. E. Haque, L. Zhong and M. F. Rahman, "A sensorless initial rotor position estimation scheme for a direct torque controlled interior permanent magnet Synchronous Motor Drive", IEEE Transactions on Power Electronics, Vol. 18, No. 6, Nov. 2003, 1376-1383

[1·83] M. Linke, R. Kennel and J. Holtz, "Sensorless speed and position control of permanent magnet synchronous machines", 28th Annual Conf. of the IEEE Industrial Electronics Society (IECON), Sevilla/Spain, 2002

[1·84] M. Linke, R. Kennel, J. Holtz, "Sensorless speed and position control of synchronous machines using alternating carrier injection," IEEE International Electric Machines and Drives Conference IEMDC'03, Madison, WI, June 1-4, 2003

[1·85] Chan-Hee.Choi, Jul-Ki.Seok, "Pulsating signal injection-based axis switching sensorless control of surface-mounted permanent-magnet motors for minimal zero-current clamping effects", IEEE Transactions on Industrial Applications,Vol.44, Issue 6, Nov.-Dec. 2008, 1741 - 1748

[1·86] N. Teske et al., "Analysis and suppression of high-frequency inverter modulation in sensorless position controlled induction machine drives," IEEE Transactions on Industrial Application, vol. 39, no. 1, Jan./Feb. 2003, 10–18

[1·87] J. M. Guerrero, M. Leetmaa, F. Briz, A. Zamarron, and R. D. Lorenz, "Inverter nonlinearity effects in high-frequency signal-injection-based sensorless control methods," IEEE Trans. on Ind. Appl., vol. 41, no. 2 , Mar./Apr. 2005, 618–626

[1·88] C. H. Choi and J. K. Seok, "Compensation of zero-current clamping effects in high-frequency-signal-injection-based sensorless PM motor drives," IEEE Transactions on Industrial Applications, vol. 43, no. 5 , Sep./Oct. 2007, 1258–1265

[1·89] Y. S. Kwon, C. H. Choi, and J. K. Seok, "Minimization of rotor position detection error due to zero-current-clamping effect in pulsating carrier signal injection-based sensorless drives," Proceeding of IEEE APEC, Anaheim, CA, Feb. 2007, 838–844

[1·90] D.D.Reigosa et al., "Measurement and adaptive decoupling of cross-saturation effects and secondary saliencies in sensorless controlled IPM synchronous machines", IEEE Trans. on Ind. Appl., Vol. 44, (6), Nov.-Dec. 2008, 1758 - 1767

[1·91] P. P. Acarnley and J. F. Watson, "Review of position-sensorless operation of brushless permanent-magnet machines," IEEE Transactions on Industrial Electronics, vol. 53, no. 2, Apr. 2006, 352–362

[1·92] P. Guglielmi, M. Pastorelli, and A. Vagati, "Cross-saturation effects in IPM motors and related impact on sensorless control," IEEE Transactions Industrial Applications, vol. 42, no. 6,, Nov./Dec. 2006, 1516–1522

[1·93] N.Bianchi, S.Bolognani, "Influence of rotor geometry of an IPM motor on sensorless control feasibility", IEEE Transactions on Industrial Applications, Vol. 43, Issue 1, Jan.-Feb. 2007, 87 – 96

[1·94] B. Stumberger, G. Stumberger, D. Dolinar, A. Hamler, and M. Trlep, "Evaluation of saturation and cross-magnetization effects in interior permanent-magnet synchronous motor," IEEE Trans. Ind. Appl., vol.39, no.5, Sep./Oct. 2003, 1264–1271

[1·95] C. Silva, G. M. Asher, and M. Sumner, "Hybrid rotor position observer for wide speed-range sensorless PM motor drives including zero speed," IEEE Transactions Industrial Electronics, vol. 53, no. 2, Apr. 2006, 373–378

[1·96] Y.Li, Z. Q.Zhu, D.Howe, C. M.Bingham, D. A.Stone,"Improved rotor-position estimation by signal injection in brushless AC Motors, accounting for cross-coupling magnetic saturation", IEEE Trans. on Ind. Appl., 45, (5), Sept.-Oct. 2009, 1843 – 1850

[1·97] http://en.wikipedia.org/wiki/Mechatronics

[1·98] http://en.wikipedia.org/wiki/Lathe_ (metal)

[1·99] K.Iizuka et al., "Microcomputer control for sensorless brushless motor", IEEE Transactions on Industrial Applications, Vol.IA-21, Issue 3, May 1985, 595 - 601

[1·100] Allan.B.Plunkett, Fred.G.Turnbull, "Load-commutated inverter/synchronous motor drive without a shaft position sensor", IEEE Transactions on Industrial Applications, Vol.IA-15, Issue1, Jan. 1979, 63 – 71

[1·101] J.C.Moreira,"Indirect sensing for rotor flux position of permanent magnet AC motors operating over a wide speed range" ,IEEE Trans. on Industrial Applications, Nov.-Dec. 1996 ,Vol. 32 , Issue 6, 1394 - 1401

[1·102] J.X.Shen, Z.Q.Zhu, D.Howe, "Improved speed estimation in sensorless PM brushless AC drives", IEEE Trans. on Ind. Appl.,38, (4), July-Aug. 2002, 1072 –80

[1·103] R.Wu, G.R.Slemon, "Permanent magnet motor drive without a shaft sensor", IEEE Trans. on Industrial Applications, Vol.27, Issue 5, Sept.-Oct.1991, 1005 – 1011

[1·104] L.A.de S Ribeiro, M.C.Harke, R.D.Lorenz, "Dynamic properties of back-emf based sensorless drives", 41st IEEE Ind. Appl. Ann. Meeting , Vol. 4, 8-12 Oct. 2006, 2026 – 2033

[1·105] Joohn-Sheok Kim, Seung-Ki Sul, "New approach for high-performance PMSM drives without rotational position sensors", IEEE Transactions on Power Electronics, Vol.12, Issue. 5, Sept. 1997, 904 – 911

[1·106] S. Bolognani et al. "Extended-range PMSM sensorless speed drive based on stochastic filtering," IEEE Trans.on. Power Electronics, vol.16, Jan. 2001, 110–117

[1·107] S. Bolognani et al., "Extended Kalman filter tuning in sensorless PMSM drives", IEEE Trans. on Ind. Appl.,39 (6), Nov.-Dec. 2003, 1741 –47

[1·108] J. Solsona et al., "A nonlinear reduced order observer for permanent magnet synchronous motors", IEEE Trans. on Ind. Electronics, Vol.43, (4) Aug. 1996, 492 –7

[1·109] P. Snary et al., "Matrix converters for sensorless control of PMSMs and other auxiliaries on deep-sea ROVs", IEE Proceedings -Electric Power Applications, Vol.152, Issue.2, 4 March 2005, 382 – 392

[1·110] K.Tatematsu et al., "Sensorless permanent magnet synchronous motor drive with reduced order observer", IEEE 13th Annual Applied Power Electronics Conference and Exposition(APEC'98), 15-19Feb. 1998, Vol.1, 75 - 80

[1·111] K.Tatematsu, D.Hamada, K.Uchida, S.Wakao, T.Onuki,"Sensorless control for permanent magnet synchronous motor with reduced order observer", 29th Annual IEEE Power Electronics Specialists Conference(PESC 98),Vol.1, 17-22 May 1998, 125 – 131

[1·112] D.Hamada et al., "Stability analysis of sensorless permanent magnet synchronous motor drive with a reduced order observer", International Electric Machines and Drives Conference (IEMD '99),9-12 May 1999, 95 - 97

[1·113] N. Matsui, and M. Shigyo, 'Brushless dc motor control without position and speed sensors', IEEE Trans. on Ind. Electron., Vol. 28, (1), Jan.-Feb. 1992, 120–127

[1·114] Guchuan.Zhu, A.Kaddouri, L.A.Dessaint, O.Akhrif, "A nonlinear state observer for the sensorless control of a permanent-magnet AC machine", IEEE Transactions on Industrial Electronics,Vol.48, Issue 6, Dec. 2001, 1098 - 1108

[1·115] C.DeAngelo, G.Bossio, J.Solsona, G.O.Garcia, M.I.Valla,"Mechanical sensorless speed control of permanent-magnet AC motors driving an unknown load", IEEE Transactions on Industrial Electronics, Vol. 53, Issue 2, April 2006, 406- 414;

[1·116] Kuang-Yow.Lian; Che-Hsueh.Chiang, Hui-Wen.Tu, "LMI-Based Sensorless Control of Permanent-Magnet Synchronous Motors", IEEE Transactions on Industrial Electronics, Vol.54, Issue 5, Oct. 2007, 2769-2778

[1·117] A.Piippo et al., "Adaptation of Motor Parameters in Sensorless PMSM Drives", IEEE Transactions on Industry Applications, Vol.45, Issue1, Jan.-feb.2009, 203 – 212

[1·118] M.Hasegawa, K.Matsui, "Position sensorless control for interior permanent magnet synchronous motor using adaptive flux observer with inductance identification", IET Electric Power Applications, Vol.3, Issue 3, May 2009, 209 – 217;

[1·119] P.Garcia, F.Briz, M.W.Degner, D.Diaz-Reigosa, "Accuracy, bandwidth, and stability limits of carrier-signal-injection-based sensorless control methods", IEEE Transactions on Industry Applications, Vol.43, Issue 4, July-Aug. 2007, 990 – 1000

CHAPTER 2. CONSTRUCTION OF EXPERIMENTAL APPARATUS

2.1 INTRODUCTION

In order to substantiate the five sensorless operation approaches proposed, field-oriented space-vector PWM control strategy is applied to an experimental DSP-based PMSM drive apparatus for demonstration and validation of the prospective sensorless performance. This chapter details the construction, realization and specification of the experimental equipment. The test rig is considered to suit all types of microprocessor-based control motors testing.

The electromagnetic load (the shaft of a DC shunt generator) is coupled to that of a PMSM drive comprising of a PMSM and full-bridge inverter controlled by a full-digital DSP-based controller. The PMSM drive system can implement the speed adjustment according to demand from the DSP-based full-digital control platform employed to facilitate the high-precision system-wide full-digital control of the PMSM. A simplified overview of the experimental apparatus is given in fig. 2·1.

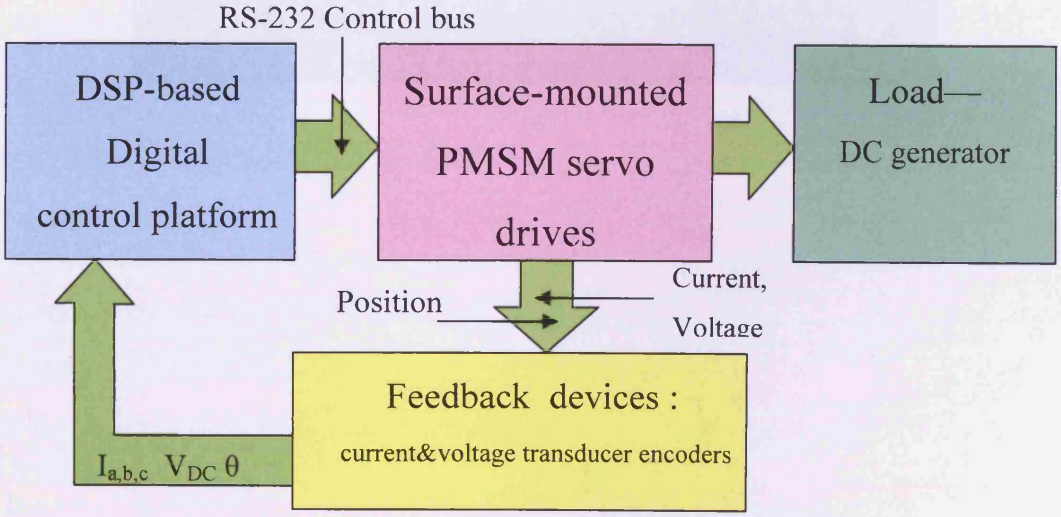

Fig. 2·1 Block diagram of the proposed experimental PMSM drive

The experimental test rig comprises:

1. The DC shunt generator with its shaft coupled to a PMSM is driven to feed the circuit where the armature and resistor are connected in series shown in fig.2·3;
2. The three phase surface-mounted 600 W, 60 v, 1000 rpm PMSM commercial servo motor SSD ACM2n shown in fig.2·3;
3. The DSP-based full-digital control platform plus 3 phase, full-bridge inverter—TMS320C31DSK, 12-bit AD/DA boards, etc shown in fig.2·2;
4. The basic field-oriented space-vector PWM control strategy employed to control the PMSM prototype as a base for proposed sensorless control methods;
5. A commercial Farnell 70 V 1400 W constant voltage constant current DC link regulated DC power supply providing a steady 60 V DC voltage to the three phase inverter.

(a)

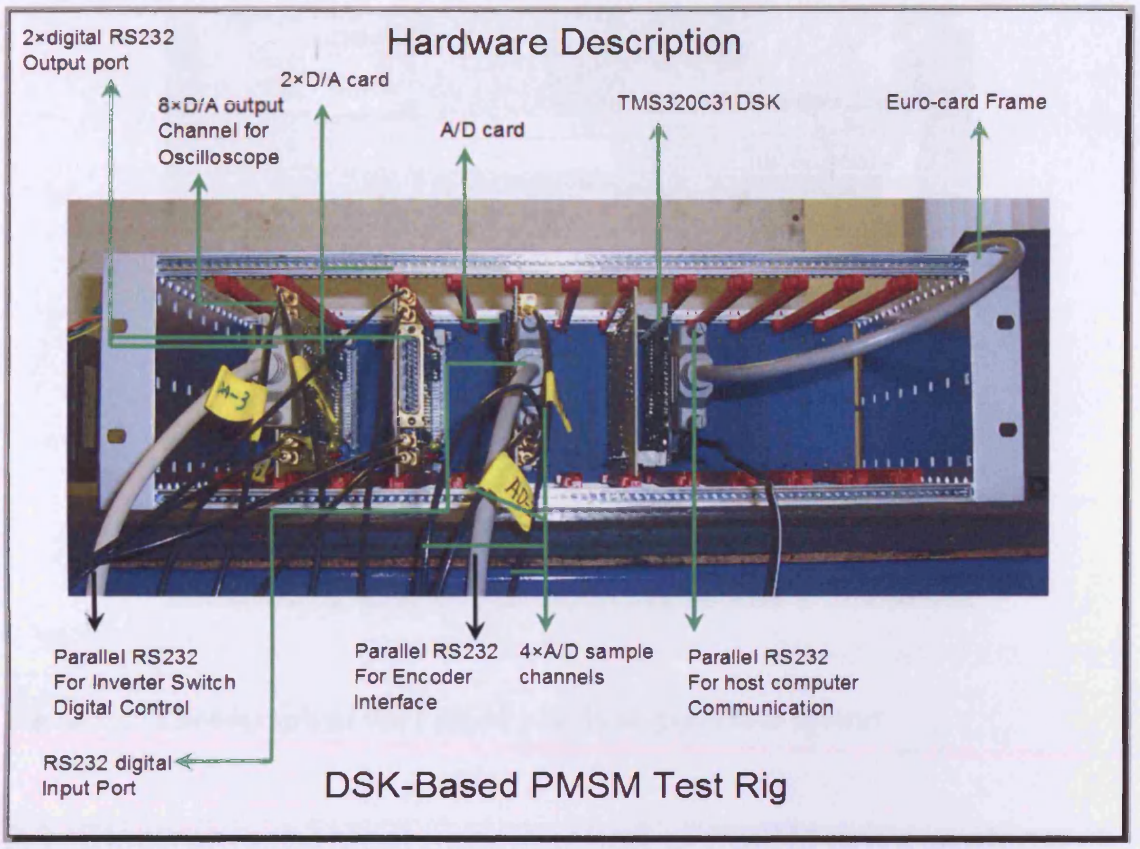

(b)

Fig. 2·2 (a) The DSP-based full-digital control platform plus 3-phase full-bridge inverter: overview (b) the DSP platform

2.2 Objective Prototype Structure

To assess the performance of the sensorless controlled PMSM, a commercial servo AC motor is employed in the test. The commercial servo AC motor is a 3 phase surface-mounted PMSM mechanically coupled to a DC shunt generator as the electromagnetic-mechanic load. The shunt generator can operate in three load modes: constant torque mode when no field excitation is applied and the output loop is open-circuited, semi-excitation when field excitation is applied and the output loop is open-circuited; constant output power when field excitation is applied and the output loop is connected with a series resistance load. The controlled objective prototype is shown in fig. 2·3.

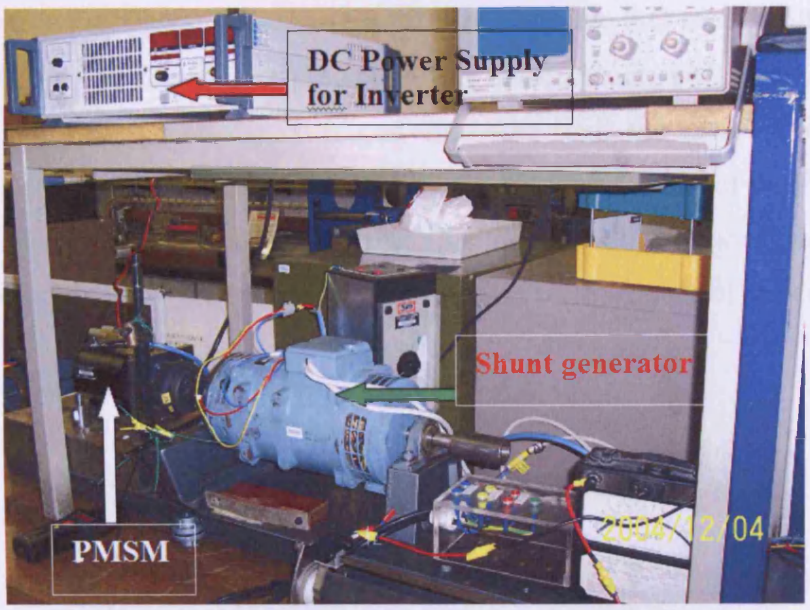

Fig. 2·3 Photograph of the PMSM plus load-generator system

2.3 Electromechanical specification of PMSM drive systems

To validate the flexibility and applicability of the proposed sensorless methods, the commercial servo AC motor is chosen as the prototype. Since the surface-mounted PMSM is widely used in the AC servo motor industry, it is considered here for sensorless approaches.

2.3.1 Commercial surface-mounted servo AC PMSM (ACM2n)

Table 2·1 Specifications of the PMSM (ACM2n320-4/2-3)

Rated power	600 W
Rated DC-link voltage	60-100 V
Pole pair number	3
Phase resistance	1 Ω
Phase inductance	5.5 mH
Rated speed	1200 rpm
Magnetic material	NdFeB
Rated torque	3.2 Nm
Rated current	6.4 A
Torque constant	0.49N m/A
E.M.F constant	35V/1000 min^{-1}

The motor, ACM2n, was a standard three-phase surface-mounted PMSM made by SSD Drive Ltd. The specifications are listed in table 2·1. The PMSM and three phase inverter are fed by a 60 V DC-link from a constant voltage, constant current regulated DC power

supply shown in fig. 2·3(a). Instead of a DC link from the AC input rectifier, the DC power supply provides sufficient protection like short circuit, EMI, etc. Also the DC link fed by the DC power supply is convenient to limit the inverter output power through regulating the current threshold manually. The rated speed of the PMSM under the experimental situation is 1100 rpm. Since the focus is variable speed performance in sensorless controlled PMSM, no torque loop exists in the loop control system.

2.3.2 Single-phase DC generator

Rated field excited voltage	220 V
Field excitation winding resistance	8 Ω
Rated Field excitation current	2.2 A
Rated power (motor)	2.2 kW
Rated current (motor)	10 A
Rated voltage (motor)	220 Vdc

Table 2·2 Specifications of the single-phase DC shunt motor/generator

The electromagnetic mechanic load driven by the PMSM is a single phase DC generator, which is also shunt motor Fig.2·4(a) and (d) shows a diagram of the motor and power supply. The DC shunt motor is fed by a constant current DC power supply shown in fig.2·4(a). The power supply shown in fig.2·4(d) has two output ports: one port marked with terminals "A1, A2" feeds constant current to the motor armature, the other port marked with terminals "F1, F2" generates field excitation current. Both ports are internally regulated to keep constant current, meanwhile two ports shares the same voltage shown in fig.2·4(d).

The approximate speed-torque load characteristics of the DC shunt motor is shown in fig.2·4(f). The different connection between shunt motor and supply shown in fig.2·4(b~c) make the original shunt motor work as a generator. The specifications of the shunt motor are listed in table 2·2.

If the field coil is connected to terminals "F1,F2" of the power supply while the armature terminals are connected to the terminals "A1, A2" of the power supply, the connection make the motor work as a shunt motor because the same applied voltage make the armature and field winding connected in parallel.

The DC shunt motor is used for a load to operate as a generator shown in fig.2·4(c).

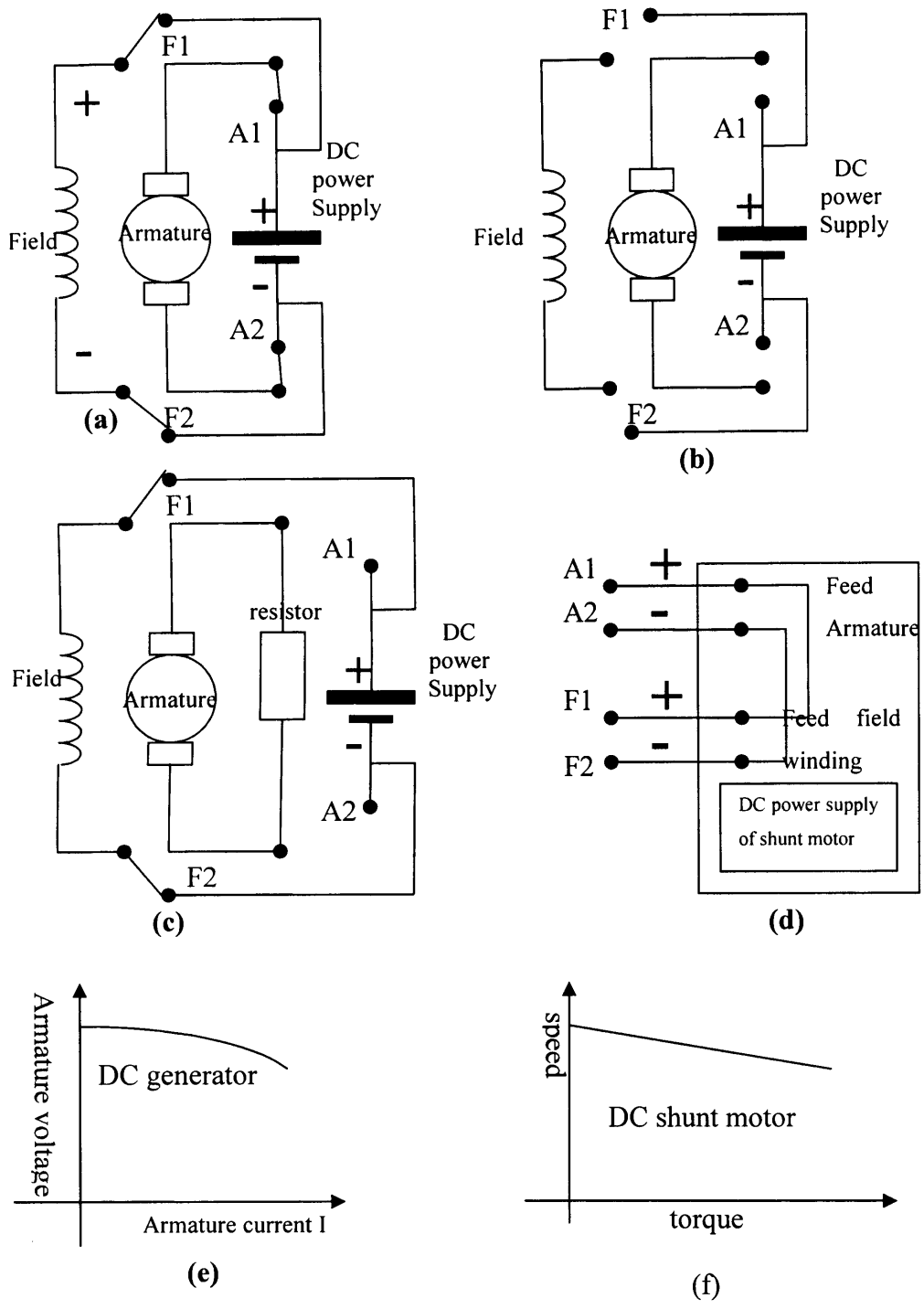

Fig. 2-4 The connection mode for the DC motor/generator (a) DC shunt motor (b) DC shunt generator in no load mode (c) DC shunt generator in load mode (d) constant current DC power supply for shunt motor (e) approximate V-I load characteristics of DC generator (d) approximate speed-torque characteristics of DC shunt motor

The armature terminals is connected in series with only a resistor or rheostat to close the circuit while the terminals of the field excitation winding are connected to terminals "F1, F2". Terminals "A1, A2" are disconnected from the armature terminals as shown.

If the armature terminals are disconnected to "A1, A2" while the terminals of field excitation winding are disconnected from "F1, F2", the machine operates as a generator on no load.

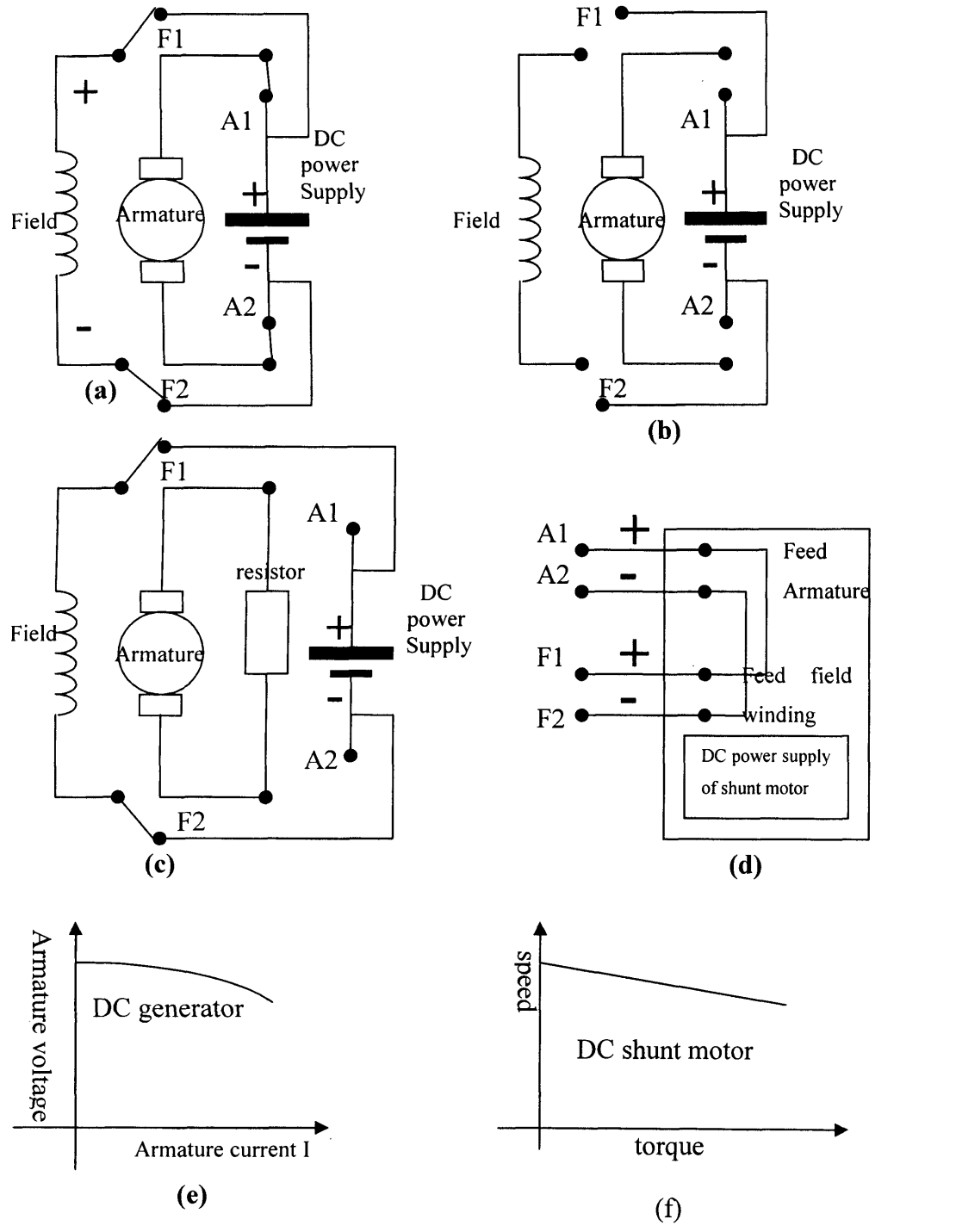

Fig. 2-5 Connection mode for DC shunt motor/generator (a) DC shunt motor (b) DC shunt generator in no load mode (c) DC shunt generator on load (d) constant current DC power supply for motor (e) approximate V-I characteristics of the DC generator (d) approximate speed-torque characteristics of DC shunt motor

Due to different load capacities various sensorless estimation methods, the DC shunt generator operates in two modes:

1. No load mode: Fig.24(b) shows that open-circuited armature terminals without field excitation applied. In this mode the PMSM is loaded with only the rotor of the shunt motor without any braking torque. The shunt generator on no load carries only mechanic load, which varies with speed. The torque measured by the torque meter is about 0.8~1 Nm when the speed is 1100 rpm;
2. Pure generator mode: Fig.2·4(c) shows that closed circuit armature terminals with field excitation applied. Here the shunt motor operates as a generator, The energy produced by the armature flows across the close circuit comprised of armature winding and external resistor. The generator armature current generates braking torque at the shaft coupled to that of the PMSM. The approximate load characteristics of DC generator is shown in Fig.2·4(e) .

2.4 DSP-based control system for the PMSM

The schematic diagram of the experimental system shown in fig. 2·5 comprises the 3 phase PMSM servo motor, load generator, full-bridge power electronics inverter, constant DC voltage, constant DC current output power supply unit (PSU) and TMS320C31 DSP-based controller.

The common power electronics inverters employed to drive three phase sinusoidal PMSM are fed by the DC Power Supply labelled "DC PSU" as shown in fig. 2·6. "DC PSU" is a commercial Farnell (Wayne/Kerr) AP70-30 single phase AC input regulated power supply with constant DC output voltage 0~70 v and constant DC output current 0~30 A providing stable DC regulated power output. The peak values of the DC PSU output are 70 V and 30 A. The benefits of using a commercial DC PSU instead of a rectifier circuit are that it is convenient to obtain reliable protection during the experiment and that the required DC voltage output is very stable and the DC current output can be regulated easily according to power demand.

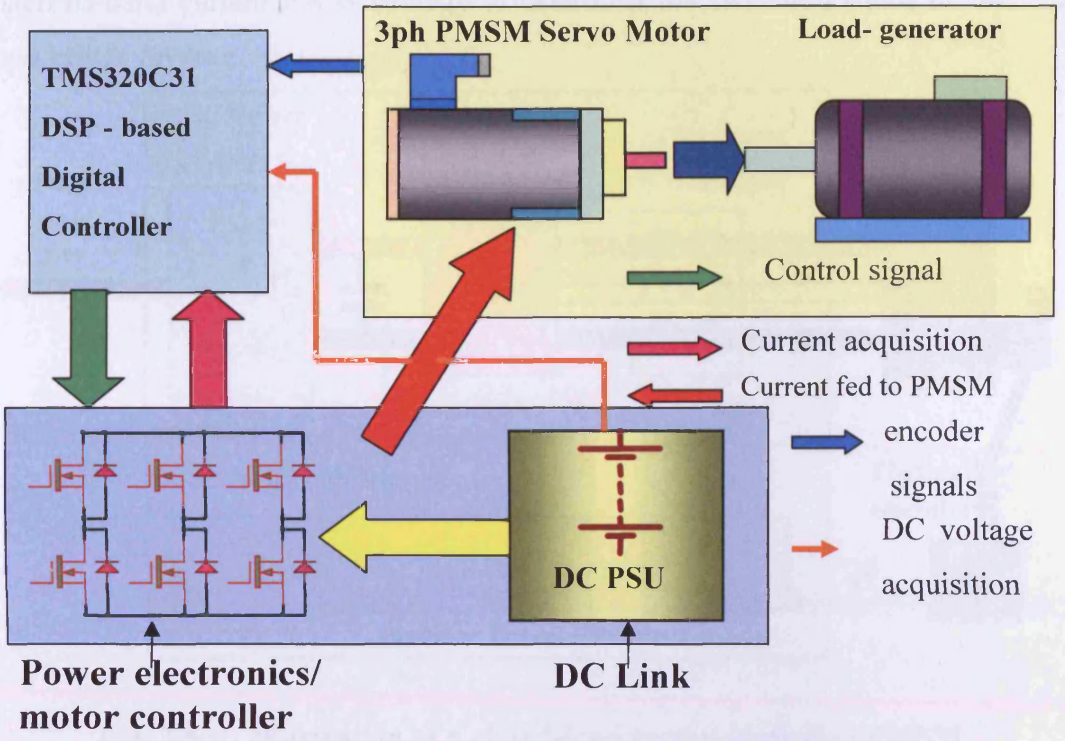

Fig. 2·6, Schematic of system controllers and actuator devices

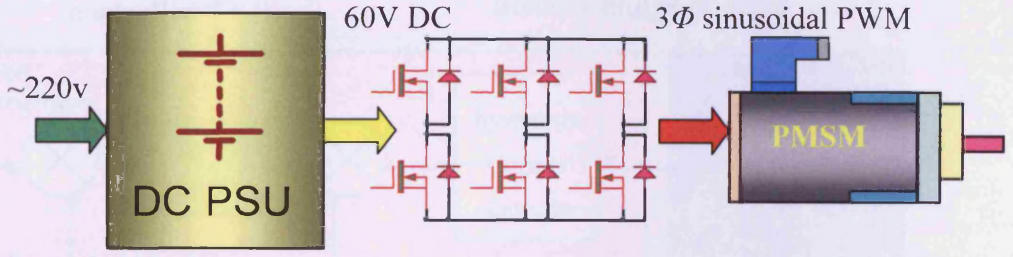

Fig. 2·7 Schematic diagram of the power circuit

The three phase bridge MOSFET inverter and freewheel power diode are controlled through a bus from a "TMS320C31" DSP-based platform. The output from the full-bridge inverter can generate three phase sinusoidal PWM voltage and current to supply the PMSM as illustrated in fig. 2·6.

Field oriented space vector hysteresis-band current PWM strategy is used to control the PMSM as shown in fig. 2·7. Three-phase current and DC link voltage information need to be acquired by 3 current transducers and a voltage transducer. These three current transducers are connected in series with 3-phase input lines while the voltage transducer is connected in parallel to DC link bus shown in fig. 2·7. The shaft position angle θ is obtained from the optical encoder which has a precision of 2048 ppt. These five sampled signals are required by the field oriented space vector

hysteresis-band current PWM strategy to determine the switching status of the three phase bridge inverter.

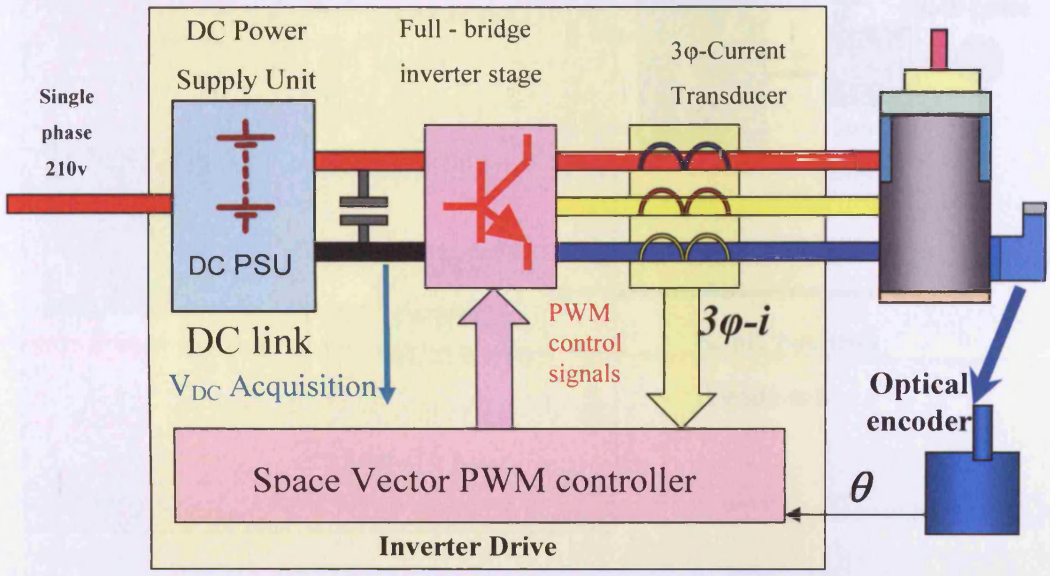

Fig. 2·8 Illustration of a closed-loop vector-controlled PMSM

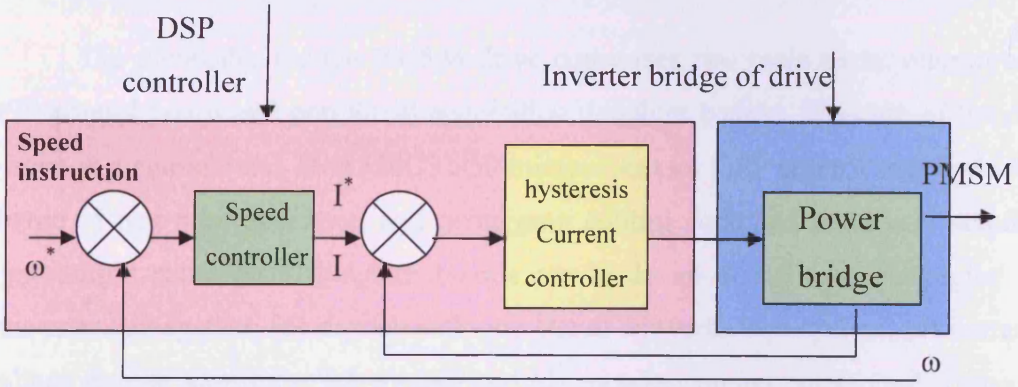

Fig. 2·9 Proposed structure for speed control of the PMSM

Fig. 2·8 shows a block diagram for speed control of the PMSM. The switching status for the 3 phase bridge inverter is determined by the software-based hysteresis-band current controller. Compared with general space-vector PWM strategy, six vectors (apart from two with null lengths) are used to implement current chop according to the current reference. The speed comparator can generate the difference between speed instruction ω^* and speed feedback ω, the difference is used to feed the speed PI controller to subsequently generate current instruction I^* for the hysteresis-band current controller.

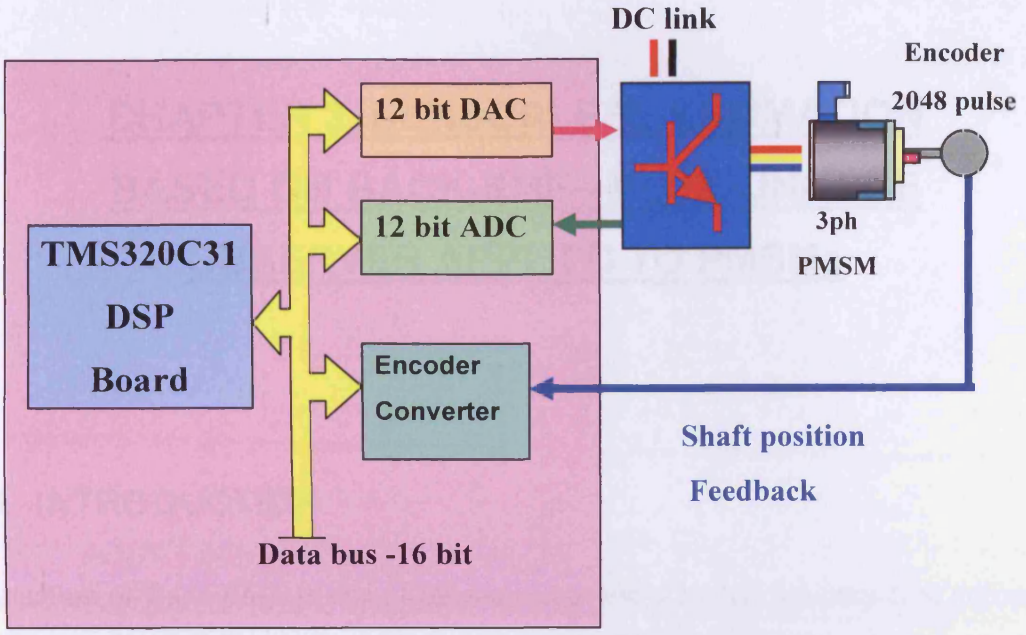

Fig. 2·10 Schematic diagram of the digital control platform and its interface with the PMSM drive system

The controller for the PMSM drive comprises two main parts: microprocessor DSP control board and peripheral acquisition daughter boards. The core of the control system is a commercial TMS320C31-50 microprocessor DSP control board which is in charge of real-time execution and debugging control code and peripheral acquisition. Input/output sub-system daughter boards are made up of (a) analogue/digital signal converter sub-system; (b) digital/analogue signal converter sub-system; (c) current and voltage sample transducer sub-system and.(d) encoder counter convert sub-system. Part (a) provides converts the standard industrial analogue signal (from –5 V to 5 V) into digital binary value which can be read by DSP microprocessor. Part (b) executes the reverse function converting the digital binary value into the standard industrial analogue signal (from –5 V to 5 V) through a specific scale. Part (c) measures the actual current and voltage and generates the corresponding scaled signal (from –5 V to 5 V). Part (d) doubles the pulses generated by the encoder and transforms them into discrete binary values for the DSP to read and determine the incremental position. The entire system is illustrated in fig. 2·9.

CHAPTER 3, SENSORLESS ESTIMATION BASED ON BACK-EMF—FLUX LINKAGE OBSERVER APPLIED TO PMSMs

3.1 INTRODUCTION

Estimation of Back-EMF is one of the main sensorless control schemes first utilized at the beginning of the 1980s [3·1, 3·2, 3·3, 3·4, 3·5]. The PMSM AC motor operates with a sinusoidal BACK-EMF waveform created in the stator armature. The Back-EMF varies regularly with shaft angle. The shaft or rotor angle position information can be deduced through terminal voltages and phase currents. The position angle from the Back EMF when the motor is running is not considered as the shaft/rotor position. From permanent magnet AC motor theory, two parts of the magnet field contribute to the Back EMF. One is from stator flux linkage generated by the armature winding; the other is from the rotor flux linkage created by the PM body mounted on the rotor. Synthetic flux linkage comes from the two parts of the magnetic field shown in fig. 3·1.

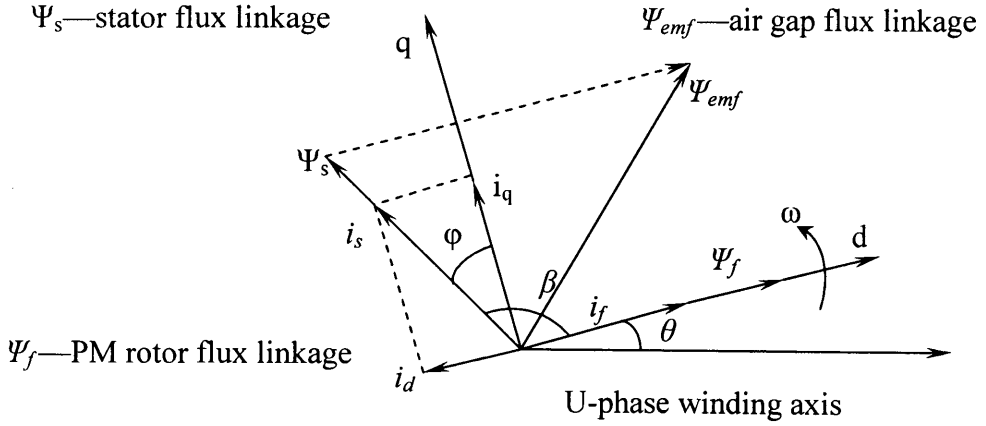

Fig. 3·1 Vector diagrams of the PM AC motor

The flux linkage vector Ψ_s from the stator winding and flux linkage vector Ψ_f from the PM rotor forms the angle (electric) β shown in fig. 3·1. The Back-EMF eventually comes from synthetic flux linkage Ψ_{emf}. The angle θ between the d and U-

phase winding axes is the position angle for the sensorless control scheme and clearly Ψ_f is aligned with the d-axis. Therefore, PM rotor flux linkage Ψ_f needs to be deduced from the synthetic Back-EMF.

Numerous methods have been investigated to explore how to estimate the rotor position angle from Back-EMF but there are two main methods:

1. Direct calculation [3·1, 3·2, 3·3]: d-q and α-β models for the PMSM need to be built up, thus $\sin\theta$ and $\cos\theta$ can be deduced from the voltage and current equations from d-q and α-β models. Eventually position angle θ can be calculated through $\sin\theta$ and $\cos\theta$.
2. Algebraic calculation through flux [3·4, 3·5]: flux models in α-β stationary frame for the PMSM need to be used to calculate rotor position angle through trigonometric functions. Flux linkage can be obtained through the integration of Back-EMF. Due to zero-drifting integration, errors occur in integration of the flux linkage. When the speed of the motor is low, the issue is more serious. In order to overcome this problem, an error compensation link needs to be introduced to make the estimated flux linkage equal to the actual value. The velocity can be calculated by the derivative of the estimated position.

The two Back-EMF methods share the same characteristics: fast, dynamic response without delay. However, the two Back-EMF schemes are required to precisely measure the stator terminal electrical quantities such as voltage or line current to accurately calculate rotor position and velocity because the two schemes highly rely on the accuracy of the given parameters such as resistors. With the motor experiencing changes (e.g. temperature) parameters such as R and Ψ_r also generate the errors. When there is an error in the PMSM parameters, the estimated variables deviate from the real values. Currently, the tendency is to combine the on-line motor parameter identification techniques with this Back-EMF method.

3.2 PROPERTIES OF TWO MAIN BACK-EMF ESTIMATIONS

3.2.1 Direction Estimation

The voltage equations in d-q axis coordinate frame are as follows

$$u_d = (R+pL_d)i_d - \omega L_q i_q \qquad (3\cdot1)$$

$$u_q = (R+pL_q)\, i_q + \omega L_d i_d + \omega \Psi_r \quad (3\cdot2)$$

where R — phase resistance; p — pole pairs; $L_{d,q}$— inductance in d-axis or q-axis; i_{dq} — current in d-axis or q-axis; ω — angular velocity; $u_{d,q}$ — voltage in d-axis or q-axis; Ψ_r — rotor flux linkage.

The transformation for quantities between d-q and α-β axes coordinate frames is illustrated below

$$u_d = u_\alpha \cos\theta + u_\beta \sin\theta \quad (3\cdot3)$$

$$u_q = u_\beta \cos\theta - u_\alpha \sin\theta \quad (3\cdot4)$$

$$i_d = i_\alpha \cos\theta + i_\beta \sin\theta \quad (3\cdot5)$$

$$i_q = i_\beta \cos\theta - i_\alpha \sin\theta \quad (3\cdot6)$$

where $u_{\alpha,\beta}$— voltage in the α -axis or β -axis; θ — rotor position reference to α -axis in the stationary frame. Subsequently exchanging (3·3) (3·4) (3·5) and (3·6) for the quantities u_d, u_q, i_d, i_q, respectively, generates the following equations

$$u_\alpha \cos\theta + u_\beta \sin\theta = (R+pL_d)(\, i_\alpha \cos\theta + i_\beta \sin\theta) - \omega L_q (i_\beta \cos\theta - i_\alpha \sin\theta) \quad (3\cdot7)$$

$$u_\beta \cos\theta - u_\alpha \sin\theta = (R+pL_q)(R+pL_q) + \omega L_d\, (i_\alpha \cos\theta + i_\beta \sin\theta) + \omega \Psi_r \quad (3\cdot8)$$

From (3·7), the expression for the rotor position θ can be deduced as

$$\theta = arctg(\frac{A}{B}) \quad (3\cdot9)$$

where $A = u_\alpha - R\, i_\alpha - L_d p\, i_\alpha + \omega\, i_\beta\, (L_q - L_d)$ (3·10)

$$B = -\, u_\beta + R\, i_\beta + L_d p\, i_\beta + \omega\, i_\alpha\, (L_q - L_d) \quad (3\cdot11)$$

Therefore, the rotor position θ can be expressed by the stator terminal voltage, current and angular rotor [3·2].

Since saliency can be neglected in a surface-mounted PMSM, approximately $L_q = L_d = L$. The velocity ω can be obtained from

$$\omega = \frac{\sqrt{C}}{D} \quad (3\cdot12)$$

where

$C = (\, u_\alpha - R\, i_\alpha - L p\, i_\alpha)^2 + (\, u_\beta - R\, i_\beta - L p\, i_\beta)^2$

$D = \Psi_r$

3.2.2 Algebraic Calculation by Flux — Flux Linkage Observer

The equation for the PMSM in the d-q axis coordinate frame can be expressed by the following matrix

$$\begin{bmatrix} u_d \\ u_q \end{bmatrix} = \begin{bmatrix} R + pL_d & -\omega L_q \\ \omega L_d & R + pL_q \end{bmatrix} \begin{bmatrix} i_d \\ i_q \end{bmatrix} + \begin{bmatrix} 0 \\ \omega \Psi_r \end{bmatrix} \tag{3·13}$$

Converting by coordinate transformation into α-β coordinate frame yields

$$\begin{aligned} \begin{bmatrix} u_\alpha \\ u_\beta \end{bmatrix} &= C_{dq-\alpha\beta} \begin{bmatrix} u_d \\ u_q \end{bmatrix} \\ &= C_{dq-\alpha\beta} \begin{bmatrix} R + pL_d & -\omega L_q \\ \omega L_d & R + pL_q \end{bmatrix} \begin{bmatrix} i_d \\ i_q \end{bmatrix} + C_{dq-\alpha\beta} \begin{bmatrix} 0 \\ \omega \Psi_r \end{bmatrix} \\ &= R \begin{bmatrix} i_\alpha \\ i_\beta \end{bmatrix} + p \begin{bmatrix} \Psi_\alpha \\ \Psi_\beta \end{bmatrix} \end{aligned} \tag{3·14}$$

where

$C_{dq-\alpha\beta}$—coordinate transformation from d-q axis frame to α-β axis frame;

Ψ_α, Ψ_β—flux linkage in α-β axis frame (obtained by the integration for Back EMF)

The Back EMF equations are

$$\begin{aligned} e_\alpha &= u_\alpha - Ri_\alpha \\ e_\beta &= u_\beta - Ri_\beta \end{aligned} \tag{3·15}$$

From (3·14), Ψ_α, Ψ_β can be expressed as

$$\begin{aligned} \begin{bmatrix} \Psi_\alpha \\ \Psi_\beta \end{bmatrix} &= L_q \begin{bmatrix} i_\alpha \\ i_\beta \end{bmatrix} + (L_d - L_q) \begin{bmatrix} \cos\theta & 0 \\ 0 & \sin\theta \end{bmatrix} \begin{bmatrix} \cos\theta & \sin\theta \\ \cos\theta & \sin\theta \end{bmatrix} \begin{bmatrix} i_\alpha \\ i_\beta \end{bmatrix} + \Psi_r \begin{bmatrix} \cos\theta \\ \sin\theta \end{bmatrix} \\ &= L_q \begin{bmatrix} i_\alpha \\ i_\beta \end{bmatrix} + [(L_d - L_q) i_d + \Psi_r] \begin{bmatrix} \cos\theta \\ \sin\theta \end{bmatrix} \end{aligned} \tag{3·16}$$

thereby

$$\hat{\Psi} = \sqrt{(\hat{\Psi}_\alpha - L_q i_\alpha)^2 + (\hat{\Psi}_\beta - L_q i_\beta)^2} = (L_d - L_q)\hat{i}_d + \Psi_r$$

The expression can be obtained for rotor position angle as:

$$\cos\hat{\theta} = \frac{\hat{\Psi}_\alpha - L_q i_\alpha}{\hat{\Psi}} \quad \sin\hat{\theta} = \frac{\hat{\Psi}_\beta - L_q i_\beta}{\hat{\Psi}}$$

In order to eliminate the zero-drift brought by the integration, error, compensation is introduced

$$\begin{aligned}\hat{\Psi}_\alpha &= \frac{Te_\alpha}{1+Ts}+\frac{\Psi_\alpha^*}{1+Ts}=\frac{T_s\Psi_\alpha}{1+Ts}+\frac{\Psi_\alpha+(\Psi_\alpha^*-\Psi_\alpha)}{1+Ts}\\ &=\Psi_\alpha+\frac{\Psi_\alpha^*-\Psi_\alpha}{1+Ts}\end{aligned} \tag{3·17}$$

where $, e_\alpha = u_\alpha - Ri_\alpha, \Psi_\alpha^*$ —— initial value of flux linkage of α axis;T —— time constant; s —— Laplacian arithmetic operator. Flux linkage in β-axis can be expressed in the same way as

$$\hat{\Psi}_\beta = \frac{Te_\beta}{1+Ts}+\frac{\Psi_\beta^*}{1+Ts}=\Psi_\beta+\frac{\Psi_\beta-\Psi_\beta^*}{1+Ts} \tag{3·18}$$

The initial value of flux linkage in α-β coordinate system can be obtained from

$$\begin{bmatrix}\Psi_\alpha\\ \Psi_\beta\end{bmatrix}=\begin{bmatrix}\cos\hat{\theta} & -\sin\hat{\theta}\\ \sin\hat{\theta} & \cos\hat{\theta}\end{bmatrix}\begin{bmatrix}L_d i_d^*+\Psi_r\\ L_d i_q^*\end{bmatrix} \tag{3·19}$$

The speed can be obtained from the derivative of the rotor position angle [3·3]:

$$\hat{\omega}=\frac{d\hat{\theta}}{dt} \tag{3·20}$$

3.3 Implementation of Flux Linkage Observer for Sensorless Control of the PM Motor

3.3.1 System Model of a Sensorless-Controlled PMSM Based on Flux Linkage Observer

3.3.1.1 Hardware Outline Model of Inverter-Fed Three-Phase PMSM Drive System

The PMSM model under space-vector PWM strategy relies on the structure of a 3-phase power inverter shown in fig. 3·2, where V_A V_B V_C are the voltages applied to the star-connected PMSM windings, and V_{DC} is DC link voltage. The six switches are MOSFET. The ON-OFF sequence of all these devices must obey the conventional space-vector PWM conditions: three of the switches must always be ON and three must always be

OFF. The upper and lower switches of the same leg are driven by two complementary pulsating signals. In this way, no vertical conduction is possible, providing care is taken to ensure that there is no overlap in the power switch transition.

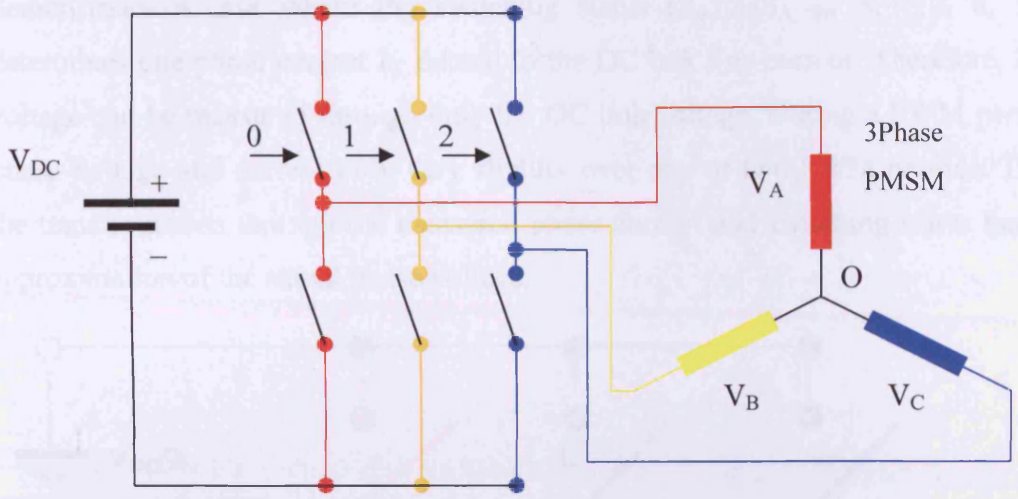

Fig. 3·2 Basic scheme of the inverter-fed, three-phase PMSM.

3.3.1.2 Space-Vector PWM Strategy model of InverterFed, Three-Phase PMSM Drive System

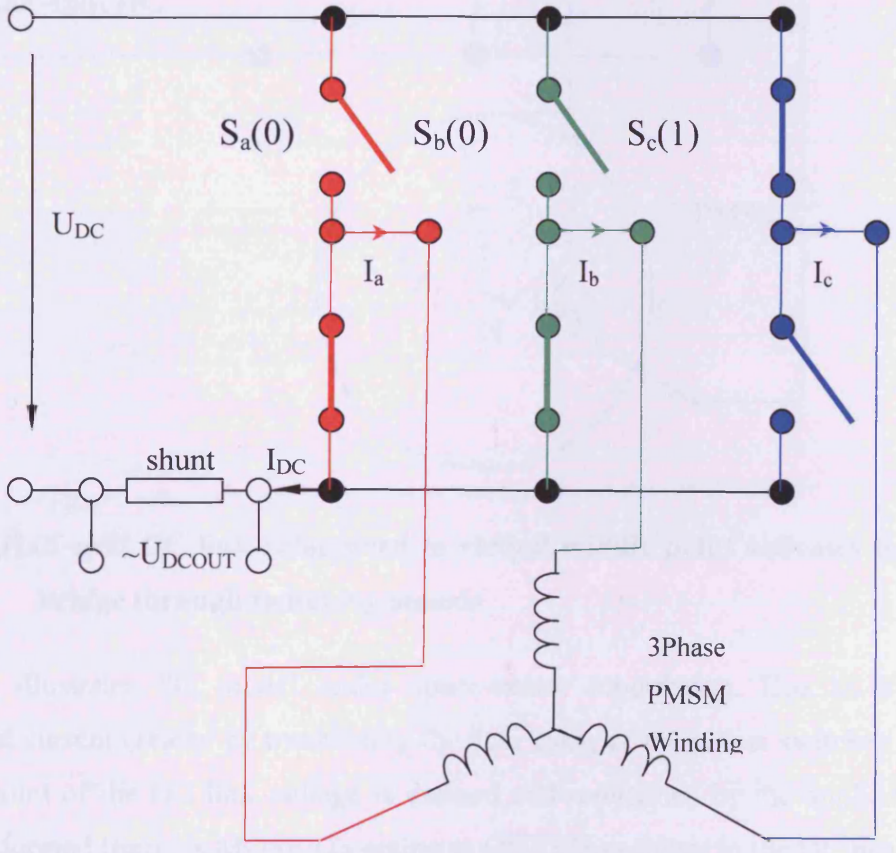

Fig. 3·3 Sensed signal for controlling inverter supplying a net of three-star winding.

Fig. 3·3 illustrates how the phase current information and DC link voltage are sampled. Three-phase currents are directly sensed by three current transducers applied to the PMSM phases. The DC link voltage is sensed by a shunt voltage transducer. Fig. 3·3 demonstrates a case where the switching status (S_A ,$S_B$$S_A$, S_B ,S_C)=(0, 0, 1) only determines one phase current I_C related to the DC link line current. Therefore, 3-phase voltage can be measured through only the DC link voltage. During a PWM period, the phase voltage and current only vary slightly over one or two PWM periods. Thereby, the transformation through the measured phase current and switching status makes the approximation of the actual phase voltage.

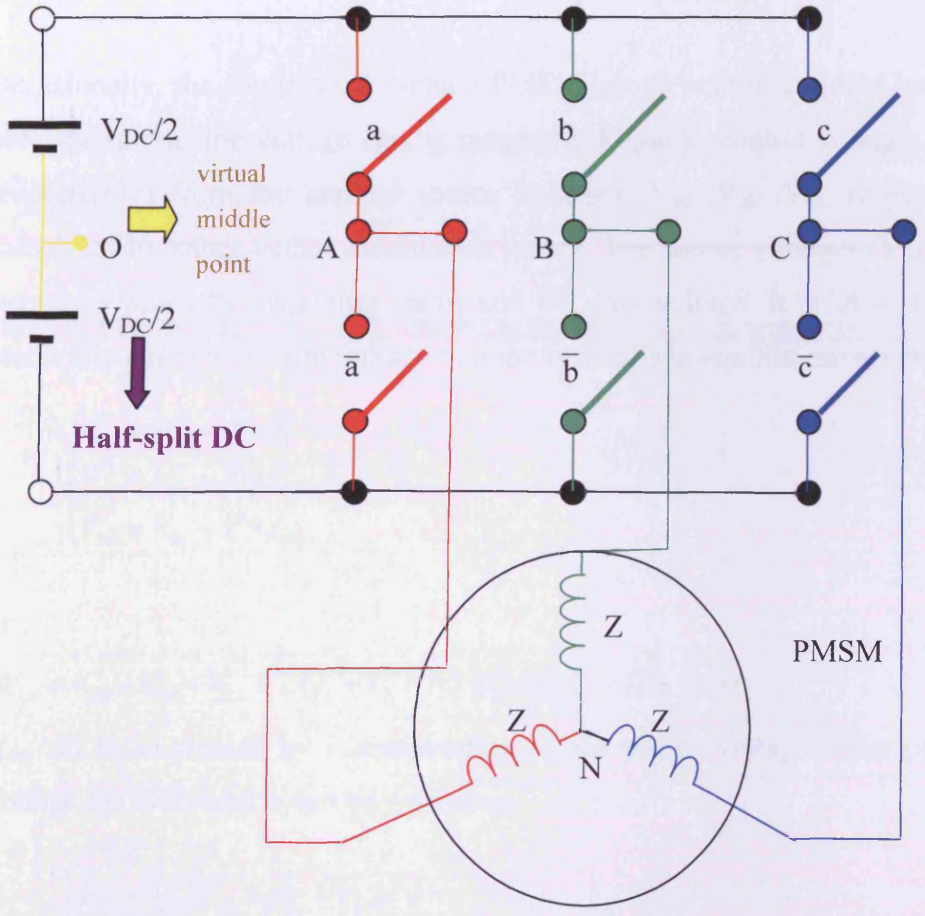

Fig. 3·4 Half-split DC link referenced to virtual middle point activates the power bridge through switching signals

Fig. 3·4 illustrates the model under space-vector modulation. Due to a pseudo-sinusoidal current created by modulating the duty cycle of the power switches, a virtual middle point of the DC link voltage is defined and referenced by the applied voltage, which is formed from six MOSFETs acting as ON/OFF switches to the DC bus voltage.

The scheme of space-vector modulation is shown in fig. 3·5. In order to generate a rotating magnetic field, space-vector modulation needs to model 3 independent voltage sources 120 degrees out of phase. The three sinusoidal voltages applied to each of the motor phases generate the sinusoidal currents. Under the space-vector PWM model, these voltage sources can be expressed as

$$\begin{cases} V_{oa} = V\sqrt{2}\cos(\omega_e t) \\ V_{ob} = V\sqrt{2}\cos(\omega_e t - \frac{2}{3}\pi) \\ V_{oc} = V\sqrt{2}\cos(\omega_e t - \frac{4}{3}\pi) \end{cases} \tag{3·21}$$

Occasionally, the commercial 3-phase PMSM has no neutral terminal leading out. Thus only the motor line voltage can be measured. Phase to neutral voltages (V_{an} ,V_{bn} ,V_{cn}, respectively) from the applied source voltages (V_{oa} ,V_{ob} ,V_{oc}, respectively) can be calculated by space-vector modulation theory. The source voltages (V_{oa} ,V_{ob} ,V_{oc}) are also determined by switching status and DC link voltage. It must be assumed before predicting phase to neutral voltage that the system is in equilibrium according to

$$\begin{cases} V_{on} = V_{oa} + Z * I_1 \\ V_{on} = V_{ob} + Z * I_2 \\ V_{on} = V_{oc} + Z * I_3 \end{cases} \tag{3·22}$$

or

$3V_{on} = V_{oa} + V_{ob} + V_{oc} + Z(I_1 + I_2 + I_3)$ where $I_1 + I_2 + I_3 = 0$

V_{on} can be expressed by a combination of the source voltages. The phase to neutral voltage for every phase can be written as

$$\begin{cases} V_{an} = \frac{1}{3}(2V_{ao} - V_{bo} - V_{co}) \\ V_{bn} = \frac{1}{3}(2V_{bo} - V_{ao} - V_{co}) \\ V_{cn} = \frac{1}{3}(2V_{co} - V_{ao} - V_{bo}) \end{cases} \tag{3·23}$$

Eight switch combinations are possible not only with the source voltage configurations shown in table 3·1 but are also possible with the phase to neutral voltage configurations shown in table 3·2.

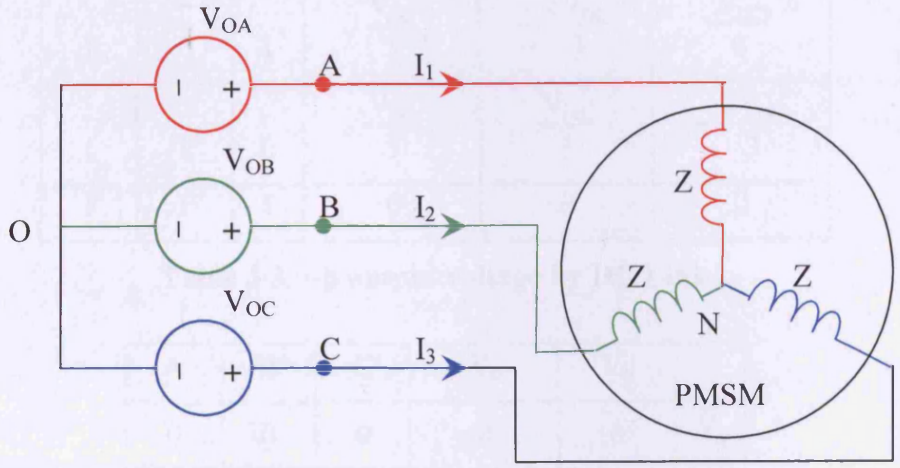

Fig. 3·5 Three-phase equilibrate system-fed PMSM

Table 3·1 Power bridge output voltage by half-split DC link referenced to the virtual middle point

A	B	C	V_{AO}	V_{BO}	V_{CO}
0	0	0	$-V_{DC}/2$	$-V_{DC}/2$	$-V_{DC}/2$
0	0	1	$-V_{DC}/2$	$-V_{DC}/2$	$+V_{DC}/2$
0	1	0	$-V_{DC}/2$	$+V_{DC}/2$	$-V_{DC}/2$
0	1	1	$-V_{DC}/2$	$+V_{DC}/2$	$+V_{DC}/2$
1	0	0	$+V_{DC}/2$	$-V_{DC}/2$	$-V_{DC}/2$
1	0	1	$+V_{DC}/2$	$-V_{DC}/2$	$+V_{DC}/2$
1	1	0	$+V_{DC}/2$	$+V_{DC}/2$	$-V_{DC}/2$
1	1	1	$+V_{DC}/2$	$+V_{DC}/2$	$+V_{DC}/2$

Table 3·2 Power bridge output voltage by phase to neutral

A	B	C	V_{AN}	V_{BN}	V_{CN}
0	0	0	0	0	0
0	0	1	$-\frac{V_{DC}}{3}$	$-\frac{V_{DC}}{3}$	$\frac{2V_{DC}}{3}$
0	1	0	$-\frac{V_{DC}}{3}$	$\frac{2V_{DC}}{3}$	$-\frac{V_{DC}}{3}$
0	1	1	$-\frac{2V_{DC}}{3}$	$\frac{V_{DC}}{3}$	$\frac{V_{DC}}{3}$
1	0	0	$\frac{2V_{DC}}{3}$	$-\frac{V_{DC}}{3}$	$-\frac{V_{DC}}{3}$

1	0	1	$\frac{V_{DC}}{3}$	$-\frac{2V_{DC}}{3}$	$\frac{V_{DC}}{3}$
1	1	0	$\frac{V_{DC}}{3}$	$\frac{V_{DC}}{3}$	$-\frac{2V_{DC}}{3}$
1	1	1	0	0	0

Table 3·3 α-β output voltage by DC Link

A	B	C	V_α	V_β	
0	0	0	0	0	$\vec{V}_0$
0	0	1	$-\frac{V_{DC}}{3}$	$-\frac{V_{DC}}{\sqrt{3}}$	$\vec{V}_1$
0	1	0	$-\frac{V_{DC}}{3}$	$\frac{V_{DC}}{\sqrt{3}}$	$\vec{V}_2$
0	1	1	$-\frac{2V_{DC}}{3}$	0	$\vec{V}_3$
1	0	0	$\frac{2V_{DC}}{3}$	0	$\vec{V}_4$
1	0	1	$-\frac{V_{DC}}{3}$	$-\frac{V_{DC}}{\sqrt{3}}$	$\vec{V}_5$
1	1	0	$-\frac{V_{DC}}{3}$	$\frac{V_{DC}}{\sqrt{3}}$	$\vec{V}_6$
1	1	1	0	0	$\vec{V}_7$

A field-oriented controlled PMSM requires that the control variable is expressed in the rotating frame (d-q) while the back-emf sensorless control needs to calculate the control variable expressed in the stationary frame (α-β). The general "Clarke" transformation can project the 3- phase to neutral voltage into the α-β frame:

$$\begin{bmatrix} V_\alpha \\ V_\beta \end{bmatrix} = \frac{2}{3}\begin{bmatrix} 1 & -\frac{1}{2} & -\frac{1}{2} \\ 0 & \frac{\sqrt{3}}{2} & -\frac{\sqrt{3}}{2} \end{bmatrix}\begin{bmatrix} V_{AN} \\ V_{BN} \\ V_{CN} \end{bmatrix} \tag{3·24}$$

Table 3·4 shows the final switching configurations for voltage prediction in the stationary frame. These 8 combinations for switch command in table 3·3 can determine the 8-phase voltage vectors ($\vec{V}_0 \sim \vec{V}_7$) shown in fig. 3·6.

3.3.1.3 Space-Vector PWM Strategy Expression by a Phasor Diagram

Space-vector PWM strategy aims to generate a spherical rotating field. Fig. 3·6 illustrates how SVPWM approximates the desired stator reference voltage with these 8 switching status configurations. The proposed hysteresis PWM strategy does not have to generate approximated reference voltage to determine the switching status of the inverter. Fig. 3·6 is used to generate α-β voltage by actual switching status.

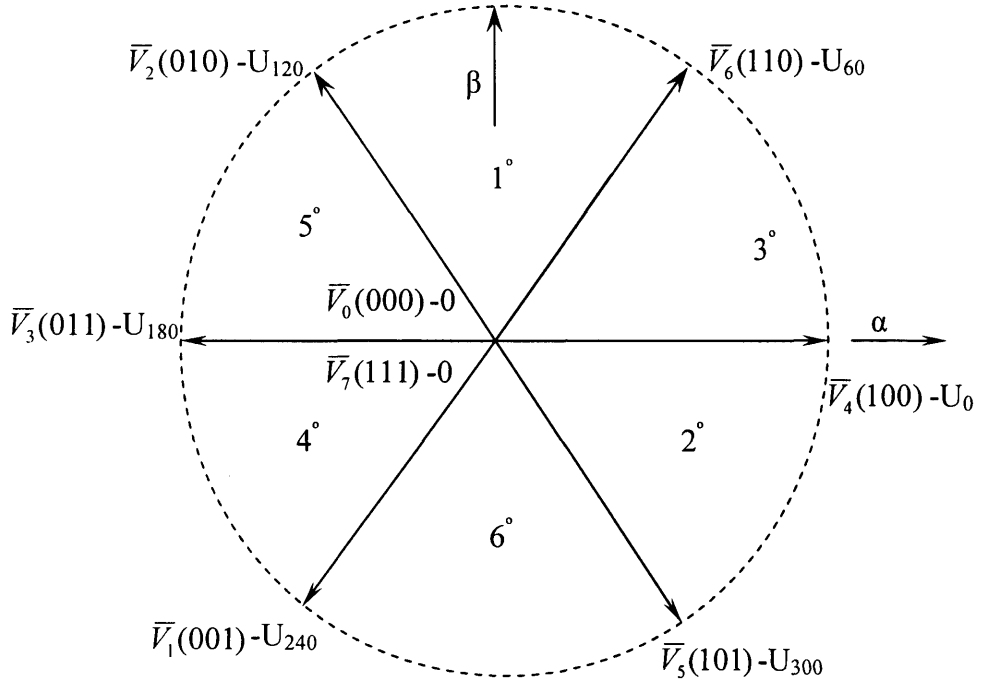

Fig. 3·6 Diagram of SVPWM, vectors and sectors.

Although SVPWM strategy is used to generate the voltage in the stationary frame and hysteresis strategy is used to determine switching status, the adjacent reference voltage vector in fig. 3·7 actually acts as a current and is limited within the desired range. Unlike the SVPWM in fig. 3·7, $\overline{V}_0(000)$ and $\overline{V}_7(111)$ are not used in the proposed hysteresis PWM — only the hexagon of SVPWM. Fig. 3·7 shows the switching status for SVPWM, where synthetic reference voltage from adjacent vectors determines the combination of 4 switching states.

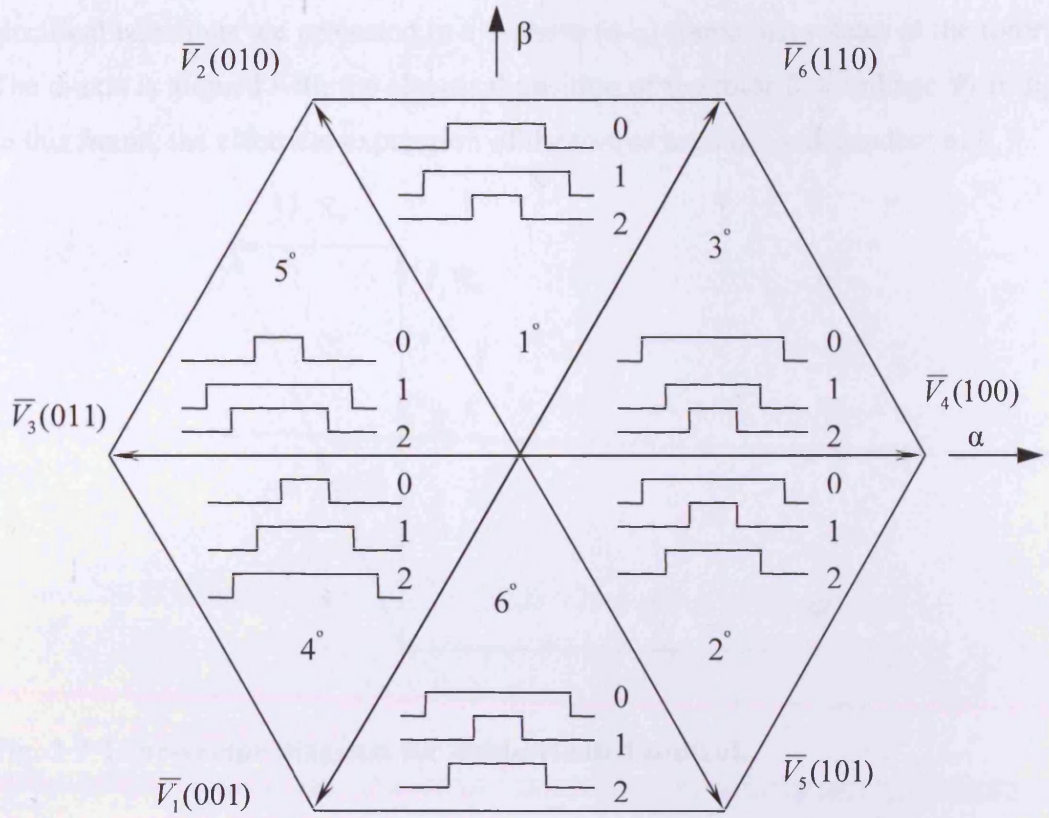

Fig. 3·7 Hexagonal SVPWM pattern.

3.3.1.4 Field-Oriented Space Vector Model for PMSM Control

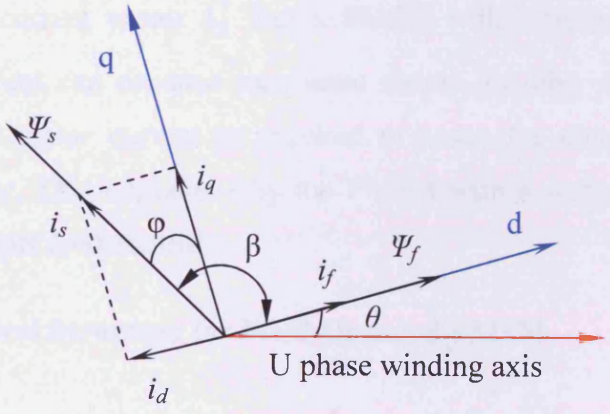

Fig. 3·8 Space-vector diagram of a PMSM.

Field-oriented control is used to perform real-time control of torque variation instructions, to control speed and to adjust phase currents. Its mathematic basis is to project the electrical equations from a 3-phase non-rotating frame into the two-phase co-

ordinate frame shown in fig. 3·8. After the "Park and Clarke" transformation, the electrical equations are projected in a 2-phase (d-q) frame that rotates at the rotor speed The d-axis is aligned with the electrical position of the rotor flux linkage Ψ_f in fig. 3·9. In this frame, the electrical expression of the torque becomes independent of θ_e.

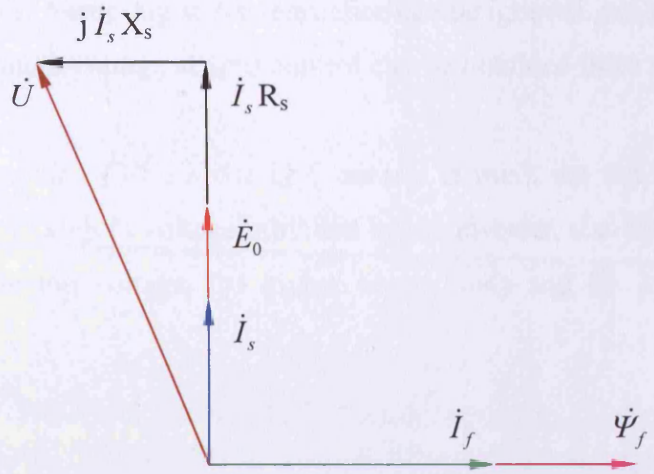

Fig. 3·9 Time-vector diagram for field-oriented control.

When i_d=0, the PMSM is regarded as an externally excited DC motor. Stator current has only a quadrant-axis component and the stator potential vector is in quadrature with the PM field vector, β=90°. Only the PM torque component exists and its value is

$$T_{em} = p\psi_f i \quad (3\cdot25)$$

The time vector map for i_d=0 control is shown in fig. 3·9. The Back-EMF vector $\dot{E}_0$ is in phase with stator current vector $\dot{I}_s$. For a PMSM with a surface-mounted salient rotor, unit stator current can produce maximum torque. In other words, for a given torque, the minimum stator current is required to lower the copper loss, and thus increase the efficiency. This explains why the PMSM with a surface-mounted salient rotor occasionally adopts i_d=0 control.

3.3.1.5 Digital Control Structure for Field-Oriented PMSM

In fig. 3·10, three series-connected closed loops are employed to implement the position, velocity, and torque control of the motor. The difference between the actual and demanded speeds is the input of the PI speed controller, the output of which is used for the instruction of quadrant current I_q. The output of such an angular velocity controller is just the instructional value of torque. The actual value of torque can be calculated

from the torque equation at a given excited flux and actual i_d and i_q transformed by vector ($e^{-j\theta}$ transform). After the difference between the actual torque signal (I_q) and torque instruction, (I_q) is transformed by the torque controller (PI speed controller) and vector inverse transform, 3-phase current instruction can be obtained to feed the motor current controller. Assuming stator resistance can be ignored, peak motor velocity under the inverter ultimate voltage at i_d=0 control can be obtained from the voltage and torque equations.

From equation (3·1), if the i_d=0 control is used, the top velocity of the motor depends on the maximum voltage provided by the inverter, also upon output torque. The higher attainable top voltage, the higher top velocity and the lower output torque is achieved.

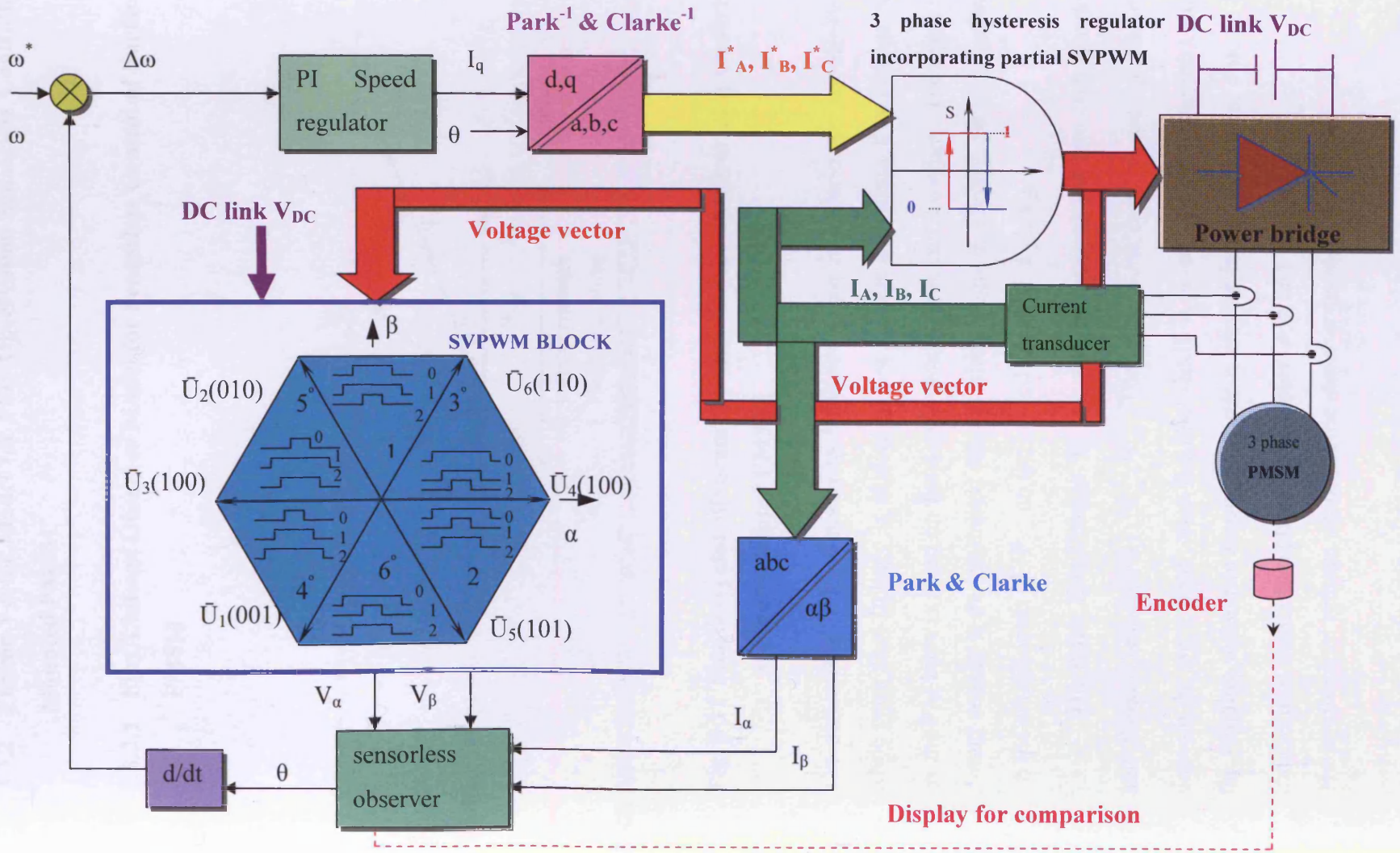

Fig. 3·10 Full-digital control scheme for the speed field-oriented PMSM.

3.3.2 Phasor-Vector Model for Flux Observation Sensorless Controlled Surface-Mounted PMSM

3.3.2.1 Flux Linkage Observer Model for Sensorless Control of Surface-Mounted PMSM

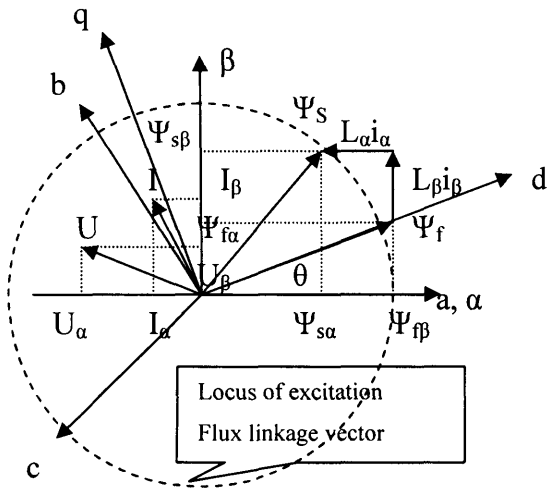

Fig. 3·11 Phasor-vector diagram for flux-linkage observer of a sensorless control surface-mounted PMSM.

The stator flux linkage needs to be investigated in a stationary coordinate frame α-β while rotor flux linkage is studied in d-q coordinates. Rotor flux linkage Ψ_f produced by the PM body is fixed on the d-axis spinning around the origin. The angle between the d- and α axes is the estimated rotor position angle θ. Clearly, position estimation relies on the components of Ψ_f on the α and β-axis: $\Psi_{f\alpha}, \Psi_{f\beta}$.

The stator flux linkage Ψ_s can also be decomposed into components at the α- and β-axes, respectively: $\Psi_{s\alpha}, \Psi_{s\beta}$. These components of Ψ_f are calculated essentially through the Back-EMF; then the Back-EMF is given by subtracting the voltage drop on the winding resistance through the stator current from the terminal voltage V_α and V_β, transformed from three phase coordinates: a, b and c.

The synthesized voltage vector of the stator is decided from

$$v = \frac{2}{3}(v_a + v_b e^{j\frac{2}{3}\pi} + v_c e^{j\frac{4}{3}\pi}) \tag{3·26}$$

where v_a, v_b and v_c are the instantaneous phase voltages governed by the corresponding switching status: s_a, s_b and s_c shown in fig. 3·3. s_a =1 if v_a is connected with "1" which means that the upper power semiconductor is on, as well as s_b and s_c. Fig. 3·6 demonstrates the sequence for a series of space voltage vectors in one electrical cycle $V_1(100), V_2(110), V_3(010), V_4(011), V_5(001), V_6(101)$. The other two vectors are zero: $V_7(000), V_8(111)$. Equation (3·26) can be rewritten and combined into

$$v(S_a, S_b, S_c) = \frac{2}{3} V_{dc}(S_a + S_b e^{j\frac{2}{3}\pi} + S_c e^{j\frac{4}{3}\pi}) \tag{3·27}$$

where V_{dc} is DC link voltage.

Table 3·3 lists the value of components V_α and V_β of the synthesized voltage vector v calculated from equation (3·27). The sensorless scheme is the flux linkage observer; the first step is to calculate the synthesized flux linkage ψ_s by

$$\dot{U} = \frac{d\dot{\psi}_s}{dt} + R\dot{I} \tag{3·28}$$

Here, R is the winding resistance; $\dot{\psi}_s$ is obtained from the integration of the terminally synthesized voltage $\dot{U}$ subtracted by the voltage drop $R\dot{I}$, shown in

$$\dot{\psi}_s = \int (\dot{U} - R \cdot \dot{I}) dt + \dot{\psi}_{s(0)} \tag{3·29}$$

$\dot{\psi}_{s(0)}$ represents the initial value for the synthesized flux linkage, because at the initial instant, the rotor is aligned by applying one voltage vector to the stator. $\dot{\psi}_{s(0)}$ is considered equal to the initial-stator flux linkage vector since at that moment, the current in the stator winding is zero.

The second step is to calculate the PM excitation flux linkage $\dot{\psi}_f$. From fig. 3·11, $\dot{\psi}_f$ is obtained by subtracting $\dot{I} \cdot L_s$ from the synthesized flux linkage $\dot{\psi}_s$. Since the SSD ACM2n PMSM is a surface-mounted PMSM, the saliency can be ignored and $L_\alpha = L_\beta = L_s$. The approximated equation for ψ_f, can be simplified to

$$\dot{\psi}_f = \dot{\psi}_s - L_s \dot{I} \tag{3·30}$$

Therefore, in the $\alpha-\beta$ coordinate, (3·30) can be used to calculate the components $\dot{\psi}_{f\alpha}$ and $\dot{\psi}_{f\beta}$ of $\dot{\psi}_f$, as shown in fig. 3·11. The rotor position θ_r can be computed from

$$\theta_r = \arctan\frac{\psi_{f\beta}}{\psi_{f\alpha}} \tag{3·31}$$

3.3.2.2 Start-Up for Flux-Linkage Observer of Sensorless Control Surface-Mounted PMSM under Flux-Linkage Observer

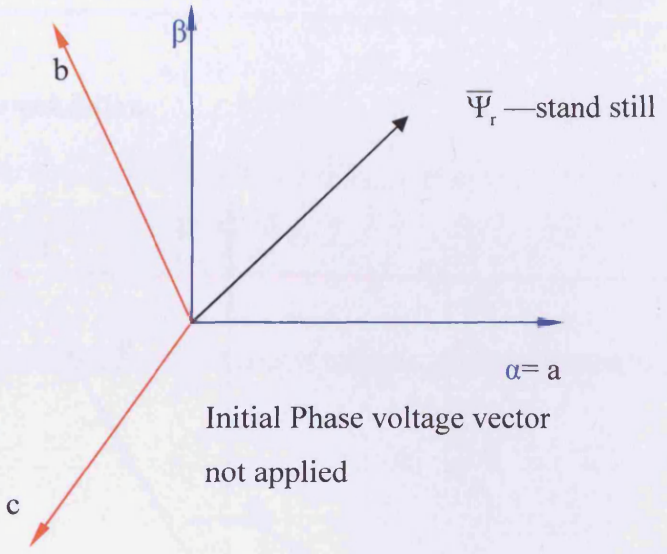

Fig. 3·12 Rotor flux position at standstill.

The start-up procedure requires the initial applied voltage vector to align the rotor with the fixed position. After DSP reset, the axis of the rotor flux stays at the random and unknown position shown in fig. 3·12. At this moment, the rotor position is uncertain. The initial shaft position needs to be recognized by applying a fixed stator voltage/current vector $\bar{I}_{sref}$ to the stator winding. The d-axis lies at the angle θ_e, shown in fig. 3·13. Afterwards, the rotor flux linkage is supposed to align with the d-axis shown in fig. 3·14. Meanwhile, the d-q axis is not rotating. The rotor flux is in a known position but this position is not yet aligned with the d-axis. 90° electrical degrees are added to the value of θ_e. This action is equivalent to the frame rotation in fig. 3·14.

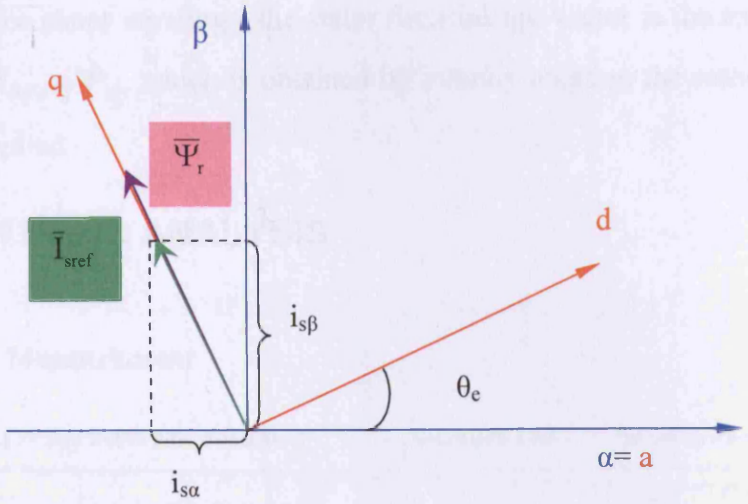

Fig. 3·13 Stalled rotor condition.

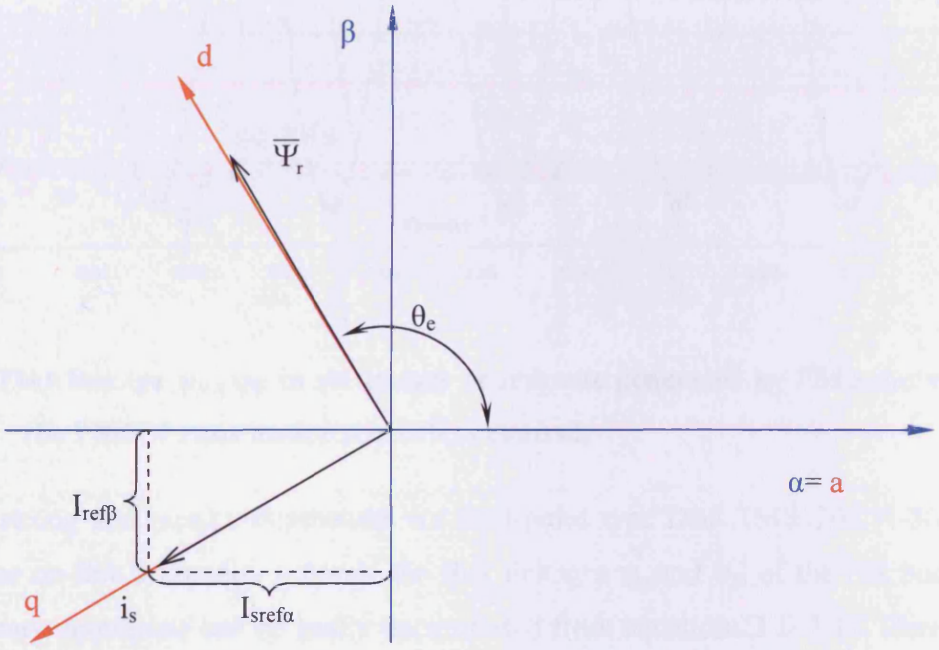

Fig. 3·14 +90° electrical shift.

Instantaneously, the stator current reference vector is moved to 90° from its first position shown in fig. 3·14. The rotor is physically at the same position as previously. The d-axis now corresponds exactly to the position of the rotor flux.

As there is a 90° angular difference between the rotor and stator flux, their interaction produces torque and the rotor starts to rotate in order to align itself with I_{sref}. The initial value θ_e has been chosen to equal -90°. This makes the d-axis correspond to the 0° electrical position at the start. The value -90° was chosen for convenience as the first value for θ_e.

With zero current in the stator windings, the stator flux-linkage vector is the excitation flux-linkage vector, $\dot{\Psi}_{s(0)} = \dot{\Psi}_f$, which is obtained by initially aligning the rotor before the flux observer is applied.

3.4 EXPERIMENT AND ANALYSIS

3.4.1 Flux Linkage Measurement

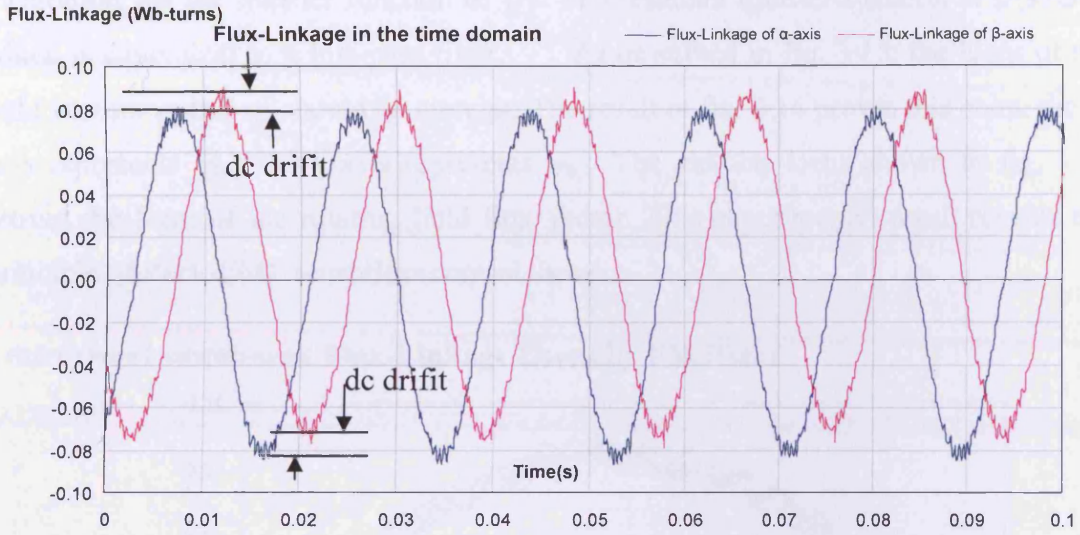

Fig. 3·15 Flux linkage ψ_α, ψ_β in stationary coordinate generated by PM rotor when the PMSM runs under sensorless control.

With the strong and rapid computation via float-point type DSP TMS320C31-50 and through the on-line arithmetic process, the flux linkages ψ_α and ψ_β of the PM body in the stationary coordinate can be easily decomposed from equations 3·1~3·12. Here, the variables ψ_α and ψ_β represent $\psi_{f\alpha}$ and $\psi_{f\beta}$ in fig. 3·15. They are rotating vectors in space similar to other field vectors in fig. 3·15. Every point in the locus of vector behaves sinusoidally with time. Thereby, the ideal flux linkages ψ_α and ψ_β should be sinusoidal with 90 electrical-degree phase shift as demonstrated in fig. 3·15.

Experimental observation indicated in fig. 3·15 proves this matches theory. The amplitude of flux linkages ψ_α and ψ_β appear constant as the theory predicts and the phase shift between them is measured as 90 electrical degrees. The waveform capture of flux linkages ψ_α and ψ_β is based on the following experimental condition: 3-phase PMSM sensorless control is via the flux-linkage observer and the 60 V inverter. The motor system operates at 1000 rpm sensorless mode under no load. The variables ψ_α and ψ_β are calculated by DSP on-line and achieves synchronous output by a 16-bit parallel

bus into a DA channel after the appropriate display pre-scale. It is noted that dc drift of flux linkage ψ_α and ψ_β exists in fig. 3·15. DC drift is the error between the amplitude of flux ψ_α and that of ψ_β in the same polar axis. The cause of DC drift is thermal drift in the AD convert from the measurement. The integration can amplify the error generated by DC drift from the measurement. The algorithm already applies a high-pass filter with transfer function s/(s+ω0) to the variables used in the integration, where ω0 is the minimum angular velocity for a FOL-based sensorless controlled PMSM because the integration has the transfer function of 1/s. The resultant transfer function is 1/(s+ω0), which is equivalent to a low-pass filter. As described in fig. 3·15, the locus of the field vectors ψ_f and ψ_s should be circular. The result in fig. 3·16 proves this point: the y-axis represents ψ_β ; the x-axis represents ψ_α . The circular locus shown in fig. 3·16 proves the form of the rotating field flux vector. This experimental result reveals the principle of Back-EMF sensorless control theory.

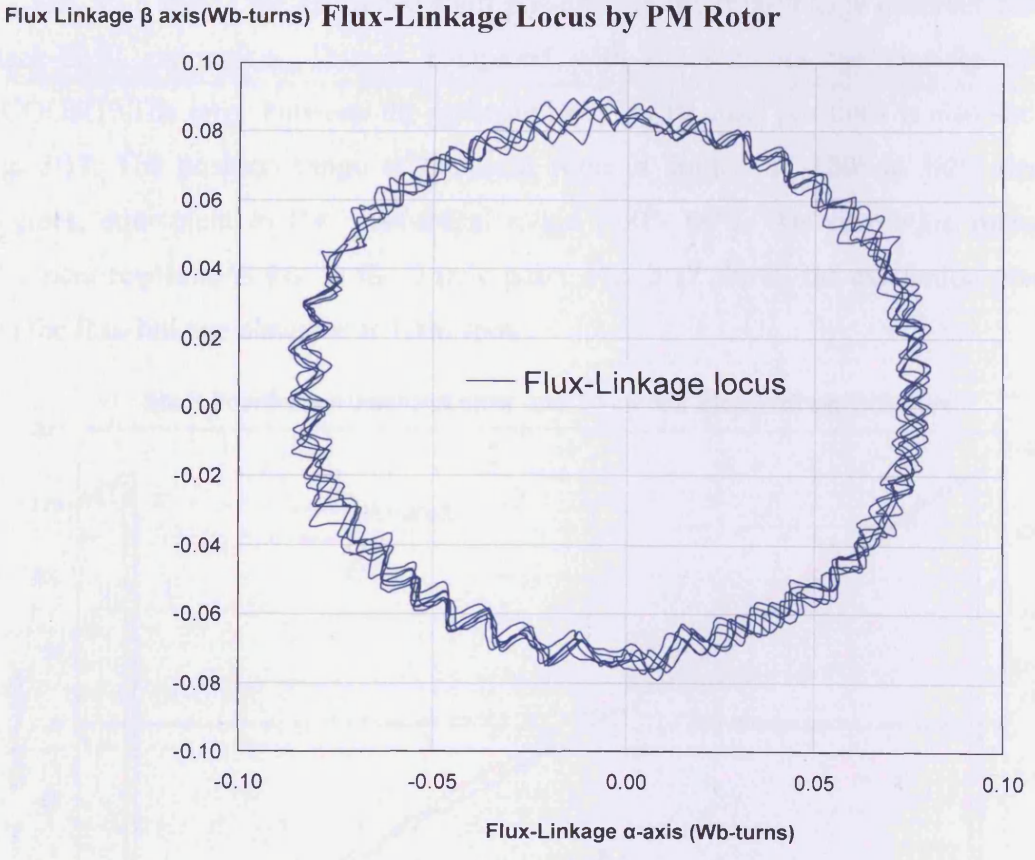

Fig. 3·16 Flux linkages ψ_α and ψ_β in stationary coordinate displayed mutually in x-y axes forming a circular locus of the spinning vector.

3.4.2 Shaft Rotor Position Detection and Error Analysis

A flux-linkage sensorless observer has been successfully applied in the proposed test on a 3-phase 6-pole synchronous PM motor, of which "ACM2n320-4/2-3 (SSDRIVE UK)" was chosen as the commercial servo experimental drive. The experimental set-up is configured as 60 V dc DC link voltage, 600 W, and 1100 rpm.

A high precision encoder was used for comparing estimated and actual position. The precision of the 775R2S4HV2048STD (British Encoder Product) encoder was 2068 pulses per turn. The decoder between the encoder and parallel bus of the DSP is was an ECOUNT (US Digital) which converts the A/B quadrature output of the incremental encoder into 24-bit binary count value with 4 times the original value. The precision of the original encoder was 8192 pulses per turn: the read-in value for the rotor position in DSP varies from 0000H to 1FFF=; therefore, the binary precision of the encoder increases from 11-bit to 13-bit.

Fig. 3·17 shows the estimated shaft position via the flux-linkage observer based on Back-EMF estimation. This is compared with the real via the encoder utilizing ECOUNT. The error between the estimated and actual shaft positions is also shown in fig. 3·17. The position range of the shaft rotor is limited to -180° to 180° electrical degrees, equivalent to the mechanical range [-60°- 60°]. One revolution includes 3 electrical revolutions due to the 3 pole pairs. Fig. 3·17 shows the estimation precision via the flux-linkage observer at 1000 rpm.

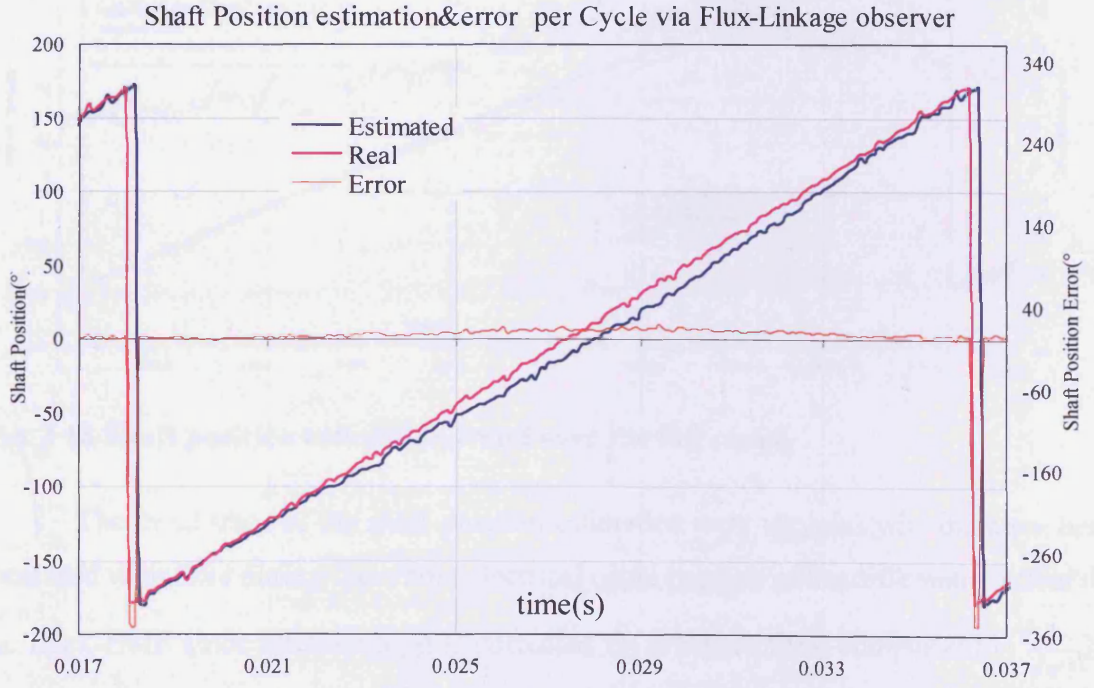

Fig. 3·17 Shaft position estimation and error by flux linkage observer.

The shaft position estimation always traces the real value as shown in fig. 3·17. The flux linkage observer is based on the differential method, and inevitably, the error from the integration is also introduced into the final result, since the low-pass filter is applied to compensate for and reduce the error amplified from integration. Fig. 3·18 clearly indicates the full trend of the estimated position tracing the real position during the cycle of one turn. The course of the position variation includes two parts which have opposite directions plus extra segments of terminal offset: positive offset and hysteresis offset. Fig. 3·18 illustrates the estimated position trace via the flux-linkage observer and starts from a small segment of the hysteresis offset. Then it lasts as the segment of negative offset for almost 80% of the cycle. The extra offset segment lies in the terminal of the cycle -360 (elec °), representing maximum phase shift. The peak values of the estimated position are separately 20 (elec °) and -360 (elec °). The average value is 7.9 (elec °). The error during the +180 (elec °) has a much higher mean value than that during the -180 (elec °). The range from 60-100 (elec °) is the area where maximum error happens. The error characteristics gradually increase to 60 (elec °) peaks and smoothly descends to the extra segment of the terminal fall offset -360 (elec °).

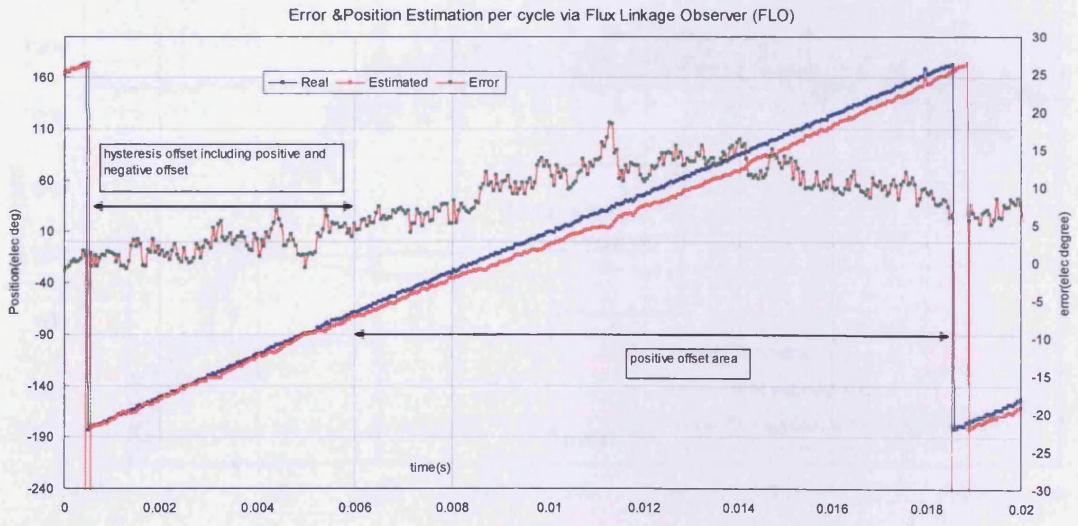

Fig. 3·18 Shaft position estimation trend over the full range.

The trend trace of the shaft-position estimation error explains why the error first increased with time during the whole electrical cycle because of the differential effect of the Back-EMF since afterwards, it is corrected by low-pass filter compensation $\frac{1}{s+1}$ in the control program, thereby descending until the end of the cycle.

3.5 SPEED FEATURE BASED ON FLUX-LINKAGE OBSERVED POSITION INCREMENT

There are multiple speed measurements of sensorless control such as direct measurement based on position increment or the indirect derivation from Back-EMF. Equation (3·32) indicates the direct measurement of the position increment.

$$\omega_r = \frac{\theta_1 - \theta_2}{\Delta t} \tag{3·32}$$

where ω_r — angular velocity, θ_1 , θ_2 , — estimated positions which are measured in sequence and Δt— measured time.

Although the indirect derivation from Back-EMF allows the control system to carry out fast computation while also reducing the calculation load, the direct measurement has fewer errors. The proposed sensorless control of the flux-linkage observer adopts the direct position increment measurement without 2nd order error from Back-EMF estimation.

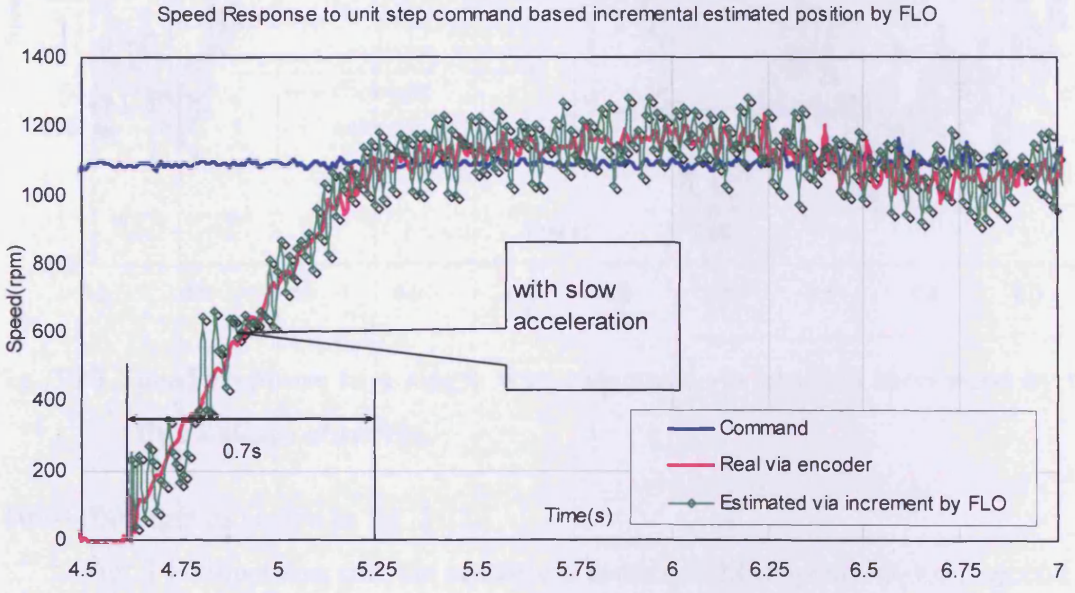

Fig. 3·19 Speed response to the unit step of speed command 1100 rpm via a flux linkage observer based on the direct position increment

Most industrial servo fields require single-direction and dual-direction speed adjustment. The speed characteristic is the second element for assessing sensorless performance. The proposed sensorless method of the flux linkage observer is assessed by three types of commands, i.e., step-unit single-way, and dual-way instructions.

The step-unit instruction for speed is the jump command of 1100 rpm given in fig. 3·19 where the speed command is applied at 4.6 seconds. The single-way instruction for speed is a square wave with a toggle between 500 rpm and 1000 rpm, which has a 4-second period, as shown in fig. 3·20. The dual-way instruction for speed is also the square wave with a toggle between -1100-11000 rpm as illustrated in fig. 3·21.

The step-unit instruct for speed is the jump command of 1100 rpm as depicted in fig. 3·19. The single-way instruction for speed is the square wave with a toggle between 500 and 1000 rpm, which has a 4-second period as shown in fig. 3·20. The dual-way instruction for speed is also the square wave with a toggle between

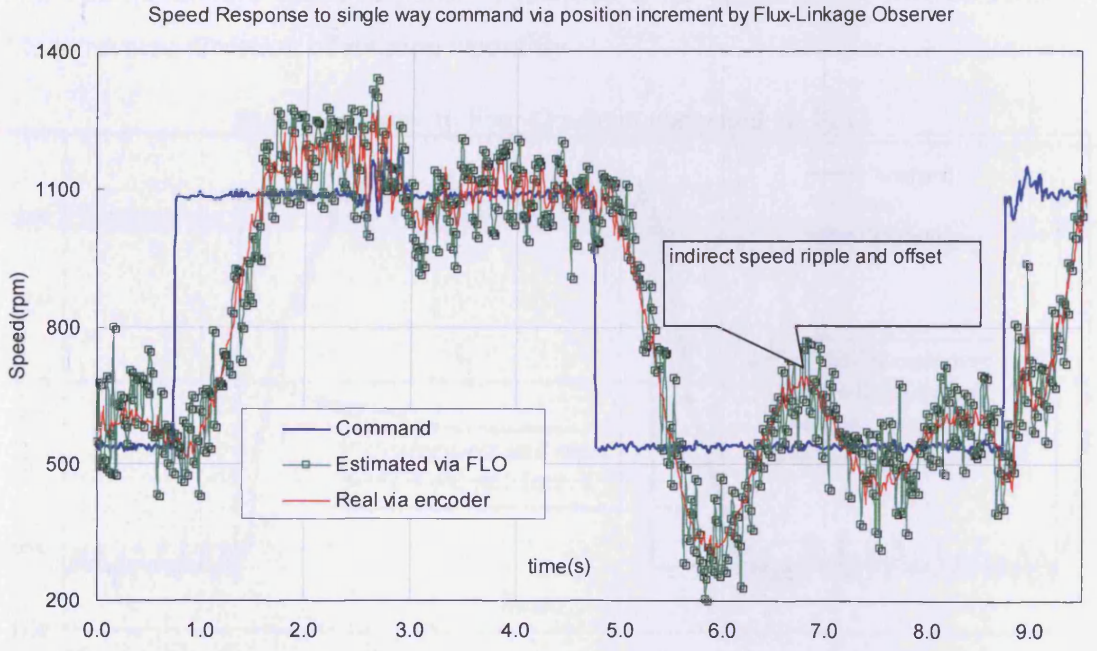

Fig. 3·20 Speed response to a single way command via position increment by the flux linkage observer.

1100-11000 rpm as shown in fig. 3·21.

Fig. 3·19 illustrates that the sensorless control PMSM spends about 1 second on accelerating from zero speed to the command value of 1100 rpm with "+" and "-" offsets. The estimated position increment will be fed as an angular velocity back into the PID regulator to compare with the speed command. The PID regulator automatically gives the responding current control instruction to adjust the speed. The step-unit speed characteristics in fig. 3·19 proves the estimated position is sufficiently precise for a 2nd increment algorithm to indirectly compute speed on-line. Since a large error in

estimated rotor position exists in the low-speed zero range, the acceleration characteristics are slow.

Fig. 3·20 shows how a sensorless controlled PMSM precisely responds to a single-way square wave which toggles between 600 rpm and 1100 rpm. Based on sensorless position estimation, the estimated angle velocity from the indirect increment algorithm is able to reflect the real value with positive or negative offset. The acceleration or deceleration can be fairly approximated. The overshoot of real speed can even be clearly traced by simple indirect increment.

Fig. 3·21 describes the quadrature speed response characteristics for the sensorless controlled PMSM. The quadrature speed reference toggles between 1100 rpm and 1100 rpm. The quadrature speed response is justified if the sensorless controlled PMSM is able to reverse direction of rotation smoothly.

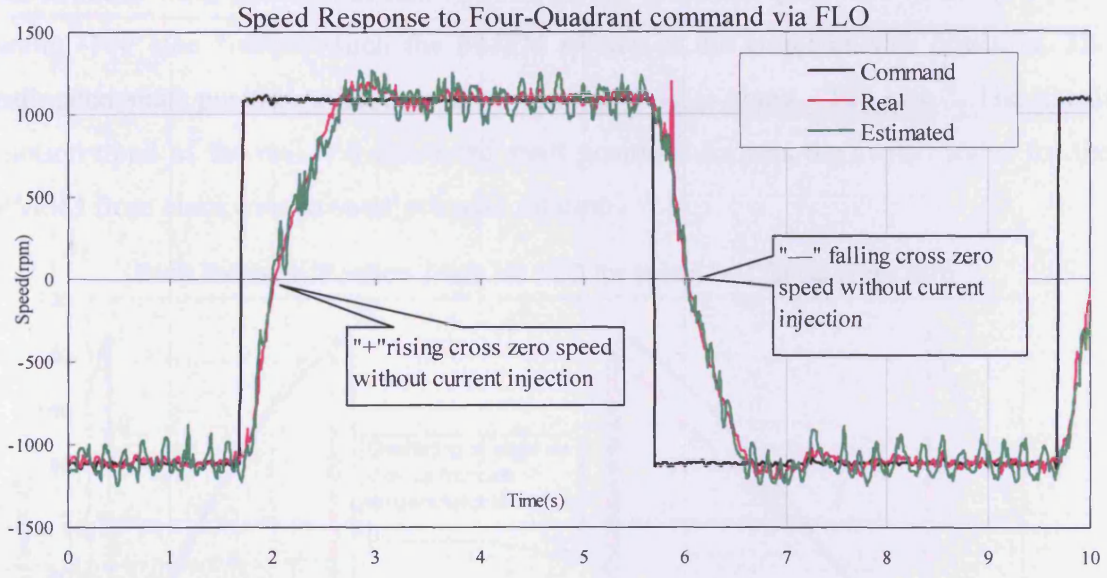

Fig. 3·21 Speed response to 4-quadrant speed command via the flux linkage observer.

The speed based on estimated rotor position via the flux linkage observer goes through zero clockwise and anticlockwise direction tracking real speed with a small error. The actual speed acceleration is tracked precisely the estimated speed. Also the overshoot and steady value of the real speed closely approaches the estimated speed. The zero-crossing for the angle velocity does not rely on current injection for the flux-linkage sensorless observer. It should be noted that the rotor is occasionally found to swing when the speed of the sensorless controlled PMSM crosses zero under the bidirectional speed command. To avoid rotor swings, the peak current command I_q^* can

be forcibly applied by the software when the speed is crossing zero as such current injection helps the rotor smoothly change its rotational direction.

3.5.1 Shaft Estimated Position Trace Feature when in Four Quadrant Operation

The reason that the angular velocity for the flux linkage observer approximately goes through zero, shown in fig. 3·21, is that the estimated shaft position can be close to the real shaft position which can vary during the speed "+" or "-" cross zero as indicated in figs. 3·22 and 3·23. The shaft position of the rotor could change from clockwise to anticlockwise or from anticlockwise to clockwise.

The two types of extreme waveforms representing such specific transition situations are shown in figs. 3·22 and 3·23. The 1st transit situation shown in fig. 3·22 is the concave, well-shaped curve in which the estimated position transits at the bottom of the concave well, which is about -180 elec °. The milestone point shown in fig. 3·22 is about -140 elec ° after which the PMSM rotates in the anticlockwise direction. The estimated shaft position milestone shown in Fig. 3·32 is about - 125 elec °. The transit motion trend of the real and estimated shaft positions reflects the switch status for the PMSM from clockwise to anticlockwise rotation.

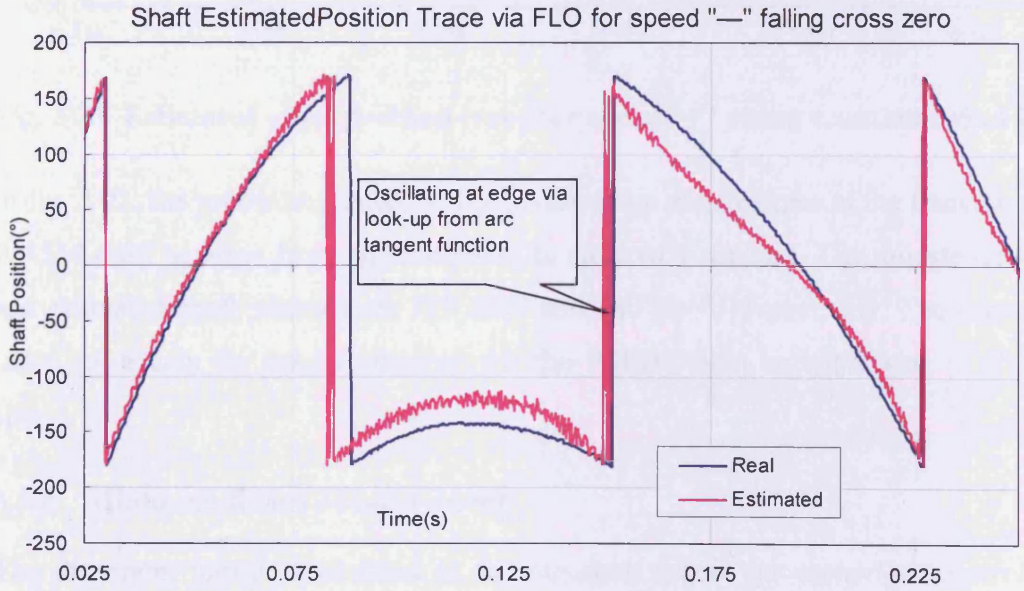

Fig. 3·22 Estimated shaft position trace via FLO for speed "-" falling cross zero.

The concave well-shaped transit trend can test the trace capability of sensorless control. Fig.3·22 shows the oscillation of the estimated position at ±180° when the speed crosses zero. The reason is that the Back-EMF is too weak to detect while the noise of the measurement is greater than the detected signals when the speed cross zero. It is noted that there is a relatively great error in estimated rotor position in the time

domain [0.125, 0.175]s shown in fig.3·22. When the speed of the PMSM starts to increase from zero to "-" command, it does so in the time domain [0.125, 0.175]s, the speed is near zero. The slow speed in the time domain [0.125, 0.175]s causes weak Back-EMF, which great estimated rotor error is also attributed to. A similar explanation applies for the oscillation and the high estimated rotor error in the time domain [0.275, 0.325]s shown in fig.3·23.

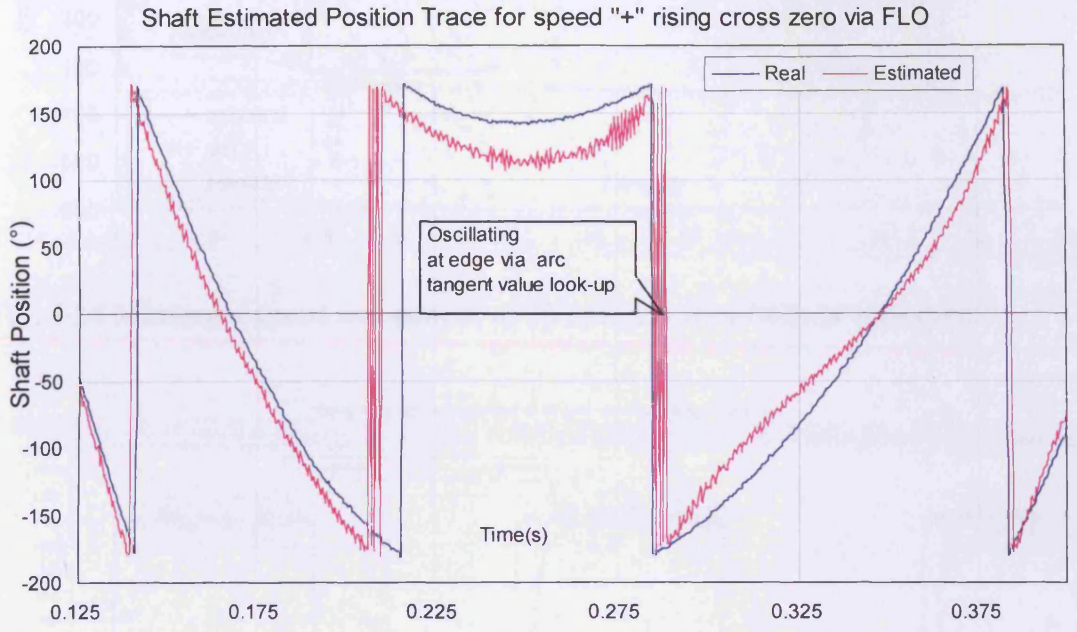

Fig. 3·23 Estimated shaft position trace for speed "+" rising cross zero via FLO.

In fig. 3·23, the protruding pulse with a concave-top also features at the transition of the PMSM shaft position from anticlockwise to clockwise rotation. The milestones for real and estimated shaft position are 125 elec° and 140 elec°, respectively. The concave-top pulse represents the transit situation for the PMSM from anticlockwise to clockwise spin.

3.5.2 Minimum Speed Measurement

The minimum speed assessment is an important aspect for sensorless control when replacing high precision sensors such as encoders or revolvers. Sensorless control highly depends on electrical signal measurement such as current and voltage. If speed falls to or near to zero and also the sensed current is weak, the noise and error from the measurement system might swamp the real signal which will result in incorrect estimation.

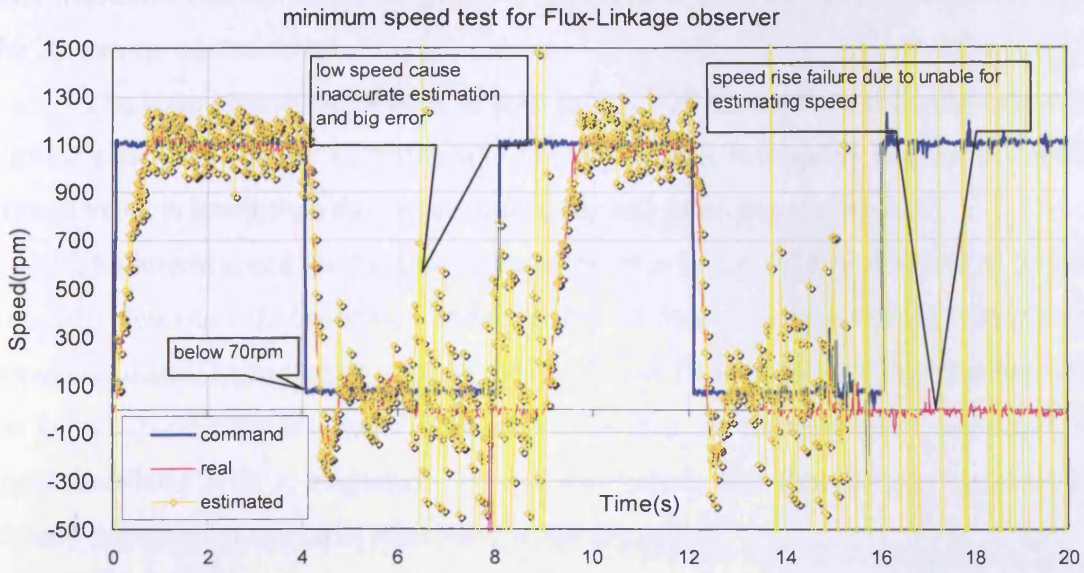

Fig. 3·24 Minimum speed assessment of 70 rpm via flux-linkage observer.

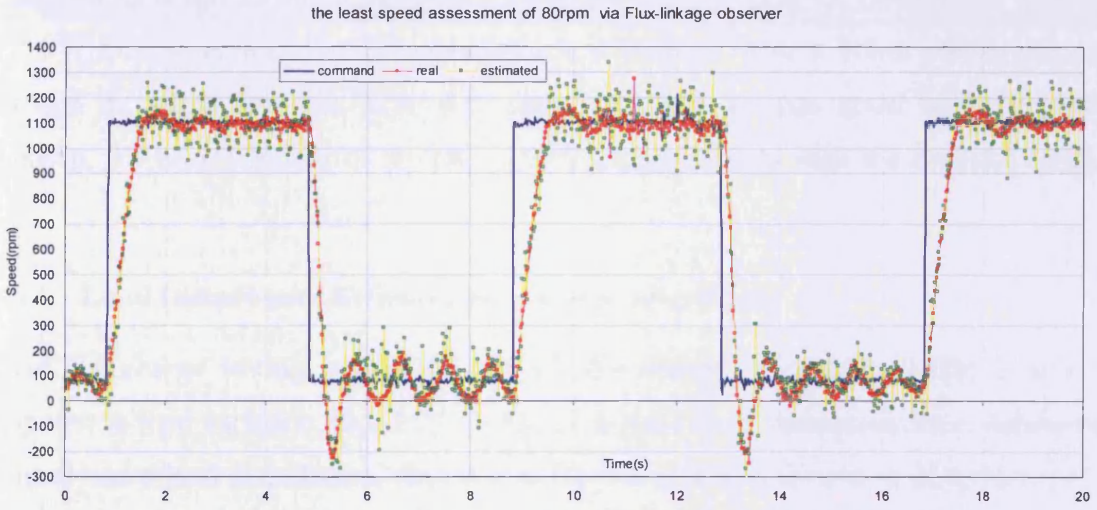

Fig. 3·25 Minimum speed assessment of 80 rpm via flux-linkage observer.

The experimental condition for minimum speed assessment is set up above as: 1 Nm torque linked with the PMSM in non-electromagnetic load mode. The angular velocity command is configured as the square waveform toggling between 1100 rpm and minimum speed with 50% duty-cycle. The duty period of the speed command lasts 4 seconds providing sufficient operation time to observe estimation behaviour. The PMSM is instructed by the command to switch the speed area between 1100 rpm and the minimum speed of 70 rpm as shown in fig. 3·24 or 80 rpm as illustrated in fig. 3·25. The result from the experimental observation reveals that flux linkage estimation is capable of reaching its utmost of 80 rpm. The 70 rpm minimum speed shown in fig.

3·24 illustrates that the flux linkage observer failed to give the exact estimation during the 70 rpm speed command.

The large estimation error at 70 rpm in fig. 3·24 comes from the extremely weak current generated by the I_{q0} reference. During such a low-speed regime the sensed current value is lower than the noise level of the AD sampling system itself.

The lowest speed for the flux linkage observer in fig. 3·25 is observed as 80 rpm. Fig. 3·25 describes the estimated speed ability to trace real speed during the 80 rpm speed command. Even negative speed overshoot can be appropriately approached when the actual speed switches from 1100 rpm to 80 rpm. At 80 rpm speed command, the speed oscillates with a magnitude of 100 rpm where the flux linkage observer has already caused a considerable error for the above reason.

3.6 LOAD EFFECT ON SENSORLESS OPERATION

Load testing is carried out in the generation mode which makes the PMSM link with the 2.2 kW DC generator. The DC generator is connected with a 1ohm power rheostat through its output terminal. After the output terminals are connected with the power rheostat, the rotor winding of the DC shunt generator reacts with the resistant torque.

3.6.1 Load Disturbance Effect on Speed Characteristics

Load disturbance testing is used to verify if the sensorless control PMSM is able to response to load variation. Fig. 3·26 illustrates the response characteristics of sensorless control under load disturbance. An experiment was arranged for a load disturbance of 3 seconds reflected in fig. 3·26 by the 3-second pulse for I_q with a magnitude of 1.5A. The pulse, Iq, shown in fig.3·26 reveals that the load disturbance generates the variation of quadrant current Iq, because it represents the commitment from the speed regulator shown in fig.3·10.

To keep a constant speed command, the quadrant current is generated by increasing speed error. The proliferation of the load caused the relevant q-axis reference current I_q in fig. 3·26 to rise promptly. Fig. 26 also shows the true and estimated speed responses to the load disturbance decreasing from 1100 rpm to 750 rpm rapidly at first due to the reaction of I_q, where the real and estimated speeds finally recover to 1100 rpm. The speed characteristics indicate the estimated speed is capable of delivering the true position information to the input of the PI regulator shown in fig. 3·10. Thereby, the speed difference can be amplified via the PI regulator to compensate for the speed drop

and increased current reference I_q. This load experiment shows that a FLO-based sensorless controlled PMSM can produce responses that can adapt to the load disturbances. The variation of quadrant current Iq for the load disturbance shows the FLO-based sensorless system is sufficiently robust to external disturbances.

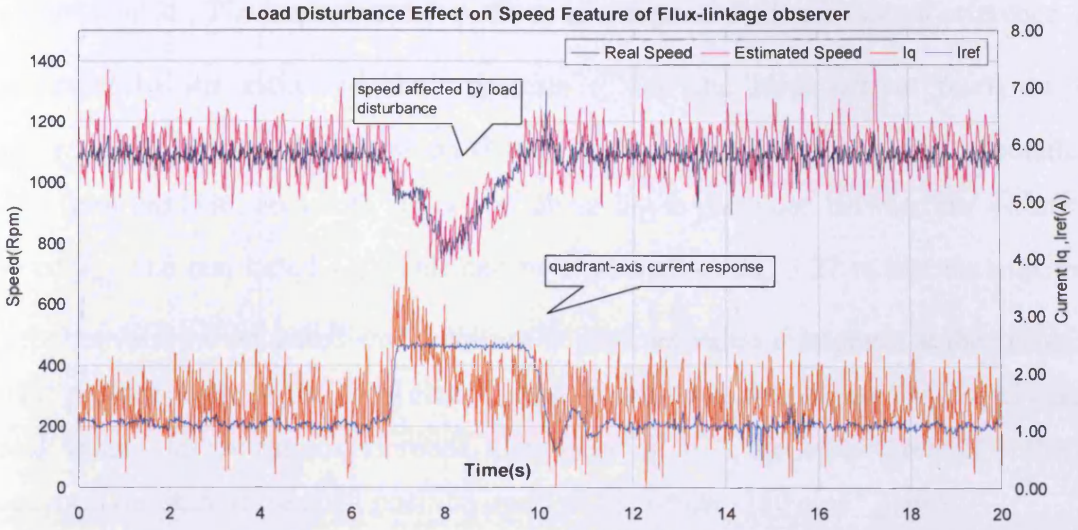

Fig. 3·26 Effect of load disturbance on speed feature of flux linkage observer.

3.6.2 Load Characteristics in the Generator mode

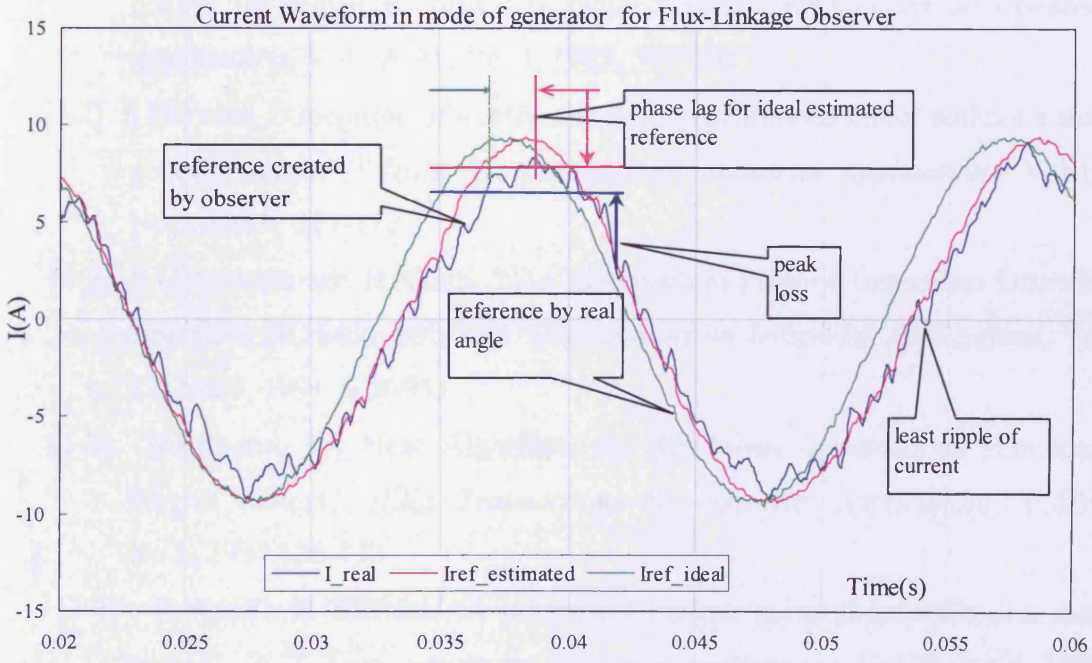

Fig. 3·27 Current waveform with load in generator mode via flux linkage observer.

The load test is carried out on the PMSM in generation mode. During generation, load torque is increased from the generator winding. Fig 3·27 shows the phase current waveform comparison in the generator mode via the flux linkage observer. This illustrates the complete current waveform cycle when the PMSM operates with the generator load . The true current waveform is compared with the current reference $\hat{I}_{ref}$ generated by the estimated shaft position $\hat{\theta}$ and the ideal current reference I_{ref} generated by the true shaft position θ from the encoder. Due to heavy computational load from the DSP, about 50 ° (elec.) of phase lag is produced between the estimated-based $\hat{I}_{ref}$ and real-based I_{ref} . This can be explained in fig. 3·27 in that the maximum error between the estimated shaft position $\hat{\theta}$ and real value θ happens at the end of the shaft position cycle of the +180 elec. ° phase. Such error also causes the loss of current peak value from the current reference. Clearly in fig. 3·27, the least current error thereby occurs at the start of the shaft position cycle of the whole -180 elec ° phase.

3.7 REFERENCES

[3·1] K. Iizuka, H. Uzuhashi, M. Kano, T. Endo, and K. Mohri, "Microcom-puter control for sensorless brushless motor," *IEEE Transactions on Industrial Applications*, Vol. IA-21, No. 4, 1985, 595-601

[3·2] J. Davoine, "Operation of a self-controlled synchronous motor without a shaft position sensor", *IEEE Transactions on Industrial Applications,* Vol.19, No.2, 1983, 217-222

[3·3] S.Ogasawara and H.Akagi, " An Approach to Position Sensorless Drive for Brushless DC Motors," *IEEE Transactions on Industrial Applications,* Vol. 27, No. 5, 1991, 928-933

[3·3] N.Ertugrul, "A New Algorithm for Sensorless operation of permanent magnet motors," *IEEE Transactions on Industrial Applications*, Vol.30, No.1, 1994,126-133

[3·4] R.Wu, G. R. Slemon, "A permanent magnet motor drive without a shaft sensor", *IEEE Transactions on Industrial Applications*, Vol.27, No.5, 1991, 1005-1011

[3·5] J. S. Kim and S. K. Sul, "New approach for high-performance PMSM

drives without rotational position sensors", *IEEE Transactions on Power Electronics*, Vol. 12, Issue 5, Sep 1997, pp. 904 - 911.

CHAPTER 4, A FULL-ORDER COVARIANCE CORRECTION STATE ESTIMATION SENSORLESS CONTROLLED PMSM TECHNIQUE—EXTENDED KALMAN FILTER OBSERVER

The Flux-linkage observer (FLO) described in Chapter 3 introduces the derivation of the Back-EMF as realizing sensorless control of the PMSM. Although a low pass filter is employed to compensate for the integration offset, the FLO directly estimates the shaft position information without the need for position error correction. Direct estimation through the FLO without error correction results in limited self start-up which requires the initial voltage vector to be applied to the PMSM, so its rotor is aligned at the most convenient location for start-up.

The EKF-based sensorless control method for the PMSM first appeared in literature in 1991 [4·1]. The mathematic model for the EKF observer is built up in a stator-fixed reference frame. It considers the full mechanic-electrical load characteristics including the full deterministic load variables such as the average load torque, rotor inertia and viscous damping. The speed equation including mechanical quantities increases the complex computation of the Jacobian matrix. The digital integration algorithm employs the 1^{st} order Euler method, which is still used in industry and academic research today. It is shown that the noise covariance Q, in the variance prediction formula represents the system model inaccuracy, disturbances and noise created by voltage measurements incorporating sensor noise, and A/D converters quantization. It is also shown that the covariance R, for the noise from the output measure system reflects the measurement noise produced by the current sensors, and the coding effects of the A/D converters. It is shown that tuning the covariance matrices Q and R affects both the transient duration and the steady state operation.

Analysis is undertaken considering the diagonal terms of the initial state covariance matrix P_0 that represent the variances or mean squared errors. The tuning P_0 results in a varying magnitude of the transient characteristics. It shows that the covariance matrices Q, R and P_0 should be assigned with a diagonal to simplify the system evaluation. The EKF-based sensorless PMSM algorithm set the standard

stochastic filtering state estimation which is adopted by the following PMSM sensorless research [4·2-4.4].

To overcome the complex structure of the Jacobian partial derivation matrix, Bolognani [4·2] introduced the infinite inertia hypothesis into the dynamic model of the PMSM. This assumes that the rotor speed derivative is negligible compared with the other system variables, and any mechanical load parameter as well as the load torque will disappear from the motor equations. This hypothesis eventually generates the zero vector in the Jacobian matrix which results in a significant reduction in the computation load. Experimentation of the EKF algorithm under such a hypothesis obtains a similar performance as with the position estimation precision, speed estimation and load disturbance as the EKF algorithm. Most sensorless professionals follow such an approach using this hypothesis. Following the success of the EKF model using the infinite inertia hypothesis, Bolognani [4·31] continued to investigate the full characteristics of this approach. He identified the deterministic element in the initial covariance P_0 for the start-up stage and how to avoid the stall condition. While robust countermeasures were also proposed against the flux linkage variation. Recently many research approaches have proposed focusing on reducing the computation load such as the reduced-order Kalman filter, but alternatively position information may be extracted through the non-linear computation method of the reverse trigonometric function. New complexity issues are increasing as well, although the computational load has hardly decreased. Current research focusing on the EKF seeks convenient initial covariance matrix tuning, expanding the ability of load delivery and combining with the PMSM operational control method.

4.1 Extended Kalman Filter (EKF) theory for the application in sensorless control of the PMSM

4.1.1 Model for measuring process and system noise in the stochastic processes

A multi-input/multi-output linear time-variant discrete system with stochastic processes have output as shown in Fig. 4·1 and equations of state

$$\begin{cases} x(k+1) = \Phi(k+1,k)x(k) + \Gamma(k)w(k) \\ y(k) = \Theta(k)x(k) + v(k) \end{cases} \tag{4·1}$$

where $\{w(\mathrm{k}), k\}$ is m-order normal independent sequence (model noise), $\{v(k), k \in \mathrm{T}\}$ is r-order normal independent sequence (measurement noise), $x(k)$ is the n-order state variable, y(k) is the r-order output, $\Phi(k+1,k)$ is the n×n state transfer matrix, $\Gamma(k)$ is a

n×m input matrix and is the r×n output matrix. Measure noises are divided into two types, white noise and colour noise. White noise is a stochastic signal / process with a flat power spectral density. In other words its power spectral density in any band has the same value. From this definition, white noise is not the same as Gaussian noise, whose probability density function obeys the normal distribution.

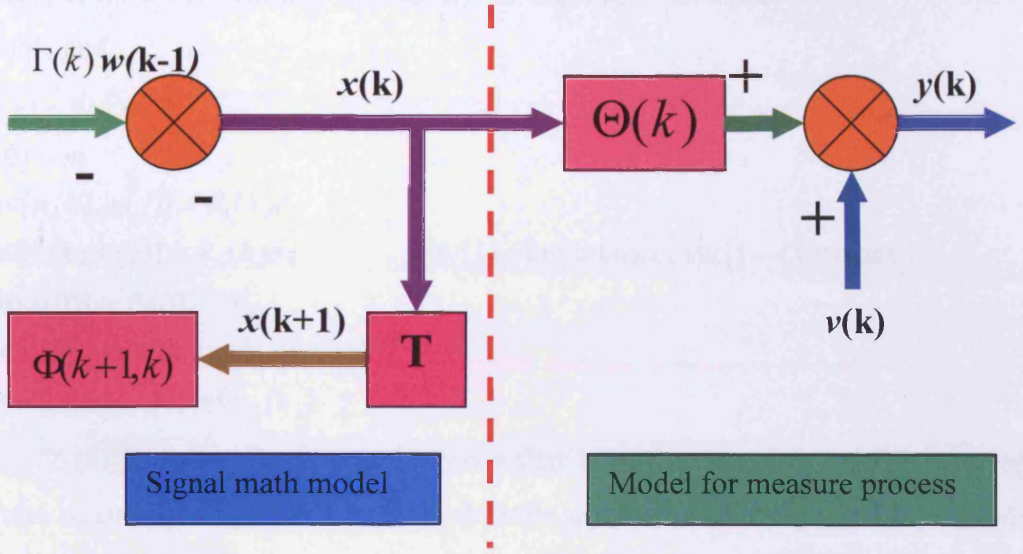

Fig. 4·1 Time-variable random signal and measurement process

The stochastic processes is $\chi=\{x(t), t\in T\}$, where t is the discrete time. Vector $x(k)$ is predicted quantity, $y_i=(y^\tau(1), y^\tau(2), \ldots, y^\tau(j))^\tau$ from the measurement of $x(k)$. If the approximation for $x(k)$ can be decided by y_i as

$$\hat{x}(k|j) = f(y_i) \tag{4·2}$$

$\hat{x}(k|j)$ is called as the estimation for $x(k)$ by y_i.

$$\tilde{x}(k|j) = x(k) - \hat{x}(k|j) \tag{4·3}$$

is the estimation error. If $\hat{x}(k|j) = Ay_i + b$, where A is matrix, b is vector, such a special estimation $\hat{x}(k|j)$ is called the linear estimation for $x(k)$.

When k>j the estimation is called the ***prediction*** or the ***extrapolation*** whereas when k=j it is ***filtering***. The estimation when k<j is called the ***smoothness*** or ***interpolation***. The Gaussian distribution is also called the normal distribution. If the stochastic variable X obeys the Gaussian/normal distribution $X\sim N(\mu,\sigma^2)$ with mathematical expectation/mean μ and standard variance σ^2 for X, σ is standard deviation.

4.1.2 Kalman filter and prediction for the linear system

Kalman filter theory investigates the least-variance filtering and prediction. Assuming that the system state and measure equation are

$$\begin{cases} x(k+1) = \Phi(k+1,k)x(k) + \Gamma(k)w(k) \\ y(k) = \Theta(k)x(k) + v(k) \end{cases} \tag{4-4}$$

where $\{w(k), k \in T\}$, $\{v(k), k \in T\}$ belongs to the Gauss distribution. $\{x(0)\}$ is the Gauss variable and

$$\begin{cases} \overline{w}(k) = \overline{v}(k) = 0 \\ \overline{x}(0) = m \\ \mathrm{cov}[w(k), w(j)] = R_1(k)\delta_k \\ \mathrm{cov}[v(k), v(j)] = R_2(k)\delta_{kj} \\ \mathrm{var}[x(0)] = Px(0) = P_0 \\ \mathrm{cov}[w(k), v(j)] = \mathrm{cov}[w(k), x(0)] \\ = \mathrm{cov}[v(k), x(0)] = 0 \end{cases}$$

, cov[]— covariance, var[] — variance

where $R_1(k) \geq 0$, $R_2 > 0$, $P_0 \geq 0$, which shows that both $R_1(k)$ and P_0 are the non-negative definite square matrix, R_2 is a positive definite square matrix. $\{x(k), k \in T\}$ is a Markov sequence. The Kalman Filter equation is actually a set of recursive linear filter equations. Their start points are $\hat{x}(0|0)$ and P(0|0). When $y(k)$ is measured every time, the recursive equation can use the previous filtered result $\hat{x}(k-1|k-1)$ and P(*k-1*|*k-1*) to calculate $\hat{x}(k|k)$ and P($k|k$). The step prediction $\hat{x}(k|k-1)$ and its error variance P($k|k$-*1*) are also a procedure result.

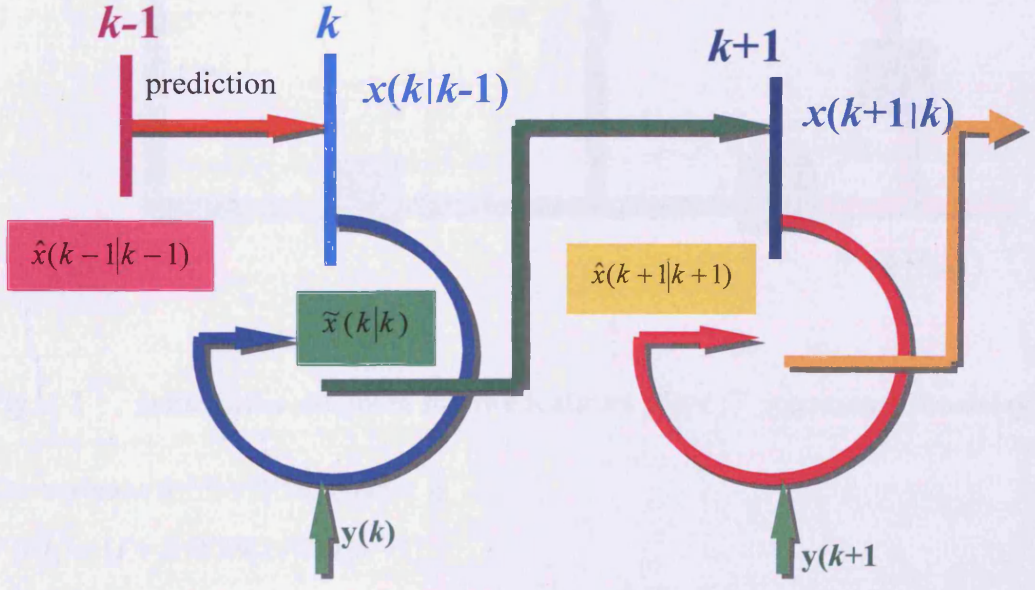

Fig. 4-2 State flowchart for Kalman Filter

The step prediction for the state is

$$\hat{x}(k|k-1) = \Phi(k,k-1)\hat{x}(k-1|k-1) \tag{4·5}$$

The error for the step prediction is

$$P(k|k-1) = \Phi(k,k-1)P(k-1|k-1)\Phi^{\tau}(k,k-1) + \Gamma(k-1)R(k-1)\Gamma^{\tau}(k-1) \tag{4·6}$$

The error for the least-variance prediction (Innovation) $\tilde{y}(k|k\text{-}1)= \tilde{y}(k)$, is based on $y_{k-1}^{T} = [y^{T}(1), y^{T}(2), \ldots, y^{T}(k\text{-}1)]$

$$\tilde{y}(k) = y(k) - \Theta(k)\hat{x}(k|k-1) \tag{4.7}$$

Filter equations:

$\tilde{y}(k)$ is independent of y_{k-1}^{T}, therefore $[\tilde{y}(k), k \in T]$ is a zero-meant independent sequence.

$$\hat{x}(k|k) = \hat{x}(k|k-1) + K(k)[y(k) - \Theta(k)\hat{x}(k|k-1)] \tag{4.8}$$

Equation (4.8) is also represented in Fig. 4·3.

The gain equation is

$$K(k) = P(k|k-1)\Theta^{\tau}(k)[\Theta(k)P(k|k-1)\Theta^{\tau}(k) + R_2(k)]^{-1} \tag{4·9}$$

where $K(k)$ is also called the filter gain matrix, which comes from the modified and predicted $\hat{x}(k|k-1)$ by innovation $\tilde{y}(k)$, and K(t) is the corrective coefficient matrix.

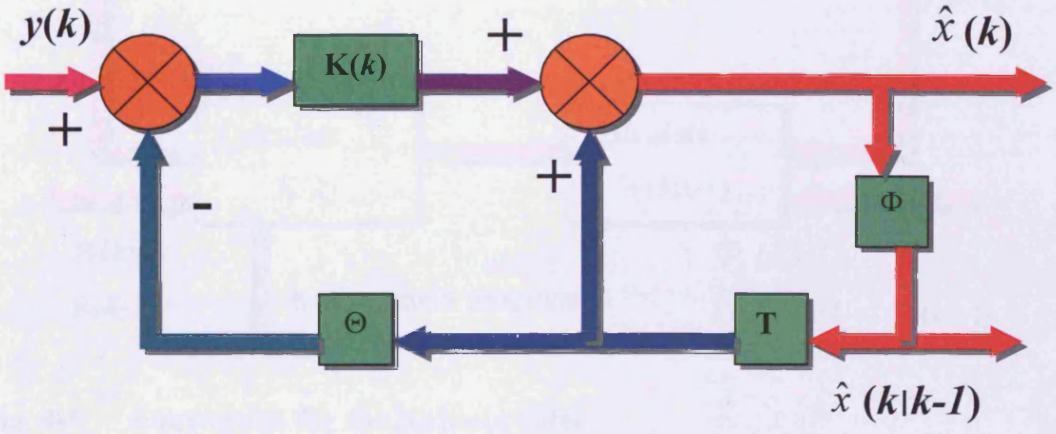

Fig. 4·3 Innovation diagram for the Kalman filter (T represents the delay)

The variance for the filtered error is

$$P(k|k) = [I - K(k)\Theta(k)]P(k|k-1) \tag{4.10}$$

The first stage of the prediction is calculated using equation (4·5) while the second stage of correction is estimated using equation (4·8), the state transition chart is shown in fig. 4·2.

4.1.3 Recursive Subroutine Algorithm

The gain matrix has nothing to do with the measurement processes, and is recursively corrected. Only the values from the previous steps are needed. The detail of the flow chart is shown in fig. 4·3. Step 1 is used to calculate P($k|k$-1) through equation (4·6) according to Φ (k,k-1), P(k-1) and $\Gamma(k-1)R(k-1)\Gamma^{\tau}(k-1)$. Step 2 aims to calculate K(k) using equation (4·10) in terms of Θ, R(k) and P($k|k$-1), K(k) will be sent to the 3rd step of the main control program above as shown in fig. 4·4. Step 3 is for P($k|k$) through equation (4·10) in terms of P($k|k$-1), K(k) and $\Theta(k)$. The final result P($k|k$) will be stored for the calculation of the next measurement step. The whole subroutine will be executed repeatedly.

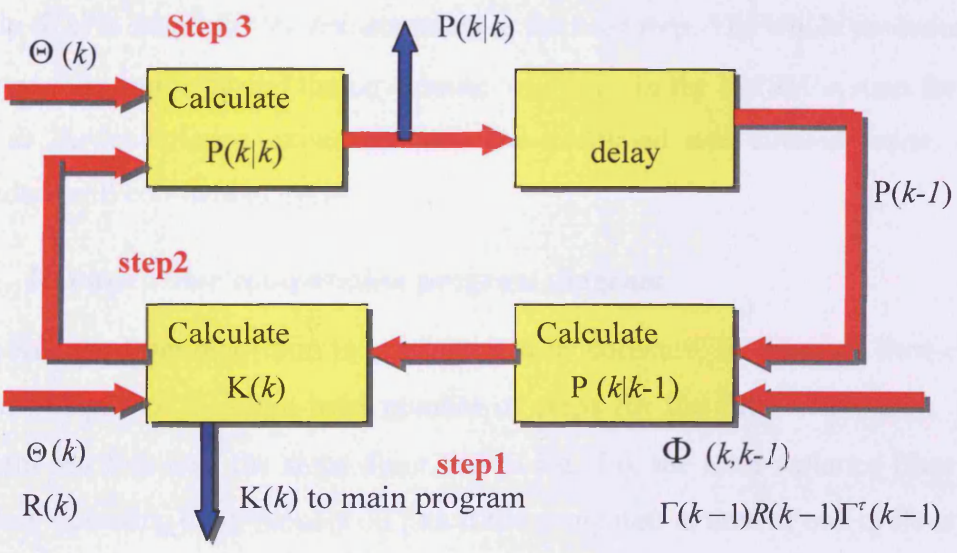

Fig. 4·4 Subroutine for the Kalman filter

4.1.4 Main program diagram for the Kalman Filter

If $\hat{x}(k-1)$ is given, $\hat{x}(k)$ can be calculated based on Y(k) for Phase 1 in fig. 4·5.

the estimated $\hat{x}(k-1)$ is multiplied by Φ, subsequently the multiplication of the predicted estimation $\hat{x}(k|k-1)$ can be expressed by $\hat{x}'(k)$. In Phase 2 $\hat{x}'(k)$ is multiplied by Θ to obtain $\hat{Y}(k)$ which is subtracted from the measured Y(k) to obtain the error $e'(k)$.

In Phase 3 the error is multiplied by K(k), the result is added to $\hat{x}'(k)$ to obtain $\hat{x}(k)$.

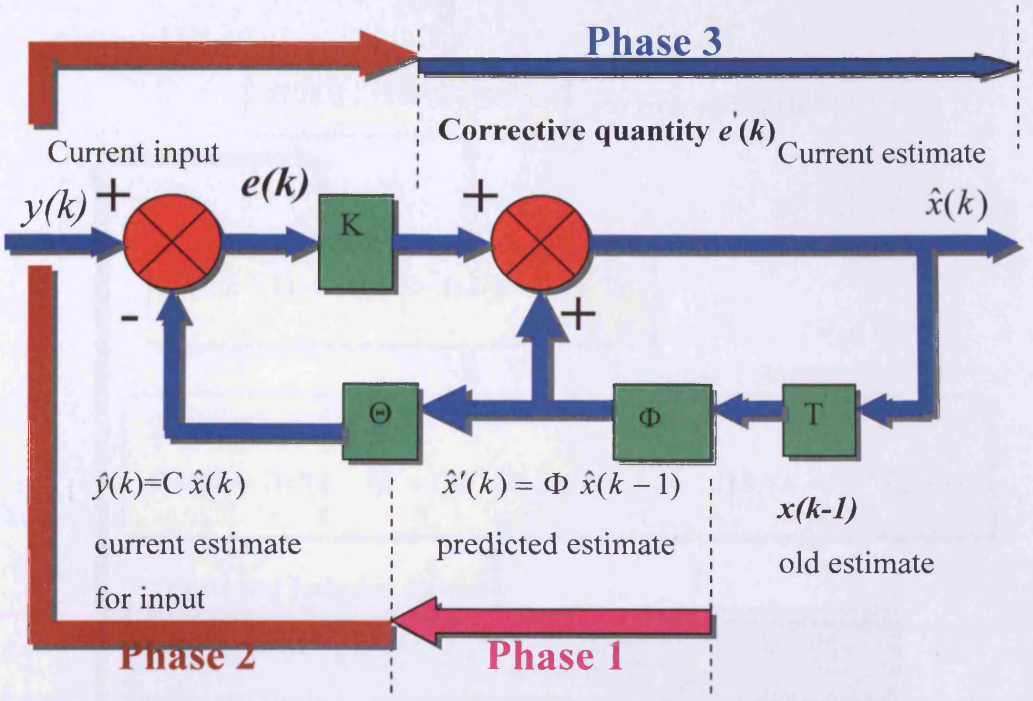

Fig. 4·5 The innovation flow chart of the Kalman filter estimator

Finally $\hat{x}(k)$ is stored for the measurement at the next step. The whole procedure will be repeated over and over and the covariance will exist in the PMSM system for ever. As long as the covariance exists between the predicted and filtered value, the EKF procedure will continue to cycle.

4.1.5 Kalman Filter computation program diagram

If the Kalman filter algorithm is implemented by software, its program flow chart is as shown in fig. 4·6. N is the total number of steps for the filter calculation. After the program has followed the steps described in fig. 4·6, the least-variance filter program can keep operating continuously on line if the computation time of one cycle is less than the interval of the discrete input. Obviously P(k|k-1), K(k) and P(k|k) are independent of the measured y(k). As long as $\dot{x}$ (0|0) and P(0|0) are given in advance, the variance and gain above can be computed and stored in memory before measurement. Although such off-line computation can take up more memory, it may obviously reduce on-line computation time.

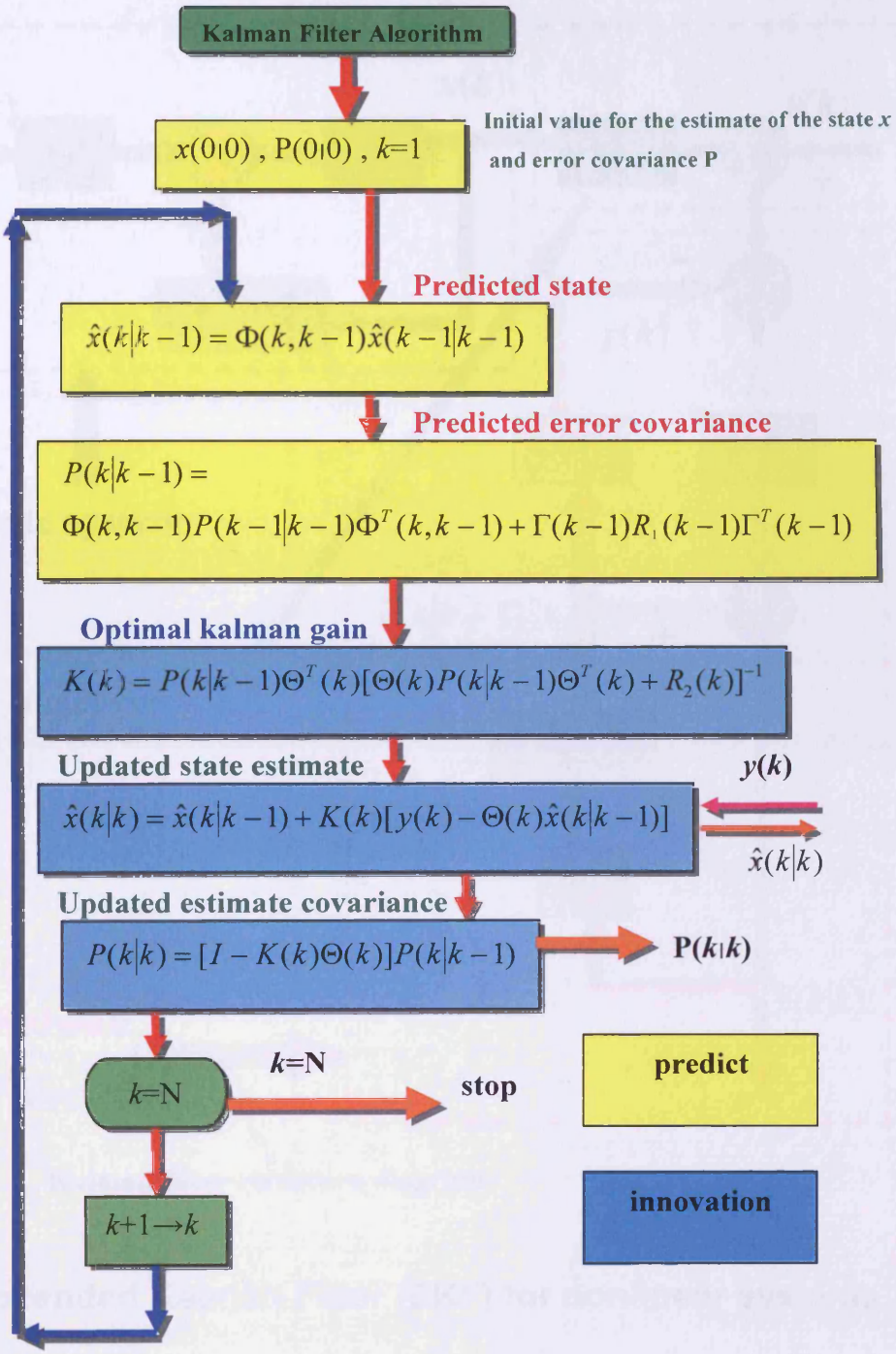

Fig. 4·6 Kalman filter program flow chart

4.1.6 Filter diagram

Fig. 4·7 describes the relationship between system, observer and Kalman filter. It is obvious that essentially covariance correction is the main feature of the Kalman filter state observer system.

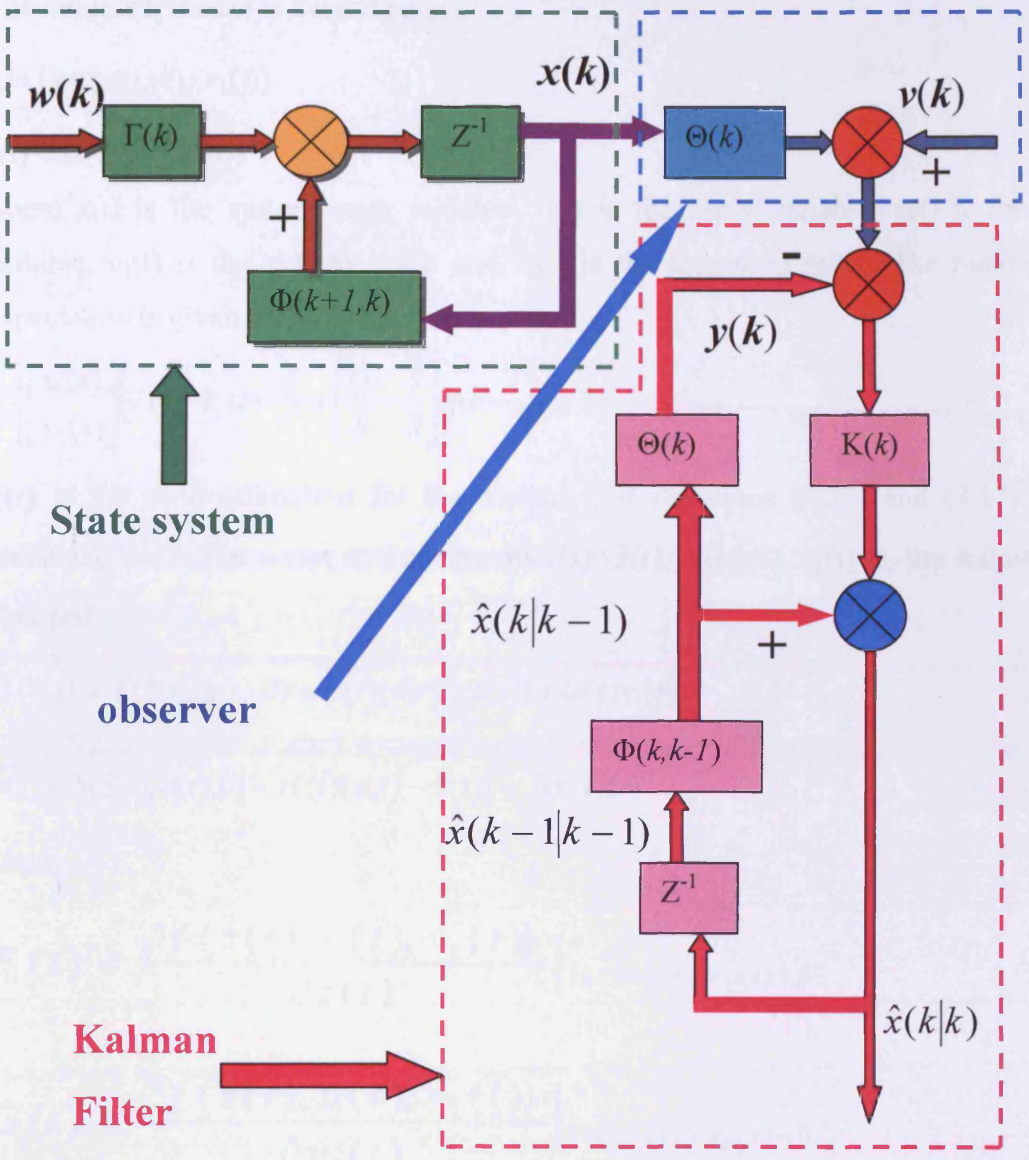

Fig. 4·7 Kalman filter structure diagram

4.2 Extended Kalman Filter (EKF) for nonlinear systems

For the state estimation to finite order linear servo dynamic system, the Kalman filter provides a simple and smart solution, but the Kalman filter cannot directly be applied to a non-linear system.

Previous derivation and the performance of the optimal estimator depend on the essential linear system. The EKF attempts to overcome this problem by the linearization approximation of instantaneous state estimation. The EKF was proposed first by Kopp and Orford (1963)[4·5]. Many previous studies have also examined the EKF such as: Sage and Wakefield (1972) [4·6], Leung and Padmanabhan (1973) [4·6], Nelson and Stear (1976) [4·8], Farson, Graham and Shelton (1967)[4·8].

The nonlinear model is described as

$$z(t+1)=f(z(t),u(t),v_1(t)) \tag{4·11}$$

$$y(t)=h(z(t),u(t),v_2(t)) \tag{4·12}$$

where z(t) is the system state variable, u(t) is the input variable, y(t) is the output variable, $v_1(t)$ is the system noise and $v_2(t)$ is the measured noise. The mathematical expectation is given by

$$E\left\{\begin{bmatrix} v_1(s) \\ v_2(s) \end{bmatrix}\begin{bmatrix} v_1(t)^T v_2(t)^T \end{bmatrix}\right\} = \begin{bmatrix} Q & S \\ S & R \end{bmatrix}\delta(t-s) \tag{4·13}$$

$\hat{z}(t)$ is the state estimation for the instant t, if equations (4·11) and (4·12) can be literalized by Taylor series at these points $z(t)=\hat{z}(t)$, $v_1(t)=0$, $v_2(t)=0$, the following are obtained

$$z(t+1) \approx f(\hat{z}(t),u(t),0) + F(t)[z(t)-\hat{z}(t)] + G(t)v_1(t) \tag{4·14}$$

$$y(t) \approx h(\hat{z}(t),n(t),0) + H(t)[z(t)-\hat{z}(t)] + J(t)v_2(t) \tag{4.15}$$

where

$$F(t) = \left.\frac{\partial f(z(t),u(t),v_1(t))}{\partial z(t)}\right|_{z(t)=\hat{z}(t),v_1(t)=0} \tag{4.16}$$

$$G(t) = \left.\frac{\partial f(z(t),u(t),v_1(t))}{\partial v_1(t)}\right|_{z(t)=\hat{z}(t),v_1(t)=0} \tag{4·17}$$

$$H(t) = \left.\frac{\partial h(z(t),u(t),v_2(t))}{\partial z(t)}\right|_{z(t)=\hat{z}(t),v_2(t)=0} \tag{4·18}$$

$$J(t) = \left.\frac{\partial h(z(t),u(t),v_2(t))}{\partial v_2(t)}\right|_{z(t)=\hat{z}(t),v_2(t)=0} \tag{4·19}$$

The linear equations (4·14) and (4·15) for the Kalman filter can be deduced in the EKF equation

$$\hat{z}(t+1) = f(\hat{z}(t),u(t),0) + L(t)[y(t)-h(\hat{z}(t),u(t),0)], \hat{z}(0)=\hat{z}_0 \tag{4·20}$$

where L(t) is the Kalman filter gain:

$$L(t) = F(t)\Sigma(t)H(t)^T + \bar{S}(t)[H(t)\Sigma(t)H(t)^T + \bar{R}(t)]^{-1} \tag{4·21}$$

and

$$\Sigma(t+1) = F(t)\Sigma(t)F(t)^T + \overline{Q}(t) - L(t)[H(t)\Sigma(t)H(t)^T + \overline{R}(t)]L(t)^T, \Sigma(0) = \Sigma \tag{4·22}$$

$$\overline{Q}(t) = G(t)QG(t)^T \tag{4·23}$$

$$\overline{S}(t) = G(t)SJ(t)^T \tag{4·24}$$

$$\overline{R}(t) = J(t)RJ(t)^T \tag{4·25}$$

4.3 Sensorless EKF-based Observer for PMSM Drive

4.3.1 Model for Sensorless EKF-based Observer

The EKF is an optimal estimator in the least square variance for estimating the states of dynamic nonlinear systems. In order to straightforwardly apply the EKF to the sensorless operation of the PMSM, the PM motor nonlinear state equations are written as

$$\begin{cases} \dot{x}(t) = f[x(t)] + Bv(t) + \sigma(t) \\ y(t_k) = h(x(t_k)) + \mu(t) \end{cases} \tag{4·26}$$

where σ(t) is the system noise, μ(t) is the measured noise , both σ(t) and μ(t) have a zero-mean white Gaussian distribution.. Q(t) is the covariance of σ(t) and $R(t_k)$ is the covariance of μ(t). The PMSM has been modelled in a two-axis stationary reference frame (α, β). The system state variable x is $[i_\alpha \quad i_\beta \quad \omega \quad \theta]'$, the input vector v is $[v_\alpha \quad v_\beta]'$ and the system output variable y is $[i_\alpha \quad i_\beta]'$.

The system matrices can be written as

$$f(x) = \begin{bmatrix} f_1 \\ f_2 \\ f_3 \\ f_4 \end{bmatrix} = \begin{bmatrix} -\frac{R_s i_\alpha}{L_s} + \frac{\omega\psi}{L_s}\sin\theta \\ -\frac{R_s i_\beta}{L_s} - \frac{\omega\psi}{L_s}\cos\theta \\ 0 \\ \omega \end{bmatrix}, \quad B = \begin{bmatrix} \frac{1}{L_s} & 0 \\ 0 & \frac{1}{L_s} \\ 0 & 0 \\ 0 & 0 \end{bmatrix}, \tag{4·27}$$

$$h(x) = \begin{bmatrix} i_\alpha \\ i_\beta \end{bmatrix}$$

where R_S is the motor phase resistance, L_s is the motor synchronous inductance and ψ is the PM flux linkage. Obviously, this system is nonlinear and the variables in the system state are closely coupled. If EKF is used to rewrite this nonlinear model, the "Jacobian" matrices are

$$F(x(t))=\left.\frac{\partial f}{\partial x}\right|_{x=x(t)}=\begin{bmatrix}-\frac{R_s}{L_s} & 0 & \frac{\psi}{L_s}\sin\theta & \frac{\omega\psi}{L_s}\cos\theta\\ 0 & -\frac{R_s}{L_s} & -\frac{\psi}{L_s}\cos\theta & \frac{\omega\psi}{L_s}\sin\theta\\ 0 & 0 & 0 & 0\\ 0 & 0 & 1 & 0\end{bmatrix} \tag{4·28}$$

$$H(x(t))=\left.\frac{\partial h}{\partial x}\right|_{x=x(t)}=\begin{bmatrix}1 & 0 & 0 & 0\\ 0 & 1 & 0 & 0\end{bmatrix}$$

After the relative linearization of the system equation (4·28), there is a partial linear relationship between states and outputs as given in equations (4·29), (4·30) and (4·31) which can be discretized into equation (4·32) with constant period T_C.

$$\dot{\hat{x}}(t)=F(x(t))\hat{x}(t)+\sigma(t) \tag{4·29}$$

$$y(t)=H\hat{x}(t)+\mu(t) \tag{4·30}$$

$$\hat{x}(t_k)=\Phi(t_k,t_{k-1},x(t_{k-1}))\hat{x}(t_{k-1})+\upsilon(t_{k-1})) \tag{4·31}$$

Φ is the state transfer matrix for the linear system (4·29) and it is an exponential matrix. It may be approximately simplified to

$$\Phi(t_k,t_{k-1},x(t_{k-1}))\cong I+FT_c \tag{4·32}$$

For a given sampling time t_k, both the optimal state estimated sequence $\tilde{x}_{k|k}$ and its covariance matrix $\tilde{P}_{k|k}$ are generated by the EKF through two steps. The first is a prediction of both quantities based on the previous estimates $\tilde{x}_{k-1|k-1}$ and the mean voltage vector v_{k-1} applied to the system in the period from t_{k-1} to t_k. A simple rectangular integration technique is used to produce the following recursive difference equations:

$$\begin{cases}\hat{x}_{k|k}=\tilde{x}_{k-1|k-1}+[f(\tilde{x}_{k-1|k-1})+B(\upsilon_{k-1})]T_c\\ \hat{P}_{k|k-1}=\tilde{P}_{k-1|k-1}+(F_{k-1}\tilde{P}_{k-1|k-1}+\tilde{P}_{k-1|k-1}F'_{k-1})T_c+Q_d\end{cases} \tag{4·33}$$

where F_{k-1} is computed for $x=\tilde{x}_{k-1|k-1}$

The second step is an innovation step, correcting the predicted state estimate and its covariance matrix through a feedback correction scheme that makes use of the actual measured quantities; it is realized by the following equations

$$\begin{cases}\tilde{x}_{k|k}=\hat{x}_{k|k-1}+K_k(y_k-H\hat{x}_{k|k-1})\\ \tilde{P}_{k|k}=\hat{P}_{k|k-1}-K_kH\hat{P}_{k|k-1}\end{cases} \tag{4·34}$$

$$K_k=\hat{P}_{k|k-1}H'(H\hat{P}_{k|k-1}H'+R)^{-1}$$

4.3.2 On-line Algorithm for the Sensorless EKF-based PMSM Drive

Fig. 4·8 illustrates the program flow chart diagram for the EKF-based sensorless full digital control system. As described in fig 4 8, after initialization, the main program executes the PI speed regulation meanwhile waiting for the timer interrupt for the current control as shown in the program diagram. The frequency for this timer interrupt is 20 kHz. The EKF algorithm is executed after the current and DC-link voltage measurement are finished. The innovation step must be conducted before the prediction step shown in the flow chart diagram. The last step is the d-q transformation and hysteresis current control. The function which is not required in real time will be conducted in the main routine such as the PI speed regulator. The EKF algorithm with the whole full-digital control as shown in fig. 3·10 of Chapter 3 has been implemented on a float-point DSP system based on TMS320C31 which is capable of a peak performance of 50 MFLOPS. The PWM control frequency is configured at 20 kHz through one timer with a duty period of 50 us. Current & DC-link voltage acquisition is performed through 12-bit parallel A/D channels which takes only 12 us for conversion. Position acquisition is conducted through the digital parallel input interface. The final voltage vector, after the execution of hysteresis current PWM, is exchanged with the digital parallel output interface. The subsequent innovation step for t_{k-1} is performed after the electrical quantities and position information are sampled. Based on the estimates from the innovation step in t_{k-1}, the EKF algorithm predicts the state in t_k with the sampling period T_c=50 us, corresponding to a PWM switching frequency of 20 kHz. As described in the following section the computation time for the EKF algorithm is 20us. The source code by TI 320C3X/4X assembly code is shown in the APPENDIX. All the null elements are treated as zero in the matrix computation.

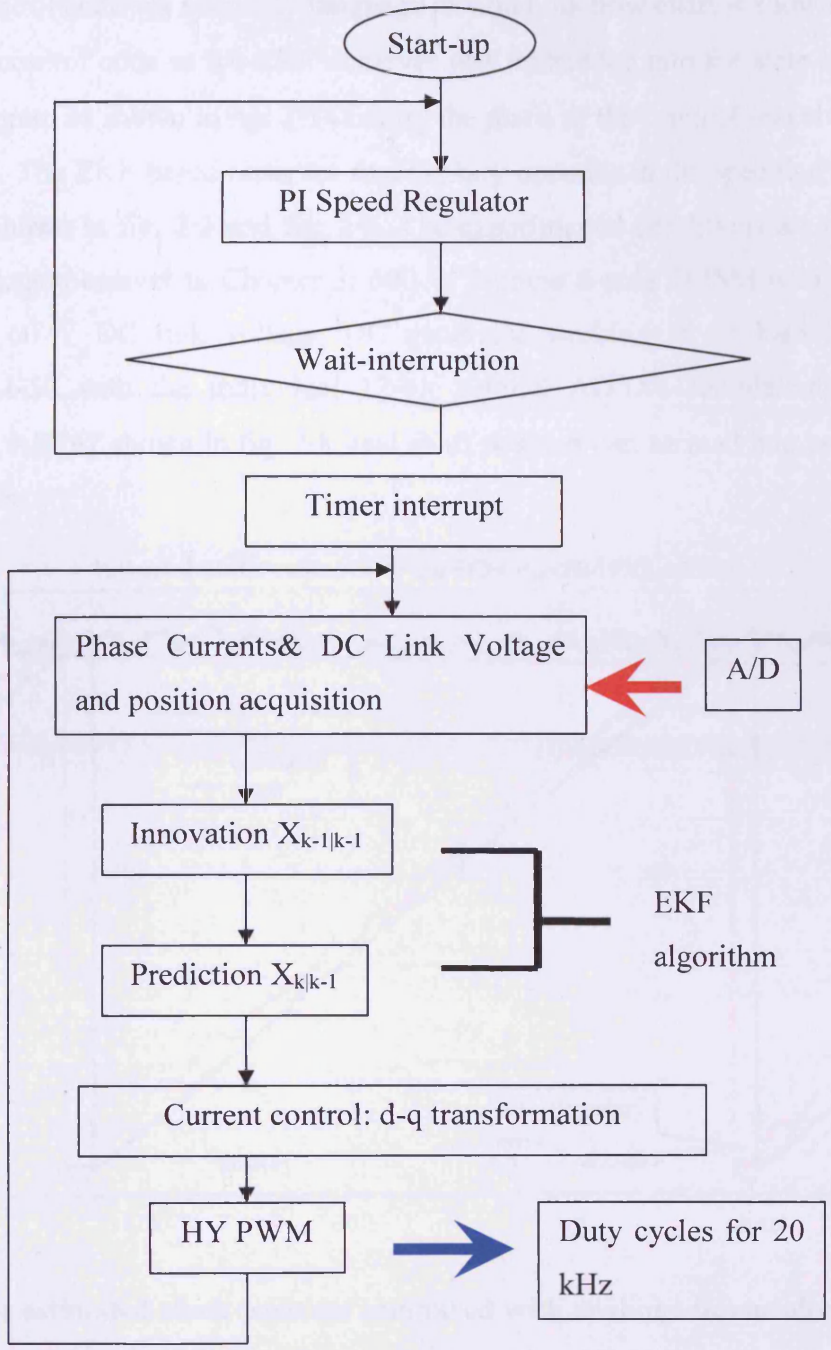

Fig. 4·8 Program diagram for the DSP code of the EKF-based sensorless control

4.4 Experimental Results and Analysis

4.4.1 Shaft & rotor position estimation and analysis

The Extended Kalman Filter algorithm from equations (4·31-4·34) based on 4-order non-linear model of a 3-phase PMSM from equations (4·26-4·28) was converted into

the DSP control code via assembly language in which its flow chart is shown in fig. 4·8. The whole control code as the EKF observer was embedded into the state space PWM control program as shown in fig. 3·14 taking the place of the original real shaft position feedback, θ. The EKF based observer successfully operates in the specified experiment facility as shown in fig. 2·2 and fig. 2·3. The experimental conditions are the same as the flux-linkage observer in Chapter 3: 600 W 3-phase 6-pole PMSM with rated speed 1100 rpm, 60 V DC link voltage, DC generator working in no load mode, DSP TMS320C31-50 with the individual 12-bit parallel AD/DA sample/output system: AD678 and AD767 shown in fig. 2·8, real shaft position can be read into encoder 2048 pulse per turn.

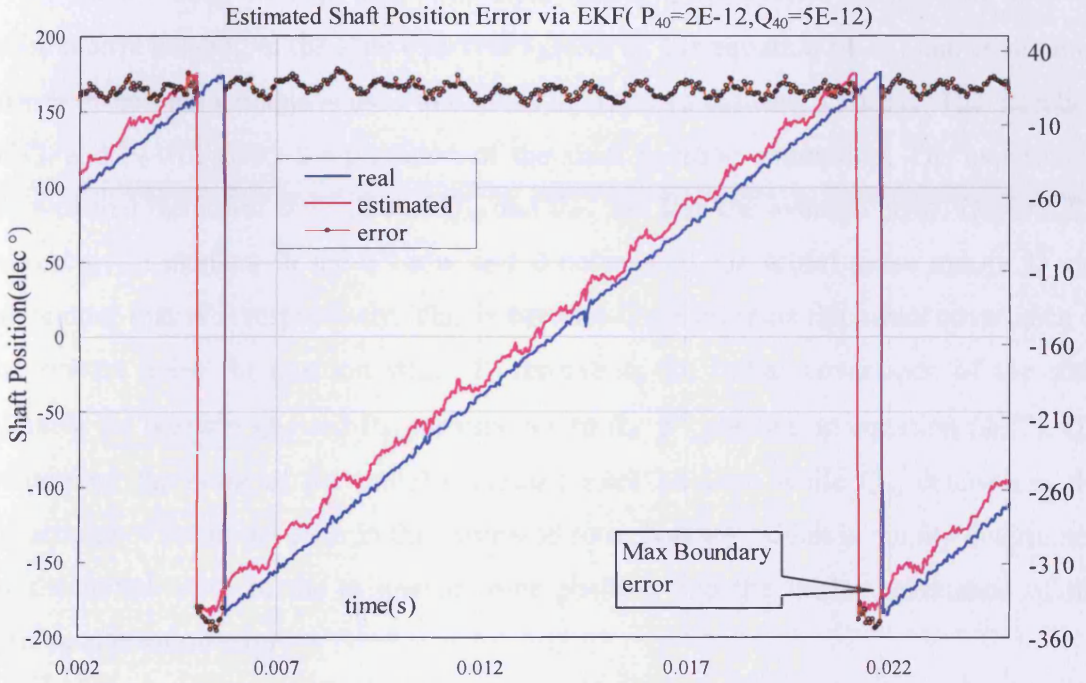

Fig. 4·9 The estimated shaft position compared with real one in one electrical cycle via EKF-based sensorless estimation (P_{40}=2E-12,Q_{40}=5E-12)

Fig. 4·9 compares the shaft position characteristics for the real and estimated values in one electrical cycle. Q_{40} is the element located at No. 4 of the initial 4-order constant diagonal covariance matrix Q_0 for system noise σ(t) in equation (4·26), P_{40} is the element located at No. 4 of the initial 4-order constant diagonal initial covariance matrix P_0 for system variable x in equation (4·33). The extremely low values for Q_{40} and P_{40} reflect the precision of computation for a floating-point DSP TMS320C31 in the data processing. The measured actual rotor position has been secured in fig. 4·9 with the

3-phase PMSM built-in encoder British 755 series 2048 ppt, using the USdigital "ECOUNT" Encoder for the Binary Counter Converter.

The experimental results have satisfactory linearity and an complete correspondence except at the terminal points ±180 elec° which exists between the estimated and the actual rotor position. Fig. 4·9 also shows that the average error between the estimated and actual rotor position is about 12 elec°. Another aspect of the time domain is that a phase lag of about 30 elec° exists. The erroneous behaviour represented in fig. 4·9 is relatively accordant with the polarity of the offset. The dynamic error undulates regularly with an almost identical peak value.

Q_0 and P_0 are the initial values of the covariance matrices Q for the system noise and P for the state variable. The covariance matrix Q for system noise is the inherent noise matrix existing in the state observer system by the equation (4·26), the covariance matrix P for state variable is used to control the error of the state variable. The selection of Q_0 and P_0 will affect the precision of the shaft position estimation. The experiment showed that the lower the value of Q_{40} and P_{40}, the less the average error. Q_{40} and P_{40} represent the element in the 4^{th} row and 0 column of the initial noise matrix Q and covariance matrix P respectively. This is because Q_{40} represents the initial covariance of the system noise for position while P_0 represents the initial covariance of the state variable for position Q_{40} and P_{40} corresponds to the 4^{th} position in equation (4·27). Q_{40} determines the noise of the initial estimated rotor position while Q_{40} determines the covariance of the initial error in the estimated rotor position which is mainly determined by the initial noise of the estimated rotor position and the initial covariance of the estimated position error.

Other elements in the initial noise matrix Q and covariance matrix P represent the indirect influence of other variables, which may be neglected. Generally many values that are too low for Q_0 and P_0 will affect the convergence of the start-up procedure. Therefore trial-and-error routine is necessary to obtain the optimal trade-off between estimation precision and convergence speed. The proposed values are reported as $P_{40}=2e^{-12}$ and $Q_{40}=5e^{-12}$. It is noted that the extremely low value of Q_{40} will slow the convergence. The proposed experiment focuses on the precision of the shaft position estimation rather than than the speed of the convergence.

The proposed experiment reported the following diagonal initial matrices

$$Q_0 = \begin{bmatrix} 0.04 & 0 & 0 & 0 \\ 0 & 0.04 & 0 & 0 \\ 0 & 0 & 0.07 & 0 \\ 0 & 0 & 0 & 5E-12 \end{bmatrix}, \quad P_0 = \begin{bmatrix} 0.01 & 0 & 0 & 0 \\ 0 & 0.01 & 0 & 0 \\ 0 & 0 & 2 & 0 \\ 0 & 0 & 0 & 2E-12 \end{bmatrix}, \quad R = \begin{bmatrix} 0.15 & 0 \\ 0 & 0.15 \end{bmatrix}$$

4.4.2 Self start-up ability

The EKF sensorless control of the PM motor in the experiment proves to be capable of self start-up through signal injection and convergence with correction. Fig. 4·10 illustrates that the EKF observer recognizes wrong convergence and gradually corrects it to recover. The initial actual shaft position in fig. 4·10 for standstill status is -140 elec ° when the estimated initial value of -170° from the wrong convergence was made, afterwards, the consequent remedial action from the EKF observer makes the estimated position approach the true shaft position. The early course of the estimated shaft position lags behind the real shaft position until they meet at -70°, after which the estimation position are kept ahead of the true one. As a result, the offset for the true position always turns positive.

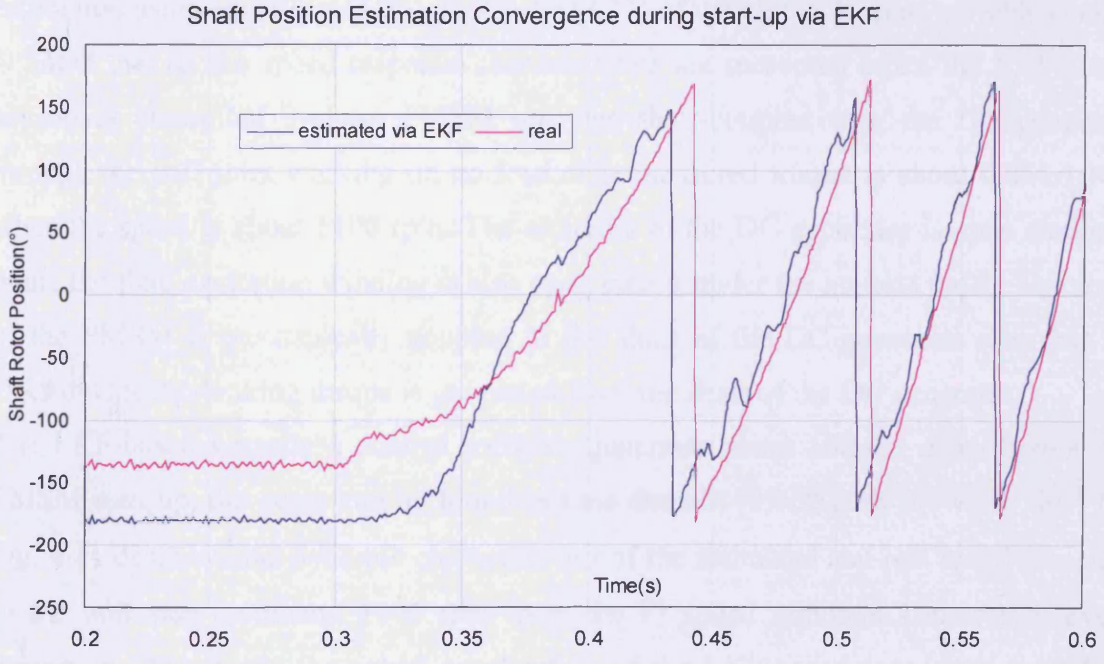

Fig. 4·10 Shaft position estimation convergence during start-up via the EKF

It is worth pointing out that the start-up in fig. 4·10 is accompanied with about 0.8~1.1 Nm, which is measured from the DC generator coupled with the shaft of the 3 phase PMSM on no load, only mechanic friction is added to the shaft of the PMSM. The control software adds 100 ms delay before the PMSM starts up, the transient period of

100 ms is in the time domain [0.2, 0.3] shown in Fig. 4·10. The initial estimated shaft position is θ= -180 elec°, while the actual rotor position θ= -140 elec°. Such biased shaft position turns the actual (i_d, i_q) vector into the biased (i_d, $i_q+\Delta i_q$) as the feedback of PI regulator in Fig. 3·14 through the stationary-to-synchronous transformation. The field oriented control (FOC) generally makes the flux current command i_d zero value, while the quadrature torque current reference i_q^* is to generate direct current reference $I^*_{a, b, c}$. The actual $I_{a, b, c}$ is converted into the stationary current (i_α, i_β) couple as the input of the 4-order EKF observer. The error of stationary current (i_α, i_β) is remedied by the EKF via covariance correction. As a result of such remedial action, the rotor moves away from the standstill towards the correct rotor position.

4.4.3 Speed Estimation from EKF observer

Figs. 4·11 to 4·13 show the estimated speed directly from the EKF response characteristics for different commands according to different speed polarity. All the true speed curves are obtained through the position derivative law in equation (3.33) as described in Chapter 3. Meanwhile all the estimated speed curves come from direct estimation using equations (4.26), (4.29), or (4.31) of which the 3rd state variable is ω. It is noted that all the speed response characteristics are measured when the EKF-based sensorless controlled 3-phase PMSM operates shaft-coupled with the DC generator through the stiff joint working on no load. The measured torque is about 0.8~1.1 Nm when the speed is about 1100 rpm. The armature of the DC generator is open circuited while the field excitation winding is also open circuit under the no load mode. The shaft of the PMSM is mechanically coupled to the shaft of the DC generator rotor but no electromagnetic braking torque is generated from the shaft of the DC generator.

The EKF-based sensorless control software generates about 100 ms delay before the PMSM start up, the delay can be found in time domain [0,0.25]s as shown in fig.4·11. Fig. 4·11 describes the dynamic characteristics of the estimated and real speed response to the unit step command 1100 rpm from the PI speed regulator considering over-correction. Apparently the actual acceleration of the EKF-based sensorless controlled PMSM in fig.4·11 takes a longer time than that of the FLO-based sensorless controlled PMSM shown in fig. 3·19.

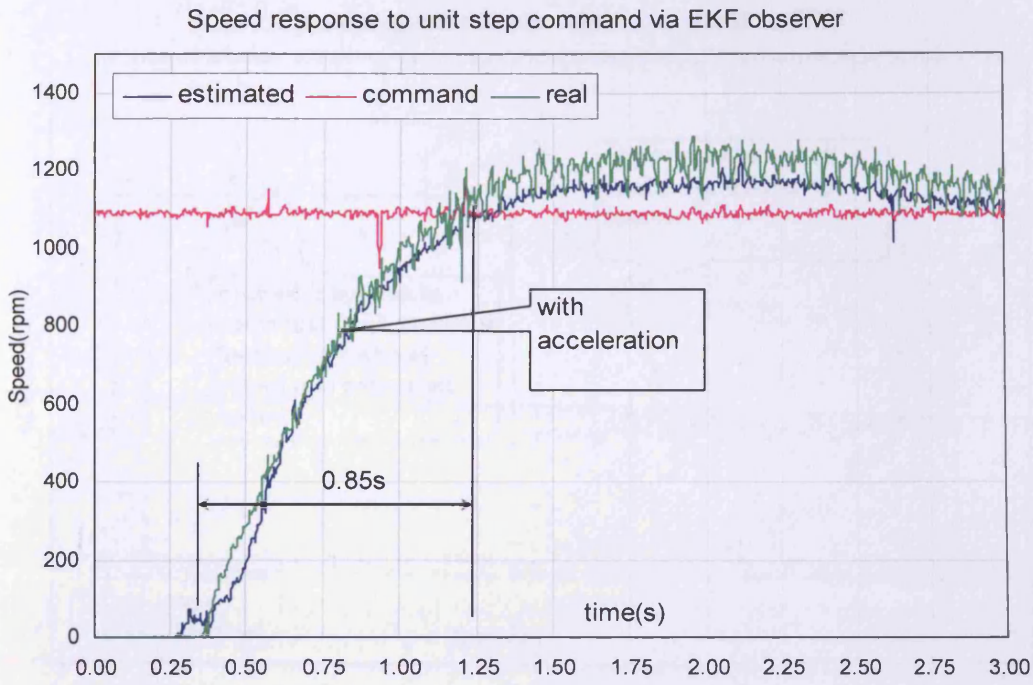

Fig. 4·11 Speed response to unit step command via EKF observer

This is because the speed in fig. 4·11 is the direct state-estimation EKF-based observation; there is a large error for the speed estimated via the EKF existing in the time domain [0.25, 0.5]s, the speed delay from the initial error causes the slower acceleration of the EKF in fig.4·11 compared to the FLO in fig.3·19.

The initial speed error during the start-up via EKF can be corrected by the related covariance; the correction period would increase the acceleration time. The dynamic process of the step unit speed response thereby consists of 3 sections: the acceleration, overshoot, and steady state. At the initial start-up stage in the time domain [0.25, 0.5]s, the wrong convergence of the EKF causes an obvious speed estimation error. Afterwards, the covariance correction of the EKF rapidly corrects the speed errors at the stage of acceleration until the overshoot and steady state follows. During the overshoot state in the time domain [1.25, 2.75]s, the steady-state error between the estimated and real speed is obvious. It is understood that the hypothesis "infinite inertia" in the system model (4·27) considers the derivate of the shaft angular velocity that is negligible compared with the other system variables, the recursive equations (4·33) and (4·34) of EKF algorithm carry no mechanical load or load torque parameters. Ignoring these could cause dynamic error.

Fig. 4·12 reported the speed response characteristics for the single-way square command.

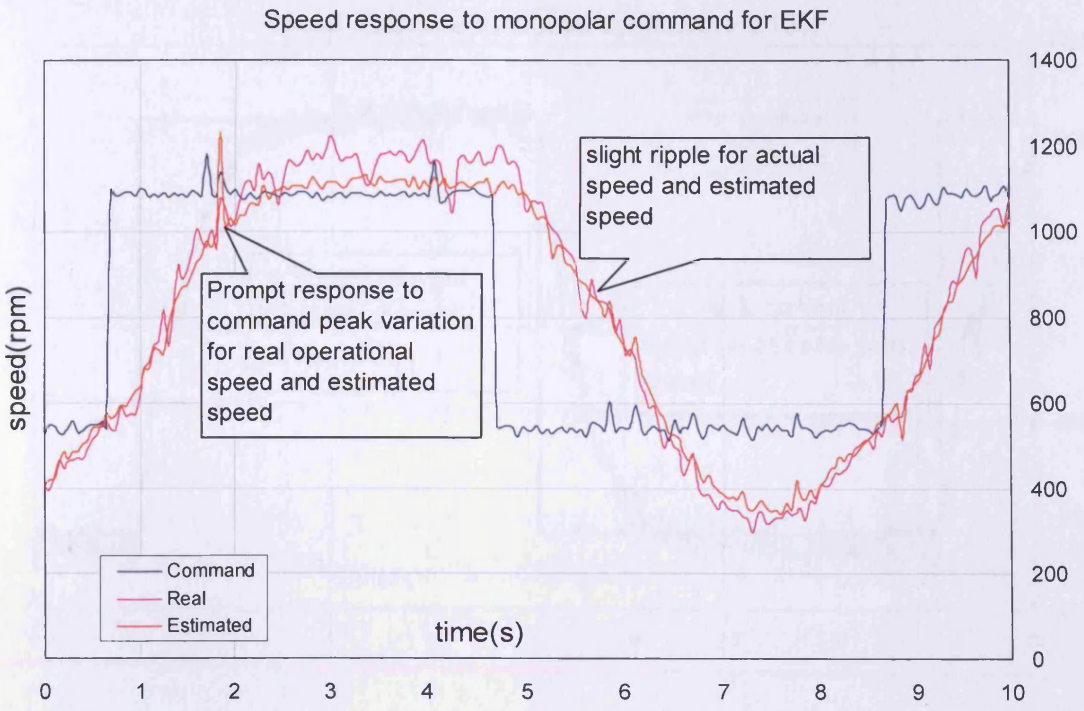

Fig. 4·12 Speed response to the single-way command for the EKF

The single-way square speed command has a duty cycle of 50% and 4 seconds for half of the cycle. The output of the single-way square speed toggles between 1100 rpm and 500 rpm. It is explicit in fig. 4·12 that the estimated speed trace takes action to follow the single-way speed command while the real speed trace always stays close to the estimated value.

Fig. 4·12 showed that the direct speed estimation from the EKF could accurately approach the real speed dynamically. It is pointed out in fig. 4·12 that the EKF can even sense and react with the noise of the speed command promptly, reflecting that the estimation of the EKF features have strong sensitivity.

Fig. 4·13 describes the dynamic speed response from the EKF to bipolar command that toggles out between "+1100 rpm" and "-1100 rpm". The estimated speed approaches the real value and responds correctly to the toggling command. The dynamic response seems satisfactory. When the speed command toggles between the bipolar outputs, the corresponding current injection command is executed to overcome the oscillating near the zero-area of the speed.

Around zero speed the current references in the PI speed regulator are so low that the actual and measured current occasionally bring much noise and are subject to AD measure precision.

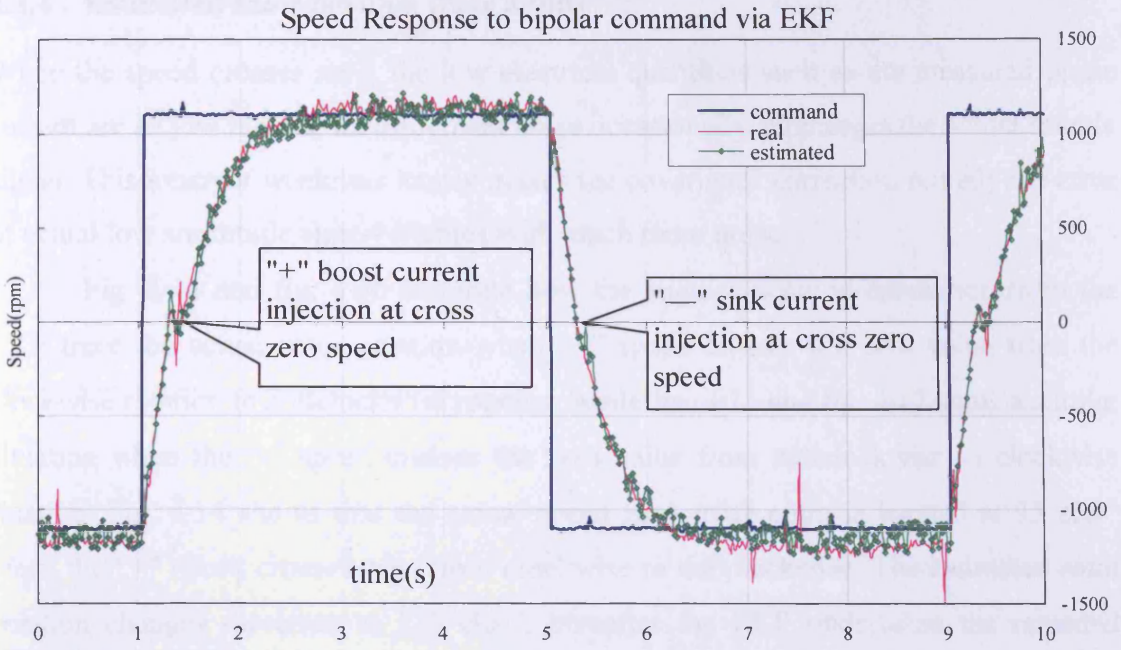

Fig. 4·13 Speed response to the bipolar command via the EKF

As such a more accurate current measurement could hardly be obtained. During the period of the speed cross-zero the wrong convergence generally occurs, which is shown in fig. 4·13 which explicitly demonstrates the wrong convergence occurring at the point of speed cross-zero and subsequently the remedy reaction generates a transient oscillation. In order to make the oscillation time shorter, the proposed experiment based on the EKF imposes the boost current command when the speed command toggles from "-1100 rpm" to "1100 rpm" while the sink current command is imposed in the PI speed regulator when the speed command toggles from "+1100 rpm" to "-1100 rpm". The error of the estimated position via the EKF can make the rotor swing when the speed crosses zero because the error correction is used by the EKF to implement rotor position estimation and occasionally the wrong convergence for the estimated position moves the rotor towards the inverse direction.

Such trial-and-error action can cause the swing of the rotor. The swing of the rotor when the speed crosses zero will delay the PMSM towards the speed command The sensorless controlled PMSM software can use the maximum current command I_{qmax} to reduce the time delay generated by the rotor swing. The applied maximum current command is named as the current injection as shown in fig.4·13, for example, the positive current command I_{qmax} is applied when the rising speed crosses zero from -1100 rpm to +1100 rpm while the negative current command I_{qmax} is applied when the falling speed crosses zero from +1100 rpm to -1100 rpm.

4.4.4 Estimated shaft position trace ability

When the speed crosses zero, the low electrical quantities such as the measured phase current are so low that the measurement noise occasionally submerges the actual sample signal. This inherent weakness hardly makes the covariance correction remedy the error of actual low amplitude state-variables with much more noise.

Fig. 4·14 and fig. 4·16 illustrate how the angular position estimation from the EKF trace the actual rotor position when "+" speed crosses the zero value from the clockwise rotation to anticlockwise rotation, while fig. 4·15 and fig. 4·17 show a similar situation when the "-" speed crosses the zero value from anticlockwise to clockwise rotation. Fig. 4·14 shows that the actual speed zero-cross point is located at 95 elec° when the "+" speed crosses zero from clockwise to anticlockwise. The estimated rotor position changes direction at 115 elec°, hereafter the EKF undertakes the remedial action to make the estimated position approach the real value and intersect at the zero-speed position 115 elec°. After changing the rotation to anticlockwise the EKF maintains the initial relatively large error for the acceleration stage in the anticlockwise direction, thereafter the covariance correction from the EKF makes the estimated position attempt to move towards the true value with not only positive but also negative offsets until the next anticlockwise cycle starts. Fig. 4.14 shows that the over-tuned correction occurs at the position -180 elec° just before the start of the next anticlockwise cycle.

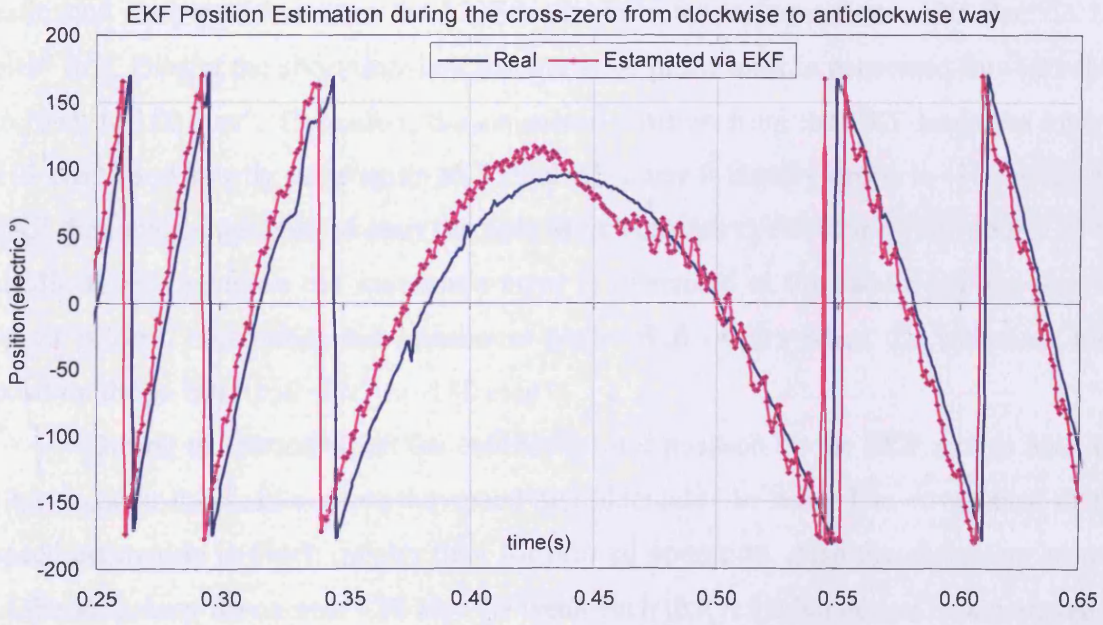

Fig. 4·14 EKF position estimation when the speed reverses direction

The wrong estimation of 180 elec° from the wrong convergence of the EKF instead of -180 elec° occurred at the terminal of the anticlockwise start-up. By restoring to the correct position proves that the remedial action is generated for the stationary currents or angular velocity to compensate the covariance of position.

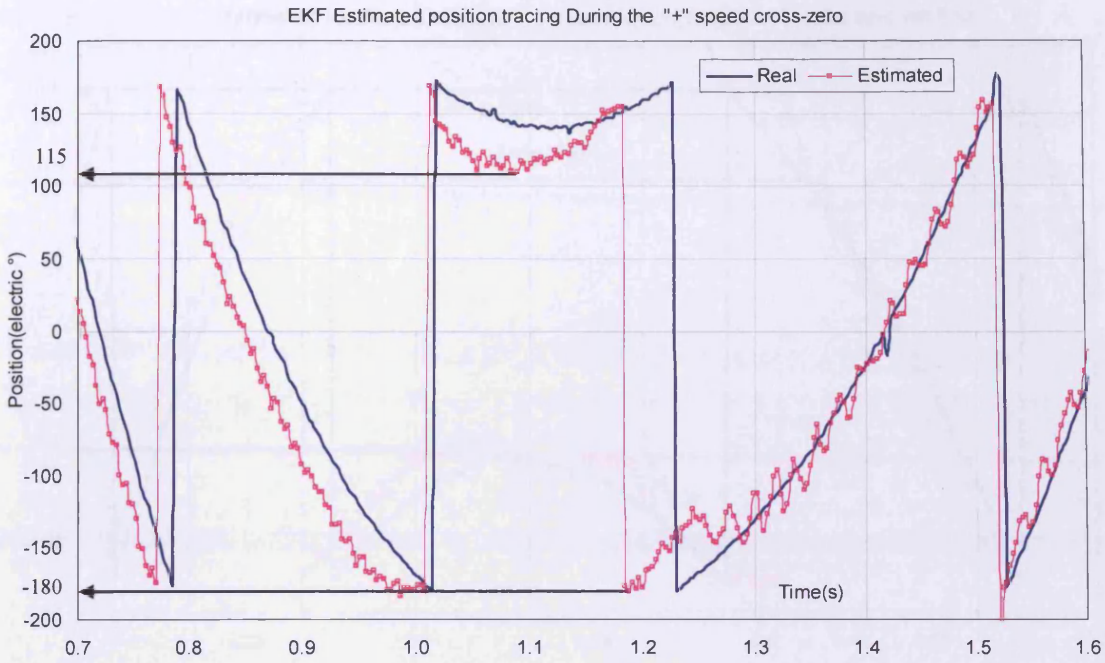

Fig. 4·15 The EKF estimated position tracing during the "+" speed crossing zero

Fig. 4·15 shows that the feature of the estimated position transient course is a saddle-shaped curve when the point for the speed crossing zero is located at -180 elec°. The estimated rotor position from the EKF leads the rotor to jump from -180 elec° to 180 elec° first. During the short transient instant, least phase shift is generated for -180 elec° to jump to 180 elec°. Thereafter, the estimated position from the EKF leads the rotor to 115 elec°, and shortly after again to 150 elec°. Later it rapidly drops to -180 elec°, the EKF then makes the PMSM start the next anticlockwise cycle. During the course of the saddle-shape operation the maximum error is generated at the saddle-point where the speed is zero, meanwhile the maximum phase shift occurs when the estimated rotor position drops from 150 elec° to -180 elec°.

During the period when the estimated rotor position by the EKF moves from the start-point to the saddle-point the speed also decreases to zero. The covariance of the speed estimation is much greater than for normal operation. Also the corrective current of the stationary frame near 180 elec° is weak such that remedial action is undertaken to reduce the rotor position error. Due to initial constant speed covariance, from the saddle-point to 150 elec°, the speed starts to increase and the rotor error is reduced. The

discrete variation from 150 elec° to -180 elec° is generated by over-correction caused by the large initial speed covariance. For the same reason the single-way offset for the next clockwise start-up between -180 elec° and -150 elec° is generated. However, afterwards, both generated positive and negative offsets correct the estimated position trace.

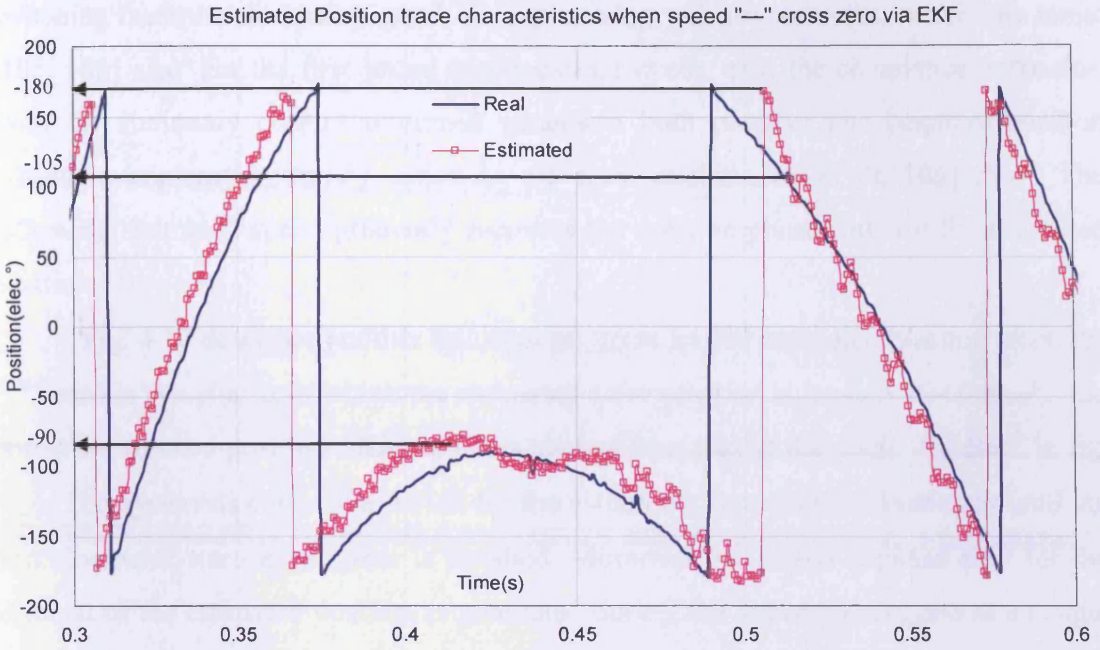

Fig. 4·16 Estimated position trace characteristics when the "+" speed crosses zero via the EKF

Fig. 4·16 illustrates the transient period for the estimated rotor position from the EKF when the "+" speed crosses the zero value where the actual rotor position is -90 elec°. Before the rotational direction changes from clockwise to anticlockwise, the decreasing speed not only increases the error of the estimated rotor position but also the phase shift between the estimated and actual rotor position. The increased error and phase shift can be explained above by the weak stationary current references for the low speed area.

There is a large phase lead between the estimated and real rotor position in the time domain [0.31, 0.42]s as shown in Fig.4·16. The ADC measurement for the weak electrical signal is not accurate and the amplitude of the measured signal might be less than the noise threshold. The estimated position error in the time domain [0.3, 0.31]s is less than that in the time domain [0.31, 0.42]s, when the speed is approaching zero. The zero speed may generate the weakest stationary current references which take the poor remedial action. The estimated rotor position range [-90,-100] elec° shown in Fig. 4·16 shows this wrong convergence caused by the poor remedial action.

Such incorrect convergence could generate the following position error for the anticlockwise start-up. The initial anticlockwise position error is the result generated by the correction from the covariance of the other state variables. It is straight forward to see the negative offset and the larger phase lag for the anticlockwise start-up after switching from the clockwise speed. Such phase lag was not corrected even in the range [105, 180] elec° for the first initial anticlockwise cycle, until the covariance correction from the stationary current reference generated both positive and negative position offsets to implement remedy action in the rotor position range [0, 105] elec°. The following estimated speed gradually recovers the positive phase shift for the estimated position.

Fig. 4·17 describes another transient progress for the estimated position when the "-" speed is crossing zero where the estimated rotor position is located at -60 elec°. The positive estimated position offset appears shorter than that at the angle -90 elec° in fig. 4·16. The hysteresis corrective period for the estimated rotor position lasts only until the first clockwise start-up progress is finished. Moreover, no negative phase shift for the terminal of the estimated position is generated during this transient progress at an angle -60 elec° for the speed crossing zero.

Fig. 4·14 to fig. 4·17 prove that the remedial action from the stationary current reference play an important role in the transient progress for the speed crossing zero. When the speed was crossing zero and the nearby area has a low speed value covariance of the estimated position becomes deeply affected by other state variables,

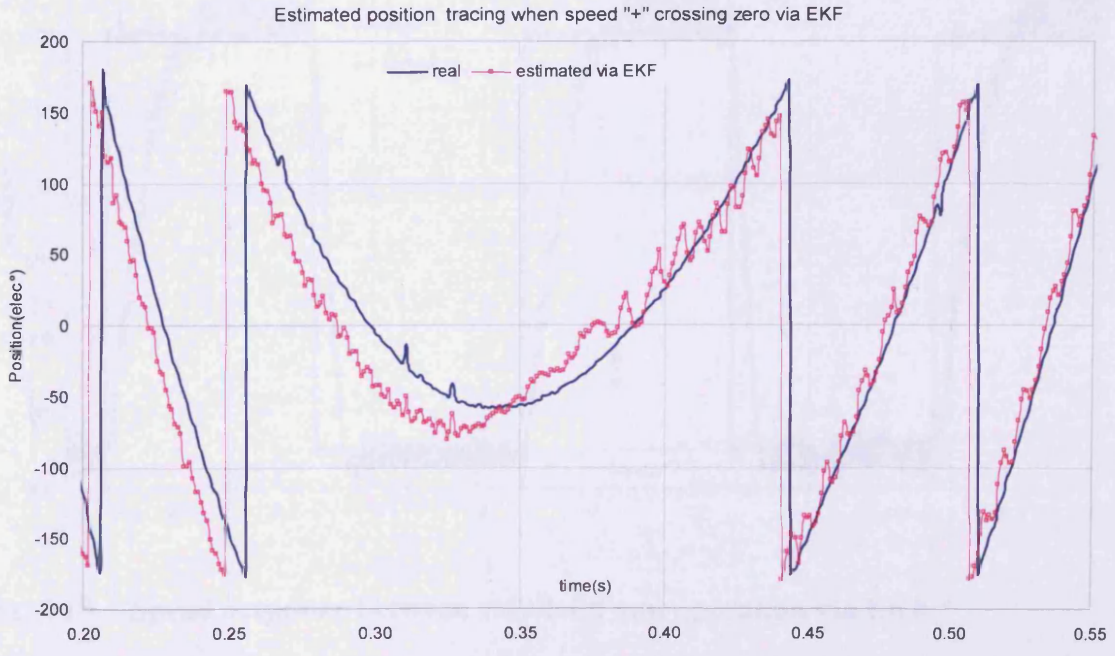

Fig. 4·17 Estimated position tracing when "-"speed crosses zero via EKF

the stationary current references These are determined by sine or cosine functions corresponding to a different rotor position where the speed is crossing zero. The point of estimation for the speed crossing zero separates the positive offset from the negative offset for the actual rotor position. The negative offset for the actual rotor position alternately makes the stationary current generate hysteresis offset for remedial action until the estimated position goes back with positive offset.

4.4.5 Low speed characteristics

The low speed is used to investigate the least operation speed (LSO) of the EKF-based sensorless control that the PMSM is capable of reaching. Its poor low speed behaviour has been investigated over the past twenty years [4·1~4·4]. The LSO measurement specifically points out the least identifying capability for the stationary current covariance. The proposed experimental prototype is again the 3-phase PMSM link-coupled with the DC generator on no load, the measured torque is about 0.8~1.1 Nm when the speed is 1100 rpm. The special square speed reference is used to investigate its zero-speed behaviour.

As shown in fig. 4·18, the square speed reference has a 50% duty cycle with a 4 second length toggling yielding to 1100 rpm and 0 rpm. The reason that the half duty cycle is 4 seconds is that the load driven by the PMSM is mechanically linked with the shaft of the DC generator.

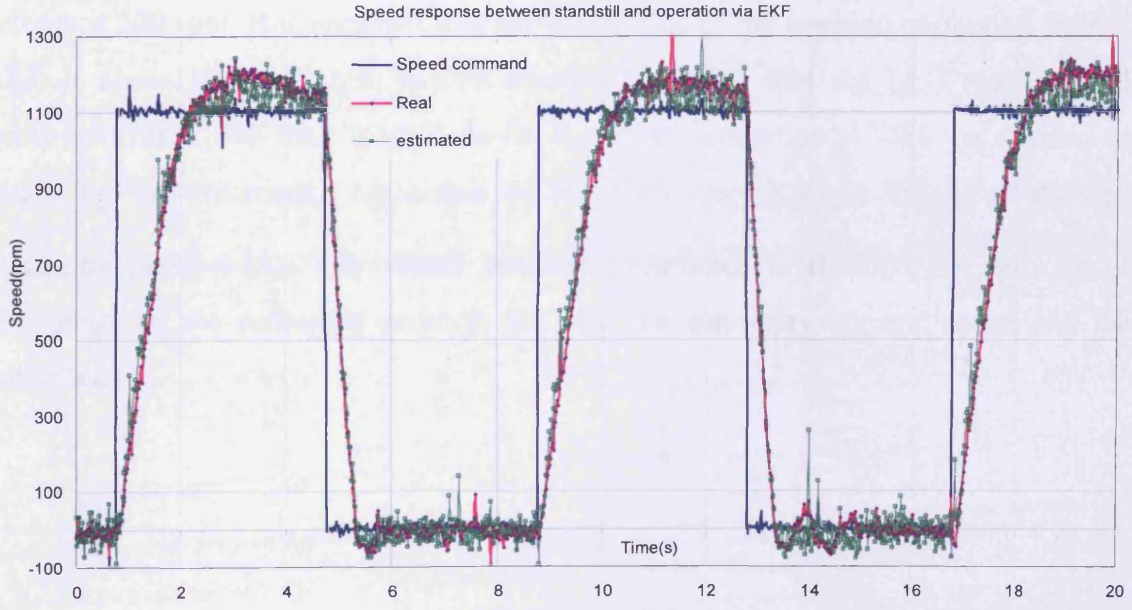

Fig. 4·18 Speed response between standstill and operation via EKF

The DC generator in no load mode has both the armature and field winding on open circuit Four seconds is sufficient to observe the dynamic speed characteristics. The actual speed shown in fig. 4·18 is measured in the same way as above from the shaft-mounted encoder via the USdigital Encounter pulse-to-binary converter after the derivation of its value. The estimated speed in fig. 4·18 is directly extracted from the EKF expressed in equation (4·34). The square speed reference regularly results in the estimated and actual speed to stay for 4 s at 1100 rpm, after another 4 s it drops to zero speed, then 1100 rpm for another 4 s after which the sequence is repeated continuously.

Fig. 4·18 illustrates that the EKF is able to estimate the zero speed although both positive and negative offsets are generated to remedy the covariance from noise near zero speed. At the end of every 4 s at zero speed, the EKF starts up by itself to the 1100 rpm speed reference. Compared with fig. 3·34, the FLO is not capable of start-up by itself but the EKF overcomes this disadvantage. As far as this point is concerned, the multiple-order state-observer always corrects the error generated by the low speed operation to extract the estimated rotor position.

Fig. 4·19 shows that the LSO reached by EKF is 50 rpm while any lower speed is not applicable for the EKF-based sensorless control proposed with the PMSM prototype. Fig. 4·20 and fig. 4·21 show that the other low speed behaviour over 50rpm could operate normally. Fig. 4·20 demonstrates that the speed response characteristics to low reference 100 rpm for the EKF while fig.4·21 shows the speed response to low reference 200 rpm. It is apparent that the magnitude of the position correction from the EKF is about 50 to 60 rpm, which decides the value that the LSO reaches at the maximum limit. The least magnitude for the speed correction (LMSC) is decided and scaled by the covariance correction of the EKF: item $K_k(y_k - H\hat{x}_{k|k-1})$ as shown in equations (4·34~4·35). The actual position covariance is decided not only by the covariance of the estimated position but also the stationary current, speed and their covariance.

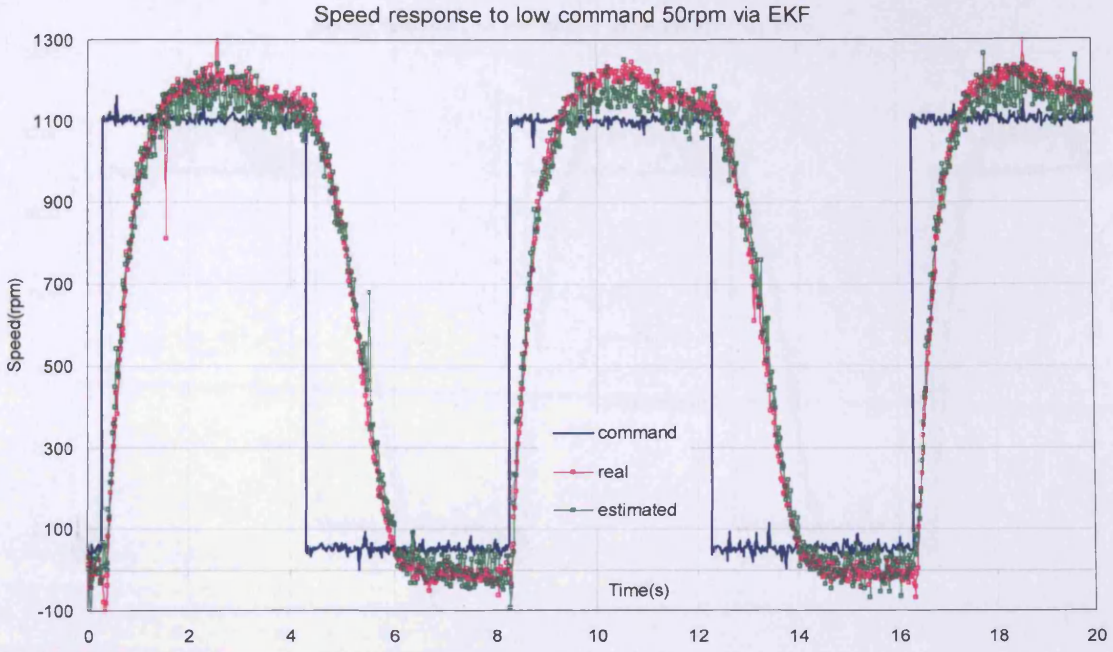

Fig. 4·19 Speed response to low command 50 rpm via EKF

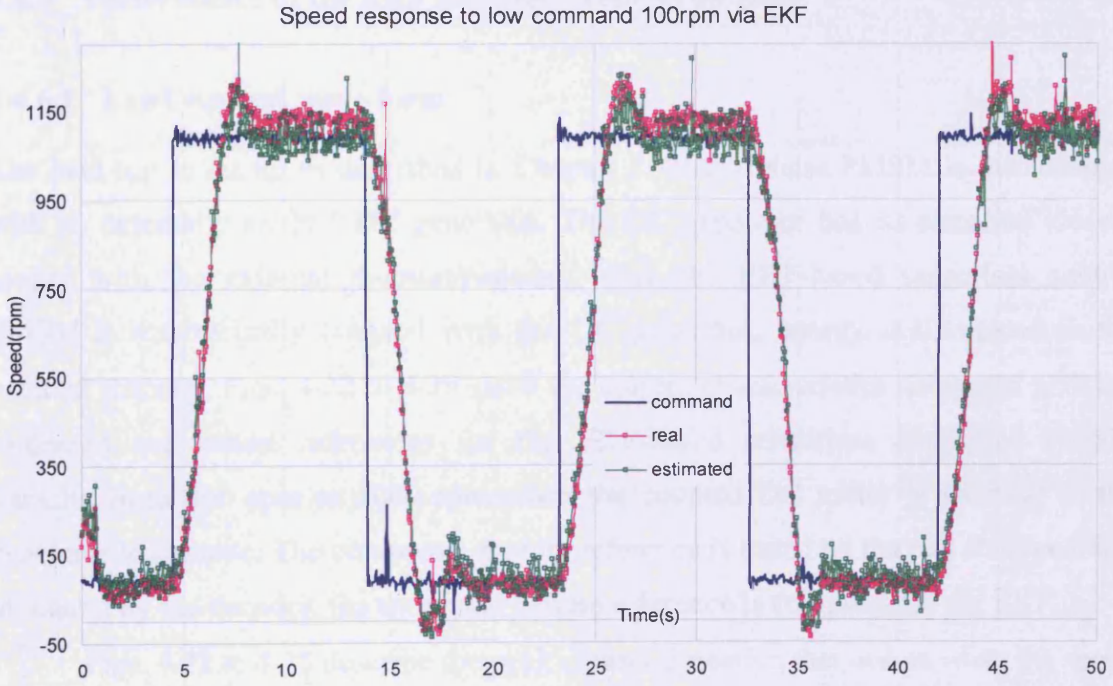

Fig. 4·20 Speed response to the low command 100 rpm via the EKF

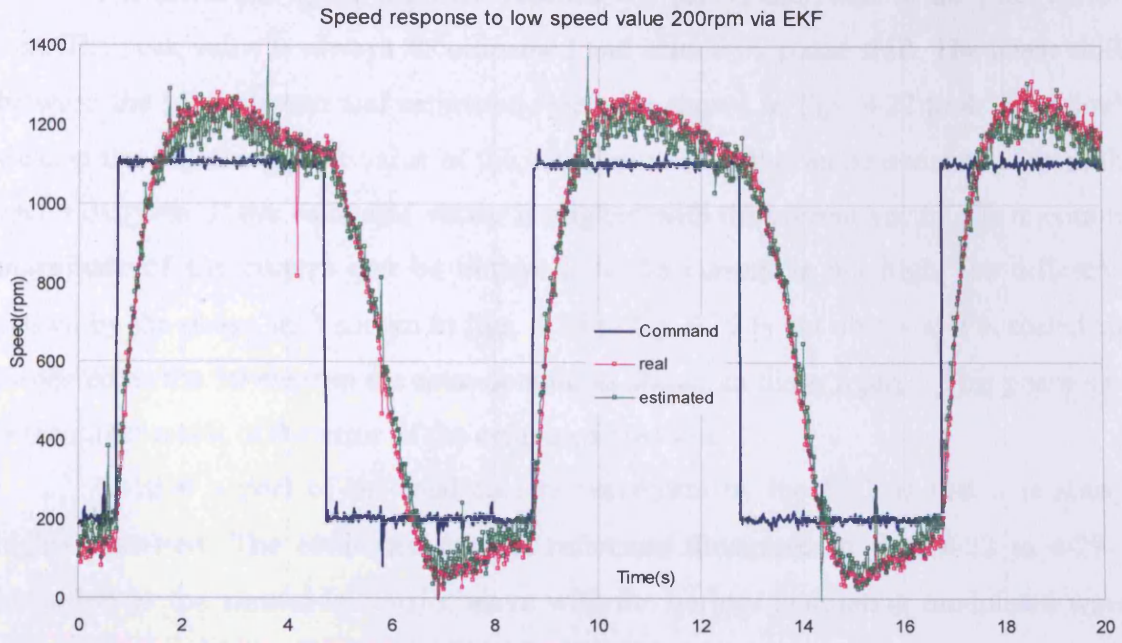

Fig. 4·21 Speed response to low speed at 200 rpm

4.4.6 Performance of the EKF sensorless control on load

4.4.6.1 Load current wave form

The load test is set up as described in Chapter 3. The 3 phase PMSM is link-coupled with an externally excited DC generator. The DC generator has its armature closed-looped with the external rheostat/resistor. When the EKF-based sensorless control PMSM is mechanically coupled with the DC generator, energy is dissipated in the external rheostat. Figs. 4·22 to 4·29 show the current characteristics compared with the estimated and actual references for the EKF-based sensorless controlled PMSM working from 300 rpm to 1000 rpm when the coupled DC motor is working in the generator load mode. The computed current reference is based on the real shaft position measured by the encoder, the estimated current reference is computed by the EKF.

Figs. 4·22 to 4·25 describe the peak current distortion that occurs when the speed becomes close to the rated speed. The current peak difference shown in fig. 4·22 for 1000 rpm operation is scaled to 3 A, the 900 rpm for the EKF–based sensorless operation generated a 2.5 A peak loss in fig. 4·23; the 800 rpm for the EKF operation obtained 1 A peak distortion in fig. 4·24; the 700 rpm for the EKF operation lost a 1 A peak value in fig. 4·25, until at 600 rpm Fig. 4·25 shows the peak current loss begin to disappear.

The lower the speed the EKF reaches, the less is the value of the peak current loss. The peak value is always accompanied and caused by phase shift. The phase shifts between the ideal current and estimated reference shown in figs. 4·22 to 4·25 no doubt weaken the following peak value of the actual current. This can be understood from the vector diagram. If the back-emf vector is aligned with the current vector, the maximum magnitude of the current can be obtained. If the current is not high, the difference caused by the phase shift shown in figs. 4·26 to fig. 4·29 is not obvious. It is scaled and measured as the 30 elec° in the time domain as shown in these figures. This phase shift is the direct result of the error of the estimated position.

Another aspect of the load current waveform by the EKF is that it is always highly distorted. The estimated current reference illustrated in figs. 4·22 to 4·29 is identified as the sinusoidal carrier wave with the narrow undulating modulated wave. Constant covariance for the stationary current reference is the feature of steady operation via the EKF, from this point it is inevitable for the actual current to keep variance with the current reference.

The hysteresis correction trace seems to appear explicitly when the speed and current are low as shown in the figures. It has been explained above that greater current ripple and distortion occurs at low speed and current reference via the EKF which could lead to more serious distortion in the actual load current via the EKF. In the speed range 500 rpm to 700 rpm shown in figs. 4·25 to 4·27 this proves that the higher current takes more remedial action for covariance correction.

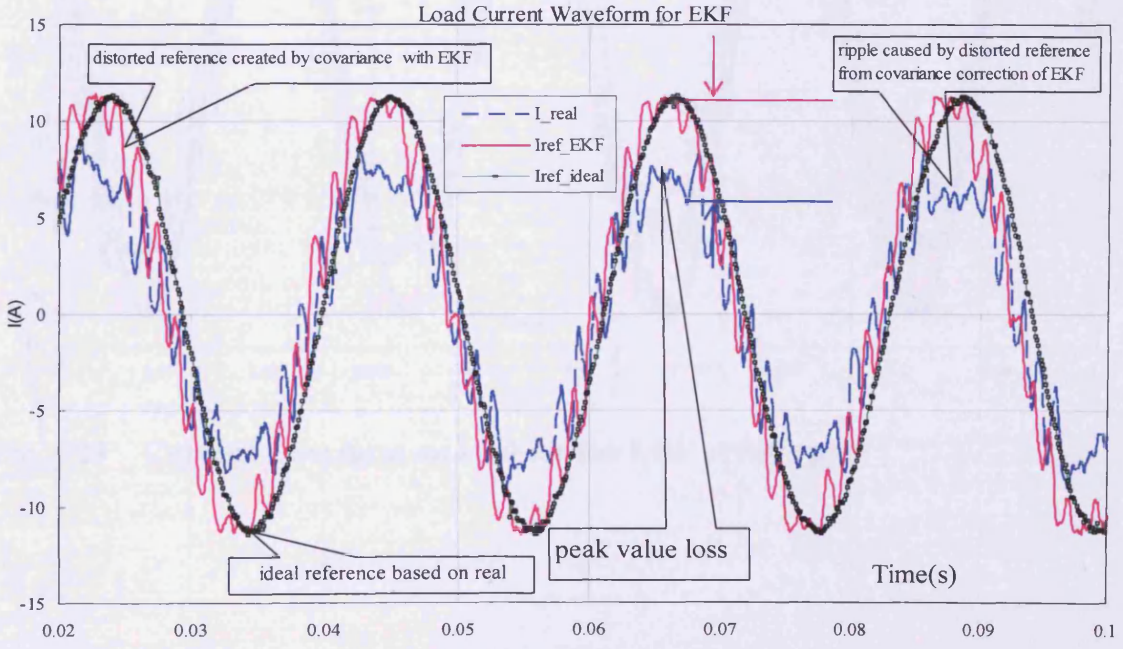

Fig. 4·22 Current waveform on load for the EKF at 1000 rpm

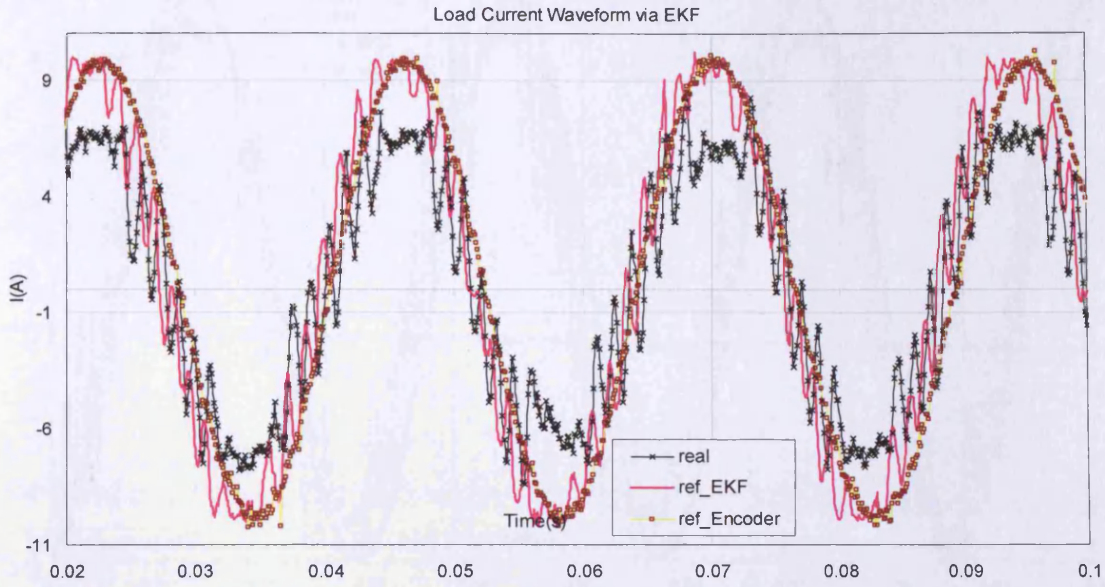

Fig. 4·23 Current waveform on load for the EKF at 900 rpm

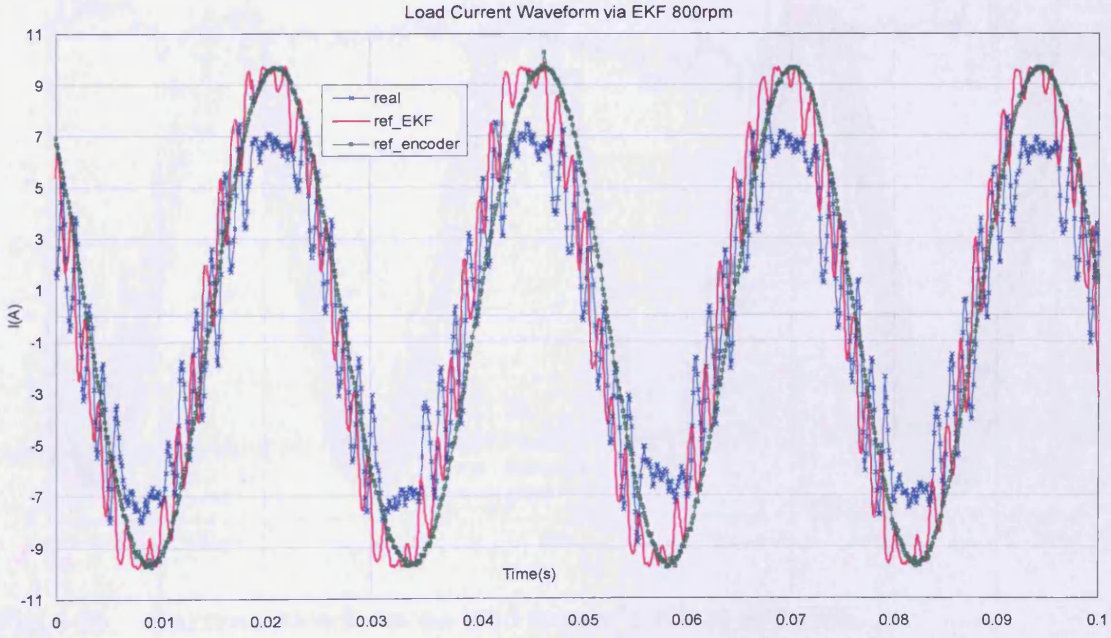

Fig. 4·24 Current waveform on load for the EKF at 800 rpm

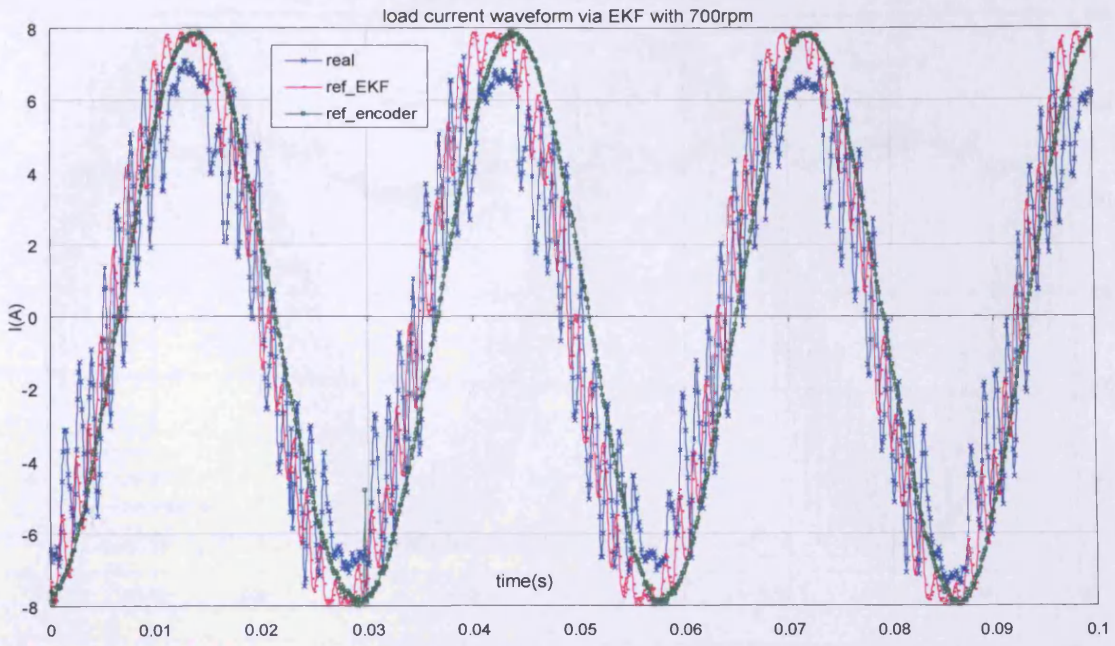

Fig. 4·25 Current waveform on load for the EKF at 700 rpm

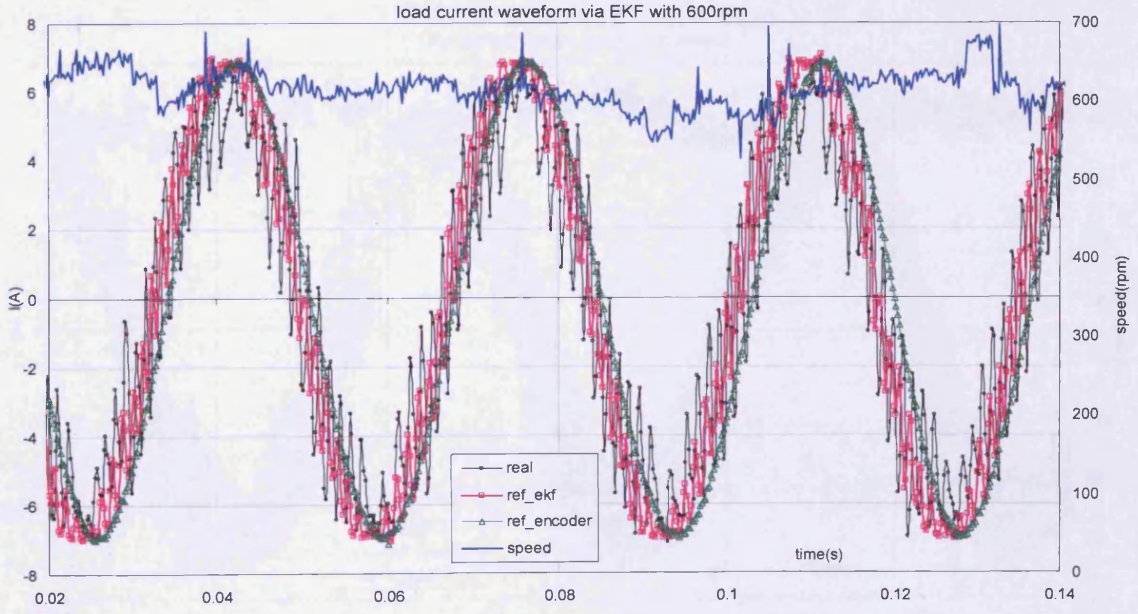

Fig. 4·26 Current waveform on load for the EKF at 600 rpm

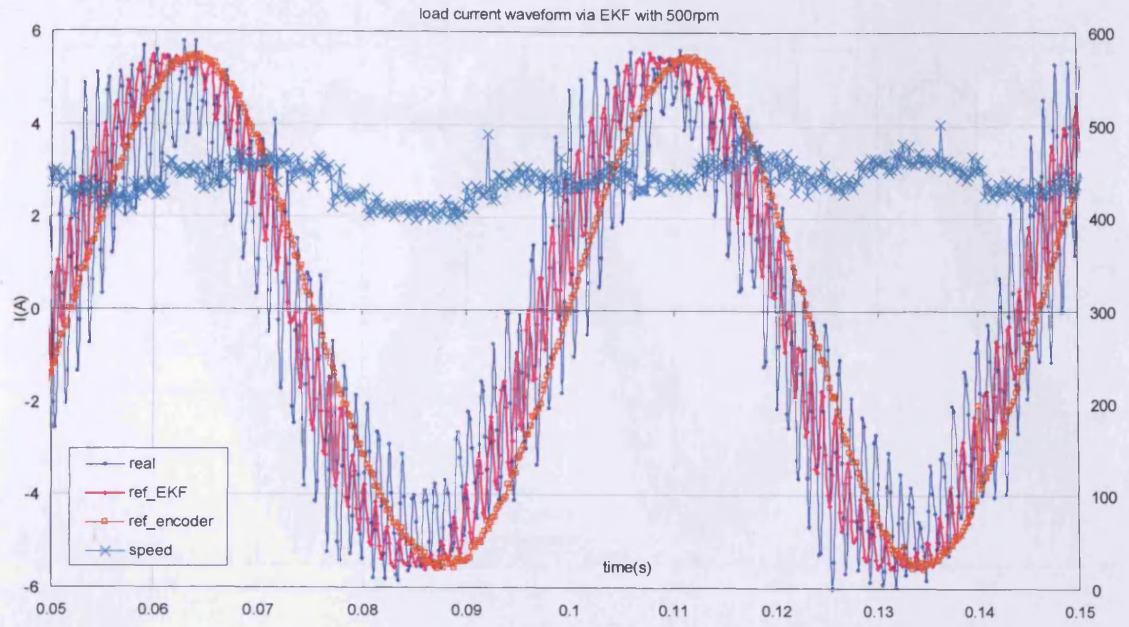

Fig. 4·27 Current waveform on load for the EKF at 500 rpm

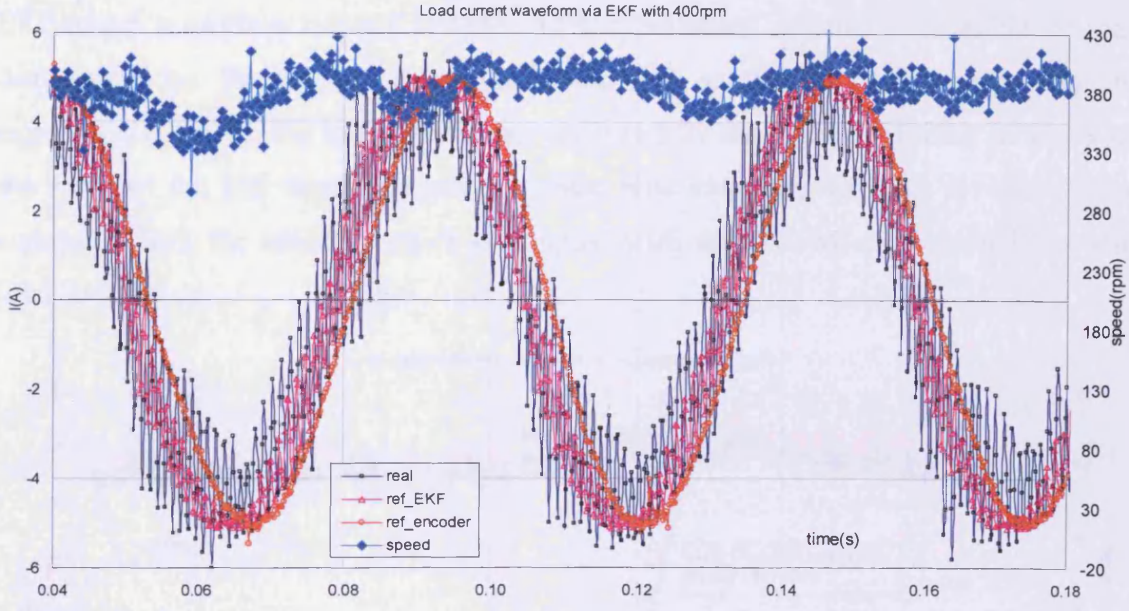

Fig. 4·28 Current waveform on load for the EKF at 400 rpm

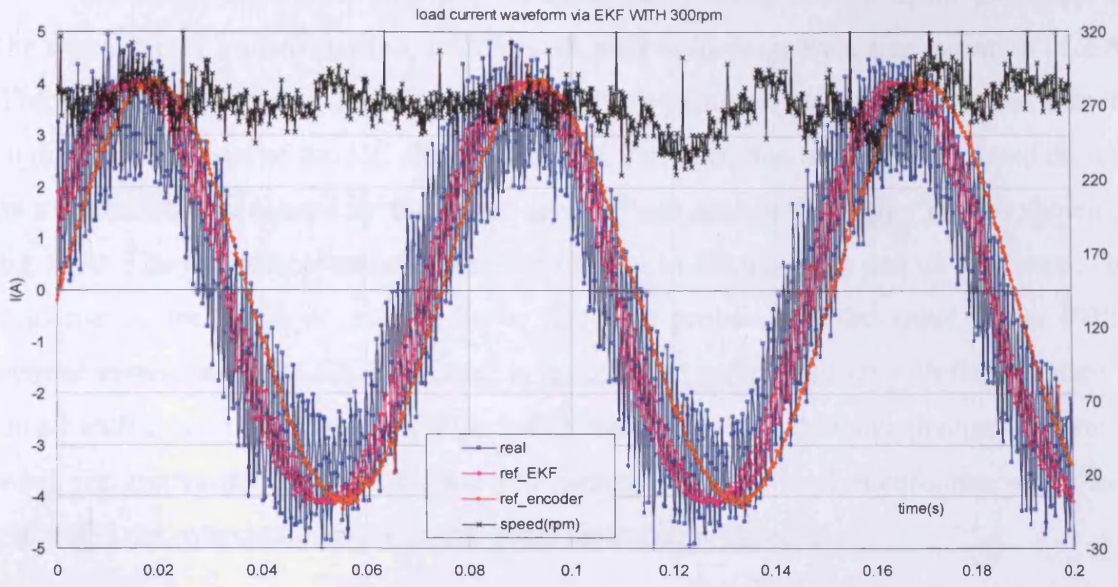

Fig. 4·29 Current waveform on load for the EKF at 300 rpm

4.4.6.2 Effect of load disturbance on the speed and Iq characteristics

Fig. 4·30 shows the speed response to a step variation of the load torque for the EKF-based sensorless control PMSM. This experiment considers the effect of load disturbance on the speed under the sensorless operational environment. In the experimental set up, the load torque was produced by the excited winding mounted on the rotor of the DC shunt excited generator with armature winding close-circuit or connected with the resistor, which is coupled with the PMSM shaft through the stiff joint coupler.

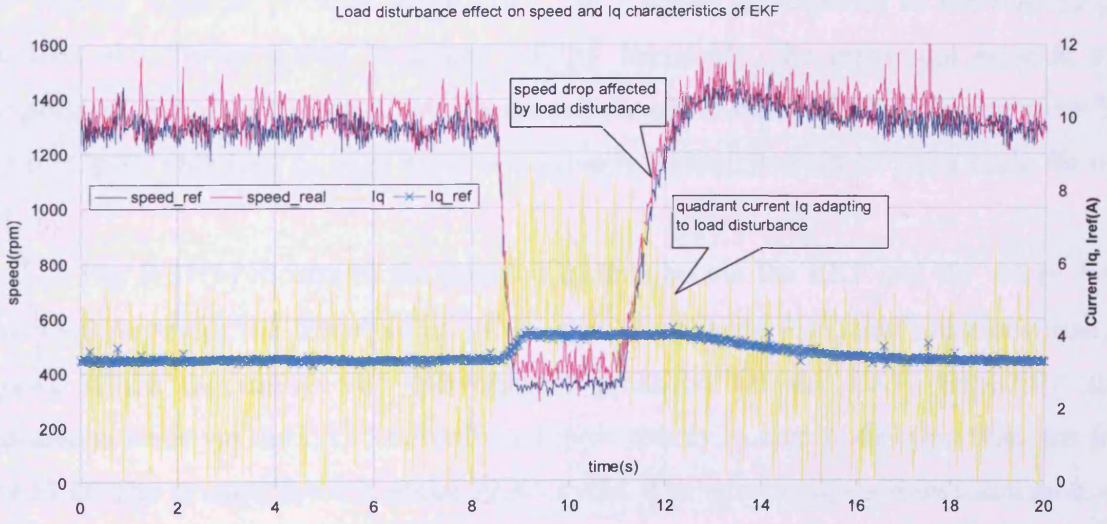

Fig. 4·30 Effect of load disturbance on the speed and Iq characteristics of the EKF

The lower two curves in Fig. 4·30 show the quadrant current Iq for the torque in the space vector transformation, which is adapted to increase by a step variation of 2 A. The specific disturbance experiment imposed the variation on the field-excited current in the rotor winding of the DC shunt generator. The variation of the field-excited current as a disturbance is caused by the speed drop of 900 rpm in the higher part as shown in fig. 4·30. The load disturbance caused the change in the quadrant and its reference. The response of the quadrant current Iq in fig. 4·30 proved that the space-vector PWM control system with the EKF observer is robust. The series resistor with the armature is tuned with a large value to obtain the small braking torque, thus the quadrant current is weak for generating so much noise while alternatively the load disturbance works as a pulse and the overshoot occurs in the quadrant current response.

4.5 Analysis of the Variant-Covariance Correction Technique used in the Full-order State EKF-based observer compared with the FLO-based direct Estimation

4.5.1 The effect of the variant-covariance correction on the position estimation precision for the EKF-based sensorless control:

The average error for the rotor position by the FLO is 8.1°/cycle as shown in fig. 4·31(a). The error analysis shows that the angle error via the FLO is less than 10° in absolute position angle [-180°, 10°] which corresponds to a time range [0.008, 0.0108]s as shown in figure 4·31(a) while the value error via the FLO varies in the range [10°, 20°] in the absolute position range [10°, 180°] which corresponds to the time range [0.0108, 0.027]s as shown in figure 4·31(a). Inevitably, the maximum error in the sensorless controlled PMSM always occurs at the cycle start and when the error can be up to ±360°. This type of edge error occasionally occupies about 10° of a cycle for the FLO.

Fig. 4·31(b) illustrates the position estimation via the EKF and the errors. P40 and Q40 represent the initial value of the state covariance $P_0(4)$ and noise covariance $Q_0(4)$, which determines the convergence precision for the EKF. Explicitly, the estimation error via the EKF is distributed quite evenly in amplitude other than that for the FLO. The average error is about 12.4°/ cycle. The error analysis shows that most of the errors fall in the range [10°, 20°]. The edge error shift where the maximum error occurs is about 13°.

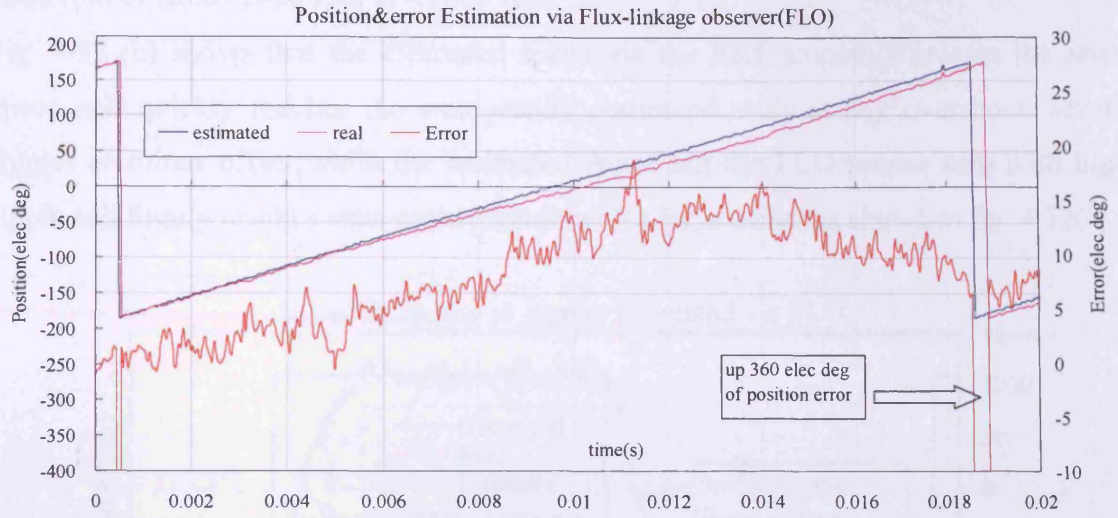

(a) Position and error estimation via the flux-linkage observer(FLO)

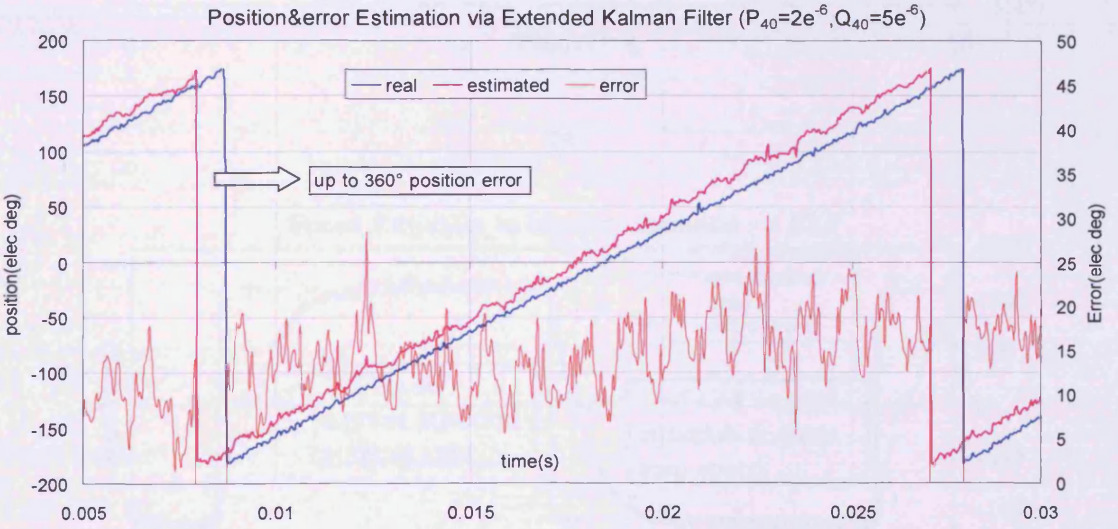

(b) Position and error estimation via the EKF ($P_{40}=2e^{-6}$,$Q_{40}=5e^{-6}$)

Fig. 4·31 Comparison of position estimation precision characteristics using the EKF and the FLO observer per electric cycle

4.5.2 The effect of variant-covariance correction on the speed response for the EKF-based sensorless control:

The modern servo industry requires actuators to have the capability of speed zero crossing in order to switch among 4 quadrants. Actuators should go through zero velocity promptly without any delay in switch instructions. Fig. 4·32 compares the characteristics of the velocity zero-crossing ability of the FLO and EKF. The

bidirectional speed command would lead the PMSM to pass zero from +1000 rpm to -1000 rpm or from -1000 rpm to +1000 rpm.

Fig. 4·32 (b) shows that the estimated speed via the EKF smoothly crosses the zero-speed and quickly reaches the state-steady command without any overshoot, severe ripples or minor offset while the estimated speed via the FLO passes zero with high ripple and finally reaches state-steady mode with a large offset as shown in fig. 4·32(a).

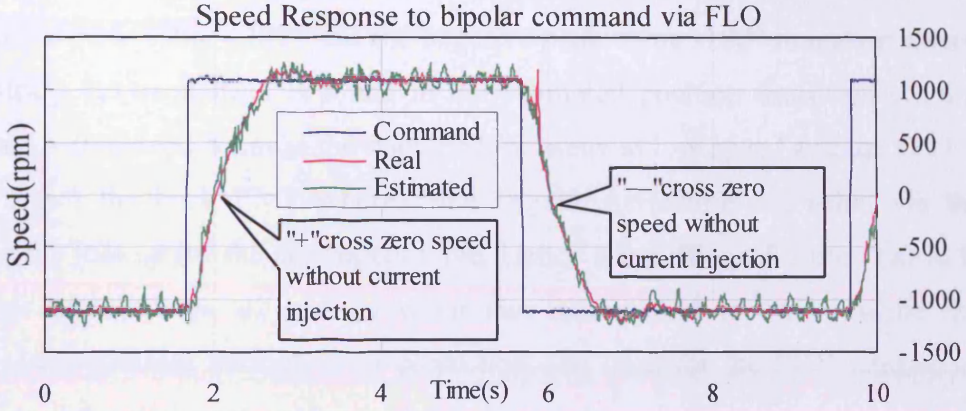

(a)

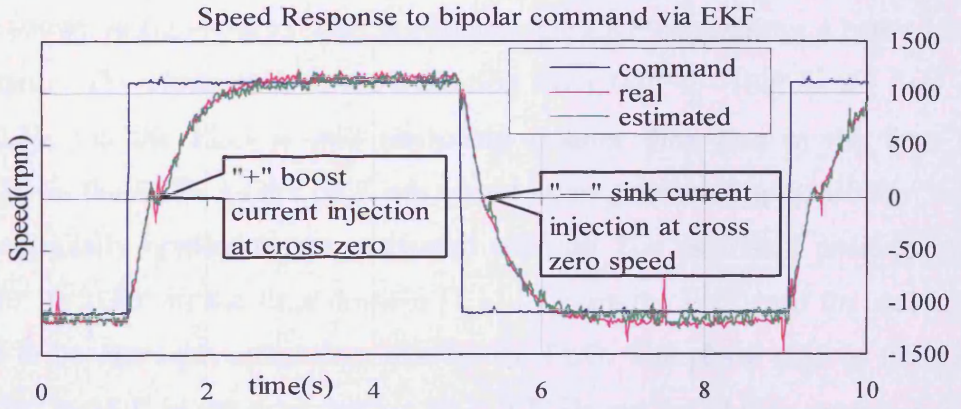

(b)

Fig. 4·32 Comparison of speed responses to the bipolar command characteristics with EKF and FLO observer

4.5.3 The effect of the variant-covariance correction on the transient position trace for the EKF-based sensorless control

Fig. 4·33 shows that the FLO and the EKF have the capability of tracking the instantaneous position transition caused by the operation when the speed crosses zero in four-quadrant operation. However, the FLO will produce the estimated position oscillation of the estimated position as shown in fig. 4·33(a) when the speed is switching in the 4-quadrant operation, the estimated angular position oscillates between the positive peak value +180° and the negative peak value -180° in a short interval. On the contrary, no oscillation is found in the estimated position transition via the EKF. This can be explained because the back EMF is weak at low speed and the FLO method has to detect the back EMF whereas the angular extraction algorithm via the FLO employs the lookup for the arctangent table. Hence it is difficult for the FLO to identify the weak flux linkage ψ_α and ψ_β when they correspond to ±180° while the EKF estimates the position through error correction The limit for the EKF estimation is the capability of the minimum analogue signal detection.

When the speed crosses zero, the general initial error caused via the FLO in the time domain [0.2, 0.3]s is relatively larger than that via the EKF in the time domain [1.1, 1.3]s as shown in fig. 4·33(b). This proves that the EKF can achieve a better low speed performance. The phase shift at the transition from 180° to -180° in the time domain [0.275,0.3]s via the FLO is still obviously smaller than that in the time domain [1.1,1.3]s via the EKF. As the EKF has a very strong self start-up capability, the phase lead occasionally applies to the estimated position The estimated position transition from 180° to -180° in the time domain [1.1, 1.3]s by the EKF lead the real estimated position to be more advanced than that by the FLO. The phase shift at the transition from -180° to 180° in the time domain [0.2, 0.225]s via the FLO is greater than that in the time domain [1.0,1.1]s via the EKF because the FLO behaves poorer at the low speed. Similar analysis explains why the error of the estimated position by the FLO is greater after the transition from 180° to -180° in the time domain [0.3, 0.5]s shown in fig. 4·33(a) than that in the time domain [1.2,1.4] as in fig.4·33(b).

Fig. 4·34(a) and (b) show that the FLO and EKF both track the true position transition when the real position is at the negative peak value –180° where the PMSM crosses zero from the clockwise to anticlockwise direction. The estimated position oscillation seen in fig. 4·33 (a) can also be seen in fig. 4·34 (a).

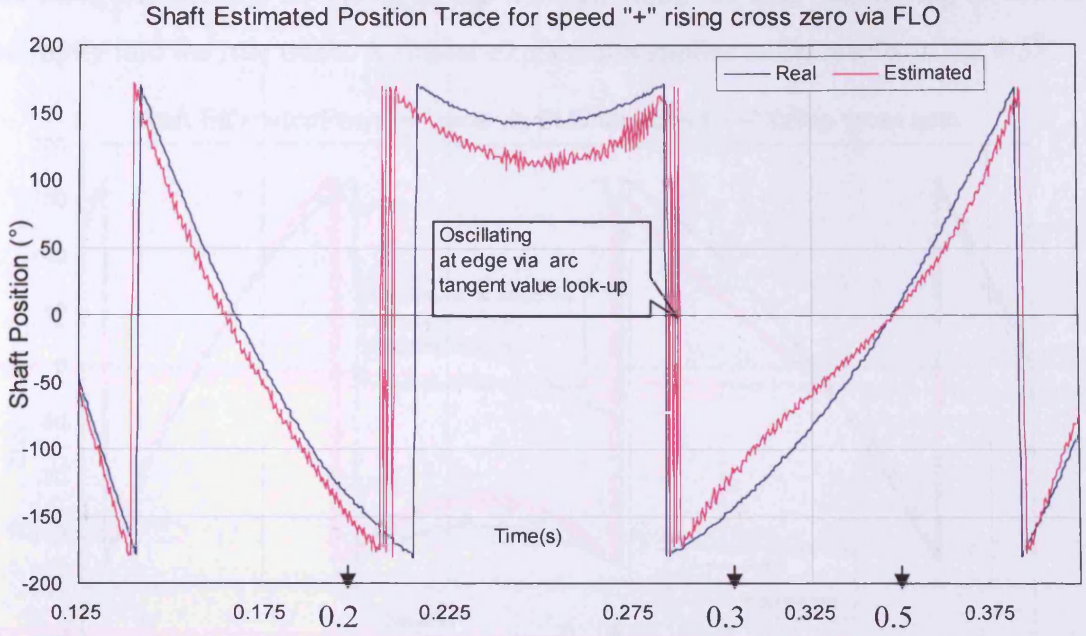

(a) Shaft estimated position trace for speed "+" rising cross zero via FLO

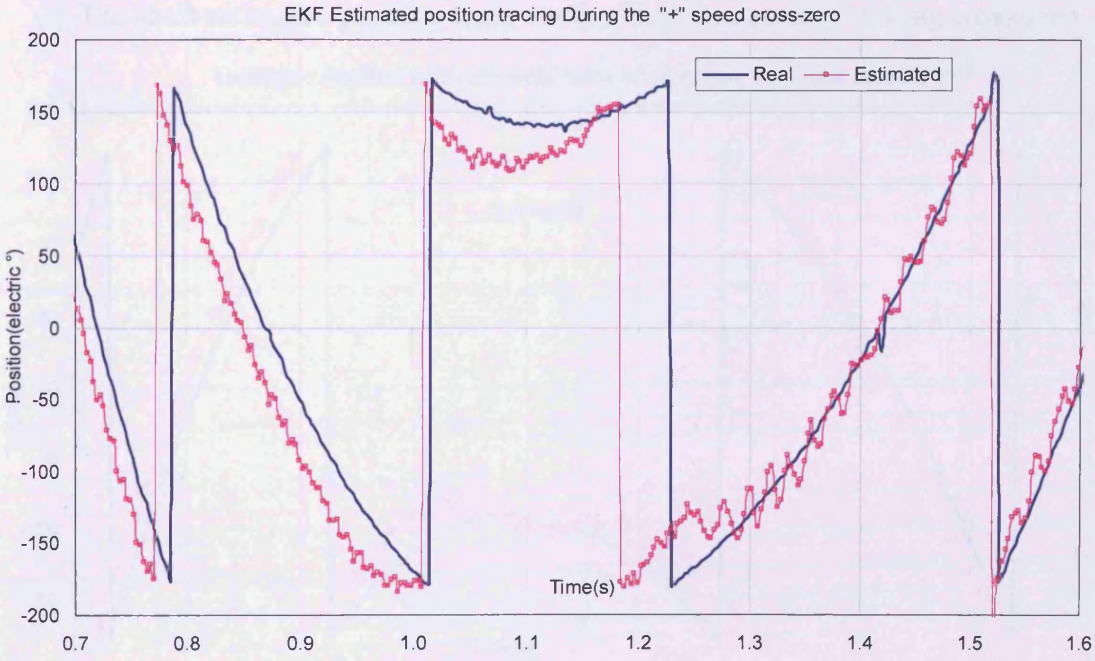

(b) EKF estimated position tracing during the "+"speed rising cross-zero

Fig. 4·33 The Estimated position transition for rising speed cross-zero

The EKF causes the phase lag at the positive transit from -180° to 180° in the time domain [0.45,0.55]s seen in fig. 4·34 (b) while the FLO causes the small phase lag in the similar situation in the time domain [1.125,0.175]s in fig. 4·34 (a). However, the FLO takes slightly more time (0.01 s) to get close to the true rotor position in the time

domain [0.15,0.175]s as shown in fig. 4·34(a), while the EKF has no lag to converge promptly into the true track. A similar explanation applies to the results in fig. 4·33.

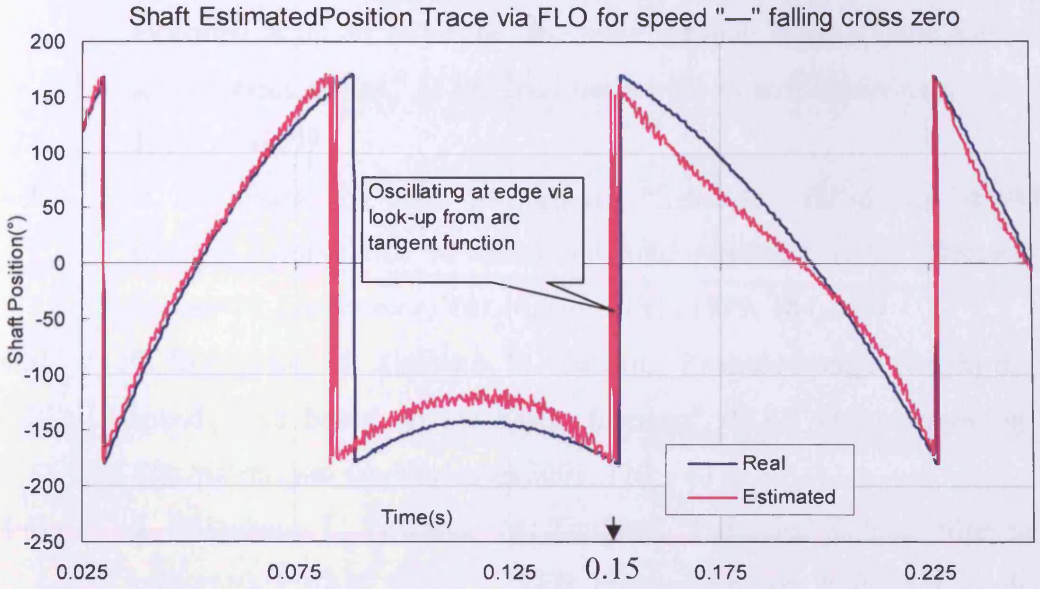

(a) The shaft estimated position trace via the FLO for speed "-" falling cross zero

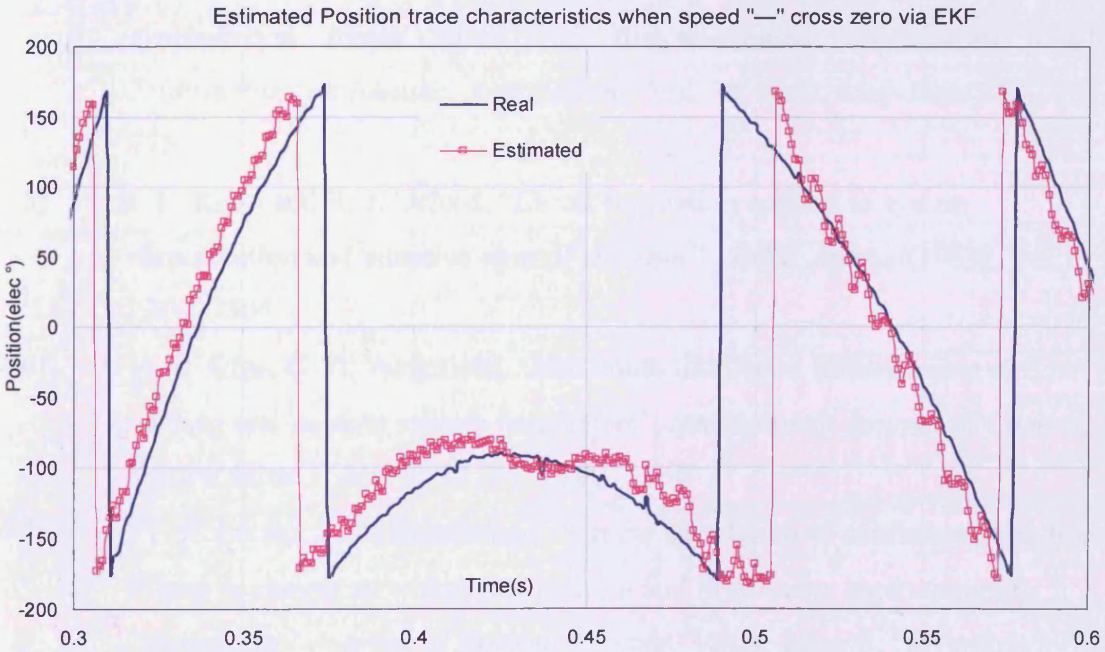

(b) Estimated position trace characteristics when speed "-" cross via EKF

Fig. 4·34 Estimated Position Transition for the falling speed cross-zero

4.6 References

[4·1] R. Dhaouadi, N.Mohan, L.Norum, "Design and implementation of an extended Kalman Filter for the state estimation of a permanent magnet synchronous motor," *IEEE Transactions on Power Electronics*, Vol. 6, July 1991, 491-497

[4·2] S. Bolognani, R.Oboe, M.Zigliotto, "Sensorless full-digital PMSM drive with EKF estimation of speed and rotor position", *IEEE Transactions on Industrial Electronics*, Vol.46, No.1, Feb. 1999, 184 - 191

[4·3] S. Bolognani, M. Zigliotto, M. Zordan, "Extended-range PMSM sensorless speed drive based on stochastic filtering", *IEEE Transactions on Power Electronics,* Vol.16, No.1, Jan.2001, 110 – 117

[4·4] S. Bolognani, L. Tubiana, M. Zigliotto, "Extended Kalman filter tuning in sensorless PMSM drives", *IEEE Transactions on Industrial Applications*, Vol.39 , No. 6, Nov.-Dec. 2003,1741 – 1747

[4·4] S. Bolognani, L. Tubiana, M. Zigliotto, "EKF-based sensorless IPM synchronous motor drive for flux-weakening applications", *IEEE Transactions on Industry Applications,* Vol. 39, No.3, May-June 2003, 768 – 775

[4·5] R. E. Kopp and R. J. Orford, "Linear regression applied to system identification and adaptive control systems " , *AIEE Journal*(1963), Vol.1, 2300–2306

[4·6] A. P. Sage, C. D. Wakefield, "Maximum likelihood identification of time varying and random system parameters", *International Journal of Control*, Vol.16, Issue 1, July 1972 , 81 – 100

[4·7] V. P. Leung, L. Padmanabhan, "On the simulation of continuous non-linear filters: A comparative study of second- and third-order approximations ", *International Journal of Systems Science*, Vol.4, Issue 6, November 1973 , 889 – 898

[4·8] L.Nelson, E. Stear, "The simultaneous on-line estimation of parameters and states in linear systems ", *IEEE Transactions on Automatic Control*, Feb 1976, Vol.21, Issue: 1, 94- 98

[4·9] J. B. Farison, R. E. Graham and R. C. Shelton, "Identification and control of linear discrete systems ", IEEE Transactions on Automatic Control, August 1967, Vol.12, Issue: 4, 438- 442

CHAPTER 5, THE CONSTANT COVARIANCE CORRECTION SCHEME— —NOVEL LINEAR KALMAN FILTER SENSORLESS TECHNIQUES

5.1 INTRODUCTION

The classic Back-EMF-based sensorless method described in Chapter 3 and the EKF-based sensorless state estimation method described in Chapter 4 has shown their respective advantages and drawbacks. The Back-EMF-based sensorless estimation method may obtain higher shaft position estimation precision than the EKF-based state estimation method while the EKF-based sensorless state estimation can implement the self-start-up with the capacity for extra speed estimation. In this chapter the novel Linear Kalman Filter (LKF) sensorless state estimation with constant variance correction instead of the variant covariance correction by the EKF-based sensorless state estimation is described.

The LKF-based sensorless estimation has proved that the constant variance correction scheme provides the same and or better sensorless performance compared with the EKF. The proposed LKF-based sensorless method secures a slightly higher shaft position estimation precision through constant covariance in the Linear Kalman Filter to correct the output of the quadrant stationary flux linkages.

The classic LKF-based sensorless control PMSM was proposed [5·1] and implemented only by simulation. The classic LKF approach is completely different from that proposed in this thesis. The mathematical model based on the classic LKF is similar to the model based on the EKF in that the dynamic electromagnetic/mechanic equations of the PMSM in the stationary reference frame α-β are shared by the EKF and classic LKF methods. However, the PMSM dynamic model via the classic LKF involves sine and cosine functions of the rotor position. The position is extracted through extra equations, and the rotor angular is still computed by the inverse

trigonometric function arctangent. However, the speed has to be calculated by the derivative of the estimated position. Considering these two facts, the actual computation cost is increased to counteract the benefit from the LKF compared with the EKF.

The proposed LKF method is based on the 3-order position-speed-noise model proposed by Harnefors [5·2] which defines the rotor speed as a double integration of the noise. The mathematic model is invariantly linear with a constant coefficient matrix. The output quantities are replaced by flux linkages rather than a trigonometric function. The orthogonal output can be used to generate the time-invariant algebraic Riccati difference equation. The proposed LKF is shown to be successfully used in experiments. The validated algorithm requires 6 multiplications and two trigonometric operations. In this chapter it is shown that the proposed novel LKF sensorless PMSM control method can be implemented with relatively low computation cost and can obtain a comprehensive performance.

5.2 Linear Kalman Filter Model for PMSM

Any discrete-time, nonlinear dynamic system with input can be expressed using the state space equation

$$X(k+1) = F_k X(k) + G_k(k)u(k) + \omega(k) \tag{5·1}$$

$$y(k) = H_k X(k) + v(k) \tag{5·2}$$

X(k): state vector; u(k): input state; y(k): output state; ω(k): system noise; v(k): measure noise. ω(t) and v(k) are not measured but are system disturbances. F_k , G_k and H_k are system matrices which are generally time-variable in most cases of nonlinear models. A discrete-time model can be obtained from any continuous-time system model through discretization.

The occasional case is when one or several elements in the state vector X(k) are needed, but not measurable. These elements can estimate X(k) using the output signal y(k). As long as ω(k) and v(k) obey the white and Gaussian noise distribution law, the Kalman filter is the optimal estimator of X(k). The optimal estimator $\hat{x}(k+1)$ is

$$\hat{x}(k+1) = F_k \hat{x}(k) + B_k u(k) + K_k[y(k) - H_k \hat{x}(k)] \tag{5·3}$$

$$K_k = F_k P_k H_k^T (H_k P_k H_k^T + R_{2k})^{-1} \tag{5·4}$$

$$P_{k+1} = F_k P_k F_k^T + R_{1,k} - F_k P_k H_k^T \times (H_k P_k H_k^T + R_{2,k})^{-1} H_k P_k F_k^T \tag{5·5}$$

The right side of equation (5·3) is regarded as the estimation, which is corrected by the feedback item including new measured data: $K_k\varepsilon_k$, $\varepsilon_k = y(k) - H_k\hat{x}(k)$.

The error signal ε_k is described as the innovation item in Chapter 4. The covariance equation (5·5) is considered as the "Riccati" differential equation (RDE). K_k is the Kalman gain, $R_{1,k}$ is the time-varying noise covariance matrix of system noise ω(k) and $R_{2,k}$ is the time-varying noise covariance matrix of measured noise v(k). $R_{1,k} = E\{\omega(k)\omega^T(k)\}$, $R_{2,k} = E\{\upsilon(k)\upsilon^T(k)\}$. In practice, the noise level is unknown. The noise covariance matrix is $R_{1,k}$, and $R_{2,k}$ are therefore treated as tuning parameters, but not from the actual measurement for the noise level. They are chosen to be the diagonal and constant. By trial-and-error, R_1 and R_2 are adjusted until the filter performs satisfactorily.

It is always suggested that the Kalman filter only works when the disturbances ω(k) and v(k) are white and stochastic. On the contrary, the Kalman filter is reported to be used for a variety of different disturbance characteristics [5·1]. If the disturbance is not white noise and Gaussian, the Kalman estimator is only sub-optimal and a sub-optimal value for K_k results in a smaller square variance. Furthermore, it is possible to model the disturbance through expanding the state-space model, so that it can be used for restraining its existence in the estimated state vector.

5.2.1 The Time-invariant Kalman Filter or Linear Kalman Filter

If we deal with the time-invariant system, the matrices F, G, H, R_1 and R_2 are constant. The Riccati Differential Equation (RDE) (5·5) shows that P_{k+1} can converge to the steady value

$$\bar{P} = F\bar{P}F^T + R_1 - F\bar{P}H^T(H\bar{P}H^T + R_2)^{-1}H\bar{P}F^T \qquad (5\cdot6)$$

Equation (5·6) is called the Algebraic Riccati Equation (ARE). The constant or linear Kalman gain is

$$\bar{K} = F\bar{P}H^T(H\bar{P}H^T + R_2)^{-1} \qquad (5\cdot7)$$

5.2.2 Extended Kalman Filter

Kalman filter theory can be extended to be applied in a non-linear system such as equations (4·11) and (4·12) in Chapter 4. This is shown in

$$X(k+1) = f(X(k),k) + g(u(k),k) + \omega(k) \tag{5·8}$$

$$y(k) = H(X(k),k) + \upsilon(k) \tag{5·9}$$

in each case, the EKF is used to estimate X(k). The EKF is given by the following equation (the same as (4·10) in Chapter 4)

$$\hat{X}(k+1) = f(\hat{X}(k),k) + g(u(k),k) + K_k[y(k) - h(\hat{X}(k),k)] \tag{5·10}$$

Kalman gain is still determined by the Riccati Differential Equation (RDE). Meanwhile, the system matrices are obtained through the linearization of the functions f, g and H as in equations (4·16), (4·17), (4·18), and (4·19) in Chapter 4.

$$F_k = \left.\frac{\partial f(x,k)}{\partial x}\right|_{x=\hat{x}(k)} \tag{5·11}$$

$$G_k = \left.\frac{\partial g(u,k)}{\partial u}\right|_{u=u(k)} \tag{5·12}$$

$$H_k = \left.\frac{\partial h(x,k)}{\partial x}\right|_{x=\hat{x}(k)} \tag{5·13}$$

5.2.3 Speed Estimation by the Kalman Filter

There is a special linear speed-position-noise model for the rotor position θ(k) and velocity ω_r(k) as with the following equations

$$\theta(k+1) = \theta(k) + T\omega_r(k) \tag{5·14}$$

$$\omega_r(k+1) = \omega_r(k) + \omega'(k) \tag{5·15}$$

$$\omega'(k+1) = \omega'(k) + \omega(k) \tag{5·16}$$

Where T is the sample cycle and ω(k) the white noise with zero mean value. If the rotor speed can be modelled as the double integration of noise ω(k), then the ramp speed changes can predicted and hence the Kalman filter can be instructed to trace the ramps. If the ω_r(k) is modelled as a single integration of the noise, the Kalman filter is instructed to expect a constant speed, which consequently causes transient lagging of the speed estimation.

The flux linkage produced by a permanent magnet in the stationary coordination axis can be expressed as components including the functions $[\psi_\beta, \psi_\alpha]^T$ of sine and cosine as

$$\begin{bmatrix}\psi_\beta \\ \psi_\partial\end{bmatrix}=\begin{bmatrix}\psi\cos\theta(k) \\ \psi\sin\theta(k)\end{bmatrix} \tag{5·17}$$

If we use the flux linkage vector $[\psi_\beta,\psi_\alpha]^T$ to take over the output vector $y=[y_1,y_2]$ in (5·18), the output equation is

$$\begin{bmatrix}y_1 \\ y_2\end{bmatrix}=\begin{bmatrix}\cos\theta \\ \sin\theta\end{bmatrix}+\begin{bmatrix}\upsilon_1 \\ \upsilon_2\end{bmatrix} \tag{5·18}$$

If we choose the state vector $x=[\theta,\omega,\omega']^T$, we obtain the following low order state model in which u(k)=0

$$X(k+1)=FX(k)+\omega(k) \tag{5·19}$$

$$Y(k)=H(X(k))+\nu(k) \tag{5·20}$$

In which

$$F=\begin{pmatrix}1 & T & 0\\ 0 & 1 & 1\\ 0 & 0 & 1\end{pmatrix} \tag{5·21}$$

$$H(X(k))=\begin{pmatrix}\cos\theta \\ \sin\theta\end{pmatrix} \tag{5·22}$$

$$R_1=\begin{pmatrix}0 & 0 & 0\\ 0 & 0 & 0\\ 0 & 0 & 1\end{pmatrix} \tag{5·23}$$

$$R_2=\lambda I=\lambda\begin{pmatrix}1 & 0\\ 0 & 1\end{pmatrix} \tag{5·24}$$

I: 2×2 unit matrix;

λ: tuning parameters, the noise eliminating function of the filter can be adjusted through tuning λ. The process noise variance R1 is chosen as 1; the actual variance is unknown. If EKF is used to estimate X(k), according to equation (5·13) H_k is written as

$$H_k=\left.\frac{\partial h(X,k)}{\partial X}\right|_{X=\hat{X}(k)}=\begin{pmatrix}-\sin(\hat{\theta}(k)) & 0 & 0\\ \cos(\hat{\theta}(k)) & 0 & 0\end{pmatrix} \tag{5·25}$$

However, H_k can be transformed into the following form

$$H_k=T^T(\hat{\theta}(k))\begin{pmatrix}0 & 0 & 0\\ 1 & 0 & 0\end{pmatrix} \tag{5·26}$$

where T(θ)=$T^T(\hat{\theta}(k))$ is the d-q convert matrix in

$$T(\theta)=\begin{pmatrix}\cos\theta & \sin\theta\\ -\sin\theta & \cos\theta\end{pmatrix} \tag{5·27}$$

The matrix in equation (5·27) is orthogonal, which means that

$$T^{\tau}(\theta)T(\theta)=I \tag{5·28}$$

It should be noted that if T_k is used for the appropriate expression $T^T(\hat{\theta}(k))$, the Riccati differential equation (RDE) (equation (5·5)) can be rewritten as

$$\begin{aligned}P_{k+1} &= FP_kF^{\tau}+R_1-FP_kH^{\tau}T_k\times(T_k^{\tau}HP_kH^{\tau}T_k+R_2)^{-1}T_k^{\tau}HP_kF^{\tau}\\ &= FP_kF^{\tau}+R_1-FP_kH^{\tau}\underline{T_k\times T_k^{\tau}}(HP_kH^{\tau}+R_2)^{-1}\underline{T_kT_k^{\tau}}HP_kF^{\tau}\\ &= FP_kF^{\tau}+R_1-FP_kH^{\tau}\times(HP_kH^{\tau}+R_2)^{-1}HP_kF^{\tau}\end{aligned} \tag{5·29}$$

Therefore, all the existing items including the converting matrix T_k disappear and the time-varying Riccati Differential Equation is left. P_k will converge to the steady-state variance $\overline{P}$ given by equation (5·6). The time-invariant variance $\overline{P}$ can be computed only once, for example, it can be implemented using the instruction DLQE in "MATLAB", this implies that a large computation time can be saved. The Kalman gain is still time-varying, however, it can be computed as

$$\begin{aligned}K_k &= F\overline{P}H^{\tau}T_k(T_k^{\tau}H\overline{P}H^{\tau}T_k+R_2)^{-1}\\ &= \underbrace{F\overline{P}H^{\tau}(H\overline{P}H+R_2)^{-1}}_{\overline{K}}T_k\end{aligned} \tag{5·30}$$

The Kalman gain is the result of the time-varying section $\overline{K}$ and T_k, since all the elements in the 1st line and column of the matrix H are zero. $\overline{K}$ can be written as

$$\overline{K}=\begin{pmatrix}0 & k_1\\ 0 & k_2\\ 0 & k_3\end{pmatrix} \tag{5·31}$$

where the constants k_1,k_2 and k_3 can be computed in advance during the filter design.

In summary, the algorithm of linear Kalman filter can be explicitly expressed as

$$\varepsilon(k)=y_2(k)\cos\hat{\theta}(k)-y_1(k)\sin\hat{\theta}(k) \tag{5·32}$$

$$\hat{\theta}(k+1)=[\hat{\theta}(k)+T\hat{\omega}_k(k)+k_1\varepsilon(k)]_{-\pi}^{\pi} \tag{5·33}$$

$$\hat{\omega}_r(k+1)=\hat{\omega}_r(k)+\omega'(k)+k_2\varepsilon(k) \tag{5·34}$$

$$\omega'(k+1)=\omega'(k)+k_3\varepsilon(k) \tag{5·35}$$

where $[\bullet]_{-\pi}^{\pi}$ implies that the estimated position is limited between [-π, π]. For equations (5·32) to (5·35), this algorithm requires only 6 multiplies: two for each of (5·32) and (5·33) and one for each of (5·34) and (5·35). Two trigonometric operations may also be required and executed by the look-up method for the control programme.

5.2.4 Block diagram of Linear Kalman Filter

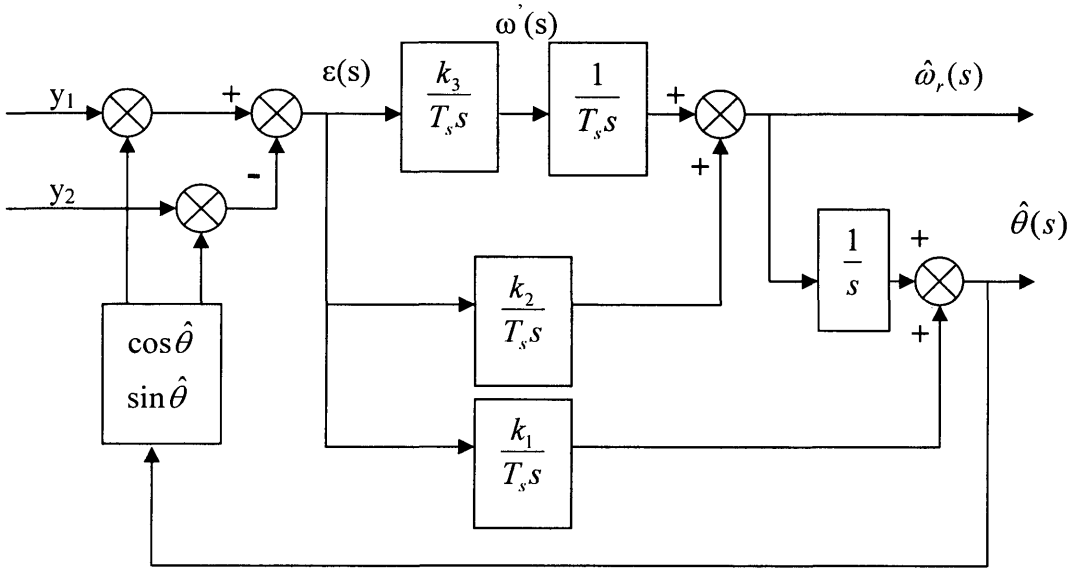

Fig. 5·1 Block diagram for the linear Kalman filter

Equations 5·32~5·35 can be expressed in the frequency domain in fig. 5·1. The Laplacian diagram reveals that the LKF consists of the feedback to the input y_1 y_2 and feeds forward to the output ω'(s). Several integral links amplify the compensated error ε(s) to yield for the output $\omega_r(s)$ and θ(s). Fig. 5·1 shows how a loop filter such as the LKF essentially takes the same role as the state observer such as the EKF.

5.3 Simulation

The linear or time-invariant Kalman filter model shown in equations (5·6~5·7) may be solved through the "DLQE" command of "MATLAB" version 4.2~6.0 which refers to discrete linear quadratic estimator design. Its syntax is

[K, P, Z, λ]=DLQE[F, E, H, Q, R], where

$P=E[x_{k|k-1}-x_k][x_{k|k-1}-x_k]^T$, the prediction error covariance matrix;

$Z=E[x_{k|k}-x_k][\ x_{k|k}-x_k]^T$, the filter error covariance matrix;

E: unit diagonal matrix n×n;

$Q: E[\omega][\omega]^T$, the system noise covariance matrix;

$R: E[v][v]^T$, the measured noise covariance matrix

λ yields to the LKF observer eigenvalue;

K is the LKF observer gain. The "DLQE" command returns the Kalman gain $K= FPH^T(HPH^T + R_2)^{-1}$ shown in equation (5·7). System and measurement noise covariance Q and R are replaced by R1 and R2 in (5·23) and (5·24). H is replaced by

$H=\begin{pmatrix}0 & 0 & 0\\ 1 & 0 & 0\end{pmatrix}$, T= 0.5e^{-4} s, F is also replaced by $F=\begin{pmatrix}1 & T & 0\\ 0 & 1 & 1\\ 0 & 0 & 1\end{pmatrix}$

After trial-and-error, λ=5000 was found to give acceptable balance between trace and noise suppression. The elements from the matrix $\overline{K}$ are secured as:

K_1=0.2243; K_2=0.2245; K_3=0.0126

5.4 Experiment results and analysis

5.4.1 Shaft Position Estimation Characteristics

The presented Linear Kalman Filter algorithm was employed to implement sensorless control of the 600 w, 6-pole PMSM. The same control development platform was adopted as with the implementation of the Flux-linkage observer in Chapter 3, the Extended Kalman Filter in Chapter 4 and the "TI TMS320C31" DSP parallel-bus system described in Chapter 2.

The load environment was set up as described in Chapters 3 and 4. The DC shunt generator was coupled and linked with the PMSM equivalent to a load of 1 Nm. The rotor position value was extracted by the parallel bus from the shaft-mounted 2048 ppt encoder via the "USdigital" pulse-to-binary-converter encounter. The Linear Kalman Filter observer is embedded into the 3-phase current hysteresis PWM vector control system described in Chapter 3 replacing the Flux-Linkage observer and EKF observer. The estimated speed from LKF observer is delivered to the speed PI regulator.

Fig. 5·2 shows the true rotor position estimation compared with the actual value including the error trend line in the full electrical cycle. The most obvious feature is the remarkably low error between the measured and real rotor positions.

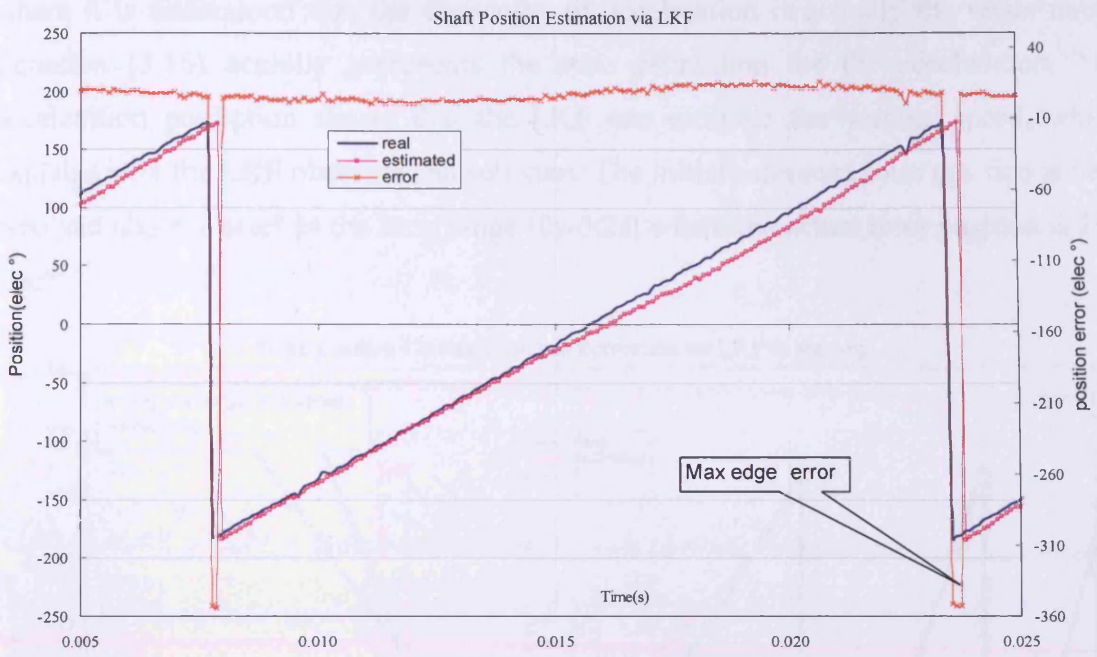

Fig. 5·2 Shaft position estimation comparison characteristics per cycle via LKF

The estimation position in the range [-180 elec°, 0 elec°] is almost aligned with the actual rotor position. Even if the position estimation error starts to increase from 0 elec° to 180 elec°, the magnitude of the error characteristic is less than that of the Flux-linkage observer shown in fig. 3·18 and that of EKF shown in fig. 4·9. This shows that the LKF based on the FLO and EKF has a surprisingly high estimation precision.

The specific constant Kalman feedback corrective matrix in equation (5·13) comes from the 3-order linear position-speed model defining a double integration of the noise as the rotor speed in (5·14)-(5·16). The output traced stationary flux linkage ψ_α and ψ_β in (5·18), which has been already corrected by the low pass filter for integration in (3·29), is used to feed this linear position-speed model to form the Linear Kalman feedback matrices. The essence of the Linear Kalman filter is the double correction including the low pass filter for the flux-linkage output and the EKF covariance correction for the position/speed.

5.4.2 Shaft position tracing and speed in the start-up characteristics

Fig. 5·3 shows that the proposed LKF sensorless control PMSM is able to self start. It is understandable for the LKF state-observer to predict the angular velocity from the position-speed-noise vector in equation (5·15). Incorrect convergence and the prompt correction in fig. 5·3 proves that the LKF can predict the ramp speed change. Equation (5·16) can be used to model the rotor speed as a double integration of the noise $\omega(k)$,

where it is understood that the derivative of acceleration is actually the white noise. Equation (5·16) actually represents the state estimation for the acceleration. The acceleration prediction shows that the LKF can estimate the varying speed, which explains why the LKF observer can self start. The initial estimated rotor position is near zero and about 7 elec° in the time range [0s-0.2s] where the actual rotor position is 130 elec°.

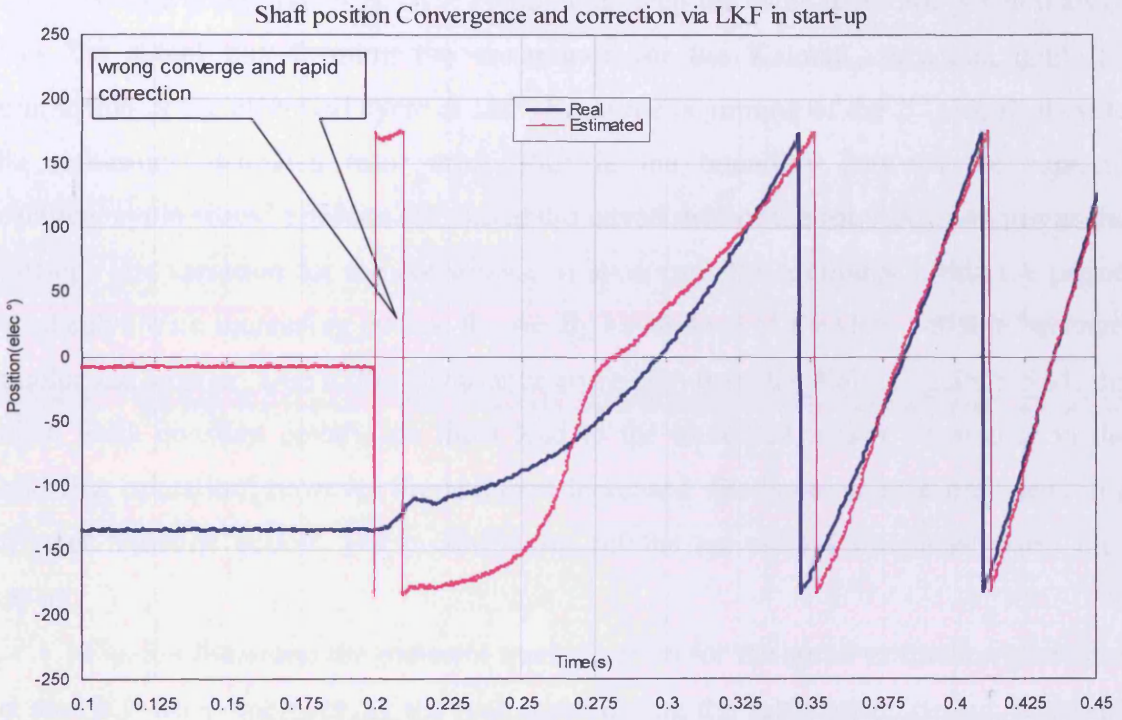

Fig. 5·3 The shaft position estimation and correction during the self-start-up progress

Under the standstill conditions at start-up, the proposed DSP control system initially calculates the stationary flux linkage $\psi_{\alpha,\beta}$, then $\hat{\theta}_1$, $\hat{\omega}_1$ and $\omega_0^{'}$ are computed from equations (5·36), (5·37) and (5·38) with initial constant Kalman gain k_1, k_2 and k_3 plus initials $\hat{\theta}_0$=0, $\hat{\omega}_0$=0, $\omega_0^{'}=0$. Initial covariance from (5·35) comes from the bias between the estimated and actual flux linkage. The Constant Kalman corrective gain makes this bias compensate for the state variables θ, ω and ω'. At the instant [0.2s] and nearby, the initial corrective angle magnitude is up to ±180 elec° until the covariance of the output (flux linkage is apparently decreasing) which is shown at the instances 0.2s and 0.22s in fig. 5·3. Between 0.22 s and 0.27 s the covariance characteristics of the flux linkage tends to decrease until the instant 0.27 s when the covariance of the rotor position decreases to zero. Afterwards, the constant Kalman gain continues tuning via

the covariance of the state variable. Such over-tuning propels the position aligned with the actual value away from the actual position curve from the instant 0.27 s until the maximum covariance of rotor position was generated at the instant 0.28 s. Thereafter, the estimated rotor position with bias makes the flux linkage take remedial action for the state variable until the instant 0.34 s when the estimated rotor position is equal to actual one for the second time.

Such a corrective effect will continue to keep the estimated rotor position away from the actual one forming the covariance for the Kalman correction until the termination of the electrical cycle at 180°. From the beginning of the 2^{nd} electrical cycle, the maximum estimated rotor error 360° in the boundary between the adjacent electrical cycle would produce the maximum covariance of the rotor position just as the start-up. The variation for the covariance of state variable continues within the period repeatedly. With increasing cycles, the steady covariance of the state variable becomes smaller and smaller. Due to the covariance correction from the Kalman gain in 5.31, the initial weak constant covariance must lead to the increased steady covariance in the following operation; however the resultant increased steady covariance must lead to a stronger remedial action. These conflicting actions are always interlaced when they appear.

Fig. 5·4 illustrates the transient tracing period for the speed estimation generated by the LKF when approaching the real speed during the self start-up period, when the LKF-based sensorless controlled PMSM is coupled with the DC generator working in the no load mode. Both the armature and the field winding are open circuit so there is no electromagnetic braking torque generated in the shaft of the DC generator. The acceleration for the LKF method is almost constant as shown in fig. 5·4, the acceleration time is 0.6 s, compared with the acceleration time of 0.8 s via the EKF in fig.4·11 and the acceleration time of 0.7 s via the FLO in fig.3·19. The estimated speed by the LKF observer is the individual state variable and is independent of the estimated position. The shorter acceleration time infers that the LKF observer provide better speed response than the FLO or EKF observers.

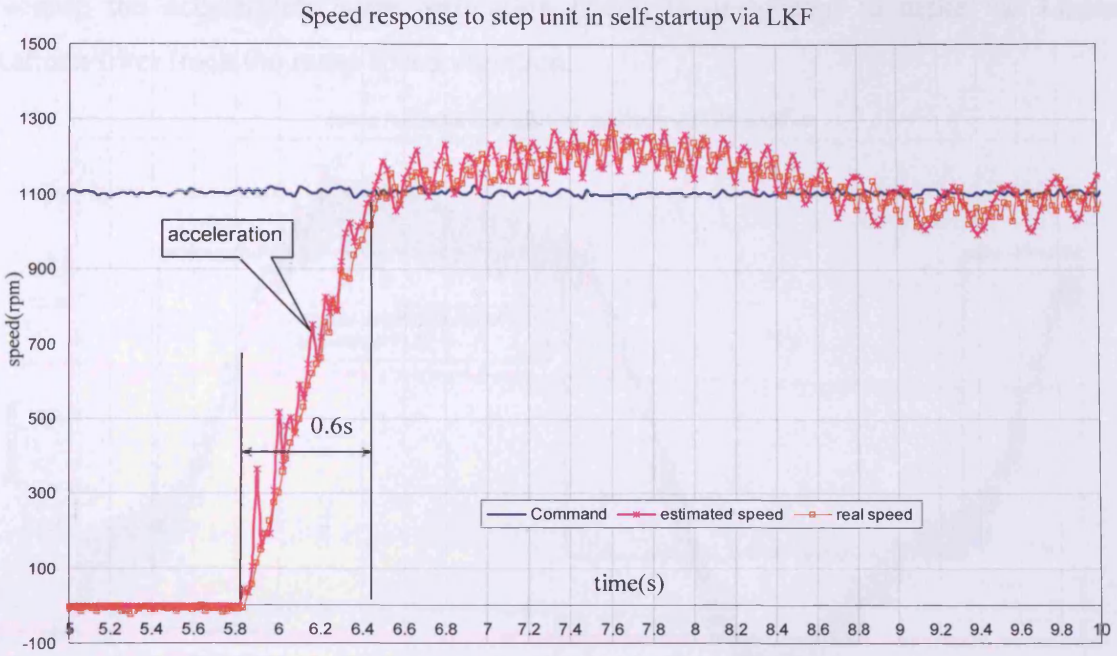

Fig. 5·4 Speed response to the step unit in the self-start-up via the LKF

5.4.3 Variable-speed ability

Figs.5·4 to 5·6 show the speed estimation and its characteristics respectively in the step unit, single-way and bipolar for the LKF sensorless controlled PMSM. The estimated speed is the state variable directly from state estimation in equation (5·34) of the LKF observer. The actual speed is calculated by the derivative on the actual rotor position measured by the shaft-mounted 2048 ppt encoder which is converted by the USdigital pulse-to-binary converter ENCOUNTER. The LKF observer is implemented in the same control platform as explained in Chapters 3 and 4: Float-point type "DSP TI TMS320C31-50Mhz-based SDK" parallel bus system, Analogue-to-Digital converter and Digital-to-Digital converter. The the measure torque in no load mode was about 0.8~1.1 Nm.

Fig. 5·4 shows the LKF-based sensorless control PMSM response to the 1100 rpm step unit reference during the self start-up period. The control structure is shown in fig. 3·10 with the LKF observer replacing the flux linkage observer. The estimated speed in the speed state estimation (5·34) from LKF observer was fed back to the input of the speed PI regulator which generated the torque current for the quadrature axis. Obviously the estimated speed via the LKF tends to accelerate at a constant value

because the acceleration state estimation (5·35) is designated to make the Linear Kalman filter track the ramp speed variation.

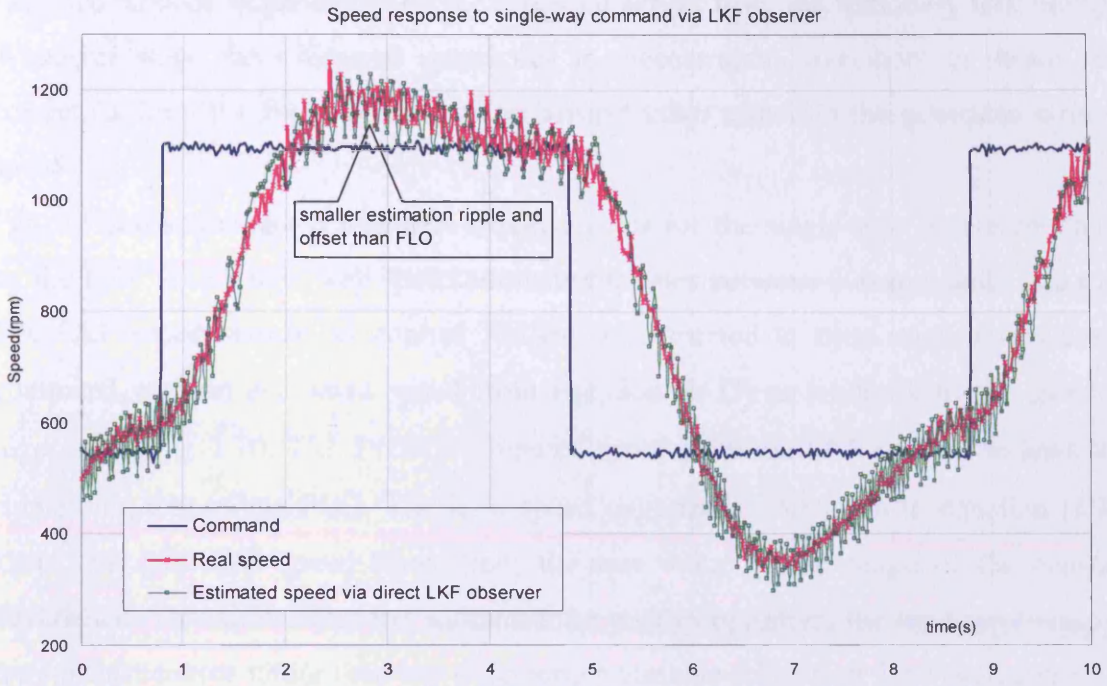

Fig. 5·5 Speed response to the single-way command via the LKF observer

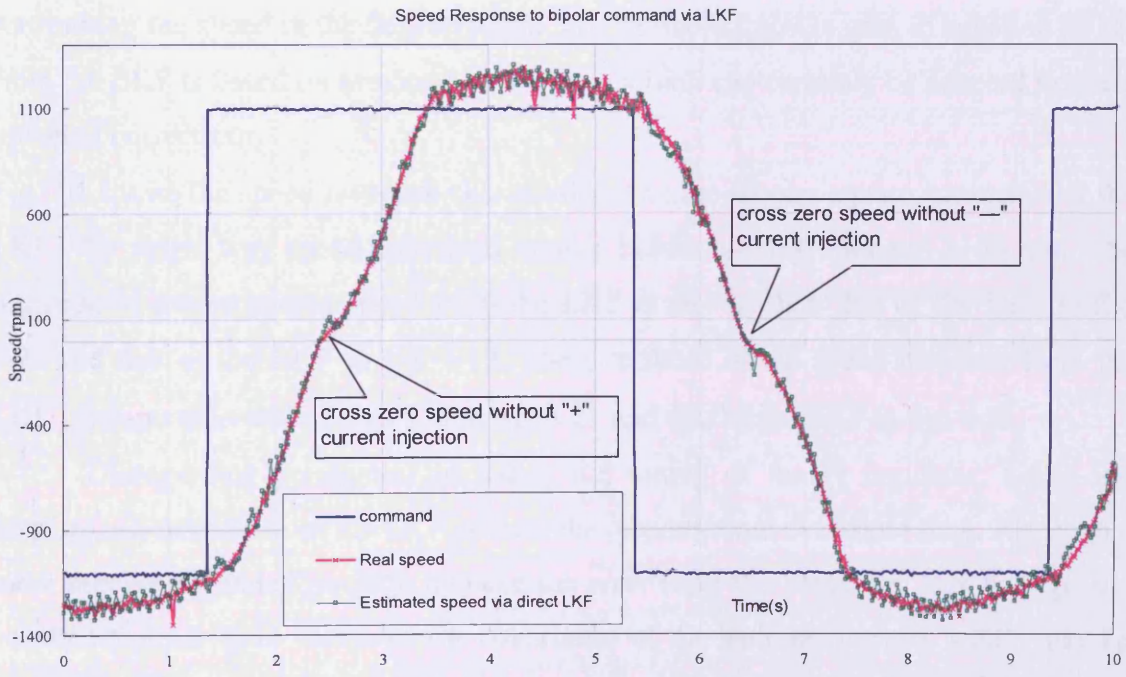

Fig. 5·6 Speed response to the bipolar command via the LKF

In fig. 4·11 the estimated speed locus from equation (5·34) via the LKF observer traces the true speed track with the hysteresis covariance, proved that the speed covariance is generated by the remedial action from the stationary flux linkage. Whatever stage the estimated speed lies in, acceleration, overshoot or steady, the correction from the linear Kalman filter always takes effect on the generated error of speed.

Fig. 5·5 shows the speed response characteristics for the single-way square command by the LKF. The single way speed command toggles between 500 rpm and 1100 rpm. The LKF-based sensorless control PMSM is instructed to trace such a single-way command with an estimated speed from equation (5·35) as feedback to the speed PI regulator in fig. 3·10. The directly estimated speed from the LKF appears to have less ripple than that of the FLO. The least speed covariance correction in equation (5·35) keeps the estimated speed away from the true value in the range of the constant covariance. This shows that the Kalman filter always optimises the least covariance of the stochastic error rather than any other single variable correction. However, compared with the estimated speed of the EKF in fig. 4·12, the estimated speed via the LKF illustrated a greater magnitude of the speed covariance for the hysteresis correction.

The greater magnitude of the covariance in the LKF could be due to the fact that the constant Kalman gain in equation (5·31) hardly makes a more precise covariance for limiting the speed in the desired range. The variable Kalman gain in equation (4·34) from the EKF is based on previous covariance, which can certainly be adapted to make updating corrections.

Fig. 5·6 shows the speed response characteristics to the bipolar square command by the LKF. The single way speed command toggles between -1100 rpm and 1100 rpm. The response of the estimated speed from the LKF is slower than that of the FLO in fig. 3·21 and that of the EKF in fig. 4·13. The overshoot of the speed response from the LKF is longer than that of the FLO in fig. 3·21 and that of the EKF in fig. 4·13.

Disregarding parameters including the tuning of the PI regulator, speed and position estimations from the LKF, affects the response and overshoot time. Although a more precise estimated position reduced the error from the corrective flux linkage, the constant Kalman gain increases the covariance of the estimated speed, which may be used to explain the slow overshoot and the response transient time. The double integration of the noise $\omega'(t)$ in equation (5·16) was designated to supposedly track the ramp speed, and not ramp speed with inflexion. Such double integration of the noise

$\omega'(t)$ is the direct reason for the straight ramp accelerating speed in fig. 5·6. On the contrary, the derivative of the estimated position increment via the FLO in fig. 3·21 probably made more ripple in the estimated speed, however, the derivative for the speed estimation could track not only ramp but also the inflexion.

The 4-order EKF observer in equations (4·33) and (4·34) define the real speed covariance as the speed variation; these may be corrected indirectly through correction for the stationary current covariance. At every step the variable Kalman gain is computed and upgraded to optimise the least covariance of the 4 state variables. It is not hard to understand that the EKF observer could approach any real speed variation seen in fig. 4·13. No forced current injection is applied to avoid the speed delay from the rotor swing when the speed via the LKF observer crosses the zero value shown in fig.5·6. No rotor swing at zero speed implies that only a little error of the estimated position is generated at zero and low speed while the forced current injection is applied for an EKF observer at zero speed in fig.4·13. It proves that the invariant covariance position correction via the LKF performs better than the variant covariance correction via the EKF.

5.4.4 Estimated Position Tracking Ability Comparison:

Fig. 5·7 shows the estimated shaft position tracking characteristics during the "+" speed rising and zero-crossing, which corresponds to the rising speed slope in fig. 5·6. This illustrates that the estimated position is in advance of the real one in the cycle before the transient situation of the saddle-shape. In order to complete the speed rising zero-crossing, the electrical cycle terminal estimated by the LKF appears ahead of the real one in 25 elec° for the time-domain. The top of the saddle-shape in fig. 5·7 shows the transient progress: the estimated rotor position switches from -180 elec° to 180 elec°, and then drops to 120 elec°, afterwards it rises in reverse to 180 elec° where the estimated rotor estimation switches the second time from 180 elec° to -180 elec°. From this original switching point the estimated rotor position starts the 1st clockwise cycle.

Except for the switching point ±180 elec° and the nearby region, the maximum value of the rotor position occurred at two places: one is located where the speed is zero actually lying at the bottom of saddle-shape, and the other is located at the starting point of the first clockwise cycle. The error for the first point is at approximately 30 elec° while for the second it is approximately 50 elec°. The first maximum error could be understood as the zero speed generated the maximum position covariance in

equation (5·33), meanwhile the white noise and its double integration in equation (5·35) has dropped to the least value. In another respect, the maximum position covariance was used to remedy the stationary flux linkage in equation (5·18) generating the clockwise torque.

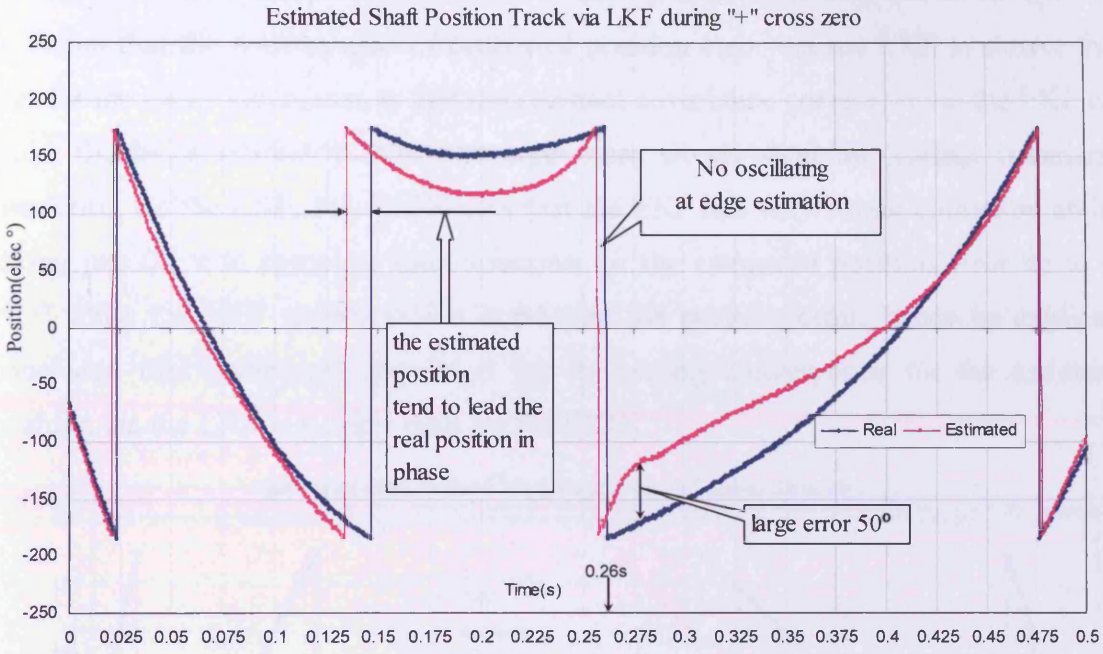

Fig. 5·7 Estimated shaft position track via LKF during the "+" speed crossing zero

The second maximum position error was generated by the estimated position switching from 180 elec° to -180 elec°. Such a 360 elec° position difference was inevitable for the lead stationary flux linkage to take too much correction. It is observed in fig. 5·7 that the starting speed boosts at the switching point for the 1st clockwise cycle. The correction from the LKF consequently decreases the speed after the estimated position passes the maximum error.

The remarkable point about the 2nd maximum position error is that there is no oscillating value of the estimated position at the edge/terminal ±180 elec° of the electrical cycle. Considering the oscillation with the FLO in fig.3·22 and no oscillation with the EKF in fig.4·15, it can be concluded that the covariance correction can avoid the wrong identification for the electrical cycle terminal precisely. Using the direct computation via the FLO it is not easy to overcome such error at low speed. This proves that the covariance correction technique can be effective in dealing with wrong identification at low speed. Meanwhile, it is noted that the large error of the estimated

position exists in the time domain [0.26, 0.4]s as shown in fig.5·7 when the PMSM starts-up from the negative terminal -180 elec° after the position switches from +180 elec° to -180 elec°.

The position error rises up to a maximum of 50 elec° in the time domain [0.26, 0.275]s and then it decreases in the time domain [0.275, 0.4]s both shown in fig.5·7. It is shown that the convergence of estimated position error via the LKF is slower than that for the EKF. The reason is that the constant covariance correction via the LKF can make the large estimated error converge more slowly than the variant covariance correction via the EKF. Fig.4·15 shows that the EKF has very strong correction ability taking just 0.1 s to complete the correction for the estimated position error up to 47 elec° while the LKF spends 0.14 s correcting the position error. It can be explicitly concluded that invariance correction for the wrong convergence for the estimated position via the LKF is weaker than for the EKF.

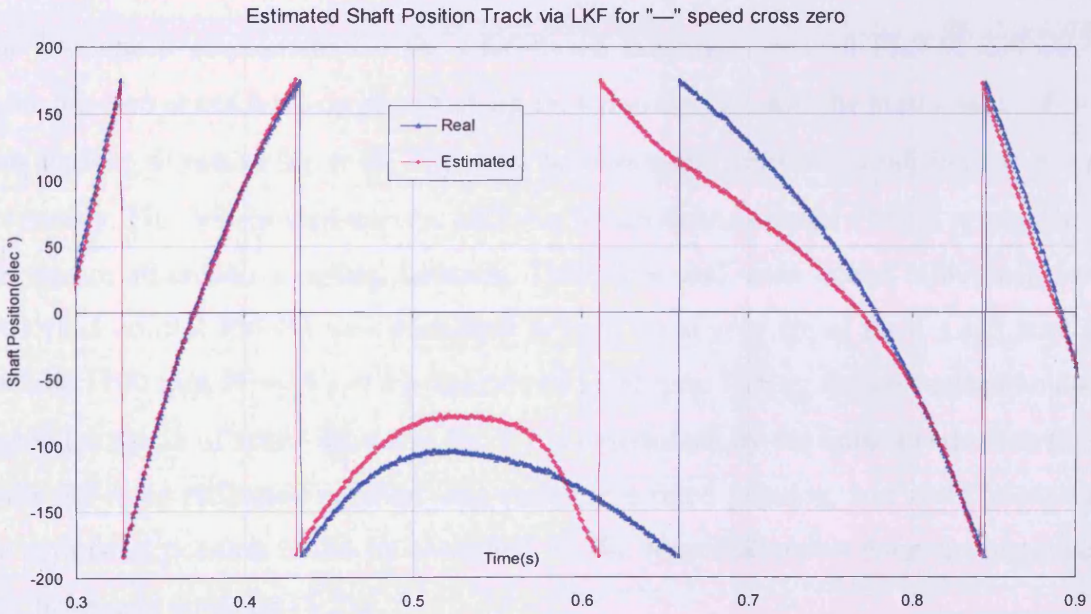

Fig. 5·8 Estimated shaft position track via the LKF for the "-" speed crossing zero

Fig. 5·8 shows the estimated shaft position tracking characteristics via the LKF for the "-" speed zero-crossing, which represents the speed falls from the "+" value to "-" value. The vaulting shape represents the estimated position generating the transient state transition when the speed switches from 1100 rpm to -1100 rpm as shown in fig. 5·6. It can be seen in fig. 5·8 that the estimated position via the LKF leads the actual rotor ahead of time before the speed changes from -1100 rpm and 1100 rpm.

The vaulting describes the estimated rotor position transformed into -90 elec° from -180 elec° in the course of the last clockwise rotation, thereafter transfers back into -180 elec° in the course of the 1st anticlockwise rotation. In order to follow the negative speed reference -1100 rpm, an approximate 90 elec° phase shift in time-domain is used to lead the estimated position transforming from -180 elec° to 180 elec°.

The 1st maximum estimated rotor error of 30 elec° occurred at the top of vaulting representing where the speed becomes zero. The 2nd maximum estimated rotor error occurred at -90 elec ° phase for the time-domain. The 1st reason for this is as explained earlier that the double integration for the noise is least for the maximum rotor position covariance to take the remedial action of the anticlockwise spinning. The 2nd reason is as mentioned earlier that the maximum rotor covariance generates the maximum remedy action to tune the stationary flux linkage.

5.4.5 Low speed performance:

The low speed assessment for the LKF-based sensorless control PMSM includes 2 parts: the zero speed hold-on plus start-up shown in fig. 5·9, and the least speed hold-on plus start-up shown in fig. 5·10. The other hardware and software conditions are the as previously. Fig. 5·9 showed that the LKF-based sensorless control PMSM responded to the square reference toggling between 1100 rpm and zero speed. Obviously, the sensorless control PMSM was instructed to hold on at zero speed for 4 s and start up towards 1100 rpm every 4 s at a cycle rate of 1100 rpm. During the zero-speed hold-on period the ripple of speed shown in fig. 5·9 is determined by the noise in equation (5·34) while the rotor estimated position was varied at a fixed position, and any variation of the estimated position could be corrected by the remedial action from the stationary flux linkage in equation (5·33).

Fig. 5·10 showed that the lowest speed for the LKF-based sensorless control was 70 rpm. The minimum speed correction magnitude in the LKF speed estimation equation (5·33) can reach only 70 rpm, which was indirectly decided by the magnitude of the flux linkage correction. The magnitude of the speed correction is actually determined by the voltage and current A/D sample decision and output frequency band of the DSP control system. The LKF-based sensorless controlled PMSM can acquire a lower minimum speed than that of the FLO. However this is still higher than that of the EKF. Here the variant Kalman gain feedback and covariance correction in the EKF is understood to adapt to the filter noise generated by low speed better than the constant

covariance correction in the Linear Kalman filter. From the point of correcting the flux linkage, the linear Kalman filter is applied successfully in adding the function of the covariance correction into the flux linkage observation.

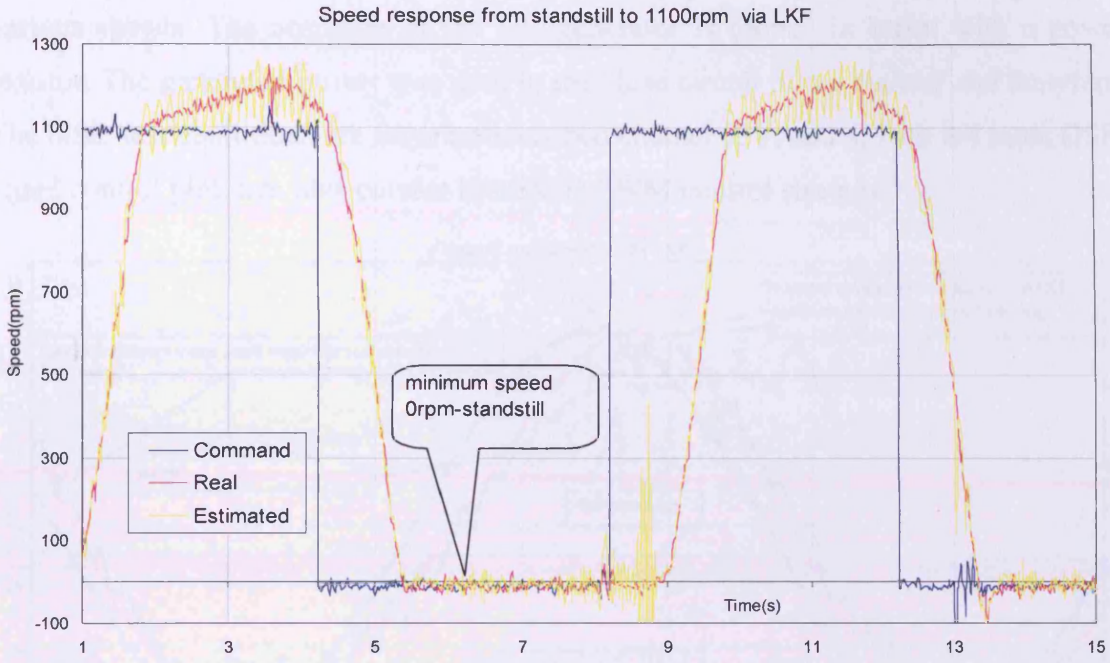

Fig. 5·9 Speed response from standstill to 1100 rpm via the LKF

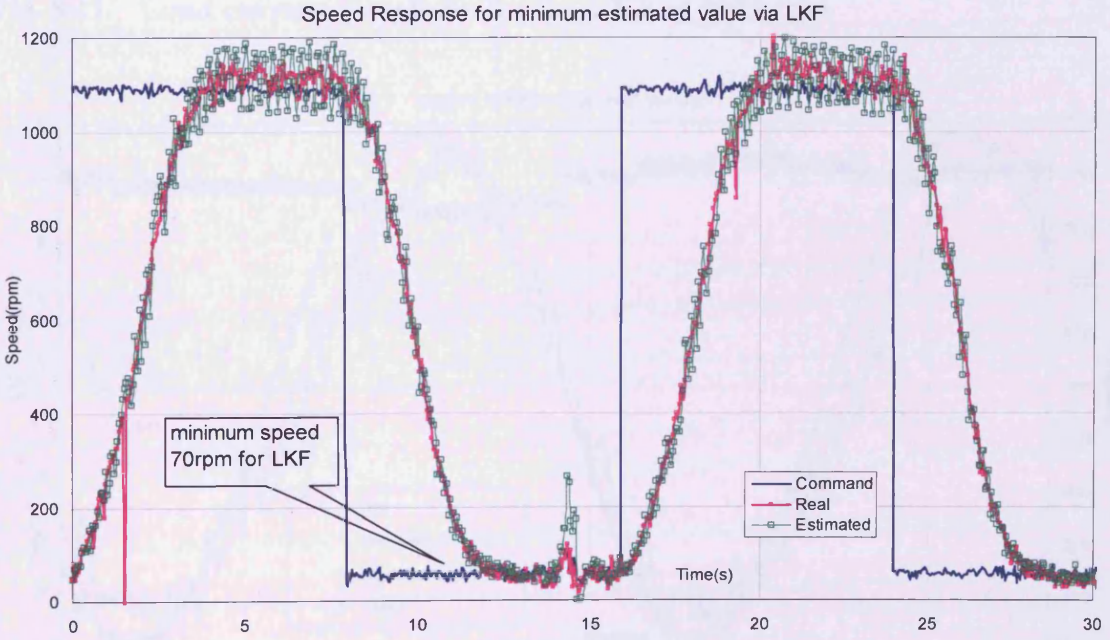

Fig. 5·10 The speed response for the minimum estimated value via the LKF

5.4.6 Load performance:

Fig. 5·11 to 5·19 show that the phase current waveform behaviour when the LKF-based sensorless PMSM was coupled with DC generator operated as a generator at various speeds. The armature of the DC generator is looped in series with a power resistor. The generated power was used in the close circuit of the resistor and armature. The other test conditions are same as described chapter 2, 3, and 4, with the same DSP-based control platform plus current hysteresis PWM control strategy.

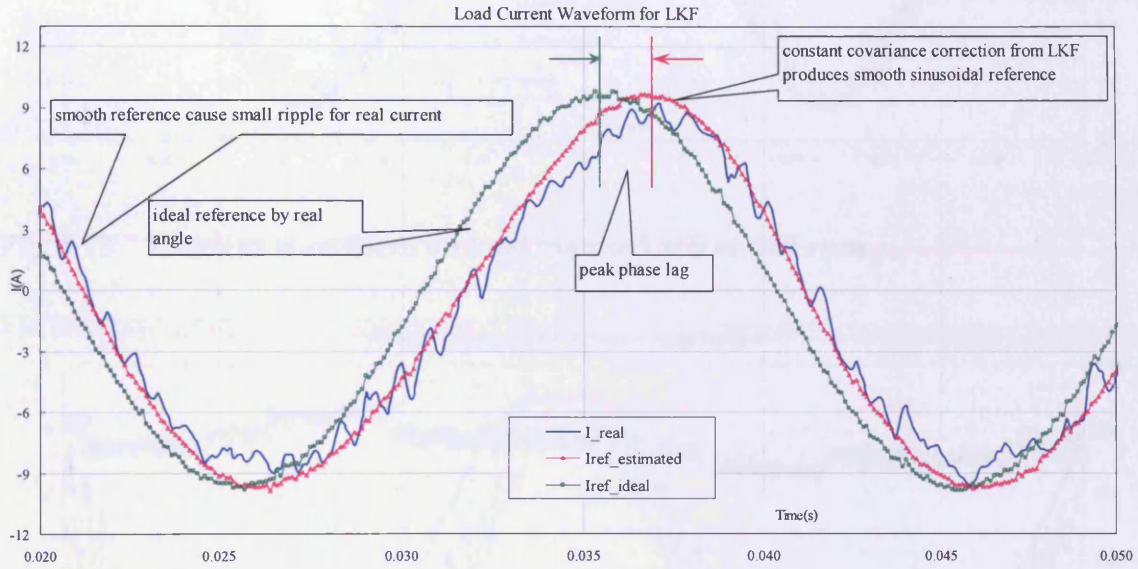

Fig. 5·11 Load current waveform for the LKF at 1000 rpm

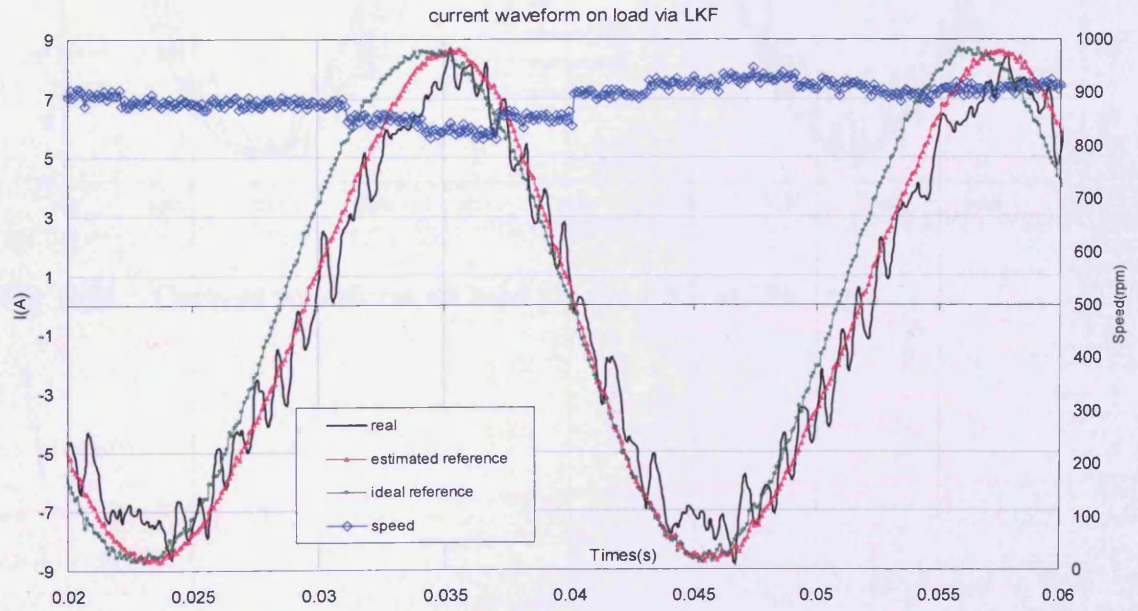

Fig. 5·12 Current waveform on load via the LKF at 900 rpm

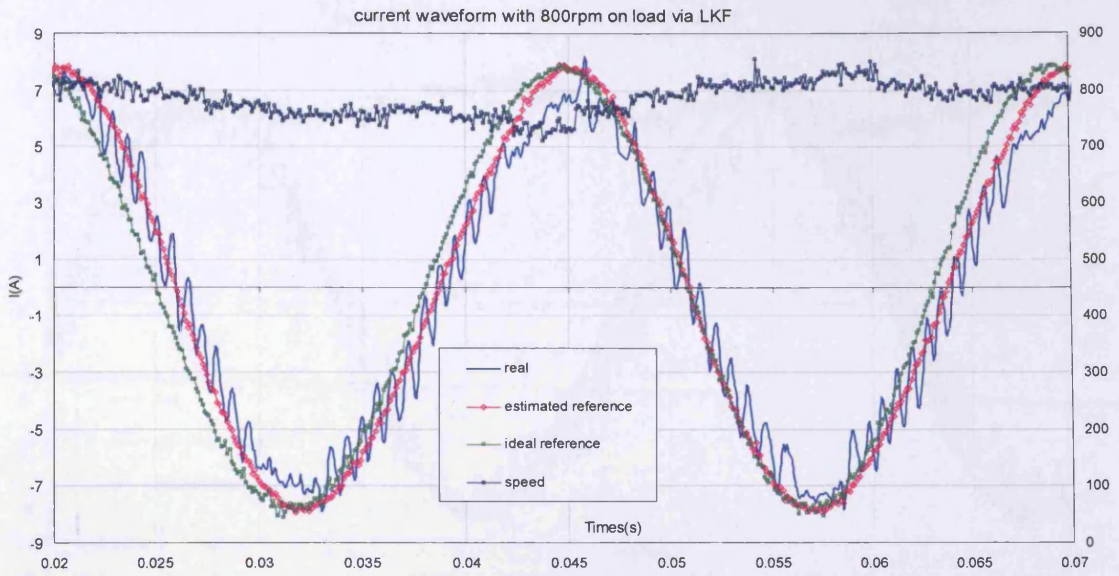

Fig. 5·13 Current waveform on load via the LKF at 800 rpm

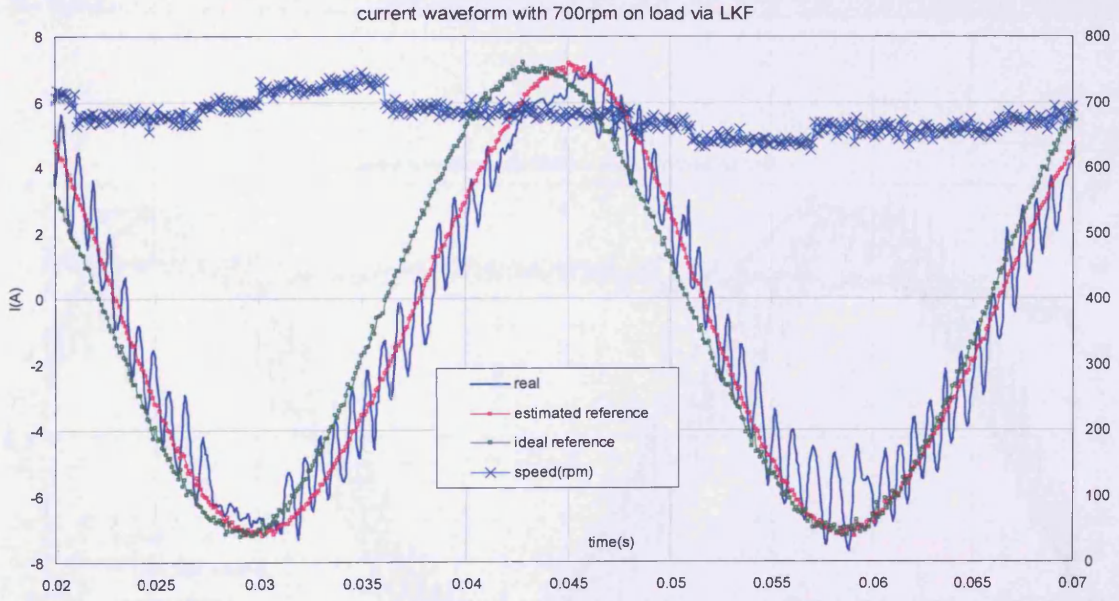

Fig. 5·14 Current waveform on load via the LKF at 700 rpm

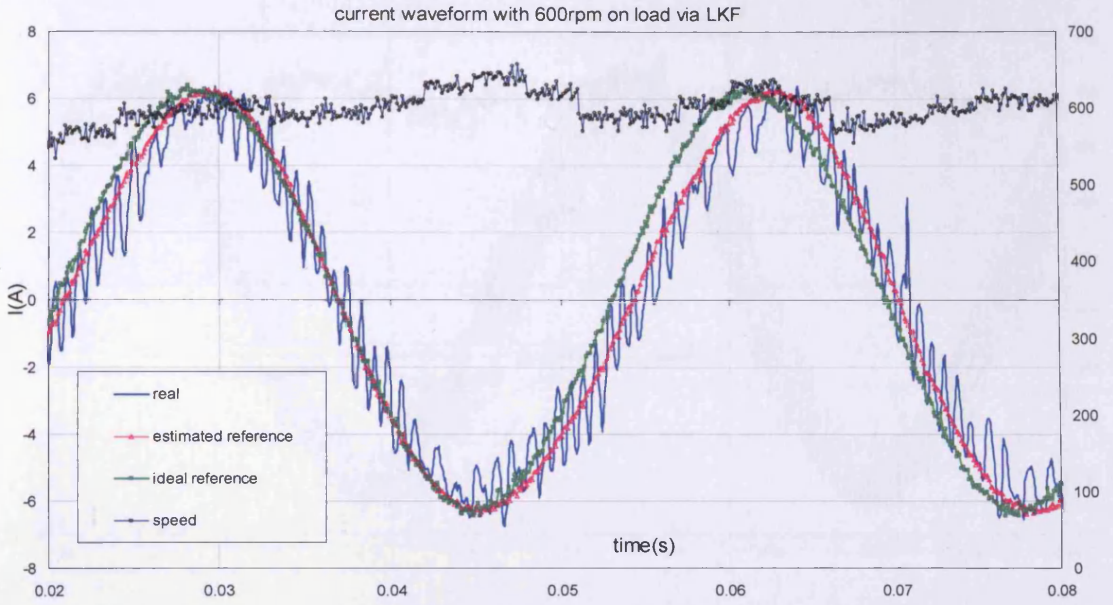

Fig. 5·15 Current waveform on load via the LKF at 600 rpm

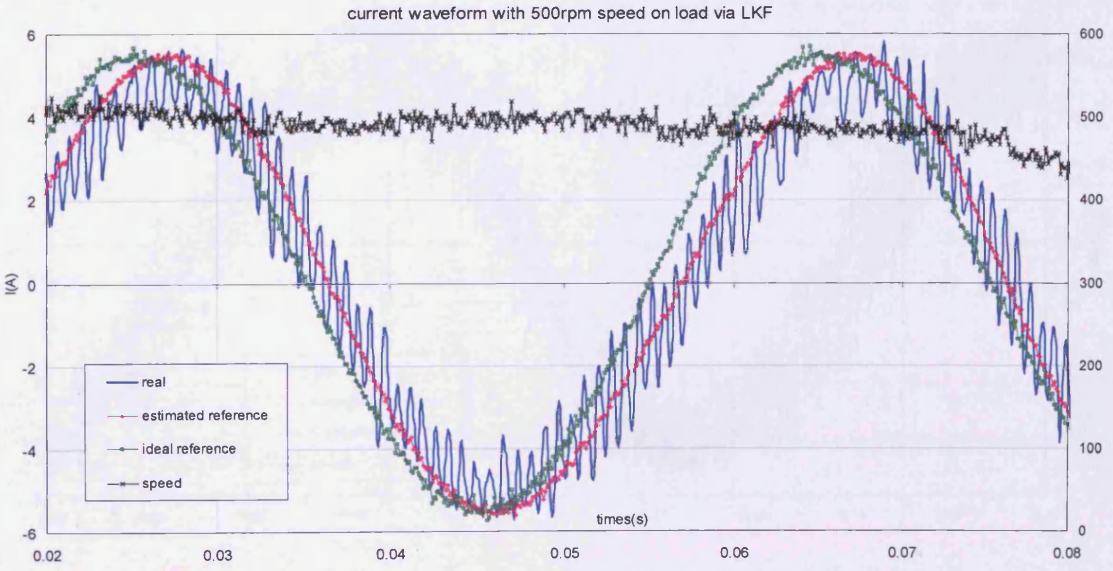

Fig. 5·16 Current waveform on load via the LKF at 500 rpm

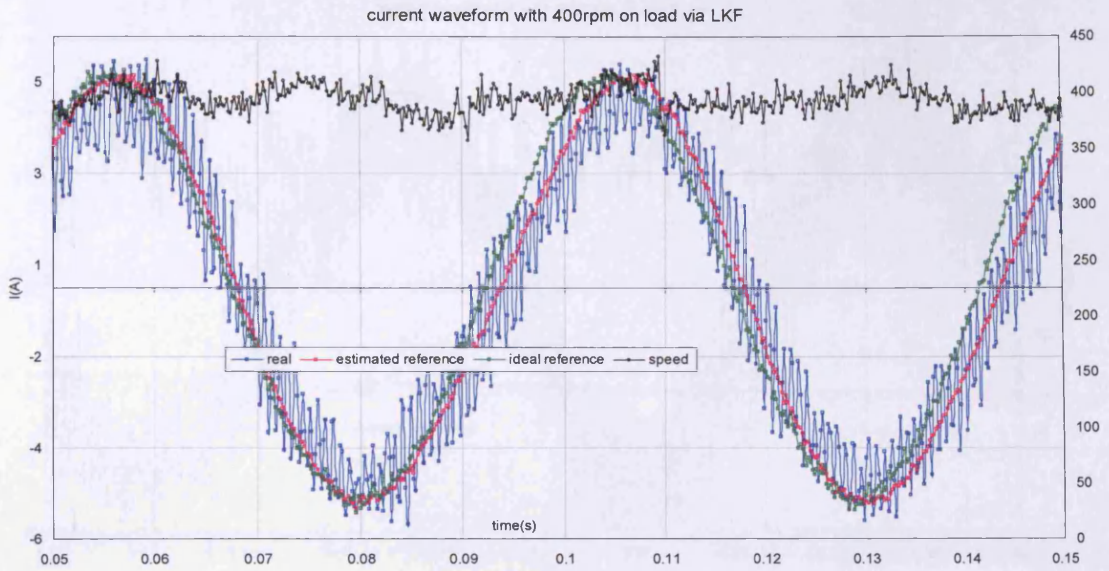

Fig. 5·17 Current waveform on load via the LKF at 400 rpm

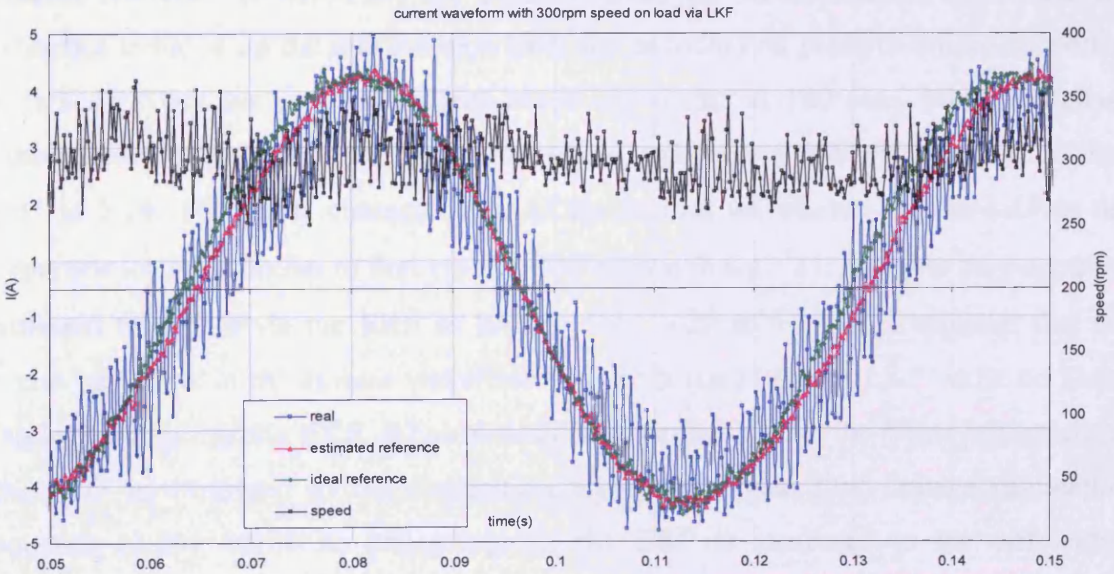

Fig. 5·18 Current waveform on load via the LKF at 300 rpm

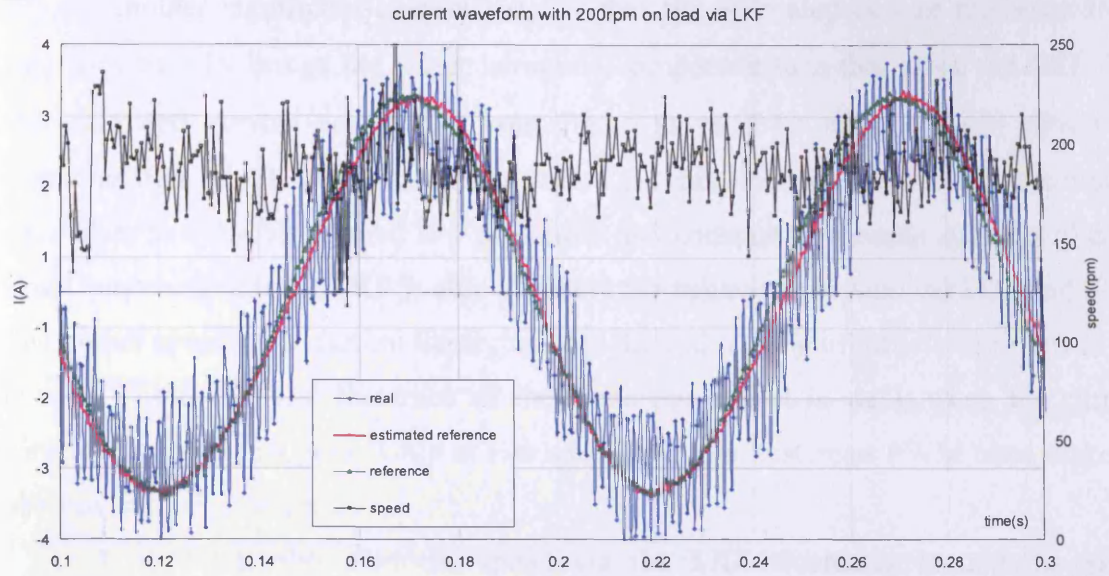

Fig. 5·19 Current waveform on load via the LKF at 200 rpm

In order to illustrate the actual current bias, figs. 5·11 to 5·19 used 3 curves in contrast to show the effect of covariance via the LKF sensorless observer: the estimated current reference is based on the position from the LKF, and the actual current reference is based on the real position from the encoder and pulse-to-binary-converter. It is shown that the greatest current phase lag occurs at 180 elec° when the phase current reaches peak value while the least phase lag occurs at 180 elec as shown in figs. 5·11 to 5·19. The phase characteristics of the current waveforms via the LKF in the generator load are similar to that via the FLO shown in fig.3·27, however they are quite different from that via the EKF as seen in Figs. 4·22 to 4·29. It is apparent that the phase lag exists in the current waveforms via both the FLO and LKF while no phase lag is found in that via EKF. It has already been explained that the phase lag issued by the FLO is attributed to the integration algorithm in the flux linkage calculation equation (3.29), while no phase lag via the EKF is attributed to the differential recursive algorithm in equations (4.33) and (4.34).

The LKF is a Kalman filter state estimation method based on the differential algorithm in the equations (5.32 to 5.35), but trigonometric functions in the output related equation (5.32) are replaced by the flux linkage as equation (5.17) indicated in the implementation procedure. The flux linkage calculation is still reliant on the integration algorithm so the flux linkage calculation in equation (5.17) brings the phase lag into the resultant phase characteristics of the current waveform via the LKF.

Another significant characteristic is that the estimated current reference from figs. 5·11 to 5·19 brings the fewer harmonic component than that using the EKF. All the estimated current references from fig. 5·11 to 5·19 show smooth sinusoidal characteristics. The LKF observer is based on the flux linkage estimation first, which is equivalent to a double filtered low pass filter and constant covariance Kalman filter. It is not surprising that the LKF is able to secure the behaviour beyond the FLO and EKF. The higher speed peak current hardly reaches the estimated current reference due to the greatest phase lag, and the trace of the hysteresis PWM is weak when the current waveform reaches its peak. Only at low speed does the hysteresis PWM trace make an obvious adjusting effect.

It is remarkable that the speed via the LKF fluctuates around the given command shown in figs. 5·12 to 5·19. The LKF observer uses invariant covariance to correct the errors for the state variables, the invariant covariance correction via the LKF is slower than the variance correction via the EKF if the amplitude of the estimated error is large, so it takes a while for the LKF to correct the speed error. It shows that invariant covariance correction via the LKF is weaker than the EKF to make the large estimated error converge rapidly.

It is also noted that more ripples are found in the actual current waveform at low speed than at high speed. As the DSP-based field oriented PWM control strategy used the hystersis-band current PWM with the fixed frequency of 20 MHz, the higher the speed, the smaller the electrical cycle. The period of the 20 MHz switching frequency is 50us and is much smaller than the period of the phase current. For example, when the speed is 300 rpm as shown in fig.5·18, the period of the phase current is 30 ms, so 300 chopped pulses are generated during the electrical cycle period.

5.4.7 Load Disturbance Performance:

Fig.5·20~5·21 shows the speed ω and quadrant current Iq response to a step variation of the load torque which is reflected by the quadrant current reference Iq_ref. The lower of the two curves in fig.5·20 is the response of the normalised quadrant current Iq, which generated 4.0 A step variation load disturbance while the speed estimated by the LKF in the upper two curves was caused to fall by 880 rpm from 1100 rpm to 300 rpm.

Fig.5·21 shows the low load disturbance effect on the speed and Iq response characteristics for the LKF-based sensorless control. The low load disturbance was imposed on the rotor field-excited winding which is reflected by the quadrant current

reference Iq_ref shown in fig.5·21 as the step variation. The actual quadrant current Iq adapted to generate a step variation of which the amplitude was 1.5A while the estimated speed from the LKF observer dropped from 1100 rpm to 500 rpm. The results confirm that the LKF-based sensorless control system is able to make the robust adaptation to respond to load disturbance.

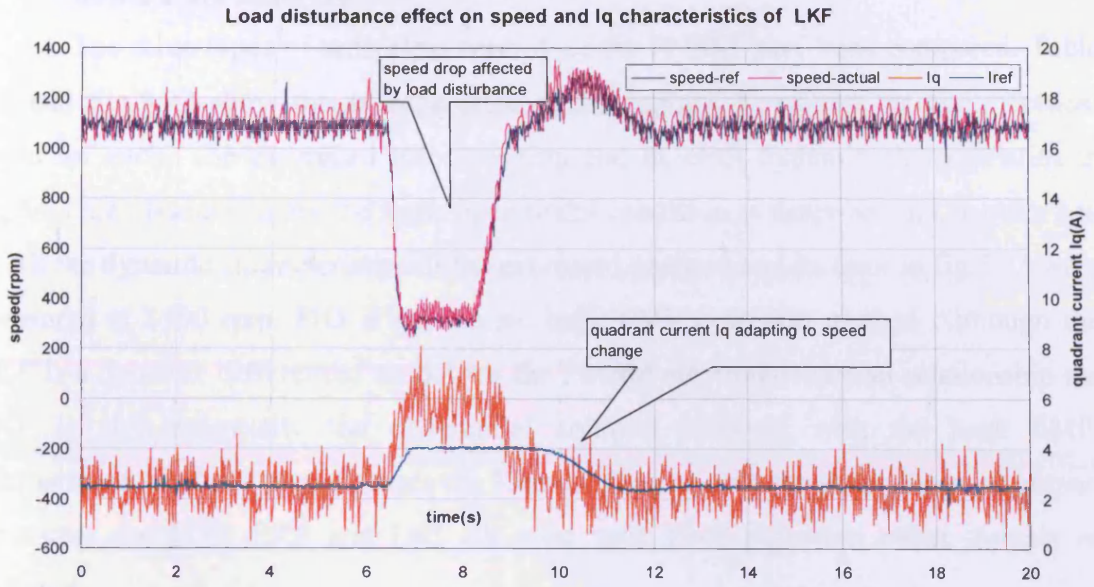

Fig. 5·20 Load disturbance effect on speed and Iq characteristics for the LKF

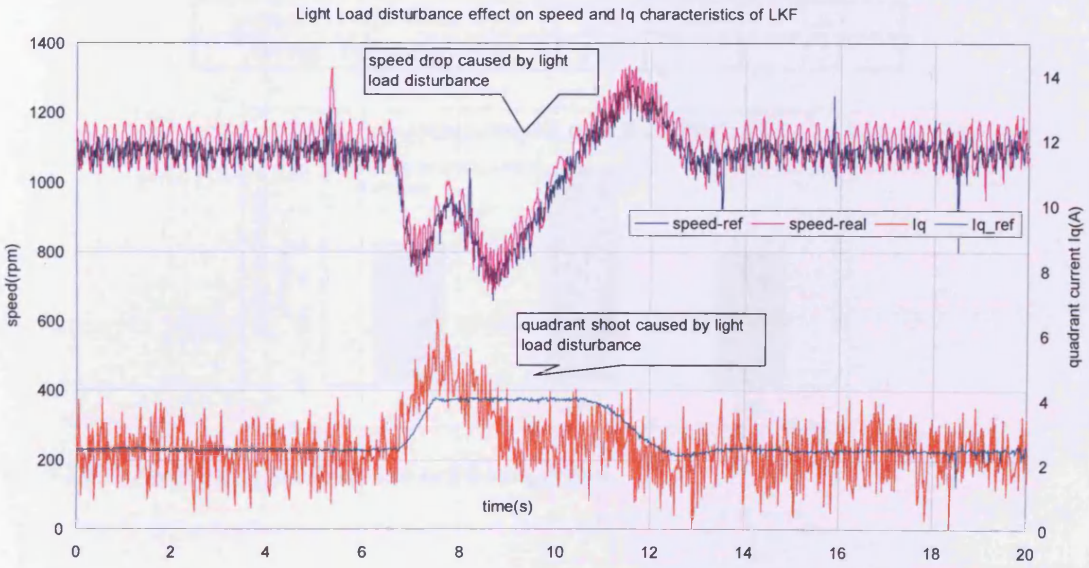

Fig. 5·21 Effect of disturbance on low load speed and Iq characteristics for the LKF

5.5 Comparison between constant-covariance and the variant-covariance correction scheme for the LKF and EKF state observers

5.5.1 Position estimation precision by the constant-covariance and variant-covariance correction schemes respectively for the LKF-based and EKF-based state observer

The three types of sensorless control of the PMSM have been compared. Table 5·1 and Fig.5·22 show the average error of the estimated position for one electrical cycle for each. The estimated rotor position and its error dynamic characteristics in fig.5·23 are obtained under the same operational condition as described in Chapters 2 to 4. All the dynamic characteristics of the estimated position and its error in fig.5·23 were measured at 1100 rpm. FlO is the classic back EMF detection method Although the EKF is a dynamic differential model for the PMSM electromechanical relationship the EKF is also essentially the differential solution involved with the back EMF. Furthermore, the LKF actually uses the Kalman filter to tune the flux linkage as output. Therefore the FLO, EKF and LKF all need back EMF detection either directly or indirectly.

Table 5·1 Position Estimation Precision Comparison

Sensorless Algorithm Type	FLO	EKF	LKF
Average estimation error	8.09°	12.4°	7.51°

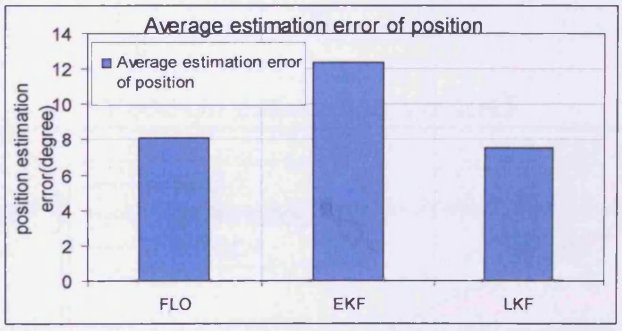

Fig. 5·22 Average position estimation errors

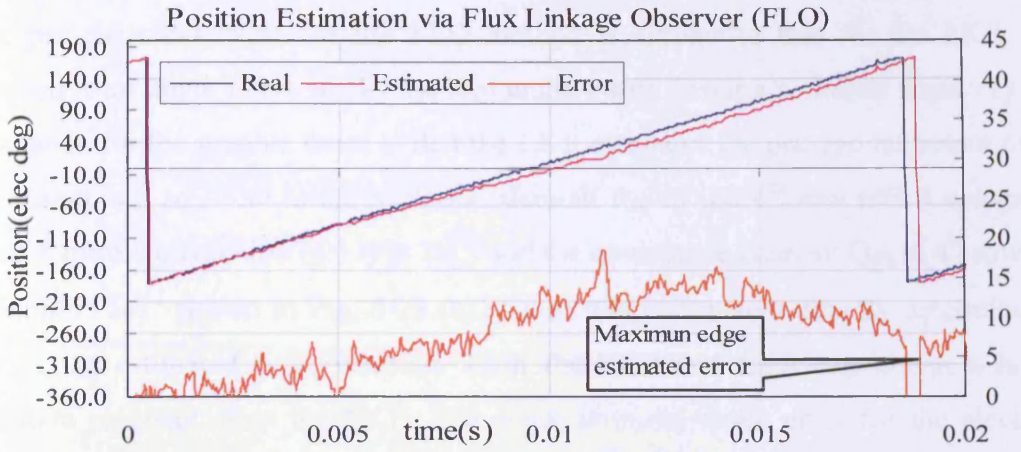

(a)

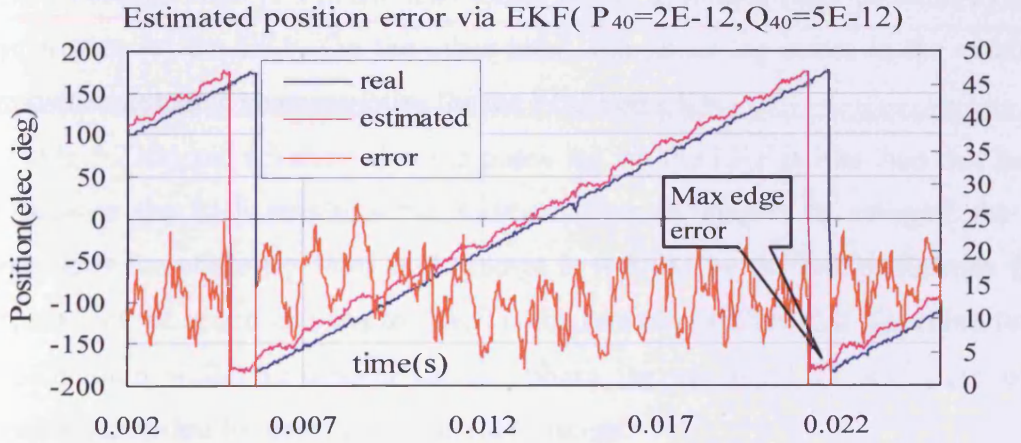

(b)

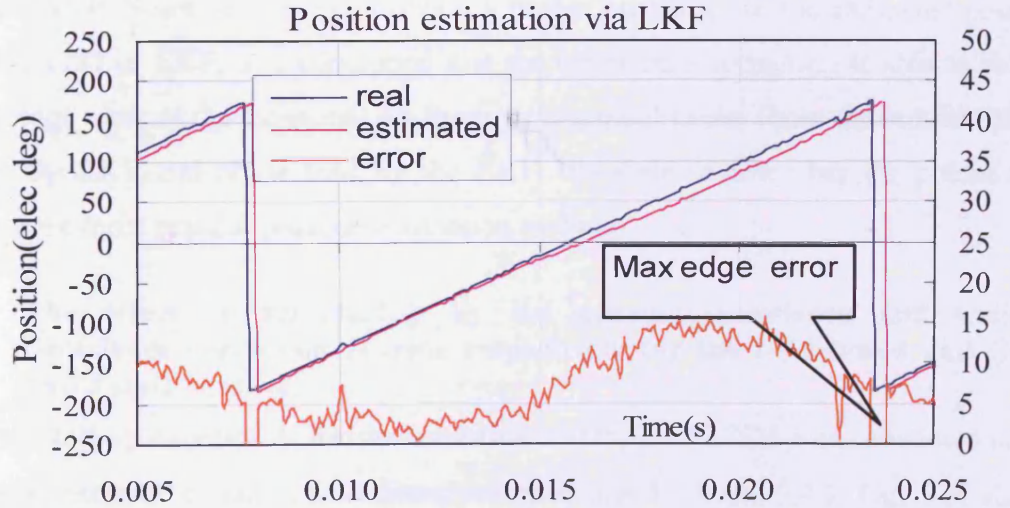

(c)

Fig. 5-23 Position estimation comparison between (a) FLO, (b) EKF, (c) LKF

Fig. 5·23 (a, c) shows that the dynamic characteristics of the estimated rotor angle per electrical cycle for the FLO method is similar to that for the LKF. The estimated rotor angle curve tracks the real angle curve through a similar trajectory. An explanation for the graphic trend is that the LKF estimates the orthogonal output of the flux-linkage ψ_α, ψ_β. The initial variance element P_{40} in the 4^{th} row and 0 column of matrix P from the equation (4·33) is $2e^{-12}$ and the covariance element Q_{40} in 4^{th} row and 0 column is $5e^{-12}$ shown in Fig. 5·23 (b). These two parameters directly determine the error of the estimated rotor position. Both the FLO and LKF can obtain a higher estimation precision than the EKF. The edge/ terminal angle error for the electrical cycle can obviously help to indicate the actual phase shift. The maximum edge angle error for the electrical cycle by the EKF seems relatively higher than that of the LKF and LFO because there is a phase lead exists in the estimated rotor position dynamic characteristics for the EKF. On the other hand, the phase lag exists in the estimated rotor position dynamic characteristics for the FLO and LKF.

Fig.5·23(a) and (c) show that the phase lag via the LKF is less than that for the FLO because the LKF employs the Kalman filter techniques to estimate the flux linkage while the phase lag from flux linkage is reduced by the link of Kalman filter. The reason for the phase lead via the EKF is the recursive differential algorithm for the state estimation while the reason for the phase lag via the LKF and FLO is the integration algorithm for calculating the flux linkage.

The LKF observer performs the best of the three methods with regards to average error of the estimated position but, the EKF observer performs the best in terms of phase shift. Since the LKF can obtain a higher precision for the estimated position than the FLO or EKF, it is concluded that the covariance correction is able to reduce the average error of the estimated position per electrical cycle. From the reduced phase lag by the LKF and phase lead by the EKF, the Kalman filter has the potential to become the most popular position estimation method.

5.5.2 The effect on self-startup by the constant-covariance and variant-covariance correction scheme respectively for the LKF-based and EKF-based state observer

The self start-up experiment for the sensorless controlled PMSM was completed under the same hardware conditions As described in section 4.4.2 and 5.4.2. Fig. 5·24 shows that the EKF and LKF both can self start. By contrast with the EKF and LKF, the FLO has no self-start-up ability at an arbitrary position, since the self start-up via the FLO requires voltage vector injection to align the rotor in the necessary initial direction.

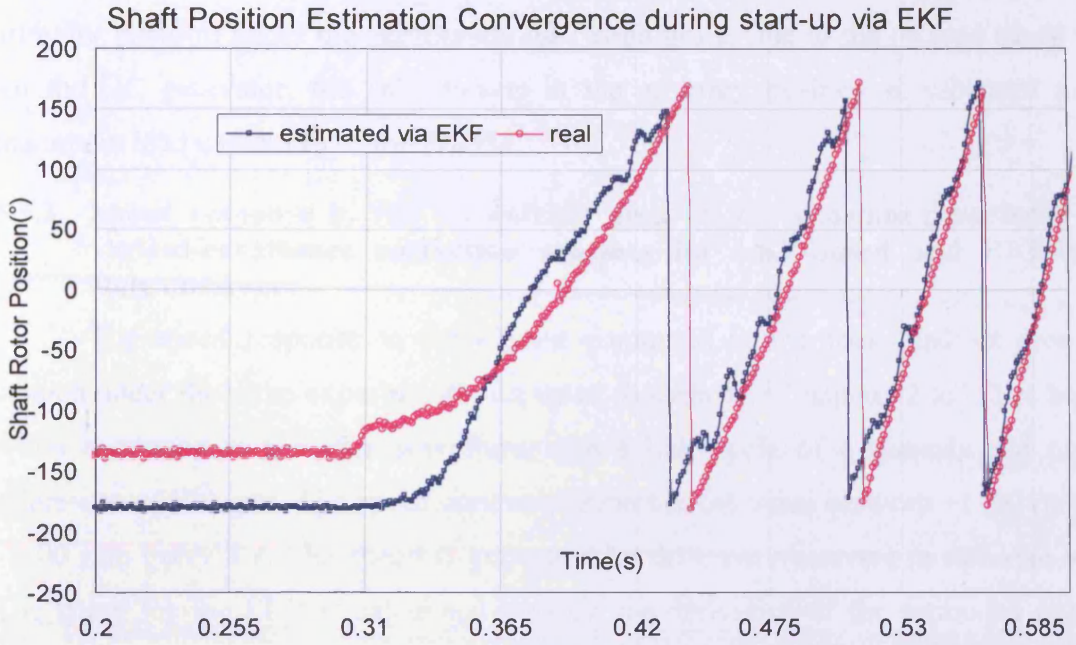

(a)

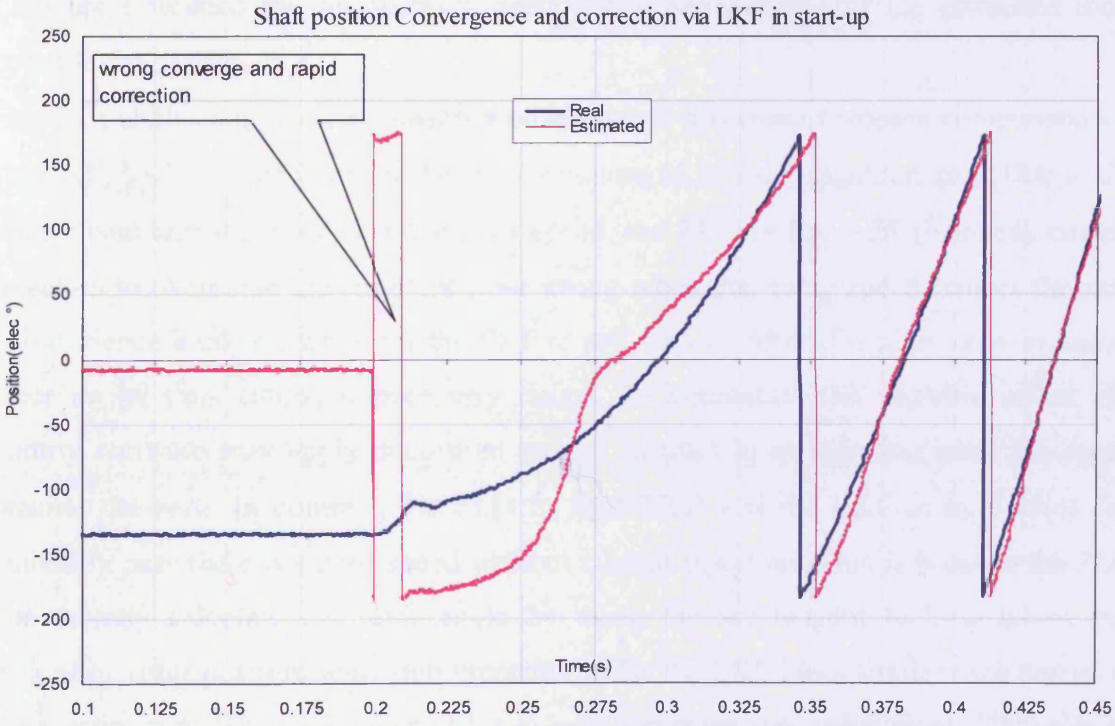

(b)

Fig. 5·24 Start-up ability comparison between the EKF and LKF

The LKF can overcome the natural disadvantage of the FLO since the Kalman filter technique with invariance correction is used to tune the output of the flux linkage

by the LKF observer. The invariance via the LKF corrects the wrong convergence of the estimated position. The covariance correction allows the PMSM self start at any arbitrary position under the appropriate load conditions. Due to the no load mode used for the DC generator, the self start-up at the arbitrary position is subjected to the maximum load capability of the PMSM.

5.5.3 Speed response in the 4-quadrant area by the constant-covariance and variant-covariance correction schemes for LKF-based and EKF-based state observers

The speed response to the bipolar command in the four-quadrant area was studied under the same experimental set up as described in Chapters 2 to5. The bipolar speed command is a square waveform with a half cycle of 4 seconds and bipolar references ±1100 rpm. The speed command switches the value between +1100 rpm and -1100 rpm every 4 s. The speed is generated by different observers in different ways. The speed for the FLO is calculated through the derivative of the estimated position from the FLO so the speed is dependant on the estimated rotor position while the LKF and EKF are the state estimation for the multi-variable. The speed with the EKF and LKF are estimated by the observer itself and is independent of the estimated rotor position.

Fig. 5·25 shows a quite distinguishing difference in the speed response comparison via the EKF, LKF, and FLO under the square command in the 4-quadrant area. Due to the wrong convergence at or near the zero speed, the EKF in fig. 5·25 (b) needs current injection to overcome the resultant rotor swing when the rising speed crosses the zero value. Hence it takes a while for the EKF to self start in either direction as the resultant rotor swing thus causes unnecessary delay. To counteract the negative effect, the control software may apply maximum current instruct Iq as injection when the speed reaches the zero. In contrast, the FLO in fig.5·25(a) and the LKF in fig.5·25(c) can smoothly pass the cross zero speed without current injection. This is because the FLO can directly calculate the rotor angle by using the arc tangent look-up tables and estimates rotor position with high precision while the LKF has a similar high precision rotor estimation. The LKF takes 2.1 s to raise the cross zero value from -1000 rpm to 1000 rpm or lower the cross zero value from +1000 rpm to -1000rpm, longer than the FLO or EKF as shown in fig. 5·25 (c), while the corresponding dynamic response times for the FLO and EKF are respectively 0.96 s 1.6 s. The state observer like the EKF and LKF has a slower dynamic speed response than the FLO. The dynamic response time for the speed command switching falls into two parts, the falling time and rising time.

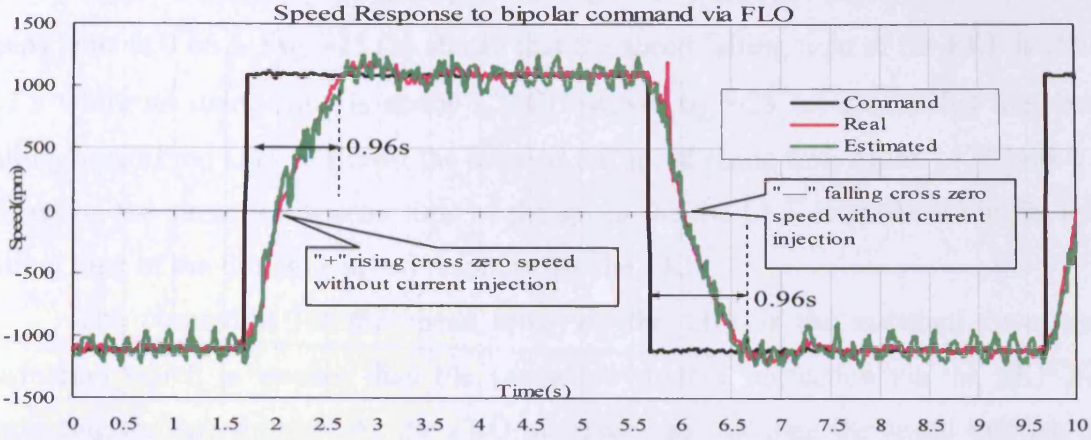

(a)

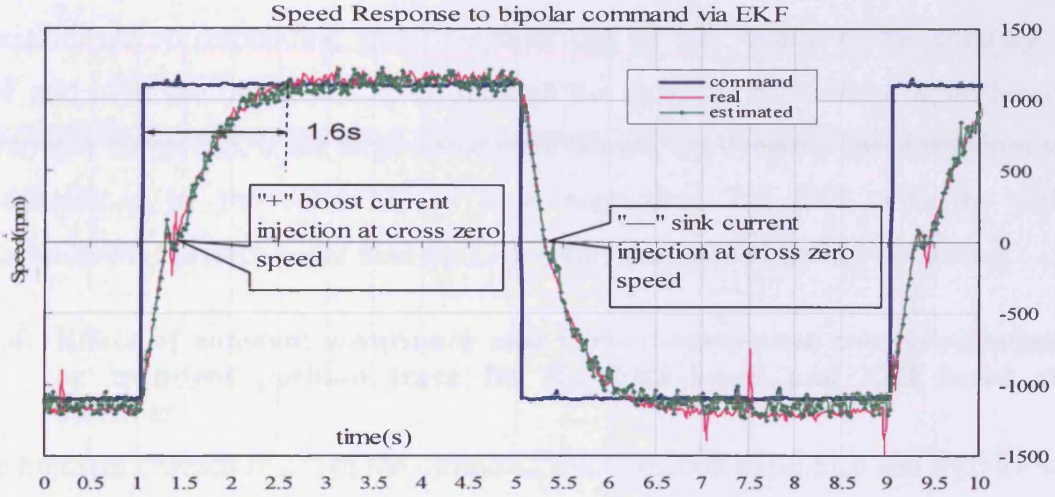

(b)

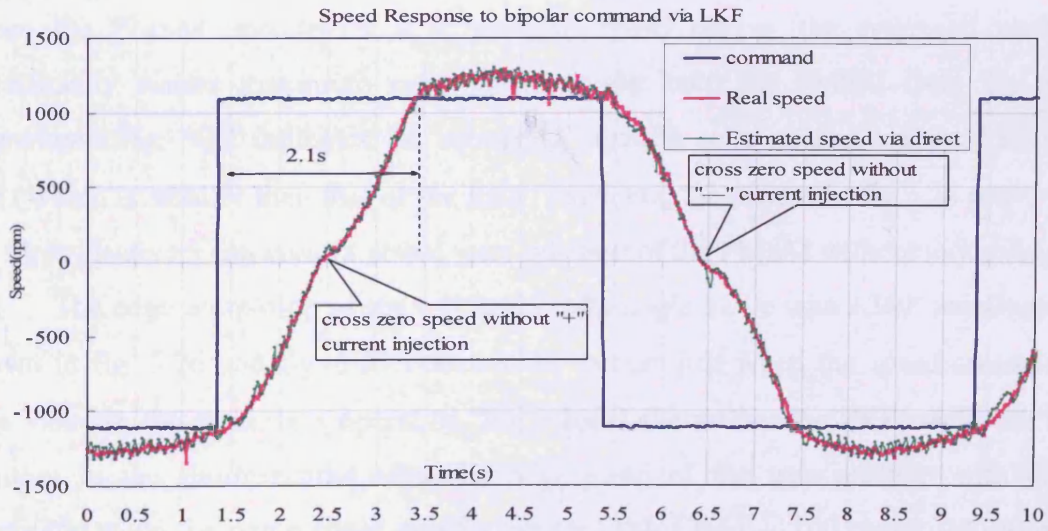

(c)

Fig. 5·25 Speed Response Comparison for the (a) FLO, (b) EKF and (c) LKF

Fig.5·25 (a) shows that the speed falling time of the FLO is about 0.3 s while its rising time is 0.66 s. Fig.5·25 (b) shows that the speed falling time of the EKF is about 0.3 s while its rising time is about 1.3 s However fig.5·25 (c) shows that the speed falling time of the LKF is almost the same as the speed rising time of the LKF, both 1 s. Therefore the slowest response time of the speed via the LKF is attributed to the long falling time of the dynamic speed response via the LKF.

The correction for the speed error via the LKF is the invariant covariance correction which is weaker than the variant covariance correction via the EKF into correcting the speed error. As the FLO observer can calculate the speed through the derivative of the estimated position, the dynamic speed response time is determined by the precision of the rotor estimation, if the rotor position estimation has sufficient precision, the corresponding speed response can be fast. While on the contrary, the EKF and LKF can obtain the speed through the recursive differential algorithm with covariance correction, if the large speed error occurs, the dynamic speed response time is determined by the capability of error correction. The EKF with the variant covariance can perform better than the LKF with invariant covariance correction.

5.5.4 Effect of constant-covariance and variant-covariance correction schemes on transient position trace for the LKF-based and EKF-based state observer

The transient characteristics of the estimated rotor position in fig.5·26 and fig.5·27 were measured when the speed crosses the zero value under the bipolar command in fig.5·25. The experimental setup and conditions are the same as those in Fig.5·26 and Fig.5·27. When the PMSM operates in a 4 quadrant speed region, the estimated position occasionally causes maximum error which might keep the PMSM from the right movement. Fig. 5·22 indicates the estimated position error caused via the LKF and FLO which is smaller than that of the EKF. However, the results in fig.5·26 prove that the three observers can control actual rotor position of the PMSM without any swing.

The edge jump/drop of the estimated rotor angle curve with ±360° amplitude as shown in fig. 5·26 and fig. 5·27 occasionally occurs just when the speed crosses the zero value in the sensorless operation. Fig.5·26(b) shows that the EKF tracks the real position in the shortest time after the edge jump of the true position with -360° amplitude when the rising speed crosses the zero value from -1100 rpm to +1100 rpm. Moreover the least phase shift via EKF occurs at the edge jump with +360° amplitude

in 1.01 s, the estimated position via the EKF converges to the real position in a time of 1.18 s as shown in fig.5·26.

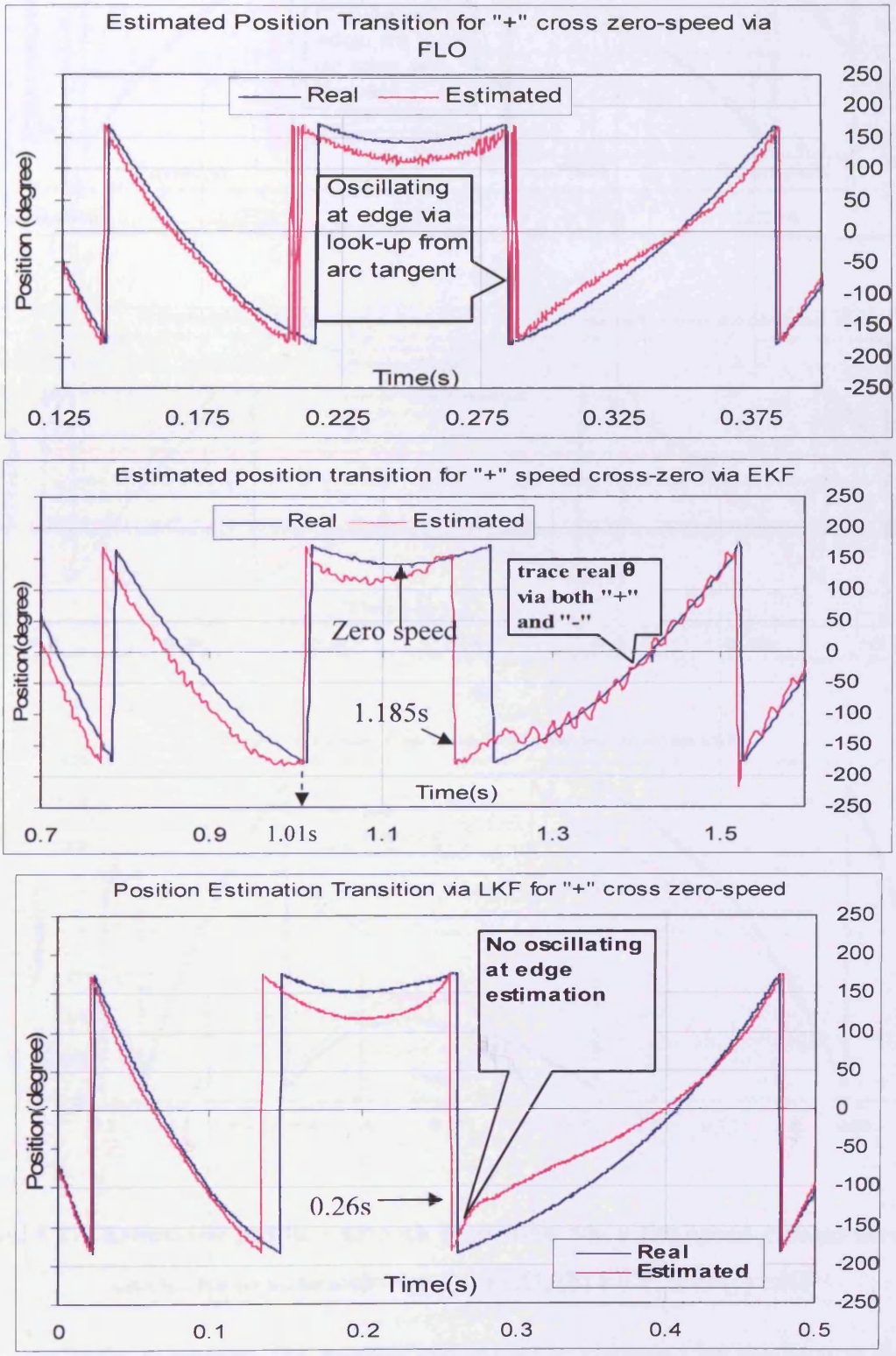

Fig. 5·26 Estimated position correction for the position edge jump when the speed crosses zero in the 4-quadrant operation from anticlockwise to clockwise, (a) FLO, (b) EKF, and (c) LKF.

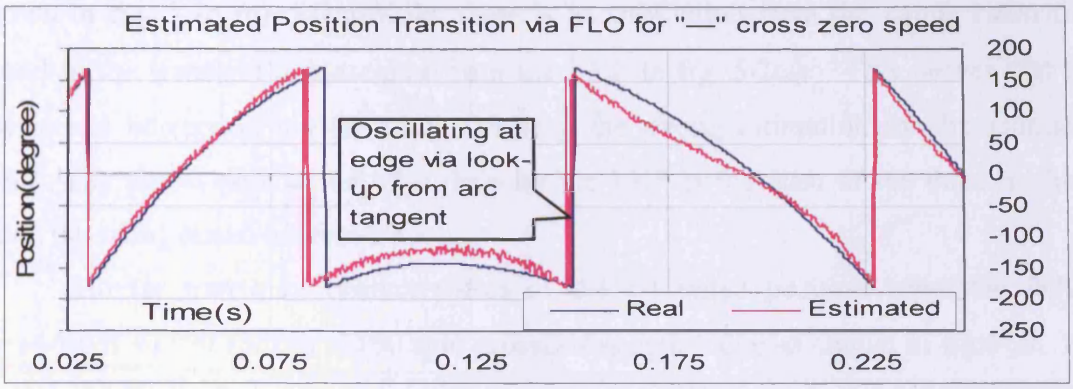

(a)

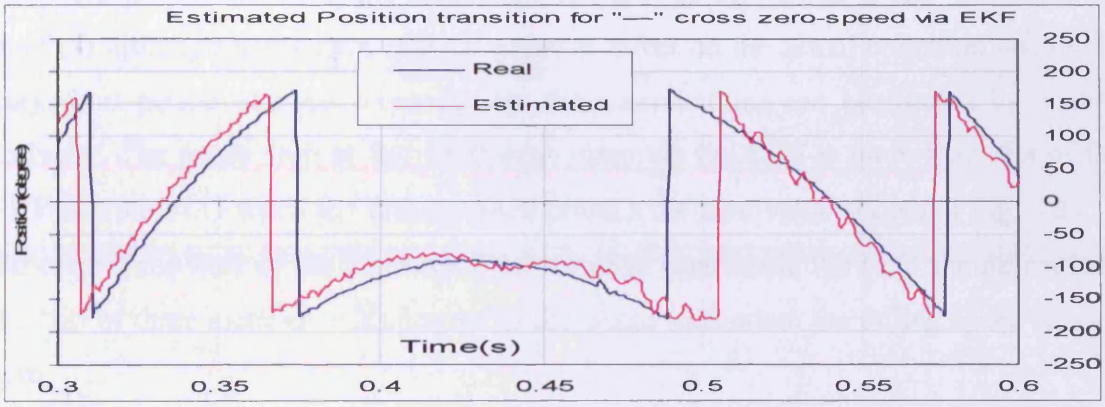

(b)

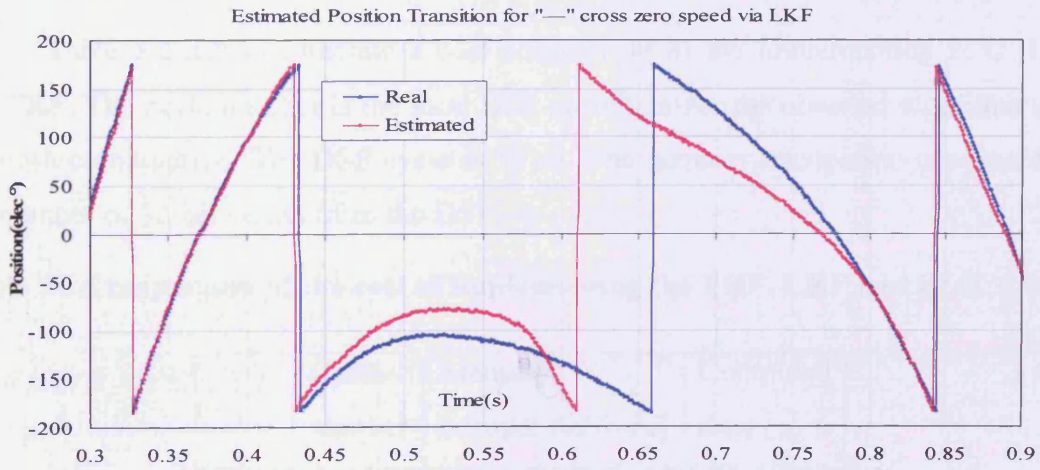

(c)

Fig. 5·27 Estimated position smooth transition when the speed crosses zero from clockwise to anticlockwise, (a) FLO, (b) EKF, and (c) LKF

In the meantime, the greatest phase lead is generated by the EKF at the edge drop with -360°. The LKF precisely tracks the edge drop of the real angle with the least phase lag in a time of 0.26 s. The FLO has a similar phase lag at the same edge drop, but unfortunately oscillation from the wrong estimation occurs at the same edge drop as

shown in fig. 5·26 (a). Meanwhile, there is no oscillation from the wrong estimation found in the transient angle curve from the LKF in fig. 5·26(c). This proves that the covariance correction via the LKF can keep the wrong estimation for the estimated value. The phase shift at the edge drop by the LKF is the least of the three methods when the rising speed crosses zero.

Similar transition characteristics of the estimated position when the falling speed from +1100 rpm to -1100 rpm crosses the zero value as shown in fig.5·27. The FLO and LKF still demonstrate the lowest phase shift respectively at the 360 ° edge jump and drop . However, the oscillation of the edge estimation is still inevitable for the FLO although it does not cause a negative effect on the actual operation due to the very short period of time. Theoretically these oscillations can be filtered by control software. The phase shift at the +360 edge jump via the LKF is more than that of the EKF and the FLO when the falling speed crosses the zero value shown in Fig. 5·27. If the control software of the FLO can filter the edge oscillation, the FLO should perform the best of three methods with respect to the phase shift when the falling speed crosses zero.

5.5.5 The algorithm computation time comparison

Table 5·2 shows illustrate a cost comparison of the implementing FLO, LKF and EKF. The cycle number is the total DSP cycle number the observer algorithm uses to finish computation. The DSP cycle is 50 ns. The memory occupation is counted by the number of 32-bit words from the DSP.

Table 5·2 Comparison of the cost of implementing the EKF, LKF and FLO

	Cycle number	Memory occupation(word)	Computed time (μs)
EKF	513	393	20.5
LKF	211	118	8.4s
FLO	265	170	10.6

The EKF needs the most cycles for programme execution which is equivalent to 20.5us, and the code length of the EKF is the longest with 393 words. The full order stationary frame the EKF model is computed through a matrix algorithm. The implementation cost is highest of the three sensorless estimations.

The data from the algorithms are calculated without considering the hysteresis current regulated program. The memory occupation rate for the LKF is about 30% of that for the EKF and 70% of that of the FLO while the execution time for the EKF is almost 2.4 times that of the LKF and 1.93 times of the FLO. The implementation is done via "TMS320 C3X/4X" assembly language.

5.6 References

[5·1] S. Stasi, L. Salvatore and F. Cupertino, "Sensorless control of PM synchronous motors based on LKF estimation of rotor position", *Industrial Electronics Society, IEEE 2002 28th Annual Conference* ,Vol. 16, 5-8 Nov. 2002, 686- 691

[5·2] L. Harnefors, "Speed estimation from noisy resolver signal", *Sixth Int. Conf, on Power Electronics and Variable Speed Drives*, 1996, 279--282

CHAPTER 6, Variable PI regulation scheme for Single Dimension Luenberger Observer Sensorless Technique

6.1 Introduction

Luenberger-based sensorless state estimation for PMSM was introduced by Tatematsu [6·1~6·3] in 1998 in terms of reduced order state observer. The PMSM dynamic model used in the Luenberger sensorless observer is the 3-order non-linear variable-coupled dynamic model in a d-q rotating coordinate frame. The d-q model needs to be linearized by the feedback of nonlinear terms. After linearization, Luenberger reduced order theory is applied to reduce the order number of linearized dynamic model from 3 dimensions to 1 dimension. Therefore, reduced-order Luenberger observer is termed a Single Dimension Luenberger (SDL) observer. The estimated speed state from this SDL observer is used for the integration to extract position. An additional position correction mechanism is required to correct for the offset of the estimated position from integration to the true one. The initial and transient positions will be obtained by correcting the offset between the estimated and actual positions. Such a correction mechanism was used by Matsui [6·4] where: the error between actual and estimated d-axis voltage is proportional to the error between actual and estimated position angle.

The remedy regulation of the estimated position is generated by applying a PI regulator which accepts the difference between actual and estimated d-axis current to compensate the offset from the position of integration to actual one. The experiment by Tatematsu [6·1~6·3] proved that such a reduced order Luenberger observer can be used to estimate shaft position information for sensorless control of a PMSM by selecting the Eigen value of the system matrix. It is pointed out that the stability of SDL is decided by selecting Eigen values of the system matrix. The estimated speed is easily unstable if these are increased too much while the estimated speed is not accurate if the Eigen value of the system matrix is reduced too much.

The equilibrium neighbourhood in the Taylor's series is included by Tatematsu [6·1-6·3] to form the new system matrix which assigns the real part of all poles as

negative, eventually the estimated state is stabilised by this way. The benefit for SDL observer is to get required acceleration by assigning considerably greater Eigen values; obviously bringing the drawback of stabilisation for SDL observer. Chapter 6 uses an alternative approach to implement speed estimation replacing the speed directly extracted from Luenberger.

The current Luenberger-based reduced order sensorless control estimation mainly attempts to obtain stabilised speed estimation. The position PI regulator can be used to remedy the shaft position offset generated from the speed integration, although the speed convergence for the Luenberger observer is still decided by the Eigen value of the system matrix. Therefore, the focus for Luenberger-based sensorless observer here is position estimation and its correction characteristics decided by the position PI regulation scheme under the stabilised speed by alternative speed estimation.

6.2 Luenberger Observer Model for Sensorless Control PMSM

6.2.1 Luenberger Observer Theory for the State-estimation System

Assume that the state space of the N order linear constant coefficient controllable system $\{A, B, C\}$ is:

$$\begin{cases} \dot{x} = Ax + Bu \\ y = Cx \end{cases} \tag{6·1}$$

Where x is the N order system state; y is the output of system $\{A, B, C\}$, U is the input vector for system $\{A, B, C,\}$, A is the system coefficient matrix; B is the input coefficient matrix and is the output coefficient matrix.

Figure 1 illustrates the actual system $\{A, B, C\}$ with state observer $\{A', B', C'\}$. The actual controllable system is not precisely expressed by the system $\{A, B, C\}$, which is a theoretical model with many assumption and simplifications. The state observer $\{A', B', C'\}$ is constructed to imitate the actual system with theoretical model $\{A, B, C\}$, coefficient values of the state observer is the same as that of the theoretical model $\{A, B, C\}$: $A'=A$, $B'=$, $C'=C$. The general input "r" is compared with the feedback from the state observer $\{A', B', C'\}$ which is the amplified state $\hat{x}$ by Luenberger coefficient L.

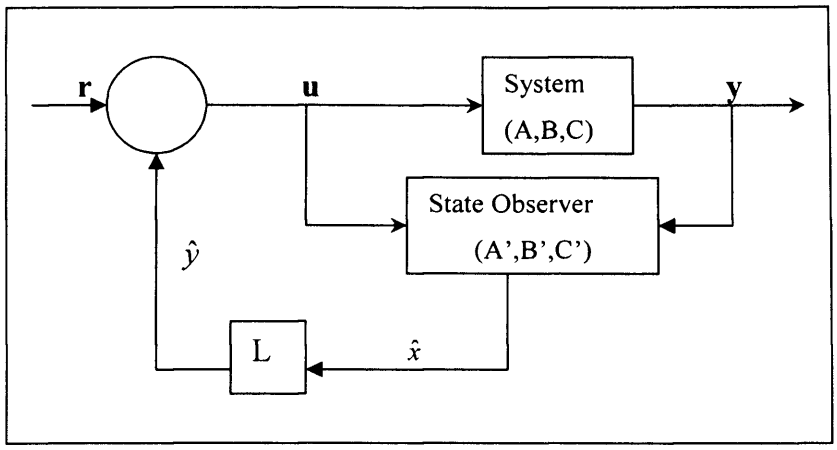

Fig. 6·1 State feedback system with state observer

If the controllable system $\{A, B, C\}$ in equation (6·1) is absolutely state-controllable, it is a trial-and-error procedure for n Eigen values of the feedback system to be configured using the state feedback L shown in fig. 6·1. However, the validity of the feedback system result depends on whether the n state variables can be obtained before the feedback system is configured. When the state feedback is used in a practical application, there must be n sensors and n state variables. When the order number of the controlled system is high, the number of precision sensors needed is consequently large and costly.

However, a greater problem is that some state variables of the controllable system cannot be tested directly due to the limit of the non-linear system structure and other reasons such as the lack of a practical physical measurement tool and inaccurate maths models. As pointed out by Bertran [6·5] and Bass [6·6], if the controllable system $\{A, B, C\}$ shown in fig. 6·1 can be estimated by the state observer $\{A', B', C'\}$ from the outputs **y** and input **u**, a simulated system $\{A', B', C'\}$can be constructed according to the state space equation-based controllable system$\{A, B, C\}$. The directly obtainable input **u** and output **y** from the controlled system $\{A, B, C\}$ (those two variables can be directly obtained) are used to drive the simulated state observer system$\{A', B', C'\}$shown in fig. 6·2, the system$\{A', B', C'\}$ makes the state $\hat{x}$ gradually approach close to the actual state x from the controllable system$\{A, B, C\}$.

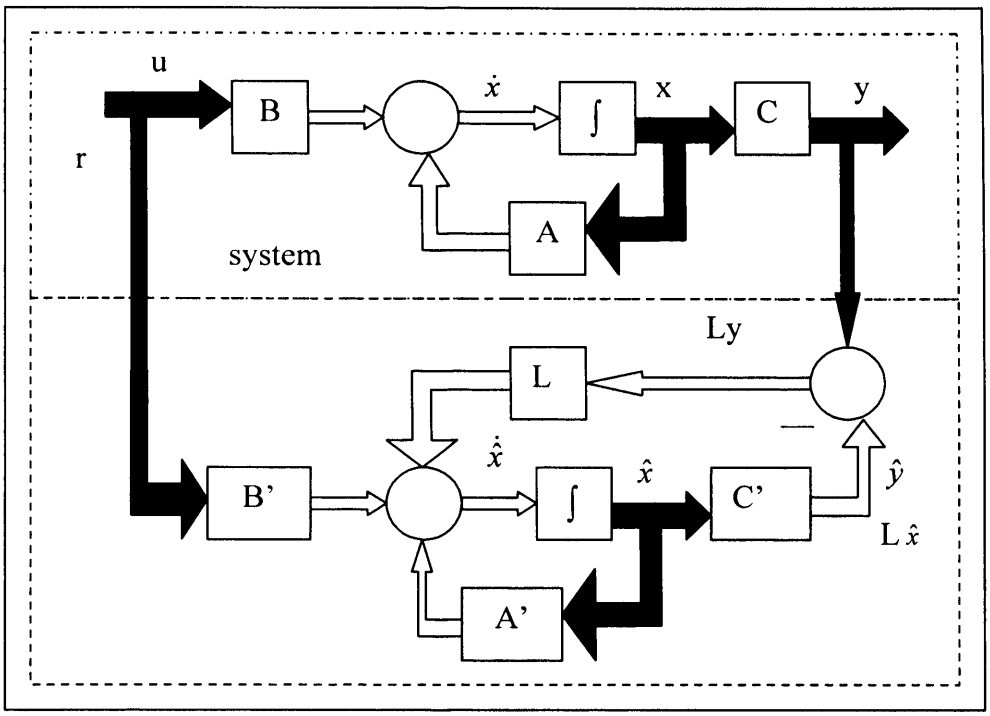

Fig. 6·2 Layout of the state space system {A, B, C} with state observer {A', B', C'}

Fig. 6·2 illustrated that the estimated states $\hat{x}$ is constructed within the state observer. The estimated state $\hat{x}$ can take the place of the real state x which can not be directly obtained from the controllable system {A, B, C}, and furthermore $\hat{x}$ will be used to form the state feedback $L\hat{x}$ shown in fig. 6·2 to configure the n order Eigen value of the state observer system {A', B', C'}.

The state space equations of the state observer {A', B', C'} are the simulation of the controllable system {A, B, C}. It means the two systems are expected to have the same mathematical model: A= A', B= B', C= C'. However it is not necessary to construct the state observer with the same scale and complexity as the controlled system. For example, for the same cost electronic model systems {A', B', C'}, the initial conditions and noise disturbance such as the variance of the parameters in the model systems might not be the same as the controlled system {A, B, C}. So an error x_e shown in (6·2) must exist between the real state x and estimated state $\hat{x}$.

$$x_e = x - \hat{x} \tag{6·2}$$

x_e is the estimated or reconstructed error.

If the state x for the actual system {A,B,C} can be observed through the state observer {A',B',C'}, the state error x_e between the state x and x' can be uniquely decided through measuring the error between the output y of the controllable system

{A,B,C} and the output $\hat{y}$ of the state observer{A',B',C'} shown in fig. 6·2. The error $(y-\hat{y})$ is multiplied by an appropriate $n\times 1$ order constant matrix L first, and then the result $L(y-\hat{y})$ is fed back to the input of the state observer {A', B', C'} shown in fig. 6·2. This feedback matrix L not only makes it unnecessary to detect the initial states of the controllable system and state observer instantaneously, but also makes the estimation error x_e gradually approach zero, which means the estimated state $\hat{x}$ becomes close to the real state x.

The state space equation of the state observer {A', B', C'} is

$$\begin{cases} \dot{\hat{x}} = A\hat{x} + Bu + L(y-\hat{y}) \\ = A\hat{x} + Bu + L(y - c\hat{x}) \\ = (A - Lc)\hat{x} + Ly + Bu \\ \dot{\hat{y}} = c\hat{x} \end{cases} \tag{6·3}$$

assuming that A≈A', B≈B', C≈C'.

The state space equation (6·1) is subtracted from state observer equation (6·3) to obtain the estimated error $x_e = \dot{x} - \dot{\hat{x}}$ from the subtraction for the left side of equation (6·1) and (6·3),then, after substituting the item $x-\hat{x}$ by (6·2), the same-order state equation subtraction from the right side of equation (6·1) and (6·3) results in

$$\dot{x} - \dot{\hat{x}} = (A - Lc)(x - \hat{x}) \tag{6·4}$$

After substituting the item $x-\hat{x}$ with equation (6·2), the equation (6·4) is transformed into

$$\dot{\hat{x}}_e = (A - Lc)x_e \tag{6·5}$$

The solution of the state equation (6·5) is

$$x_e(t) = \phi(t - t_0)x_e(t_0) = e^{(A-Lc)(t-t_0)}x_e(t_0) \tag{6·6}$$

If the system {A, B, C} is the observable for state x, the appropriately chosen matrix L can configure the Eigen value of item *(A-Lc)*. Obviously the greater the real part of the negative Eigen value amplitude for item *(A-Lc)*, the faster will be the speed the error x_e approaches zero. This means the speed is higher for the estimated state $\hat{x}$ to approach the real state x than the negative Eigen value with a smaller absolute real part.

If the real parts of all the Eigen values for the item *(A-Lc)* are smaller than $-\sigma(\sigma>0)$, (even if the initial estimated error $x_e(t_0)$ is considerably greater than that in normal operation at the initial instant t_0, $\hat{x}(t_0) =\neq x(t_0)$, the estimated state $x_e(t)$ includes every component each of which approaches zero at a rate not less than $e^{-\sigma t}$.

Thus, the estimated state $\hat{x}$ will gradually approach and eventually become equal to the real state x. Sometimes this is referred to as an asymptotic state observer [6·7]. However, if the Eigen values of matrix *(A-Lc)* are complex and its negative real part has high absolute amplitude, the gain of the $n \times 1$ order output feedback matrix L is also high. This will result in the amplitude of the instantaneous response in the observer becoming higher than normal and the observer becoming more sensitive to noise. Generally the Eigen value of matrix *(A-Lc)* should be chosen according such that the amplitude of its negative real part is 2~3 time that of *(A+bK)* [6·7].

The state observer {A',B',C'} is the simulation system for the actual controllable system {A,B,C}. If the order number of the state observer is the same as the actual system, it is called a full order state observer. The output of the one-order controllable system can be always tested directly [6·7]. For single output system, if the order number of the state observer can be reduced to one order, it makes little contribution. However, for the output y of a multi-output system{A,B,C}, if output y is a $q \times 1$ order vector (q<n) , the order number of the state observer{A',B',C'} can be reduced from n to q. Hence the q order of output can be measured to simulate the complex state controllable system {A,B,C}.

6.2.1 Reduced-order Luenberger Observer Design

Assume that the controllable system Σ(A,B,C) is observable for the state and m rows of the coefficient matrix C are foreign to each other linearly, which means that rank(C)=m. The latter is not strictly required and general systems can occasionally match this condition. If the rank value of the coefficient matrix C is less than m, it indicates that there are m correlative vectors among n-order row vectors from C matrix, some row vectors can be expressed by the linear combination of the others. Thus, the corresponding components of output vector y=Cx are not independent but can be expressed linearly by the other components of the output vector y. Those components of the output vector y can be deleted from the output vector y, correspondingly those rows can be deleted from the coefficient matrix C. After the procedure of component reduction, the m-order row vectors left from the coefficient matrix C are guaranteed to be independent.

The measured output of the absolutely observable system Σ(A,B,C) contains all the information of the full system state components. If some system state components can be expressed by the simplified linear combination of every component from output

y, it is not necessary to build up the new observer system for reconstructing the full order observer system state components. Therefore, the new system requires that the number of system state components to reconstruct will be less than n, which means that the order number of the observer can be reduced. This is the basic concept that the reduced-order observer is constructed using parts of the system state components.

The system Σ(A,B,C) has m independent output components, which can be combined and reconstructed to form m state components, which is $\tilde{x}_1$ in equation (6·7). Afterwards, the left n-m number of the state components, which is $\tilde{x}_2$ in equation (6·7), is needed for reconstruction. In order to coordinate-transform the state components from the output vector y, the first m components $\tilde{x}_1$ are selected to be made equal to that of the output y. The 2nd n-m number components $\tilde{x}_2$ need to be built through another coefficient matrix G given by

$$\tilde{x} = \begin{bmatrix} \tilde{x}_1 \\ \cdots\cdots \\ \tilde{x}_2 \end{bmatrix} = \begin{bmatrix} y \\ \cdots\cdots \\ \tilde{x}_2 \end{bmatrix} = \begin{bmatrix} Cx \\ \cdots\cdots \\ Gx \end{bmatrix} = \begin{bmatrix} C \\ \cdots\cdots \\ G \end{bmatrix} x \tag{6·7}$$

The coordinate-transformation matrix has the converse matrix

$$T^{-1} = \begin{bmatrix} C \\ \cdots\cdots \\ G \end{bmatrix} \tag{6·8}$$

where

C is the coefficient matrix of the system Σ(A,B,C), the rank of matrix C is m and G is the $(n-m)\times n$ matrix where $(n-m)$ row vectors are chosen randomly so as to make the matrix T^{-1} non-singular. G is not unique. The only simple form should be considered. For example, the matrixes in system Σ(A, B, C) has been already transformed in rows and columns. Another separated form of the coefficient matrix C is: $C = [C_1 \ \vdots \ C_2]$, where the rank of the square matrix C_1 is m, correspondingly the separated form of the G matrix can be chosen as : $G = [0 \ \vdots \ I_{n-m}]$, I_{n-m} is a diagonal matrix. So the converse matrix of the transformation matrix is

$$T^{-1} = \begin{bmatrix} C_1 & \vdots & C_2 \\ \cdots & \cdots & \cdots \\ 0 & \vdots & I_{n-m} \end{bmatrix} \quad T = \begin{bmatrix} C_1^{-1} & \vdots & -C_1^{-1}C_2 \\ \cdots & \cdots & \cdots \\ 0 & \vdots & I_{n-m} \end{bmatrix} \tag{6·9}$$

The coefficient system matrix $\tilde{C}$ after the coordinate-transformation is

$$\tilde{C} = \left[\tilde{C}_1 \ \vdots \ \tilde{C}_2\right] = CT = \left[C_1 \ \vdots \ C_2\right] \times \begin{bmatrix} C_1^{-1} & \vdots & -C_1^{-1}C_2 \\ \cdots & \cdots & \cdots \\ 0 & \vdots & I_{n-m} \end{bmatrix} = \left[I_m \ \vdots \ 0\right] \tag{6·10}$$

and the measured output equation is

$$\tilde{y} = \tilde{C}\tilde{x} = \left[I_m \ \vdots \ 0\right] \begin{bmatrix} \tilde{x}_1 \\ \cdots \\ \tilde{x}_2 \end{bmatrix} = \left[\tilde{x}_1 : 0\right] \tag{6·11}$$

Because the m order state vector $\tilde{x}_1$ is equal to the output y in equation (6·7), (n-m) order components of the output $\tilde{y}$ in equation (6·11) are a zero vector. As long as n-m dimension components state $\tilde{x}_2$ are reconstructed, the task of reconstructing states is complete. Then, the dimension number of the observer is n-m. Generally, the minimum order number of the observer is n-m.

If the absolutely observable and controllable system Σ(A,B,C) matches the condition: rank(C)=m, it can be transformed into $\tilde{\Sigma}(\tilde{A}, \tilde{B}, \tilde{C})$ by coordination conversion as

$$\tilde{\Sigma}(\tilde{A},\tilde{B},\tilde{C}) = \begin{cases} \dot{\tilde{x}} = \tilde{A}\tilde{x} + \tilde{B}u = \begin{bmatrix} A_{11} & \vdots & A_{12} \\ \cdots & \cdots & \cdots \\ A_{21} & \vdots & A_{22} \end{bmatrix} \begin{bmatrix} \tilde{x}_1 \\ \cdots \\ \tilde{x}_2 \end{bmatrix} + \begin{bmatrix} B_1 \\ \cdots \\ B_2 \end{bmatrix} u \\ y = \tilde{x}_1 \end{cases} \tag{6·12}$$

The coordination transformation does not affect the visibility or observability of system $\tilde{\Sigma}$, $\tilde{\Sigma}(\tilde{A},\tilde{B},\tilde{C})$ is also observable for the state $\tilde{x}$. Among the states $\tilde{x}$ of the $\tilde{\Sigma}(\tilde{A},\tilde{B},\tilde{C})$, the component state $\tilde{x}_1$ is the output y shown in equation (6·12). The information of $\tilde{x}_2$ can be passed into output y through the media component η shown in equation (6·13). Therefore the media component η might include all the information of $\tilde{x}_2$, η is defined and derived from equation (6·12), it means that the media component η can be used to observe $\tilde{x}_2$ absolutely. Therefore the system by matrix pair (A_{22}, A_{12}) in equation (6·13) is absolutely observable. In order to reconstruct $\tilde{x}_2$, the matrix expression in equation (6·12) must be replaced by an equation group including only $\tilde{x}_2$ in equation (6·13) if the variable y is used to replace state $\tilde{x}_1$.

$$\begin{cases} \dot{\tilde{x}}_2 = A_{22}\tilde{x}_2 + B_2u + A_{21}y \\ \eta = A_{12}\tilde{x}_2 \end{cases} \tag{6·13}$$

The subsystem in equation (6·13) is the n-m dimension system. This subsystem has two inputs, the 1st state equation in equation (6·13) has the input item $B_2u + A_{21}y$. The subsystem in equation (6·13) has the n-m dimension vector η as the output, which can be expressed by another subsystem shown in equation (6·14), which is also derived from equation (6·12).

$$\eta = \dot{y} - A_{11}y - B_1u \tag{6·14}$$

The reduce-order observer will be designed according to the subsystem in equation (6·3) with the output y in equation (6·3) substituted by item η in equation (6·14) and feedback L in equation (6·3) substituted by item H. That will obtain the new system expressed as

$$\dot{z} = (A_{22} - HA_{12})\dot{z} + (B_2u + A_{21}y) + H(\dot{y} - A_{11}y - B_1u) \tag{6·15}$$

where z is the reconstruction of n-m dimension component state $\tilde{x}_2$. The matrix H is of $(n-m)\times m$ dimension. The chosen matrix H can be used to configure the Eigen value of the matrix $A_{22} - HA_{12}$.

However, this new reconstruction equation in equation (6·15) has the derivative item $\dot{y}$ appearing on the right side of equation (6·15). The derivative item increases the high frequency noise in the output y. In the worst case the observer cannot work. In order to avoid unnecessary noise enhancement, the item $\hat{z}$ shown in equation (6·16) below is substituted into the reconstruction system in equation (6·15).

$$\hat{z} = z - Hy \tag{6·16}$$

The new system expressed in equation (6·17) is obtained as

$$\begin{cases} \dot{\hat{z}} = (A_{22} - HA_{12})\hat{z} + (B_2 - HB_1)u + (A_{21} - HA_{11})y \\ z = \hat{z} + Hy \end{cases} \tag{6·17}$$

The equation group in equation (6·17) is the reduced order observer equation group for the system Σ(A, B, C), where $\tilde{x}_1 = y$, $\tilde{x}_2$ has the reconstruction value z, which can be used for counter transformation T^{-1} to obtain the state reconstruction value $\hat{x}$.

The design procedure of the reduced order observer can be summarised as :

1st step: judge the observability for Σ(A, B, C).

2nd step: After the coordination transformation for Σ(A,B,C), the converse transformation matrix T^{-1} in equation (6·8) makes its first m row n-line vectors construct the coefficient matrix C of which rank is m. Supplemented by n-m rows

the component matrix G in equation (6·8), T^{-1} in equation (6·9) becomes non-singular.

3rd step: Design the basic observer in equation (6·13) to replace the observer system in equation (6·3) and substitute output η in equation (6·13) by the expression η in equation (6·14) to form the rearranged equation in equation (6·15).

4th step: The conversion in equation (6·16) is introduced into the subsystem in (6·15) to obtain the new reduced-order system in equation (6·17). The conversion is designed to eliminate the negative effect.

6.2.2 Reduced-order Luenberger Observer Model for Sensorless Controlled PMSM

The dynamic electromagnet-mechanic model Σ for the permanent magnetic synchronous motor under reduced-order Luenberger observer-based sensorless estimation is based on the following d–q rotor-fixed rotational reference co-ordinates

$$\Sigma=\begin{cases}\dfrac{di_d}{dt}=-\dfrac{R}{L_s}i_d+\omega i_q+\dfrac{1}{L_s}v_d\\ \dfrac{di_q}{dt}==-\dfrac{R}{L_s}i_q-\omega i_d-\dfrac{K_e}{L_s}\omega+\dfrac{1}{L_s}v_q\\ \dfrac{d}{dt}\omega=\dfrac{K_t p}{J}i_q-\dfrac{B}{J}\omega\\ \dfrac{d\theta}{dt}=\omega\end{cases} \tag{6·18}$$

where R, L_s, K_e, K_t are respectively the phase resistance, phase synchronous inductance, back-emf constant and torque constant, ω is the rotor angular velocity, θ is the rotor position, p is the number of pole pairs, J is the rotor inertia, B is the motor viscous friction, system state variable is $x=[i_d\ i_q\ \omega\ \theta]^T$, input vector $u=[v_d\ v_q]^T$ and the measured output $y=[i_d\ i_q]^T$. The equation group in equation (6·18) is the dynamic model for PMSM in d-q rotor-fixed co-ordinates rotational frame. Apparently the system is nonlinear and system quantities are tightly coupled while Luenberger observer theory can apply to only linear system. Therefore [6·1~6·3] introduced that the feedback in equation (6·19) can be used to linearize the system model in (6·18).

$$\begin{cases}u_d=v_d+\omega L_s i_q\\ u_q=v_q-\omega L_s i_d\end{cases} \tag{6·19}$$

After substituting equation (6·19) into equation (6·18), the first two-order linearized d-q dynamic equations group from (6·18) is rearranged as

$$\frac{d}{dt}\begin{bmatrix}\hat{i}_d\\ \hat{i}_q\end{bmatrix}=\begin{bmatrix}-\frac{R}{L_s} & 0\\ 0 & -\frac{R}{L_s}\end{bmatrix}\begin{bmatrix}\hat{i}_d\\ \hat{i}_q\end{bmatrix}+\begin{bmatrix}\frac{1}{L_s} & 0\\ 0 & \frac{1}{L_s}\end{bmatrix}\begin{bmatrix}u_d\\ u_q\end{bmatrix} \tag{6·20}$$

The variables i_d and i_q are the two measurable system states while ω and θ need to be predicted. The system matrix in equation (6·20) shows that the rank is 2, thus, if the 3rd equation in equation (6·18), joined with equation (6·20), both are considered as the new system dynamic model $\hat{\Sigma}$ with new state $\hat{x}$ [$\hat{i}_d$, $\hat{i}_q$, ω], reduced-order Luenberger observer theory [6·1~6·3] can be used to reduce the orders of the system $\hat{\Sigma}$ from 3 to 1, After the reduced-order Luenberger observer theory in (6·17) is applied in the new system $\hat{\Sigma}$ in (6·18), the Single Dimension Luenberger (SDL) observer model with unique state η is shown in (6·21~6·23), where η is the state reconstructed variable which can indirectly estimate the angular velocity $\hat{\omega}$ shown in (6·22). The only parameter to be assigned by value is the Eigen value λ_0 .

$$\dot{\eta} = A_0\eta + B_0u_q + K_0i_q \tag{6·21}$$

$$\hat{\omega} = D_0\eta + H_0i_q \tag{6·22}$$

$$\begin{cases} A_0 = \lambda_0, B_0 = -\dfrac{1}{K_e}(\lambda_0 + \dfrac{B}{J_m}) \\ K_0 = \dfrac{L_s\lambda_0^{\,2} + R\lambda_0}{K_e} + \dfrac{pK_e}{J_m} + \dfrac{B(L_s\lambda_0 + 1)}{K_eJ_m} \\ D_0 = 1, H_0 = \dfrac{L_s}{K_e}(\lambda_0 + \dfrac{B}{J_m}) \end{cases} \tag{6·23}$$

6.2.3 Angle PI Regulation via Single Dimension Luenberger Observers

Rotor position θ can be obtained through the integration of angular velocity given by

$$\hat{\theta} = \int \hat{\omega}dt \tag{6·24}$$

However, the position deduced by (6·24) can not cover the error from the initial condition, integration offset and wrong correction from the measurement noise or modelling error. A position correction mechanism [6·4] is introduced as

$$\begin{cases} \varepsilon_d = G_{PI}(i_d^{\,*} - i_d), \mathrm{sgn}(\hat{\omega}) = \begin{cases} 1 & (\hat{\omega} > 0) \\ -1 & (\hat{\omega} < 0) \end{cases} \\ \hat{\theta}_c = \hat{\theta} + \mathrm{sgn}(\hat{\omega})|\varepsilon_d|, \end{cases} \tag{6·25}$$

where ε_d denotes the corrective error. Position correction is decided by the output of a PI controller, the input of which is the difference between instruct value of i_d^* and actual value i_d and gain value is G_{PI}. The position correction can compensate the offset of the estimated position through integration and it is experimentally proven effective even if the estimated speed which is used for integration is unstable. Matsui [6·4] first proposed the position correction mechanism in the sensorless observer-based d-q rotational co-ordinate frame making use of the theoretical principle that the angular difference between the actual and hypothetical axes can be estimated by the voltage difference between the actual and hypothetical axes. Hereby, hypothetical axes refer to d-q rotational co-ordinate generated by the sensorless observer while actual axes refer to actual rotor-oriented rotational co-ordinates. The estimation of angular difference can be calculated in the conventional PI controller.

The symbol of corrective quantity ε_d is decided by the direction of rotation of the PMSM [6·1~6·3]. If the rotor position is estimated, the d-axis direction generated by the sensorless observer should also approximately respond to the rotor flux axis. If field-oriented theory which sets "Id=0" is applied in a sensorless observer-based PMSM control, the difference ε_d also should be zero. However, the position estimation error by a sensorless observer always exists and occasionally rises. The d-axis generated by the sensorless observer is not completely aligned with the rotor flux axis. Matsui [6·4] shows that the difference ε_d reflects the projection of the back EMF developed in the q-axis and is zero when the position estimation error is tuned towards zero by a PI regulator in (6·25).

6.2.4 Pure Flux Linkage Speed Measurement based on Back-EMF

The SDL observer-based state estimations with a large Eigen value can directly estimate speed by the state equation in (6·22) at start-up. However, shortly afterwards, the estimated speed easily becomes unstable [6·1]-[6·3]. The problem is solved by employing another speed measurement [6·8] based on pure d-q flux linkage described as

$$\begin{aligned} &\omega \approx F_q / \psi_f = (F_\beta \cos\theta - F_\alpha \sin\theta)/\psi_f \\ &\sin\theta = \psi_\alpha / \psi_f, \cos\theta = \psi_\beta / \psi_f \end{aligned} \tag{6·26}$$

where F_q is the projection of the back-EMF in the q-axis. F_α and F_β are respectively the projection of the back-EMF in the α — β co-ordinate frame. Sine and cosine functions are replaced by the pure flux linkage ψ_α / ψ_f and ψ_β / ψ_f shown in (6·26).

Equation (6·26) is deduced from the d-q rotor-oriented voltage balance equation for the PMSM : $u_q = Ri_q + L_s pi_q + \omega L_s i_d + E_m$, where E_m is the back-EMF generated by the PMSM rotor. p is the derivative expression "d/dt". As the relationship between back-EMF and flux linkage Ψ_f is " $E_m = \omega\Psi_f$ ", the angular velocity is eventually derived by substituting the expression for back-EMF into d-q rotor-oriented voltage balance equation as " $\omega = \frac{u_q - Ri_q - L_s pi_q}{\Psi_f + L_s i_d}$ ". Considering field-oriented space vector control theory "i_d=0" and the variation of i_q generates relatively smaller voltage change " $L_s pi_q$ " through the inductance L_s. The simplified deduced speed is $\omega_e \approx \frac{u_q - Ri_q}{\Psi_f}$. The electromagnet force projection in q-axis is approximately treated as " $F_q \approx u_q - Ri_q$ ", and its steady state expression is " $F_q = F_\beta \cos\theta - F_\alpha \sin\theta$ ".

Therefore, the speed is finally expressed by the α-β projection of the electromagnet force F_q in (6·26). If the α-β projection of flux linkage ψ_α and ψ_β are already known, (6·26) can be used to estimate the angular velocity directly replacing the inaccurate state estimation for speed in (6·22).

6.3 Experiment Performance

6.3.1 Shaft Position Estimation characteristics

The SDL-based sensorless controlled PMSM operated smoothly through its shaft which was coupled to a DC shunt generator in constant torque output mode or in generation mode. The test PMSM motor is shown in chapter 2. This full-digital system hosts peripherals including 12-bit A/D modules for DC-link voltage and current acquisition, a 12-bit D/A module for variable output observation and a digital interface for implementing power inverter control current through a three phase hysteresis PWM algorithm. The measurements of the actual rotor position and speed were obtained using a 2048 ppt incremental optic-encoder mounted on the PMSM shaft and converted via USdigital Pulse-to-Binary-to-Converter. The shaft position and speed characteristics were obtained and compared with the corresponding position and speed characteristics with a SDL observer with sensorless controlled PMSM.

The estimated shaft position waveform by SDL observer was found to lag the actual shaft position waveform in phase as illustrated in figs. 6·3 to 6·8. The estimated

shaft position offset to the actual shaft position waveform by SDL always plots the reversal saw-tooth- or triangular- shaped curve shown in these figures. The estimated position offset pattern similar to band-band control is implemented by the angle PI regulator such that the corresponding estimated position is maintained within the hysteresis band Δ, which is actually the corrective quantity ε_d generated by the PI regulator in (6·25).

The absolute average measured error between the estimated rotor position via the SDL observer and actual rotor position is 12.3 elec ° which is much higher than the values quoted for FLO, EKF and LKF in chapters 3, 4 and 5. The magnitude of the corrective offset from the saw-tooth-shaped waveform for the estimated rotor position via the SDL observer is decided by tuning the output ε_d generated by PI regulator. The Eigen value λ of the SDL observer in (6·25) affects the convergence speed for the estimated quantities including the angular velocity, although the rotor position is extracted from the integration of angular velocity in (6·24) with correction by PI regulator in (6·25), when the estimated position tends to freewheel down in figs. 6·3-6·8. The speed is still affected by the Eigen value after PI regulator forces the estimated position to boost via correction action at the peak point of the saw-tooth-shaped waveform. Figs.6·3-6·8 shows that the saw-tooth-shaped waveform representing the estimated rotor position consists of two parts illustrated in fig. 6·3: a boost part from the correction of $\varepsilon_d = G_{PI}(i_d^* - i_d)$ from the PI regulator in (6·25), and a freewheel part for the integration of $\hat{\theta} = \int \hat{\omega} dt$ from the SDL observer in (6·24).

Figs. 6·3-6·8 show that the estimated shaft position waveform stays far away from the actual one while the absolute Eigen value λ is increased from -800 to -3200. For example, apparently although the correction of ε_d from the PI regulator ensures that the estimated rotor position can reach the actual value in fig. 6·5, the freewheeling effect from the integration decided by the Eigen value λ= -1500 still make the estimated rotor position value remain different to the actual value.

It is obvious that the estimated saw-tooth-shaped rotor position waveform circulates the actual rotor position waveform when the Eigen value λ of the SDL observer is increased. The reason is the indirect correction scheme of the angular PI regulator, which amplified the difference of the d-axis current i_d and its reference i_d^* and uses PI regulator gain to obtain the corrective quantity ε_d.

Theoretically, if the d-axis current i_d is aligned with its reference i_d^*, there is no rotor position estimation error because the estimated d-q rotational co-ordinate frame is aligned with the actual one and the estimated rotor position is thereby aligned with the actual one. However, two factors affect the correction accuracy: the estimated error for d-axis current i_d and the appropriate gain of angular PI regulator. The estimated error in the d-axis current i_d is decided by phase current I_a, I_b and I_c measurement and the estimated rotor position via the SDL observer. The estimated rotor position via the SDL observer is the other reason that the corrective effect via angular PI regulator is worse than covariance correction used via the Kalman filter observer discussed in chapters 4 and 5.

The gain selection of the angular PI regulator also affects the corrective result via the SDL observer, for example, the over-tuning from angular PI regulator causes over estimation of the rotor position via the SDL observer shown in fig. 6·4. Besides, the selection of the Eigen value of the SDL observer affects the estimation error of rotor position greatly. The greater the chosen Eigen value of the SDL observer, the worse is the stability of sensorless control system with the SDL observer. Subsequently the unstable speed estimation could result in an unpredictable integration error from (6·24). The integration error from unstable estimation of speed could generate the greater position offset relative to the actual rotor position waveform for the axis reference circulated by the saw-tooth-shaped estimated rotor position via the SDL observer.

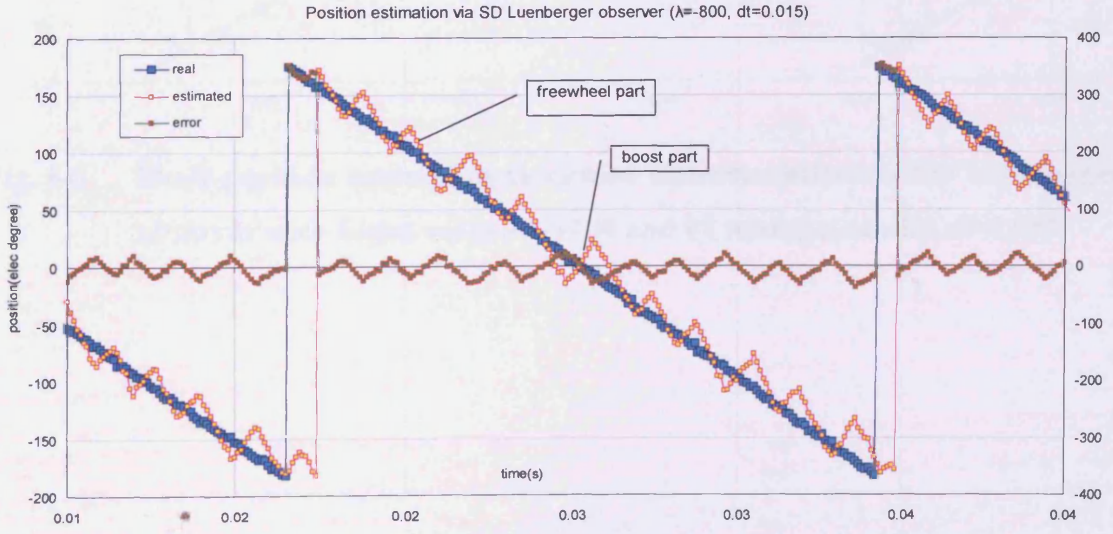

Fig. 6·3 Shaft position estimation anticlockwise characteristics via SD Luenberger observer with Eigen value λ=-800 and PI tuning quantity dt=0.015

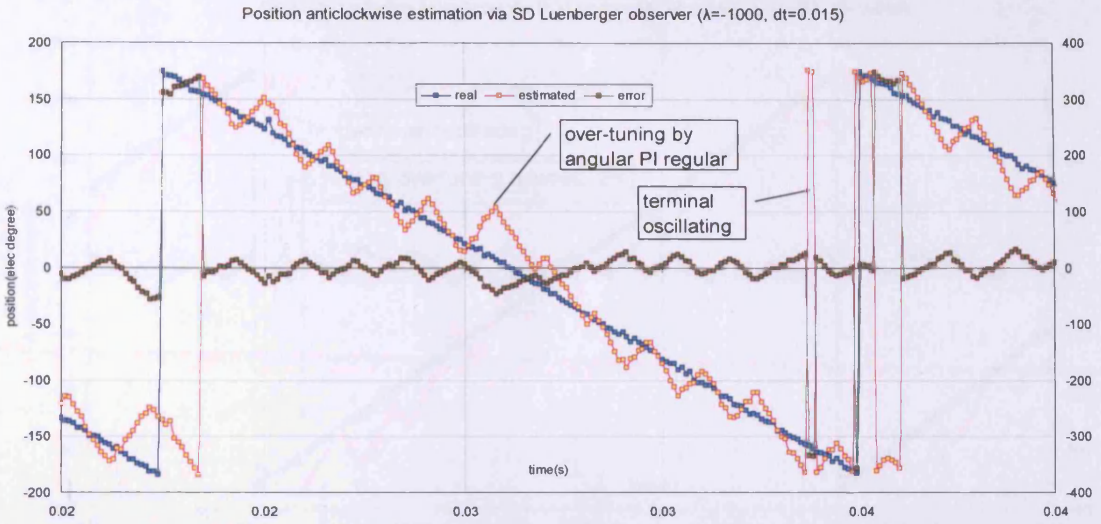

Fig. 6·4 Shaft position estimation anticlockwise characteristics via SD Luenberger observer with Eigen value λ=-1000 and PI tuning quantity dt=0.015

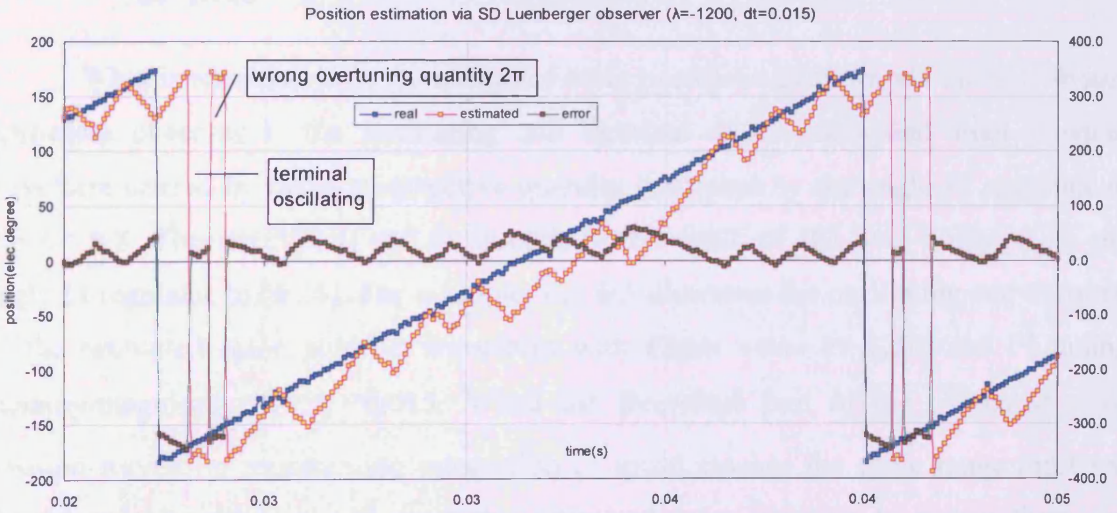

Fig. 6·5 Shaft position estimation clockwise characteristics via SD Luenberger observer with Eigen value λ=-1200 and PI tuning quantity dt=0.015

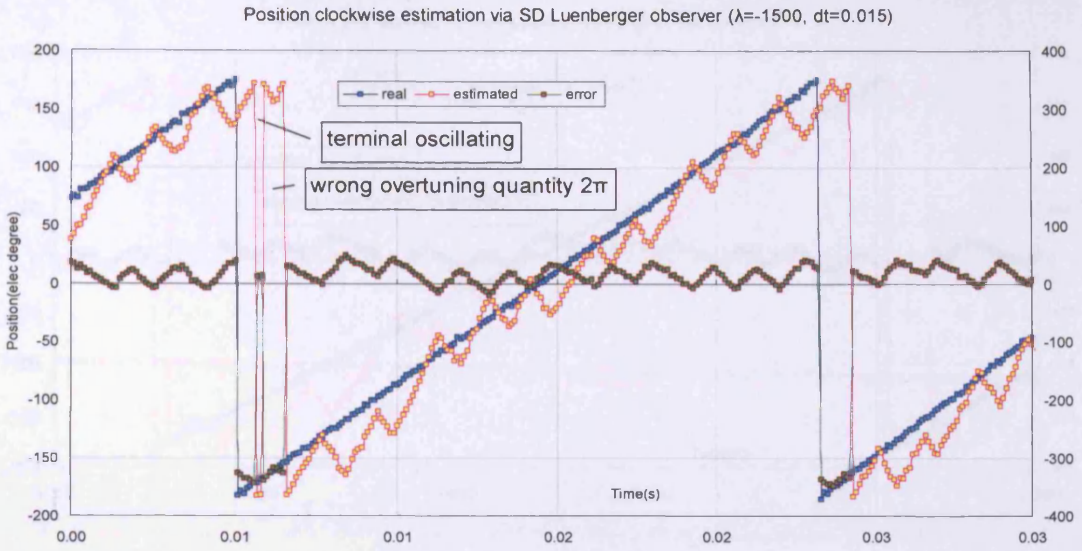

Fig. 6·6 Shaft position estimation anticlockwise characteristics via SD Luenberger observer with Eigen value λ=-1500 and PI tuning quantity dt=0.015

What is remarkable in the estimated rotor position waveform via the SDL-based sensorless observer is the oscillating end terminal of the estimated shaft position waveform caused by the ± π corrective quantity generated by the angle PI regulator in figs.6·4-6·8. The oscillating end is essentially the result of the over-tuning from the angle PI regulator in (6·25). For example, fig. 6·5 illustrates the oscillating end terminal of the estimated rotor position waveform with Eigen value λ=-1200 and PI tuning quantity/magnitude dt= ε_d =0.015. When the freewheel part of the estimated rotor position waveform representing integration of speed reaches the cycle range limit +π, the control algorithm would reset the estimated rotor position to restart from –π. However, the angular PI regulator would suffer from greatest error between the estimated d-axis current i_d and its ideal reference i_d^* when the rotor position reached the terminal of the electrical cycle (± π/180 elec°).

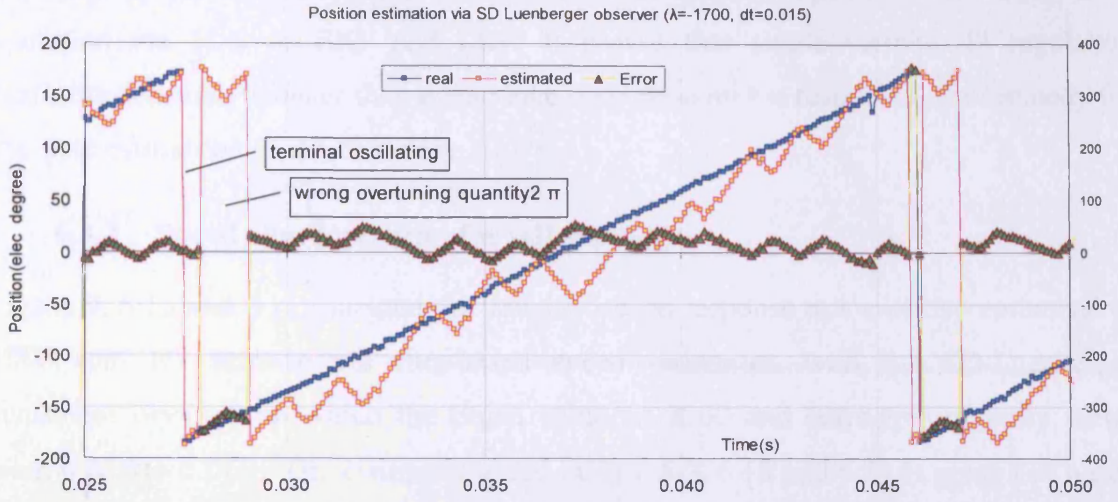

Fig. 6·7 Shaft position estimation clockwise characteristics via SD Luenberger observer with Eigen value λ=-1700 and PI tuning quantity dt=0.015

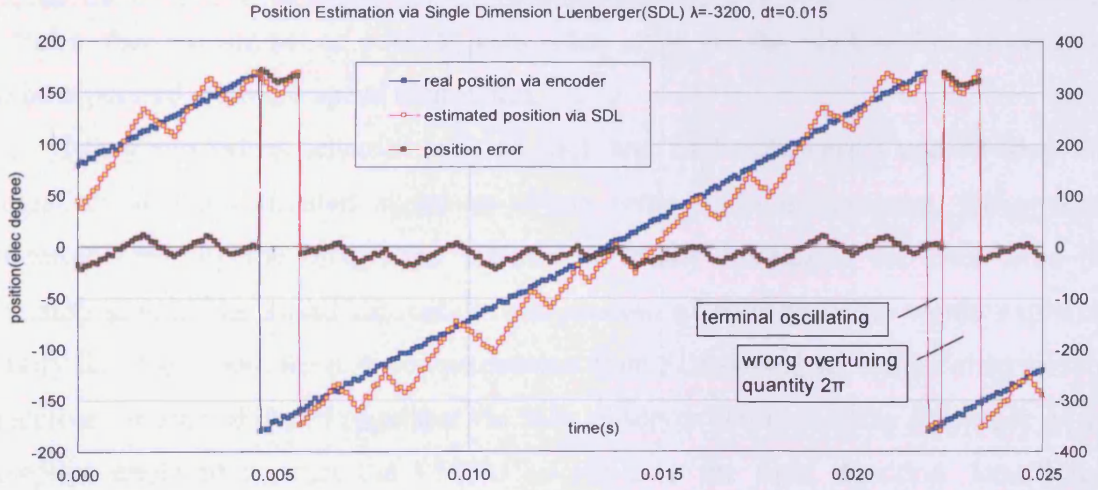

Fig. 6·8 Shaft position estimation clockwise characteristics via SD Luenberger observer with Eigen value λ=-3200 and PI tuning quantity dt=0.015

Occasionally the angular PI regulator made the wrong correction of position with a magnitude up to 2π and results in the oscillating pulse generated. Further analysis reveals that the terminal of the rotor position cycle is the transition area between +π and –π, during which the d-axis current correspondingly generates the transit between + i_d and - i_d (ideal reference i_d^* =0). The difference between the d-axis currents $\pm i_d$ eventually causes the angular PI regulator in (6·25) to generate the wrong correction quantity of up to 2 π in figs. 6·4-6·8. It is pointed out that the terminal oscillation of the estimated position curve in fig.6·3-6·8 can be filtered by control software, however, on

the contrast, the oscillation has been found in the estimated position curves at steady operation via FLO or EKF and LKF. It proves that single variable PI regulation performs definitely weaker than covariance correction on the respect of error remedy for the state estimation of the observer.

6.3.2 Speed characteristics for self-start up:

Figs. 6·9, 6·10 and 6·11 illustrate the transient speed response to a unit step command of 1000 rpm for start-up via flux-based speed estimation with the SD-Luenberger sensorless observer in which the Eigen value is -3200 and corrective quantity varies from 0.008 to 0.015 . The estimated speed in figs. 6·9, 6·10 and 6·11 is generated based on pure flux linkage speed estimation in (6·29). The reason for employing the method of flux linkage is that the estimated speed directly from the SD-Luenberger observer is unstable as explained in section 6.1.5. [6·1-6·3] also report a similar situation. The benefit of pure flux-based speed estimation used in the SDL observer-based sensorless control is that the impact of position estimation error via the SD-Luenberger observer can be separated from the speed estimation.

Many sensorless schemes such as EKF and LKF (chapters 4 and 5) adopt the integration of the estimated speed to obtain rotor position; however, the position estimation error by the integration scheme inevitably introduces the error from the estimated speed. The speed estimation independent of rotor position would explicitly identify the effect from the position estimation from SDL-based sensorless observer.The corrective variable of the PI regulator via SDL observer determines the amplitude of the corrective angle to instruct the PMSM to move in the right direction. Insufficient correction or wrong correction can cause the rotor to move toward the wrong direction, then the wrong position inversely generates the corrective input ΔId to be amplified in a single variable PI regulator, finally the right/enhanced corrective angle quantity would instruct the rotor to move in the right direction. The wrong movement first and right movement afterwards is the source of rotor swing shown in fig.6·9. The SDL observer replies on the variable correction after the failure to implement self start up at the arbitrary position. A similar situation occurs happen in EKF, which also relies on the covariance correction after the failure from wrong convergence to complete self start up.

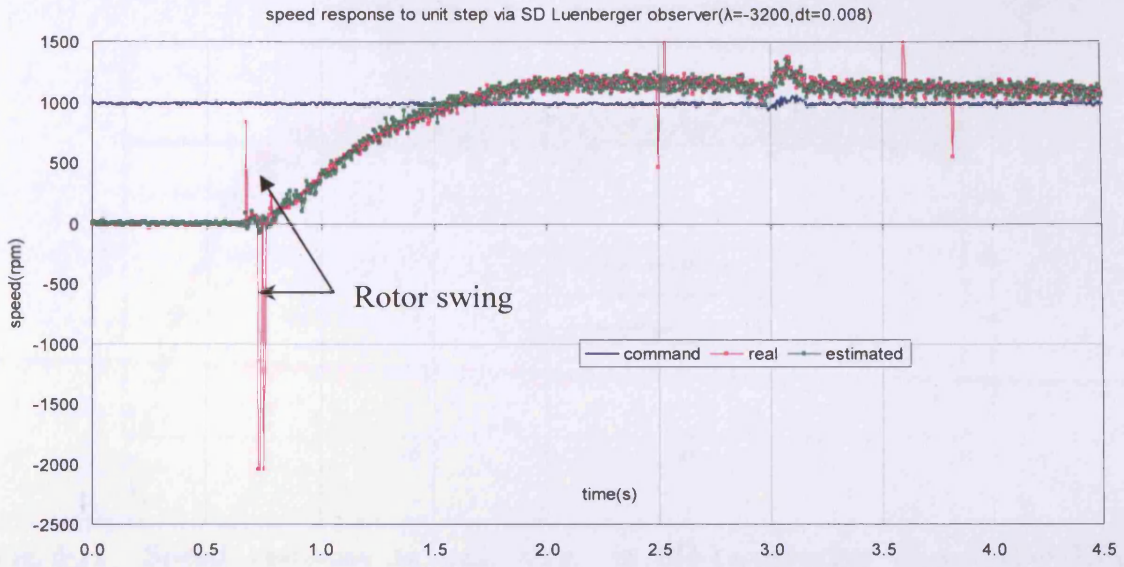

Fig. 6·9 The speed response to unit step via the SD-Luenberger observer (λ=-3200,dt=0.008)

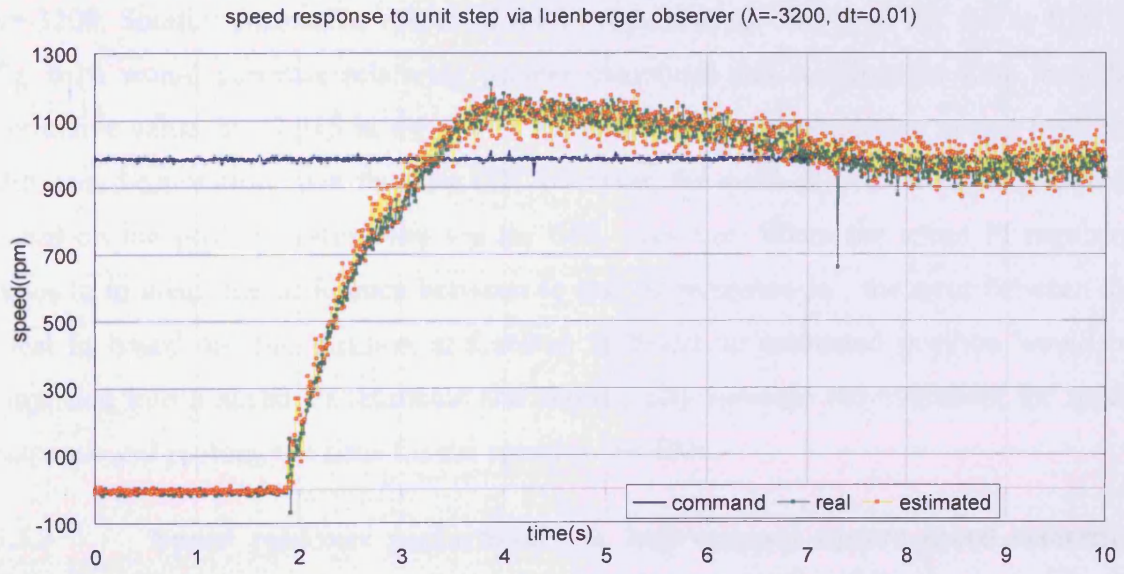

Fig. 6·10 Speed response to unit step via SD-Luenberger observer (λ=-3200, dt=0.01)

Fig. 6·11 Speed response to unit step via SD-Luenberger observer(λ=-3200, dt=0.015)

Figs. 6·9, 6·10 and 6·11 illustrated the corrective quantity $\Delta t(\varepsilon_d)$ from the angle PI regulation varied from 0.008 to 0.015 affecting the speed overshoot with Eigen value λ=-3200. Smaller corrective values of the PI regulator Δt =0.008 in fig. 6·9 or 0.01 in fig. 6·10 would generate relatively greater overshoot and stabilization time than the corrective value Δt =0.015 in fig. 6·11. Although the speed estimation comes from the flux-based estimation other than the SDL observer, the quad-axis current Iq is generated based on the position estimation via the SDL observer. When the speed PI regulator tunes Iq to adapt the difference between Iq and its reference Iq^*, the error between the ideal Iq based on true position and actual Iq based on estimated position would be amplified into a speed PI regulator and sequentially increase the overshoot for speed response and prolong the time for the speed to stabilize.

6.3.3 Speed response performance to bidirectional square speed reference via flux-based estimation under the SDL observer-based sensorless control:

The bidirectional speed reference for speed response test would change the magnitude between +1000 rpm and -1000 rpm every 4 seconds. The estimated speed for SD-Luenberger-based sensorless controlled PMSM is obtained from the pure flux linkage estimation shown in (6·26). The following experiment shows that same Eigen value with different position corrective quantity from the PI regulation would affect the speed response characteristics with a bipolar square speed reference.

Figs. 6·12-6·17 show the estimated speed response to bipolar reference transition between +1000 rpm and -1000 rpm under the SDL observer-based sensorless control

with the Eigen-value λ=-3200 when the corrective quantity $\Delta t(\varepsilon_d)$in (6·25) from the angular PI regulator was tuned from 0.0009 to 0.02. Figs.6·12-6·15 illustrate the deteriorated speed response to the bipolar reference transition due to inappropriate corrective quantity $\Delta t(\varepsilon_d)$= 0.0095~0.01. First, the inappropriate corrective quantity causes the reduced acceleration time, for example, fig.6·12-6·15 shows that the estimated and actual speed take a long time to reach +1000 rpm command and the high amplitude of overshoot also makes the speed take a longer time to stabilize at 1000 rpm. On the contrary, the appropriate corrective quantity $\Delta t(\varepsilon_d)$ =0.02 in fig. 6·16 could increase the acceleration time and reduce the overshoot amplitude.

Fig. 6·16 shows that both the estimated and actual speeds promptly reach ±1000 rpm reference and become stabilised rapidly. Fig. 6·17 shows that the inappropriate $\Delta t(\varepsilon_d)$ =0.025 over-tunes the speed response inversely, i.e., the stabilized speed is lower than the reference.

Normally, the speed performance should be affected only by the PI regulator in the field-oriented close-loop control system in fig. 3·10. The experiment shows that the inappropriate corrective quantity Δt could affect the accuracy of quadrant-axis current Iq which relies on the estimated rotor position. The inappropriate corrective quantity Δt from the angle PI regulator would make the generated quadrant current Iq different to the ideal value, thereby the required quadrant current Iq for acceleration could not be obtained to drive the PMSM and slow acceleration occurs as shown in figs.6·12-6·17.

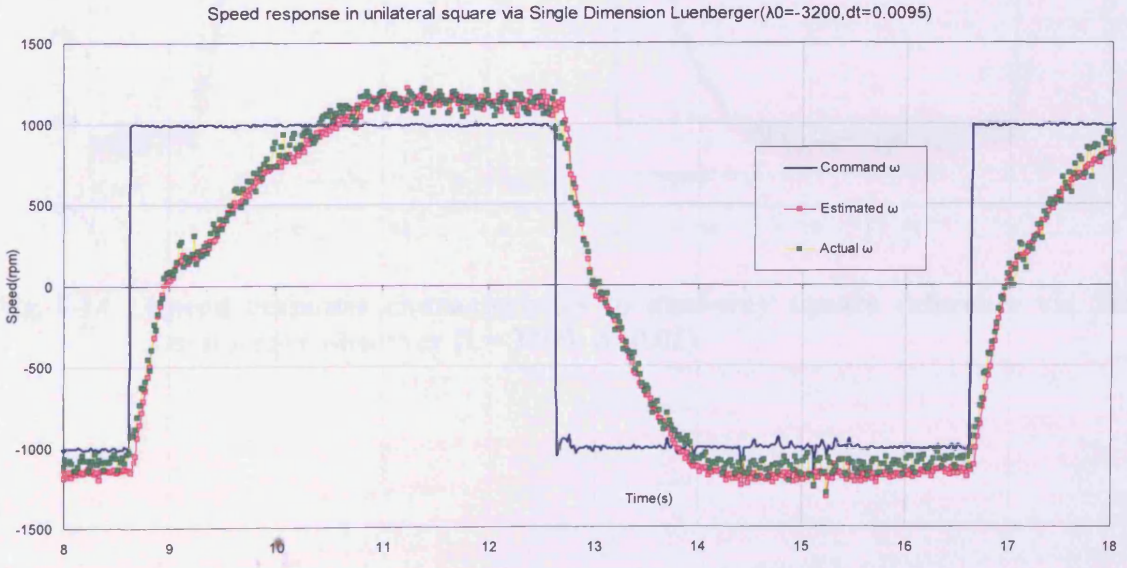

Fig. 6·12 Speed response characteristics to dual-way square reference via SD-Luenberger observer (λ=-3200, Δ=0.0095)

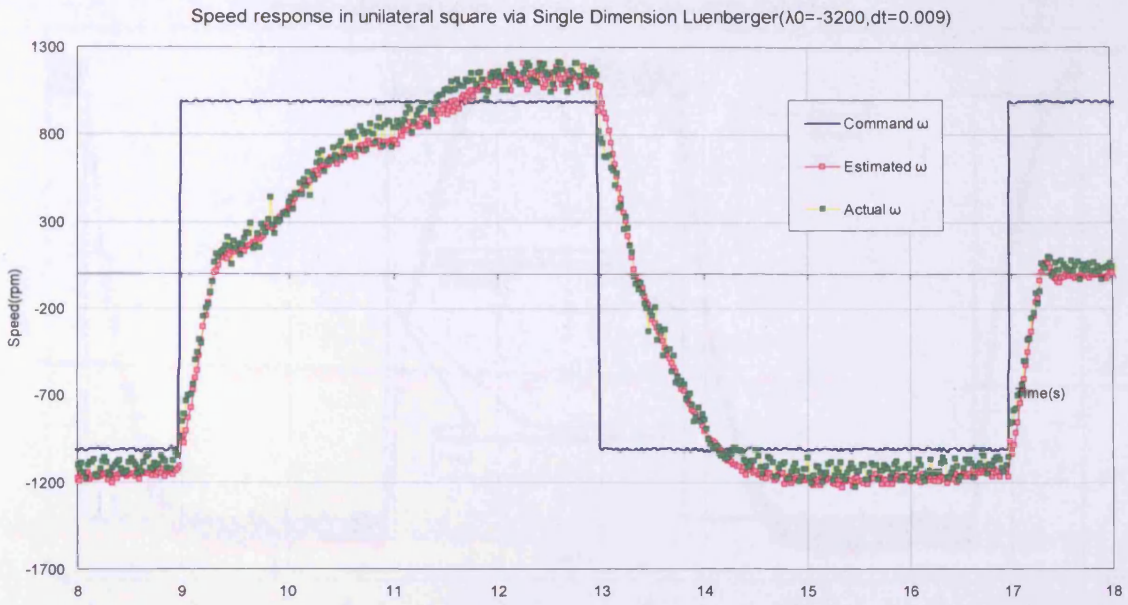

Fig. 6·13 Speed response characteristics to dual-way square reference via SD-Luenberger observer (λ=-3200, Δ=0.009)

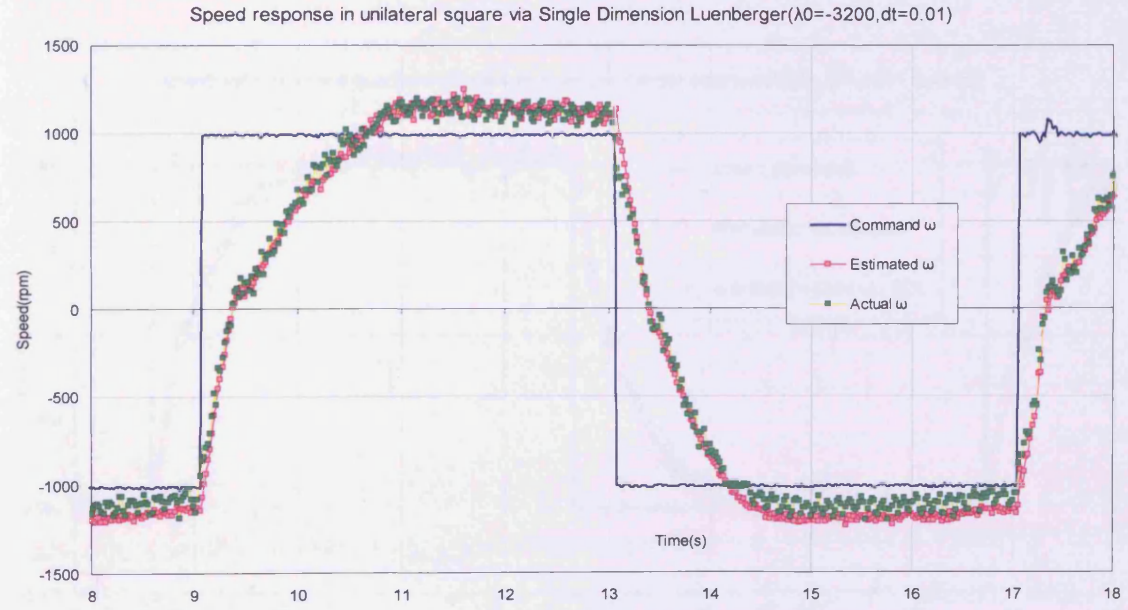

Fig. 6·14 Speed response characteristics to dual-way square reference via SD-Luenberger observer (λ=-3200, Δ=0.01)

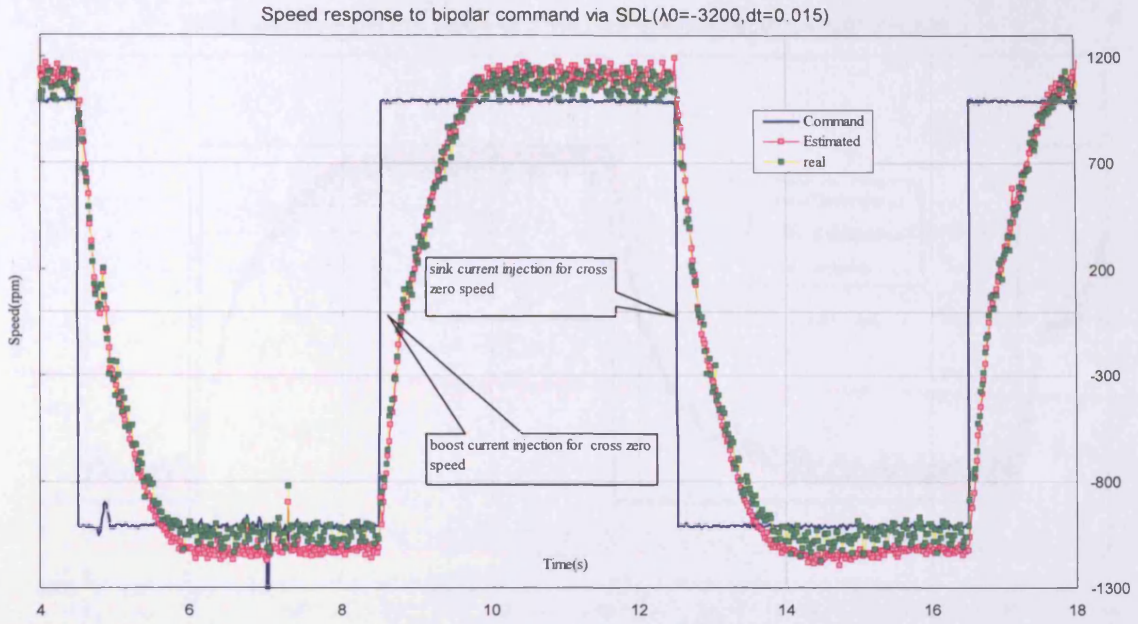

Fig. 6·15 Speed response characteristics to dual-way square reference via SD-Luenberger observer (λ=-3200, Δ=0.015)

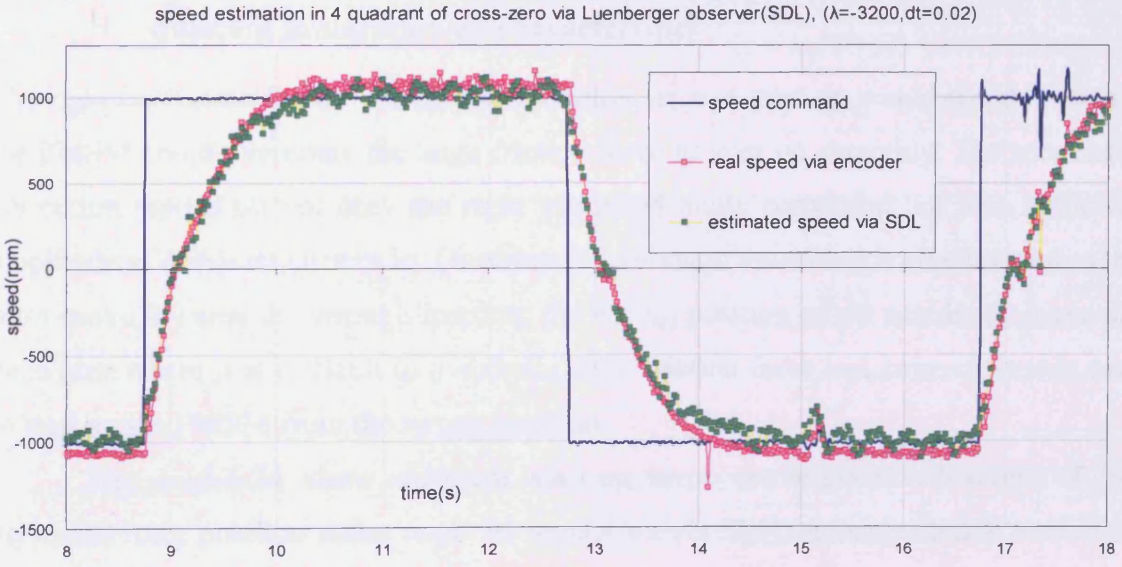

Fig. 6·16 Speed response characteristics to dual-way square reference via SD-Luenberger observer (λ=-3200, Δ=0.02)

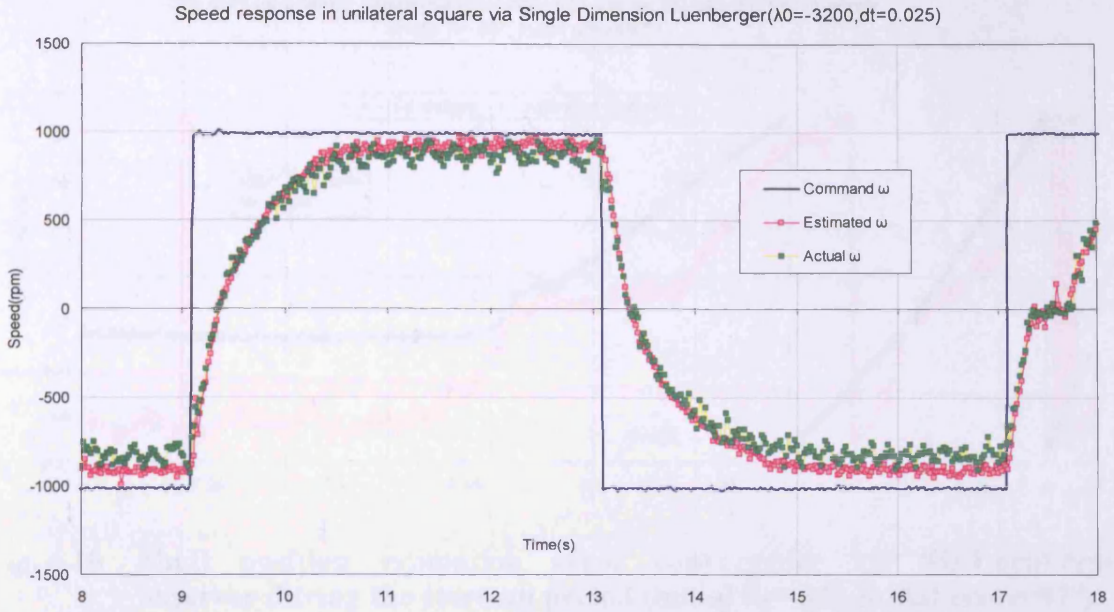

Fig. 6·17 Speed response characteristics to dual-way square reference via SD-Luenberger observer (λ=-3200, Δ=0.025)

6.3.4 Shaft Estimated Position Error Convergence by PI regulation for different initial start-up characteristics

The right correction for the initial shaft position error at start-up would decide whether the PMSM could overcome the large friction force to start up smoothly. The successful correction replies on not only the right estimated angle correction but also sufficient amplitude of quadrant current Iq. Occasionally although the wrong correction makes the rotor move towards the wrong direction, the wrong position might accidently leave the dead-area where it is difficult to overcome large friction force and conversely it is easy to start up the PMSM from the wrong position.

Fig. 6·18-6·24 show different start-up error convergence situations of the estimated rotor position under angle PI regulation via SD-Luenberger-based sensorless control where the Eigen value λ=-3200 and corrective quantity Δt=0.015. Initial shaft position errors are respectively: θ=68°, 97°, 174° and 257°. It is remarkable that the rotor swing caused by trial-and-error correction implies the flexible and imprecise correction from the angle PI regulation. The flexible correction ability can adapt the different start-up loads to pull the PMSM off the dead-area, but it is easy to generate poor correction. The results in figs. 6·18-6·24 proves that single variable PI regulation can make SDL observer start up at any arbitrary position.

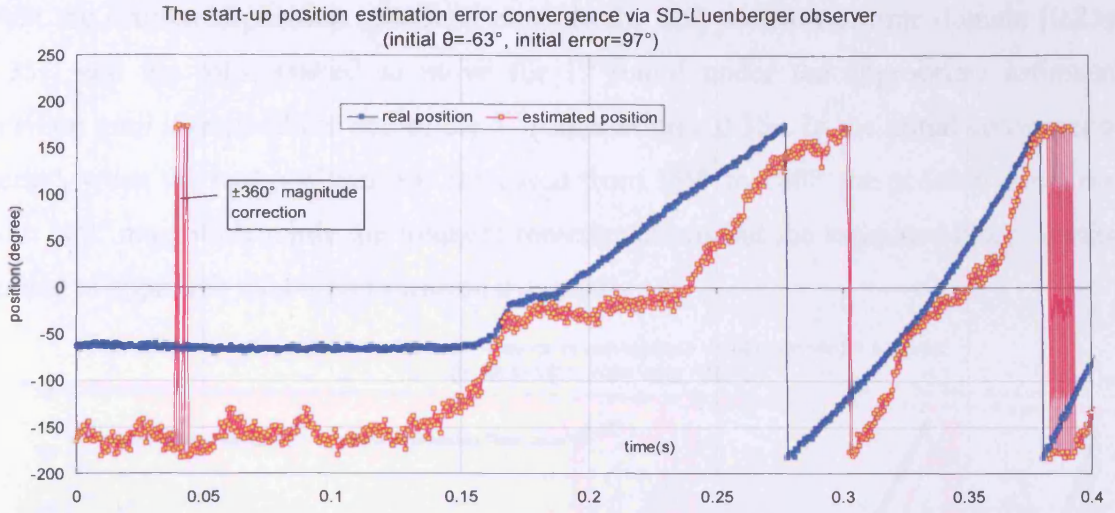

Fig. 6·18 Shaft position estimation error convergence via SD-Luenberger observer during the start-up period (initial θ_0=-63°, initial error=97°)

The initial estimated rotor position error via the SDL observer would tend to decrease under the tuning from angular PI regulator shown in fig. 6·18 where the initial real rotor position is -63° and the initial position error is 97°. During the initial tuning period, the angular PI regulator in fig. 6·18 even produces the corrective quantity with magnitude up to 360° to force the rotor to move. The transient ±360° magnitude correction at start-up in fig. 6·18 tries to move the PMSM from standstill via the position PI regulation.

Whether PMSM starts or not is decided by the fault correction capability of the PI regulator within the SDL observer. The closer the initial estimated position remains to the initial actual position, the sooner the SDL-based sensorless control PMSM rotor will start to move. After the transient ±360° correction the real rotor position gradually moves towards the estimated position as illustrated in fig. 6·18.

If the maximum 360° magnitude correction from the PI regulation via the SDL observer can compensate for the initial offset to the actual position shown in fig. 6·19 and the initial real rotor position and position errors are 159° and 257° respectively, the estimated rotor position was driven rapidly to approach the real value by the corresponding quadrant current Iq. Fig. 6·19 illustrates that several correction actions with the 360° magnitude were made in time domain [0.19s, 0.25s] to compensate the rotor initial offset 257° between the estimated and actual position. Initially the estimated position driven by the PI regulation reached -180° in time domain [0s, 0.19s] then the estimated position under correction with 360° magnitude from the PI regulation reached 180° which was close to the initial real position 159° in time domain [0.19s, 0.25s].

Next the estimated position remained close to the real position in time domain [0.25s, 0.35s] and the rotor started to move for 1st round under the appropriate estimated position until it reached the end of the 1st round at time 0.35s. In the initial convergence period, when the real position was increased from 159° to 180°, the position correction with 360° magnitude made the frequent remedy actions but the estimated rotor position tended to approach the correct position eventually.

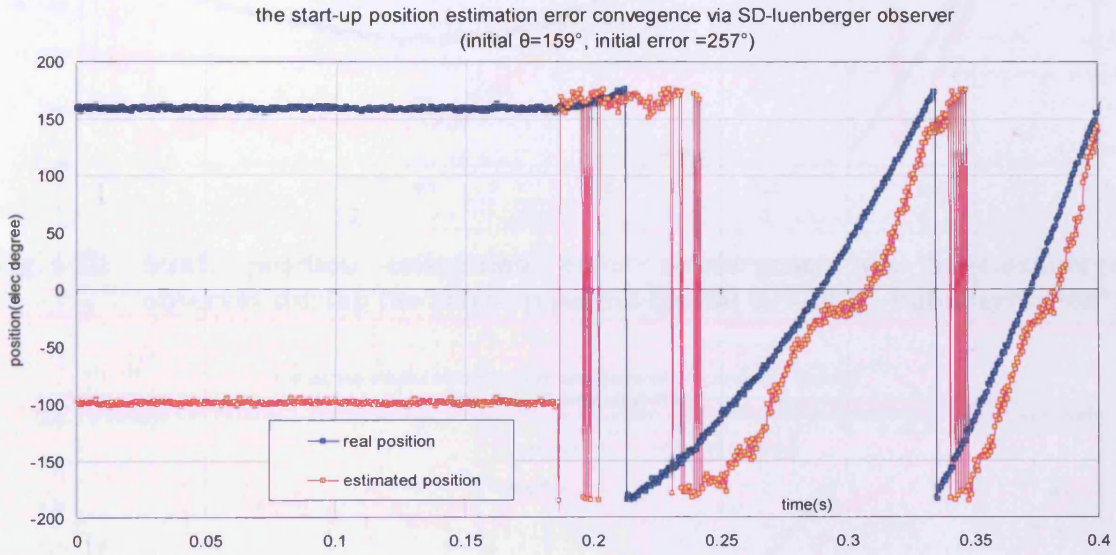

Fig. 6·19 Shaft position estimation error convergence via SD-Luenberger observer during the start-up period (initial θ_0=159°, initial error =257°)

Angular PI regulation via the SDL observer always amplifies the difference between the estimated direct-axis current I_d and its ideal value in field-oriented control to compensate for the rotor position. In the initial start-up period the correction magnitude could be increased until the difference of I_d disappears. For example, fig. 6·20 illustrates that the initial rotor error dropped on correction of the variable PI regulation when the initial position is -28.3° and initial error is 68°, was not changed until the 360° position correction forced the rotor to move towards the situation where the estimated error tended to decrease by angular PI regulation.

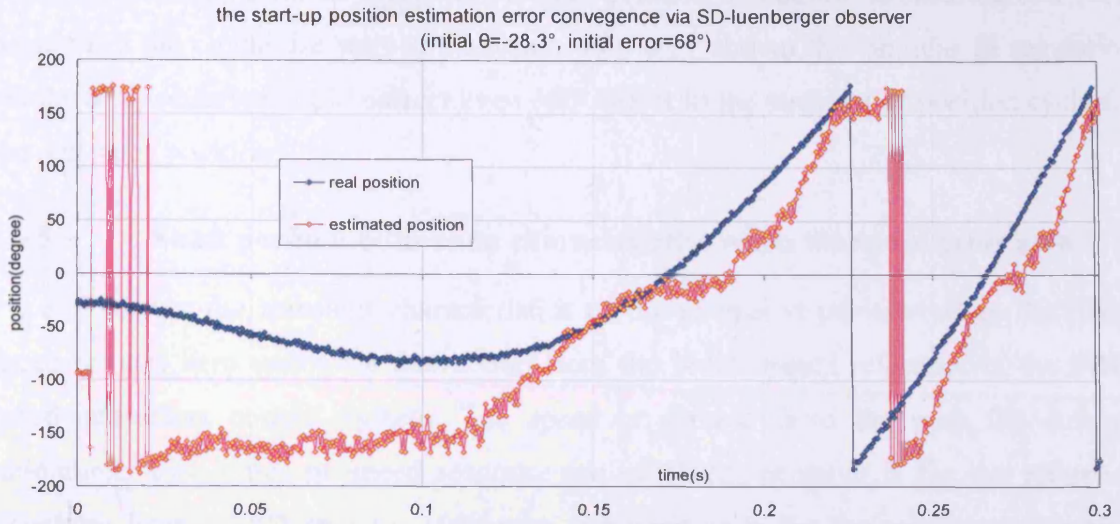

Fig. 6·20 Shaft position estimation error convergence via SD-Luenberger observer during the start-up period (initial θ_0=-28.3°, initial error=68°)

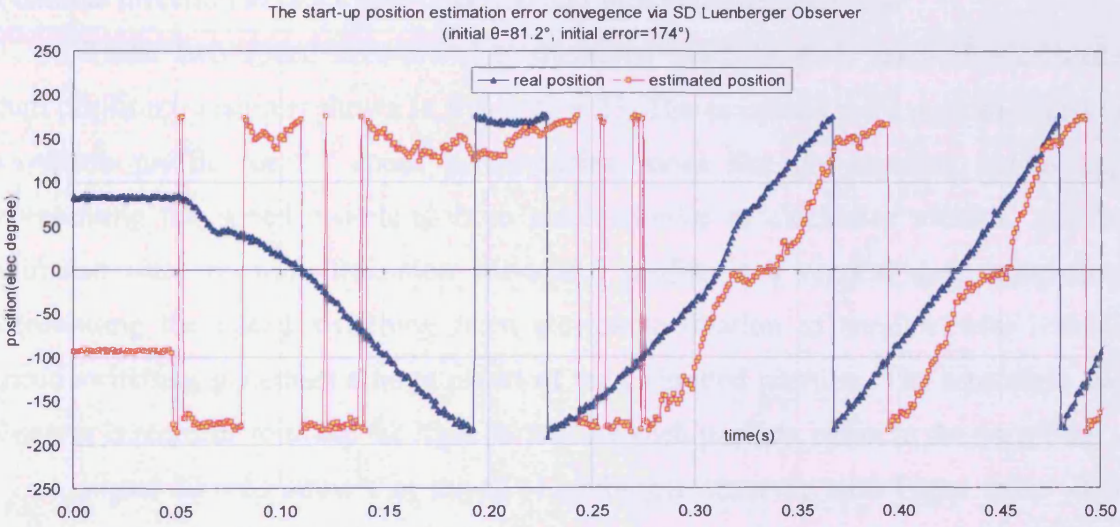

Fig. 6·21 Shaft position estimation error convergence via SD-Luenberger observer during the start-up period (initial θ_0=81.2°, initial error=174°)

Another example showing that angular PI regulation makes the major contribution to correction is shown in fig. 6·21 where the initial θ_0=81.2° and the initial error=174°. Even if the angular PI regulation via the SDL observer drives the estimated rotor position to stay away from the real position temporarily, the correction continues to amplify the corresponding difference of Id to compensate until the estimated position becomes close to the real one. Fig. 6·21 shows that the position correction with 360° magnitude easily generates the greatest estimated position error to make the real rotor position swing through quadrant current Iq. However when the estimated position naturally recovers to 180°, angular PI regulation promptly makes use of the fairly small

estimated position error to drive the positive position estimation toward the real rotor position in the clockwise start-up direction. Fig. 6·21 shown that angular PI regulation via the SDL observer could correct even 360° offset in the terminal of position cycle for the real rotor position.

6.3.5 Shaft position estimation characteristics when the speed cross zero:

Fig.6·23 shows the transient characteristics of the estimated position when the rising speed crosses zero under the instruction from the bidirectional reference in the SDL-based sensorless control system. The speed is derived from the pure flux-linkage estimation. Two types of speed response are involved: negative is for the reference switching from +1000 rpm to -1000 rpm and positive is for the reference switching from -1000 rpm to +1000`rpm, thus the two types of speed zero-crossing are involved: "+" and "-"speed zero-crossing represent the speed switching from the anticlockwise rotational direction to clockwise direction and vice versa respectively.

These two speed zero-crossing situations generate their respective estimated shaft position transitions shown in figs.6·22-6·23. The estimated rotor position transition waveform profile for "-" speed zero-crossing looks like the standing saddle-shape representing the speed switching from anticlockwise to clockwise rotation. Another estimated rotor position transition waveform profile is a vertical deep snare-shape representing the speed switching from clockwise rotation to anticlockwise rotation. Speed switching generates a large offset of the estimated position. The sensorless state observer is required to make the right correct for such position offset in the transition.

Figs.6·22-6·23 show that the SD-Luenberger observer with Eigen value -3200 and corrective quantity 0.015 can track the shaft position transition when "±" speed zero-crossing could occur. These also illustrate the estimated shaft position tracking the actual transition when at zero-crossing. The SD-Luenberger observer was able to exactly track the position transition when speed zero-crossing occurred.

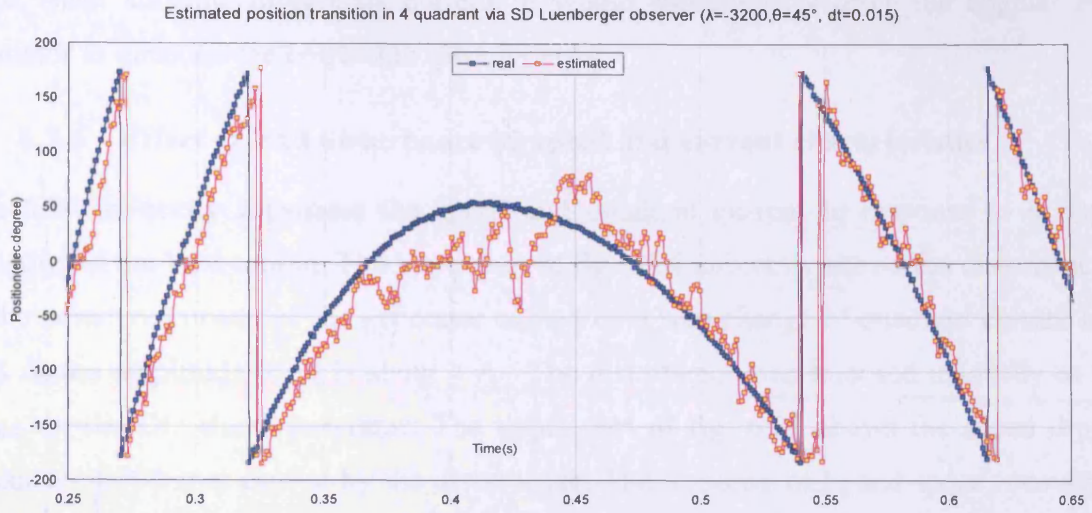

Fig. 6·22 Shaft estimated position transition via SDL (λ=-3200, θ=45°, dt=0.015)

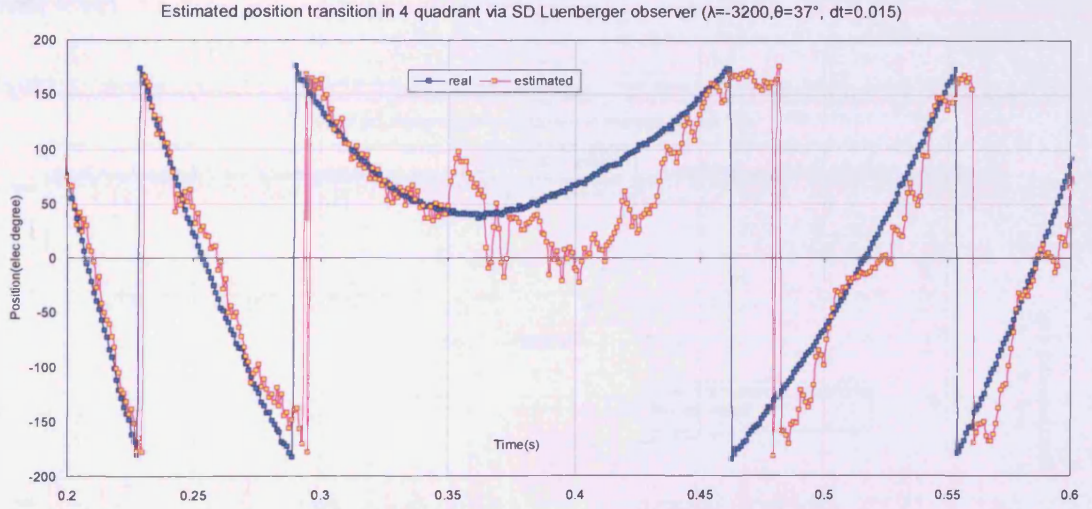

Fig. 6·23 Shaft estimated position transition via SDL (λ=-3200, θ=37°, dt=0.015)

Fig. 6·22 shown that the shaft position transit estimation characteristics at the zero-speed position 45° via the SD-Luenberger observer with an Eigen value of -3200 and angle PI regulation quantity Δ=0.015 where "-"speed reversal switched rotation direction from clockwise to anticlockwise. It can be seen that the large offset to the actual position trace was generated near the zero-speed position. This is also seen in fig. 6·23 which illustrates the shaft position zero-speed transition estimation characteristics at location 37° where the rotor switches direction. When speed crosses zero, the quadrant current Iq is controlled within the small magnitude, thereby the sensed phase current is very small and the calculated direct-axis current Id would generate a high

error. Such accurate direct-axis current Id would subsequently drive the angular PI regulator to generate the correction quantity error.

6.3.6 Effect of load disturbance on speed and current characteristics

Fig. 6·24 indirectly illustrates the speed and quadrant current Iq response to a step variation of the load torque. The lower part of fig. 6·24 indirectly shows the disturbance to the armature current of the generator caused by a step change of quadrant current Iq of 8 A, the amplitude of Iq is about 4 A. The disturbance was imposed manually as a pulse on the DC shunt generator. The upper part of fig. 6·24 shows the speed drop response of 700 rpm caused by the disturbance. The response of Iq and speed recovery show that the SDL observer-based sensorless control system can respond rapidly to adapt the load disturbance through Iq. After disturbance disappears, Iq recover to the normal level.

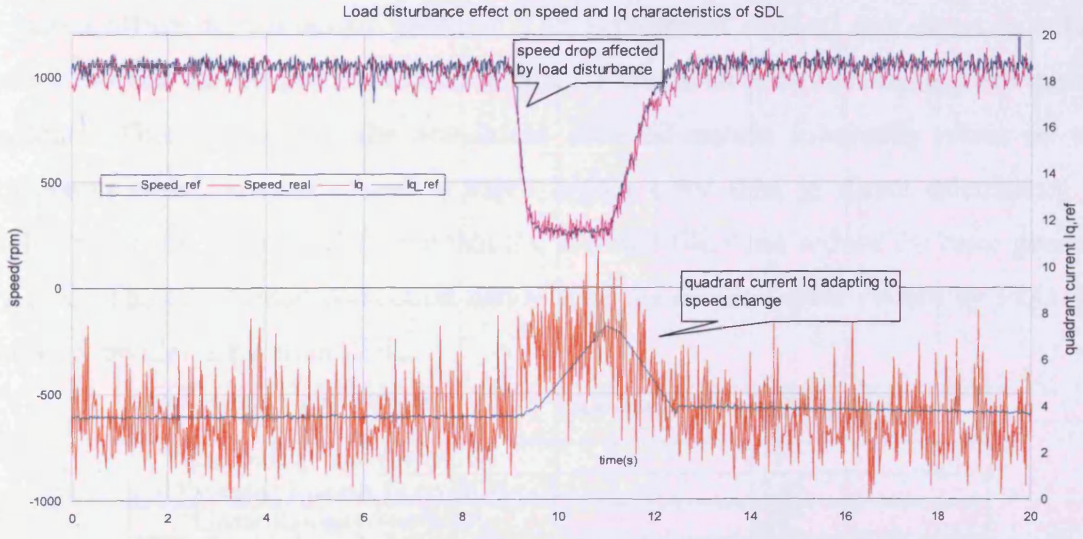

Fig. 6·24 Effect of load disturbance on speed and Iq characteristics of the SDL

6.4 Comparison between single-variable PI regulation scheme and covariance correction

6.4.1 Comparison of position estimation precision

Fig. 6·25 shows the position estimation and error in one cycle for the 4 sensorless observers. Fig. 6·26 (a) and (c) show that FLO and LKF have minimum ripple and error while EKF and SDL have greater errors (fig. 6·26 (b) and (d)). Furthermore, SDL has the highest error. Even edge jump or oscillation from poor correction happens at the terminal of the cycle shown in fig. 6·26 (d).

A comparison of estimation errors is also shown in table 6·1 and fig. 6·25. The calculated result from table 6·1 indicates that average errors are respectively 7.51° (LKF), 8.09° (FLO), 12.4° (EKF) and 13.86° (SDL). The estimation error curve via EKF is steadier than that of the other three estimates. The SDL could cause positive and negative offsets to the actual position. The experiment showed that direct calculation from FLO and the proposed method from LKF involved with flux linkage are the most accurate. This is because the sensorless state-estimation inherently relies on error correction which always causes a much higher error than in direct calculation. The higher precision from LKF shows that the Kalman filter can reduce the error generated by FLO. The covariance correction can reduce the original error caused by FLO. EKF causes a smaller error than SDL.

SENSORLESS TYPE	Average Error (degree)
flux linkage observer(FLO)	8.09°
Extended Kalman filter(EKF)	12.4°
Linear Kalman filter(LKF)	7.51°
single dimension Luenberger(SDL)	13.86°

Table 6·1 The average error list for the estimated position by 4 observers

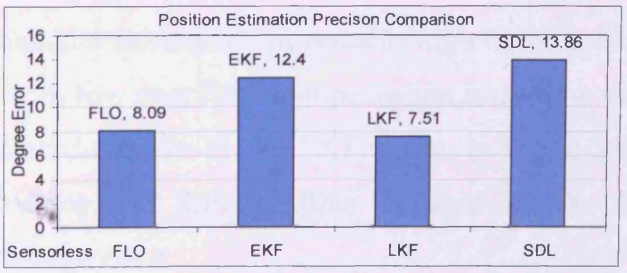

Fig. 6·25 Bar chart representation of **estimation position errors**

Fig. 6·26 compares the estimated position and error waveforms by 4 sensorless observers. The right-angled triangular-shaped curve in fig. 6·26 represents the estimated or actual rotor position tendency profile for one electrical cycle in sensorless operation. The hypotenuse in the triangle-shaped region represents the rotor angle increment for clockwise or decrement for anti-clockwise starting at -180 elec° and ending at 180 elec°. Fig. 6·26 distinctly illustrates the difference in rotor position estimations. The first type is well-proportioned error trend-line with minor ripple or noise created by FLO and LKF observers, the second type is the small-saw-tooth error trend-line with little noise generated by the EKF observer and the third type is the great-saw-tooth error trend-line with high offset and bipolar ripples created by SDL observer.

The error trend-line from the SDL observer in fig. 6·26(d) shows the essential position correction course through a single variable PI regulation. The increment hypotenuse of the ripple implies the position estimation decided by the integration of speed while the decrement hypotenuse of the ripples represents the correction by the PI regulator. The drawback of the single variable PI regulation obviously is that the SDL observer generates the ripple and offset for estimated position and the average estimated position error is greater than for other sensorless observers. Although EKF also generates a saw-tooth error trend-line similar to the SDL, the ripple in its error profile is smallest among all the observers and all the ripples of the error trend-line are not bipolar but monopole, which means they are either positive or negative but not both. This is because the EKF uses covariance correction to limit the position error in the fixed range.

Fig. 6·26(b) shows that the position error trend-line comprises many consistent ripples with almost the same positive magnitudes and noise. This shows the covariance correction can control the average estimated position error within the assigned range. The first type of position error trend-line by FLO and LKF observers in fig. 6·26(a, b) has to have a lower average value than that of EKF and SDL observers. Both position error trend-lines have negligible ripple. The position error trend-lines by FLO and LKF observers have a sinusoidal pattern which remains high in the second half cycle, for the integration of speed with low pass filter compensation is used by the two observers. The position error characteristic curve by the LKF shown in Fig. 6·26(c) has fewer ripples than that by FLO since the Kalman filter is used by the LKF to control the corresponding flux linkage error.

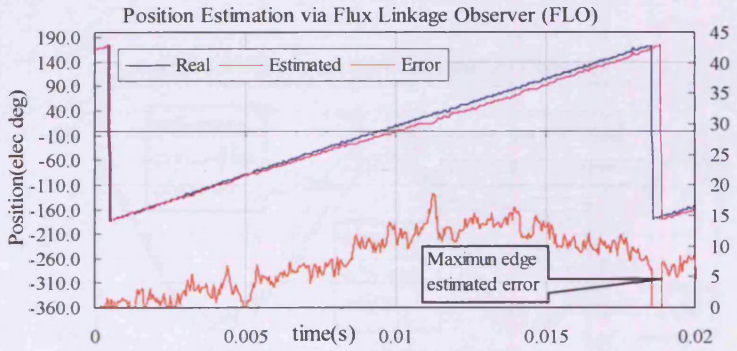

(a) position estimation via FLO

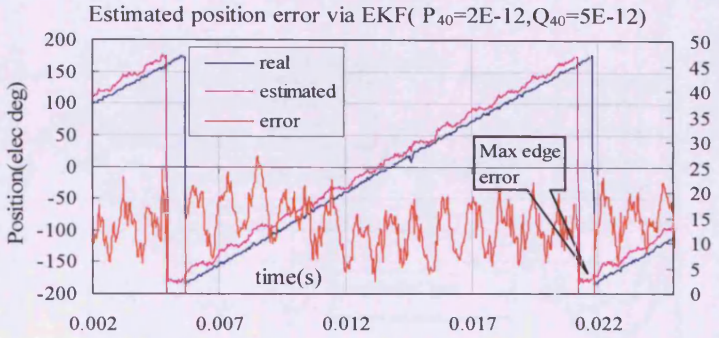

(b) position estimation via EKF

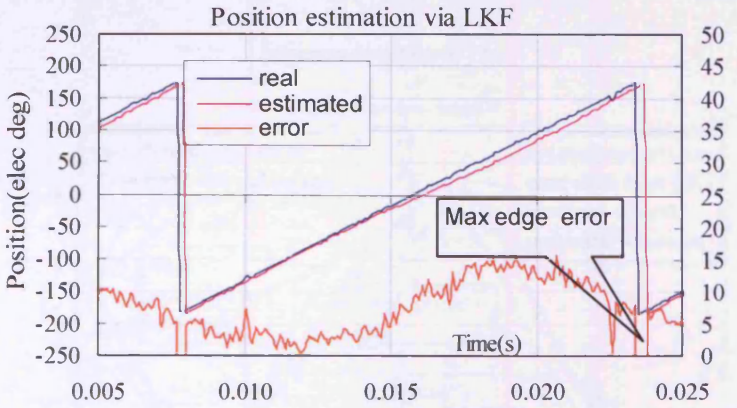

(C) position estimation via LKF

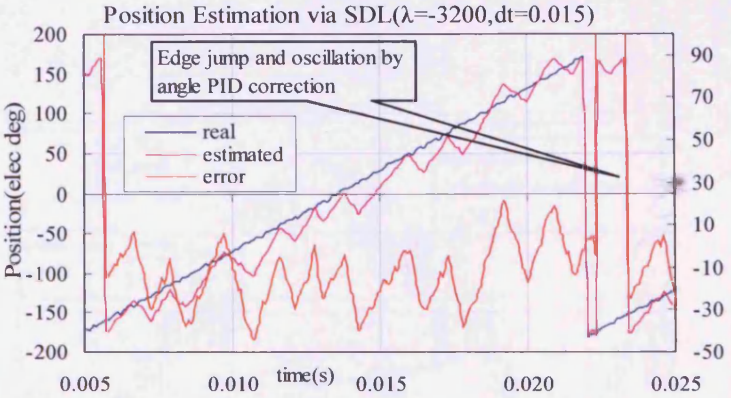

(d) position estimation via SDL

Fig. 6·26 Comparison of position estimation using FLO(a), EKF(b), LKF(c), SDL(d)

6.4.2 Current Waveform Comparison on Load

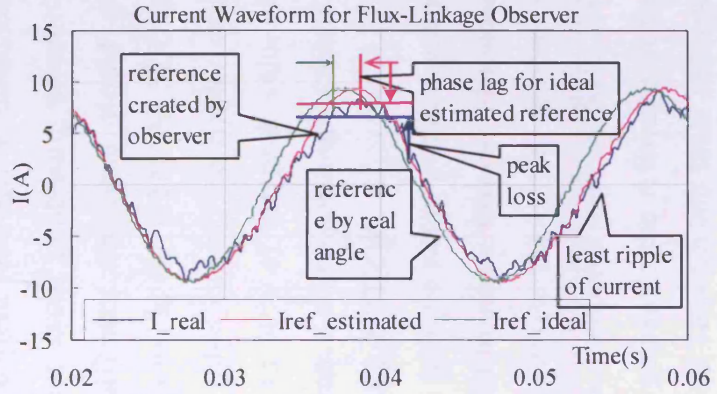

(a) current waveform by FLO

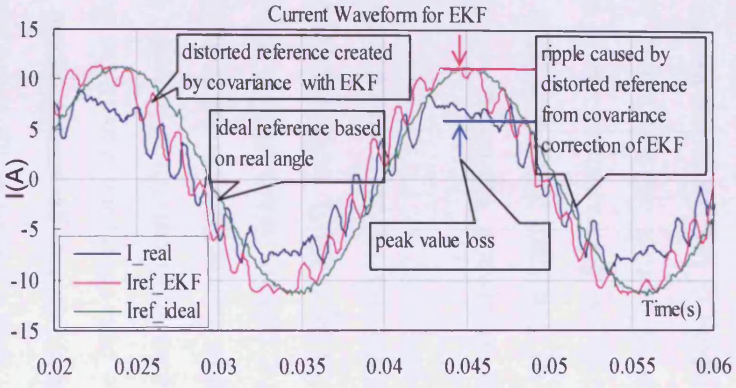

(b) current waveform by EKF

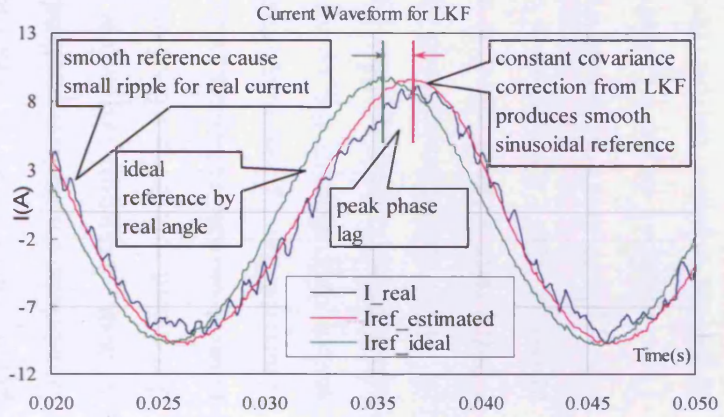

(c) current waveform by LKF

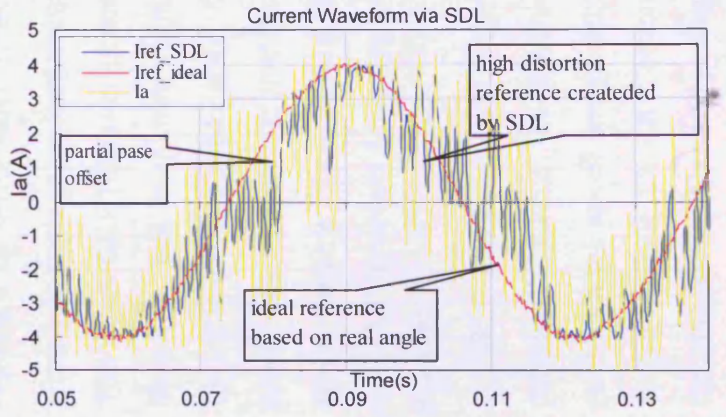

(d) current waveform by SDL

Fig. 6·27 Current Waveform for FLO(a), EKF(b), LKF(c), SDL(d)

Fig. 6·27 compares the current waveforms for the 4 sensorless estimations. They comprise true phase current waveforms, estimated current references and ideal current references, where the estimated current reference is based on the estimated position generated by observer and the ideal current reference is based on the actual position. Sensorless estimation methods cannot avoid generating current reference waveform without distortion. However, the different observers would generate significantly discrepant reference waveforms as shown in fig. 6·27. The SDL observer produces the poorest current reference waveform (blue curve), the ripples carried by the distorted reference have peak magnitudes up to 30% of the peak value of the reference. The severe distortion in the current reference correspondingly caused more ripples in the actual phase current (yellow curve in fig. 6·27(d)).

It is easily understood that the triangle-shape position estimation profile in fig. 6·26(d) with a large offset is attributed to single variable PI regulation carried by SDL observer. The EKF observer would generate the current reference in fig. 6·26(b) with the ripple of magnitude less than 10%, compared with the SDL observer in fig. 6·26(d). The back-EMF-based FLO observer generates the reference in fig. 6·26(a) with small ripple but a phase lag inevitably exists between the ideal reference and the estimated reference for FLO since it uses the integration to extract the flux linkage value and almost no peak value loss occurs in the waveform generated by the FLO observer.
The novel LKF observer generates the best reference waveform in fig. 6·26(b) with no distortion and minimum ripple, because Kalman filter is used by LKF observer to optimise the minimum error. Covariance correction via LKF or EKF can generate the much less ripple and distortion in the current waveform in fig.6·27(b) and (c) than single variable PI regulation via SDL in fig.6·27(d), furthermore, covariance correction via LKF generate less ripple and distortion in the current waveform than FLO in fig.6·27.

The phase lag still exists in the reference waveform of the LKF because the proposed LKF is the combination of Kalman filter and flux linkage estimation. Although the speed and position are listed as the variable state of the Kalman filter, the output variable for LKF observer to track is flux linkage which is extracted still from the integration. The integration is the cause of the phase lag for the FLO observer, thus, the situation is similar to FLO, the usage of flux linkage in LKF is the main reason for the phase lag in the current waveform of LKF, but the lower phase lag for the LKF than that of FLO can be explained by the fact that the Kalman filter could reduce the error from the estimated flux linkage in the LKF model.

Fig. 6·27(b) and (d) shows that the differential algorithm by EKF and SDL gives no lag in the phase current waveform. It is concluded that the derivation method of flux linkage method determines if a phase lag exists in the current characteristics, theoretically all the four sensorless methods are involved in the back EMF estimation. If the back EMF or flux linkage is extracted by the integration, a phase lag must exist in the current characteristics, for example, in the FLO or LKF shown in fig.6·27(a) and (c).

6.4.3 Speed Response:

The Luenberger observer with a large Eigen value can estimate speed at the start-up stage, but the estimated speed becomes unstable soon afterwards. This indicates that the fatal weakness of the Luenberger observer is the unstable estimated speed when it is used for the integration to obtain the rotor position.

The problem is solved by improved speed measurement based on d-q flux linkage as equations (6·26). Since the estimated position has many jumps at the end of the cycle, the sine and cosine function values are obtained by flux linkage via (6·26). Only EKF and LKF are capable of estimating the angular velocity directly. FLO needs to use flux-linkage measurement or position increment on the estimated angle in fig. 6·28 (a) to estimate speed. The SDL observer is the poorest speed estimator as it works only at the initial period of start-up and is incapable of estimating the stable velocity and it relies on external flux-linkage speed measurement shown in fig. 6·28 (d). The speed response from the LKF is slower than that of the EKF. Furthermore, the estimated speed via EKF has the least ripples in the waveform.

Speed estimation of the FLO in fig. 6·28(a) is based on estimated position increment while SDL in fig. 6·28 (d) uses pure flux-linkage measurement in (6·26). Velocity estimation of LKF and EKF in fig. 6·28 (b) and (c) is obtained from direct state-observation. The observers in fig. 6·28 can obtain good response although the speed response from the LKF is slow. Current injection is needed when the speed changes direction in EKF and SDL as seen in fig. 6·28 (b, d) while no current injection is needed for the FLO and LKF as seen in fig. 6·28 (a, c).

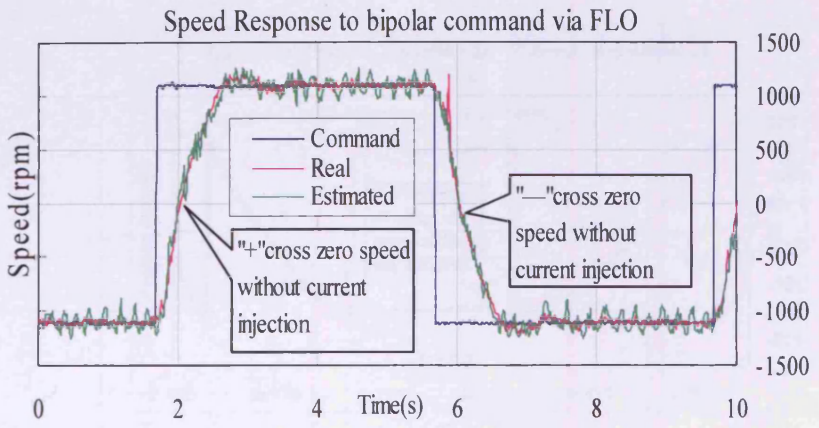

(a) Speed Response Comparison for FLO

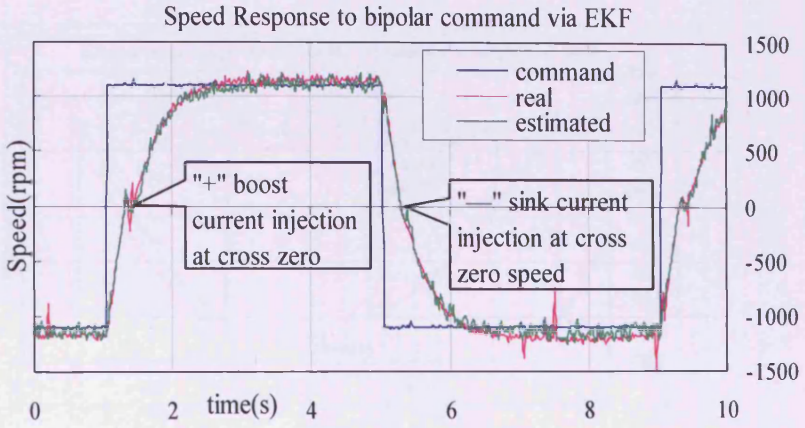

(b) Speed Response Comparison for EKF

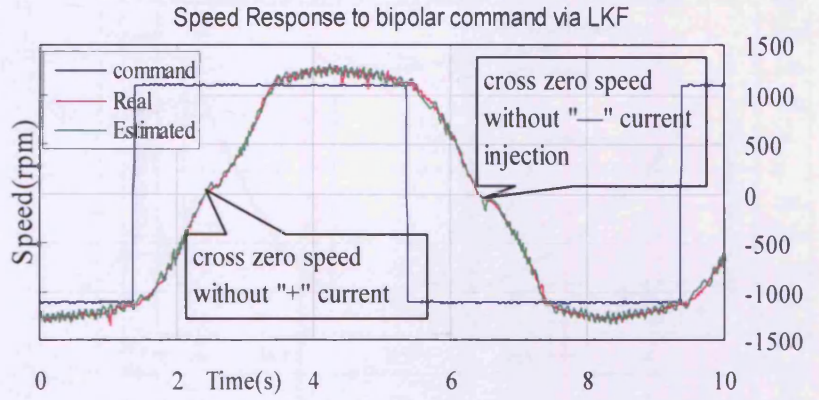

(c) Speed Response Comparison for LKF

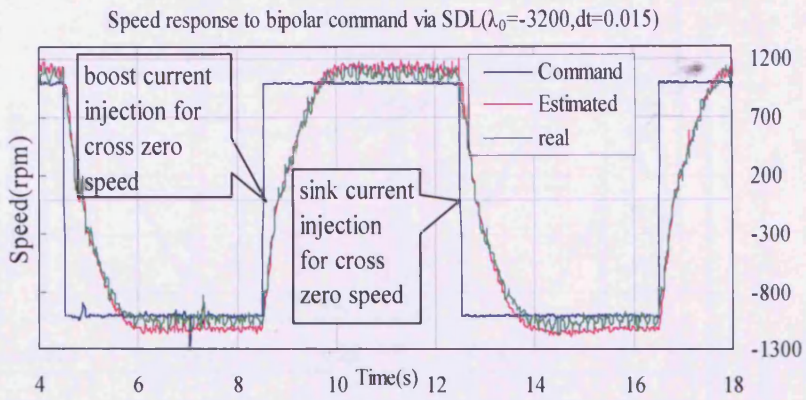

(d) Speed Response Comparison for SDL

Fig. 6·28 Comparison of speed response comparison for FLO(a), EKF(b), LKF(c) and SDL(d)

6.4.4 Estimated position transition under bidirection speed command in four-quadrant:

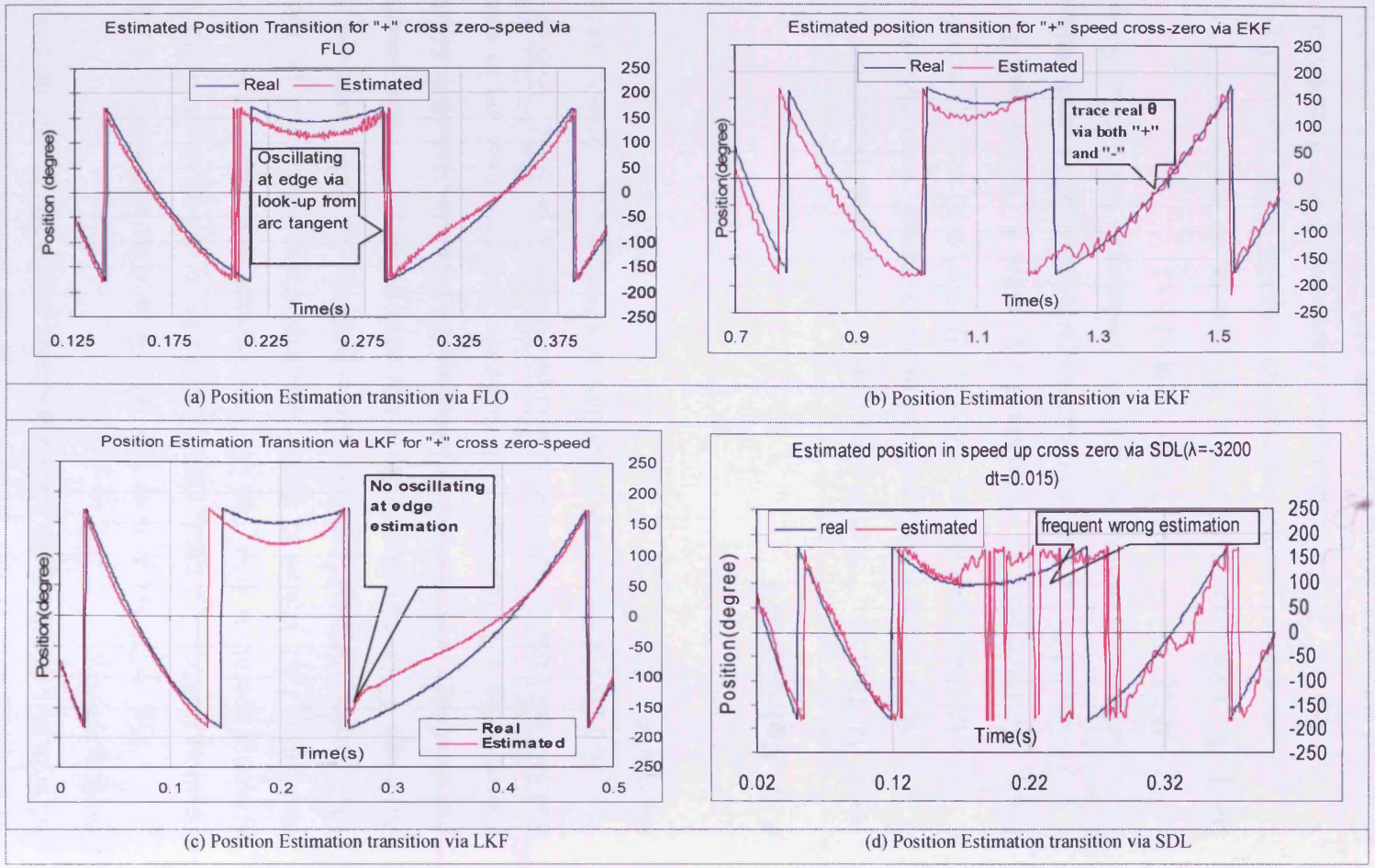

(a) Position Estimation transition via FLO

(b) Position Estimation transition via EKF

(c) Position Estimation transition via LKF

(d) Position Estimation transition via SDL

Fig. 6·29 Position Estimation for 4-quadrant operation

Assessment of the estimated position transition from speed cross-zero helps to determine whether this type of sensorless method can match the requirement for high dynamic performance. When a PMSM changes direction, the real position motion locus of the rotor will form the transition trapezoidal jump at the edge of the cycle 2π in fig. 6·29. In this situation, the ideal sensorless estimation should precisely track the position motion curve.

Fig. 6·29 show how the four sensorless estimations track the instantaneous position transition motion curve caused by speed cross-zero direction change in four quadrant operation. EKF and LKF can generate the estimated position curve to track the real curve. LKF seems to finally converge closer to the real position than EKF. Thus, EKF enters the real position curve towards the new direction quicker than LKF. Although FLO can also follow the real position variation accurately, it produced incorrect edge estimation error jumping and dropping transition for the terminal of cycle shown in fig. 6·29 (a). The SDL made the poorest estimation as shown in fig. 6·29 (d), and was not capable of tracking accurate dynamic position variation at the end of cycle. This also proves variance correction can secure higher dynamic precision than angle PI regulation.

6.5 References

[6•1] D. Hamada, "Stability analysis of sensorless permanent magnet synchronous motor drive with a reduced order observer", *International Conference Electric Machines and Drives, 1999, IEMD '99* , 9-12 May 1999 95 - 97

[6•2] K. Tatematsu, D. Hamada, K. Uchida, S. Wakao and T. Onuki, "Sensorless control for permanent magnet synchronous motor with reduced order observer", *Power Electronics Specialists Conference, 1998, PESC 98 Record, 29th Annual IEEE*, Vol. 1, 17-22 May 1998 125-131

[6•3] K. Tatematsu, D. Hamada, K. Uchida, S. Wakao and T. Onuki, "Sensorless permanent magnet synchronous motor drive with reduced order observer", *Applied Power Electronics Conference and Exposition, 1998, APEC '98, Conference Proceedings 1998, 13th Annual,* Vol. 1, 15-19 Feb. 1998 75 – 80

[6•4] N. Matsui and M. Shigyo, "Brushless DC motor control without position and speed sensors" , *IEEE Transactions on Industrial Applications*, Vol. 28 , Issue: 1 , Part 1, Jan.-Feb. 1992, 120 – 127

[6•5] R.E. Kalman and J.E. Bertram, "Control system analysis and design via the second method of Lyapunov I: Continuous-time systems", *Trans. ASME Ser. D. J. Basic Eng.* 82 ,1960, 371-393

[6•6] R. Bass. and R. Webber, "Optimal nonlinear feedback control derived from quartic and higher-order performance criteria", *IEEE Trans. on Automatic Control,* Vol. 11, Issue 3, Jul. 1966, 448 – 454

[6•7] D. Luenberger, "An Introduction to Observers", *IEEE Trans. on AC*, Vol. 16, No. 6, 1971, 596-602

[6•8] J. X. Shen, "Improved speed estimation in sensorless PM brushless AC drives", *IEEE Trans. on Ind. Appl.,* Vol. 38, Issue 4, July-Aug. 2002, 1072 – 1080

CHAPTER 7, Variable PI regulation for Full-Order Luenberger Sensorless Technique

7.1 Introduction

Non-correction direct computation with FLO and covariance correction with EKF and LKF are compared with single variable PI regulation via SDL observer. It has been proved that single-variable PI regulation with SDL observer generates poorer precision in shaft position estimation than do other covariance corrections with the Kalman filter. As SDL observer is a reduced-order Luenberger observer for the 3-order nonlinear PMSM state system, the only system state of speed is decided by the assigned Eigen value which can easily make the observer unstable. In order to overcome the impact on system stability from a single eigenvalue, the full-order Luenberger observer with multiple Eigenvalues is investigated for sensorless control with angle PI regulation.

Single-variable PI regulation with full-order feedback Luenberger sensorless controlled PMSM is introduced. The chapter first illustrates how the non-linear state system uses full-order state feedback to build up a full-order feedback Luenberger observer (FOLU). It then describes how to build a 3-order feedback Luenberger observer for a nonlinear electromechanical PMSM model in a d-q coordinate frame.

The experimental results and analysis are made for angle PI regulation from the FOLU-based sensorless controlled PMSM. The FOLU observer obtains a greater precision of position estimation than do the SDL and EKF observers, but it is still lower than LKF with constant covariance correction and FLO with non-correction. The FOLU-based sensorless controlled PMSM still shares the same drawback with the SDL-based method such as lack of stable speed estimation from the direct observer. Although multiple Eigen values could make the FOLU observer more stable than the SDL observer, the speed estimation from the FOLU observer would occasionally become unstable. Therefore, the FOLU-based sensorless control uses the pure flux linkage speed estimation as does the SDL observer.. Non-correction with FLO, covariance correction with EKF or LKF and single-variable PI regulation with the SD-Luenberger

and FOLU observer are compared. The ultimate conclusion is that covariance correction can help the state estimation system obtain better precision in shaft position estimation and also makes rapid accurate speed estimation in state-estimation sensorless control.

Full-order Luenberger-based (FOLU) sensorless state-estimation for PMSM was adapted from the observer model introduced by Bhangu [7·1]. The full-order Luenberger observer shares the same PMSM dynamic model in the d-q axis coordinate frame with the reduced-order Luenberger method. Even the feedback linearization controller is employed to apply the full-order Luenberger theory also. The difference between the reduced-order and the full-order Luenberger observer is that the Eigen values have to be pre-assigned in the diagonal Luenberger feedback matrix, while the SDL observer only needs one assigned Eigen value. The position correction scheme is also the same as in the reduced-order Luenberger observer: d-axis voltage error is approximately proportional to the error in rotor position angle.

The key procedure for the full-order Luenberger observer is to choose the Luenberger gain matrix that assigns Eigen values to the observer with a sufficiently fast convergence speed. The Eigen values are chosen to make transient convergence of state estimation for the observer rapid enough to generate minimum impact on the outer-loop control system. The appropriate Eigen values need to be chosen by 3-d simulation optimisation [7·3]. Experimentation with the FOLU observer-based sensorless control reveals that position estimation error under steady-state condition is less than 0.1 rad.

The disadvantage of FOLU is that the complex procedure of assigning Eigen values needs to be conducted through 3-d search optimisation. The convenient advantage of FOLU is its expanding ability to include other estimations of load torque or motor parameters. The experiment by Bhangu [7·2] also proves that load torque added in the state estimation in FOLU could enhance both the accuracy of the rotor position estimates when the motor is subject to transient heavy loading and disturbance rejection performance through the feed forward correction technique. However, the FOLU-based sensorless control appears undesirable in low power operation with low phase current since the propensity to noise would generate virtually low-duty phase voltages, and current convergence dynamics performance could dominate any specific low power operation.

The proposed FOLU could avoid complex optimisation for the Eigen value group to obtain the fastest convergence. Speed estimation is replaced by flux linkage estimation even if the estimated speed from the Luenberger is not stable. The emphasis of this chapter is on investigating angle PI regulator performance in FOLU-based sensorless

control. The proposed FOLU observer with flux linkage speed estimation proves that correction would be the major factor in affecting position estimation even if the integration of the estimated speed directly from the FOLU observer could not be stabilized.

7.2 Full-order Luenberger Observer Model for Sensorless Control PMSM

7.2.1 Full-order Luenberger Observer (FOLU) theory for a linear system

Full-order Luenberger observer theory was introduced in section 6·1·1. The equation group (6·3) is essentially the mathematical model for the full-order Luenberger state observer $\{A', B', C'\}$ shown in (7·1), which also corresponds to the diagram in fig 6·2.

$$\begin{cases} \dot{\hat{x}} = A'\hat{x} + B'u + L(y - \hat{y}) \\ \dot{\hat{y}} = C'\hat{x} \end{cases} \tag{7·1}$$

For the full-order Luenberger observer, the system state $\hat{x}$, input u and the output $\hat{y}$ are all vector variable. The state $\hat{x}$ is a n-order variable, the output y is a m-order variable, the input u is a r-order variable, the coefficient matrix A' is n×n order, the input matrix B' is n×r order, the output matrix C' is m×n and the Luenberger feedback gain matrix L is n×m order.

As the difference x_e between the observer state $\hat{x}$ and actual state x can be solved in the matrix exponential function $e^{(A-Lc)(t-t_0)}x_e(t_0)$ shown in (6·6), the damping speed of difference x_e is decided by the Eigen values of the exponential function coefficient matrix (A-Lc). The greater those Eigen values of coefficient matrix (A-Lc), the faster the damping speed for difference x_e between observer state $\hat{x}$ and actual state x.

Those Eigen values should be negative with high absolute amplitude. Even if they are complex, their magnitude needs to be great enough to rapid converge. The Eigen values represent the poles of the observer system; the relationship with a real system can be represented as in fig. 7·1. If the left poles for the observer are far from the right values for the real system in fig. 7·1, the damping speed of the error between the estimated state and real one can become faster. Furthermore, the damping speed of the state estimation error is decided by the Eigen values of the Eigen matrix (A-LC), and the diagonal matrix comprised of those Eigen values can be transformed into the corresponding Eigen matrix in (7·2) where T is the transformation matrix.

(7·2) introduces the approach for the full-order Luenberger observer if Luenberger matrix $L_{m\times n}$ is assigned to generate the diagonal Eigen matrix $\prod$ in (7·2) and $\prod$ possess the desirable Eigen values $\lambda_1 \ldots \lambda_n$, which creates the relationship shown in fig. 7·1.

$$(A\text{-}LC)=T^{-1}\begin{bmatrix}\lambda_1 & & 0\\ & \bullet & \\ & & \bullet \\ 0 & & \lambda_n\end{bmatrix}T = T^{-1}\prod T \qquad (7\cdot2)$$

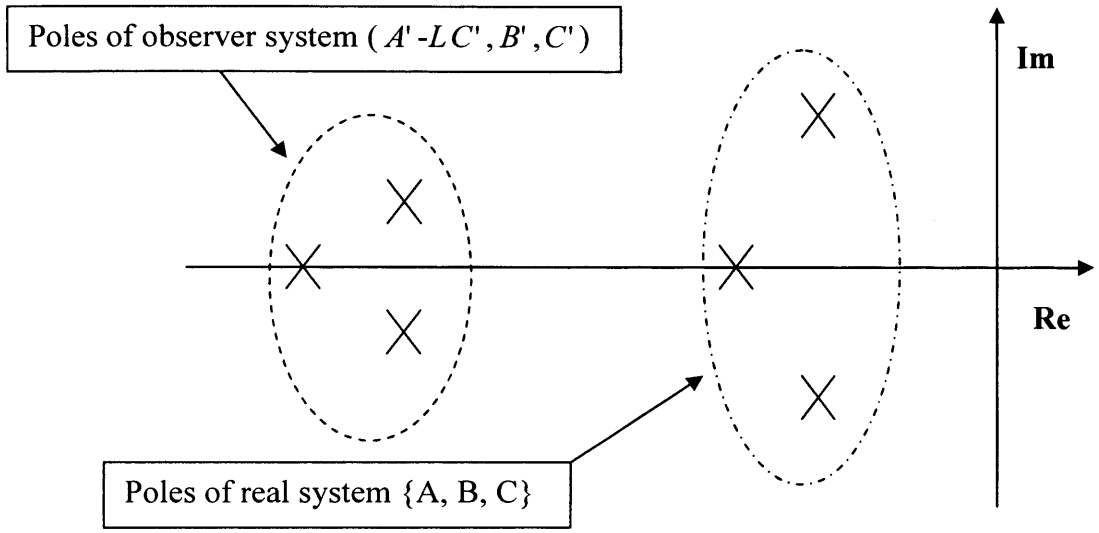

Fig. 7·1 Ideal Eigen value location for observer and system

7.2.2 Full-order Luenberger Observer for Nonlinear PMSM Drive System

The full-order Luenberger observer for the sensorless control PMSM system is generally based on the dynamic mathematic model Σ in (6·18) of PMSM in d-q rotor-oriented reference co-ordinates shared with the SD-Luenberger observer. The PMSM dynamic mathematic model Σ can be expressed by the following matrix state equations (7·3), (7·4) and (7·5). The system state $\hat{x}$, input u and output y are shown in (7·3). The coefficient matrixes of the state system are shown in (7·4). The matrix state system can be expressed in (7·5).

$$\hat{x}=\begin{bmatrix}i_d\\ i_q\\ \omega\end{bmatrix}, u=\begin{bmatrix}v_d\\ v_q\end{bmatrix}, y=\begin{bmatrix}i_d\\ i_q\end{bmatrix} \qquad (7\cdot3)$$

$$A=\begin{bmatrix} -\frac{R}{L_s} & \omega & 0 \\ -\omega & -\frac{R}{L_s} & -\frac{K_e}{L_s} \\ 0 & \frac{K_t p}{J} & -\frac{B}{J} \end{bmatrix}, B=\begin{bmatrix} \frac{1}{L_s} & 0 \\ 0 & \frac{1}{L_s} \\ 0 & 0 \end{bmatrix}, C=\begin{bmatrix} 1 & 0 & 0 \\ 0 & 1 & 0 \end{bmatrix} \quad (7\cdot4)$$

$$\begin{cases} \dot{\hat{x}} = A\hat{x} + Bu \\ y = Cx \end{cases} \quad (7\cdot5)$$

where R, L_s, K_e, K_t are respectively the phase resistance, phase synchronous inductance, back-emf constant and torque constant. ω is the rotor angular velocity; θ is the rotor position; p is the number of pole pairs; J is the rotor inertia and B is the motor viscous friction. The PMSM dynamic model includes internal mechanical parameters such as rotor inertia J, viscous friction B and torque constant Kt. Rotor inertia J describes the inherent force of the rotor to resist the change in speed. Viscous friction B represents the function of the viscosity of the shaft and changes with speed and torque constant. Kt describes the torque generated by per unit current.

However, all these mechanical parameters are not related to the load; if the load torque needs to be included, the dynamic speed equation needs to be modified: $d\omega/dt= (Kt\ p/J)\ Iq-(B/J)\omega-T_L p/J$ and $dT_L/dt=0$; the order of state observer increases to adapt the requirement of the load. This issue is outside the scope of this thesis.

The vector state estimation system in (7·3-7·5) contains no position estimation so another individual estimation for rotor position needs to be built. The rotor position can be deduced through the integration of the estimated speed from the observer in (7·1-7·3). The initial offset, error and other types of measurement drift could be added into the estimated rotor position by integrating the estimated speed. The correction scheme still uses the single variable PI regulator. The extra rotor position estimation can be expressed in (7·6) where G_{PI} is the gain of PI regulator.

$$\hat{\theta} = \int \hat{\omega} dt + G_{PI}(i_d^* - i_d), \mathrm{sgn}(\hat{\omega}) = \begin{cases} 1 & (\hat{\omega} > 0) \\ -1 & (\hat{\omega} < 0) \end{cases} \quad (7\cdot6)$$

State equation group (7·1~7·3) is the dynamic model for a PMSM in a d-q rotor-fixed frame coordinate. Apparently the system is nonlinear and system quantities are compactly coupled. Luenberger observer theory can apply to only a linear system and [7·8]-[7·10] show that such feedback (7·7) below can linearise the system model (7·1~7·3).

$$\begin{cases} u_d = v_d + \omega L_s i_q \\ u_q = v_q - \omega L_s i_d \end{cases} \tag{7·7}$$

After substituting (7·7) into (7·5), the first two-order linearized d-q dynamic model (7·5) is rewritten in (7·8). The new linearized model in (7·8) has a constant coefficient matrix.

$$\frac{d}{dt}\begin{bmatrix} \hat{i}_d \\ \hat{i}_q \end{bmatrix} = \begin{bmatrix} -\frac{R}{L_s} & 0 \\ 0 & -\frac{R}{L_s} \end{bmatrix}\begin{bmatrix} \hat{i}_d \\ \hat{i}_q \end{bmatrix} + \begin{bmatrix} \frac{1}{L_s} & 0 \\ 0 & \frac{1}{L_s} \end{bmatrix}\begin{bmatrix} u_d \\ u_q \end{bmatrix} \tag{7·8}$$

Considering the whole state system (7·1~7·3), a new coefficient matrix can be redefined in (7·9).

$$A = \begin{bmatrix} -\frac{R}{L_s} & 0 & 0 \\ 0 & -\frac{R}{L_s} & -\frac{K_e}{L_s} \\ 0 & \frac{K_t p}{J} & -\frac{B}{J} \end{bmatrix},\ B = \begin{bmatrix} \frac{1}{L_s} & 0 \\ 0 & \frac{1}{L_s} \\ 0 & 0 \end{bmatrix},\ C = \begin{bmatrix} 1 & 0 & 0 \\ 0 & 1 & 0 \end{bmatrix} \tag{7·9}$$

The new input vector u can be redefined as $u = \left[v_d, v_q\right]^T$. The linearized state system can be expressed as

$$\begin{cases} \dot{\hat{x}} = \begin{bmatrix} -\frac{R}{L_s} & 0 & 0 \\ 0 & -\frac{R}{L_s} & -\frac{K_e}{L_s} \\ 0 & \frac{K_t p}{J} & -\frac{B}{J} \end{bmatrix}\hat{x} + \begin{bmatrix} \frac{1}{L_s} & 0 \\ 0 & \frac{1}{L_s} \\ 0 & 0 \end{bmatrix} u \\ y = \begin{bmatrix} \frac{1}{L_s} & 0 \\ 0 & \frac{1}{L_s} \\ 0 & 0 \end{bmatrix} x \end{cases} \tag{7·10}$$

If the full-order Luenberger observer is applied in a new linearised state system (7·10), the diagonal Eigen matrix E must be assigned as in (7·11). The Eigen values are chosen through the law that the Eigen values of the observer should be far from those of the real system.

$$E = \begin{bmatrix} \lambda_1 & 0 & 0 \\ 0 & \lambda_2 & 0 \\ 0 & 0 & \lambda_3 \end{bmatrix} \tag{7·11}$$

The law is implemented by assigning the Luenberger matrix L to make (A-LC) equivalent to (7·2), where $\prod$ =E in (7·11). The Luenberger matrix L is selected to generate the desirable Eigen values λ_1, λ_2 and λ_3 from the Eigen matrix (A-LC). This procedure is commonly implemented through MATLAB simulation.

Full-order and SD Luenberger observers both need to utilize extra speed estimation as the individual speed control; for example, the SD Luenberger observer uses pure flux-linkage speed estimation shown in (7·12), The reason is that a full-order Luenberger observer-based sensorless control system needs extra speed estimation and is also sensitive to the selection of Eigen values for the system matrix.

$$\omega \approx F_q / \psi_f = (F_\beta \psi_\beta / \psi_f - F_\alpha \psi_\alpha / \psi_f) / \psi_f \tag{7·12}$$

Although greater Eigen values could generate quicker convergence of the state error than for the SD Luenberger observer, they can still easily cause system instability [7·8~7·10]. The estimated state-speed from the FOLU observer shows occasional instability if the Eigen values are chosen in the wrong configuration. The issue was reportedly sorted out by rearranging the feedback gain matrix to reconstruct the equilibrium linear system [7·8]. This approach makes the system more complex and an extra trial-and-error procedure for the Eigen value must be added. The benefit of pure flux-linkage speed estimation is that it can separate out the impact from the position estimation of the FOLU observer and explicitly compare the difference in position correction capability between the SD and the FOLU observers.

7.3 Experiment Results and Analysis

7.3.1 Objective of Experiment for Sensorless Full-order Luenberger Observer-based PM Control

The SD-Luenberger observer-based sensorless control PMSM was studied to assess the effect of the angle PI regulation scheme on the performance of shaft position and speed estimation. It is primarily concluded that angle PI regulation correction is worse than covariance correction in position estimation and other characteristics. Therefore the estimation characteristics for the three-order Luenberger observer with multiple Eigen values for sensorless control of a PMSM is investigated. Due to the unstable estimated speed directly from the full-order Luenberger observer, a pure flux-linkage-based speed estimation scheme was still used to replace the state speed from the FOLU observer for

speed control. In this case the shaft position and speed response behaviour were separately studied to compare with the SD-Luenberger-based sensorless scheme for exploring the impact from angle PI regulation.

7.3.2 Experimental Conditions

Full-order Luenberger observer-based sensorless control was applied under the same experimental conditions as the other sensorless observers. A full-order Luenberger observer algorithm was implemented at the TMS320C31DSK-base 16-bit parallel-bus Euro-card system with a 12-bit AD678-based acquisition parallel convert subsystem and a 12-bit AD767-based parallel-input analogue-converted output subsystem. The shaft position sensor employed British Encoder with 2048ppt precision and its interface used the USdigital pulse-to-binary-converter ECOUNTER[7·14].

7.3.3 Experiment Results and Analysis:

7.3.3.1 Shaft Position Estimation Characteristics:

The shaft position estimation characteristics for the full-order Luenberger observer in clockwise and anticlockwise rotation are illustrated in figs. 7·2-7·4. Experiments found that element L31 from Luenberger matrix L is greatly affected in the estimation error of shaft position by full-order Luenberger-based sensorless controlled PMSM in the trial-and-error procedure. The feedback matrix L via Eigen matrix (A-LC) is used to configure the Eigen vector in (7·11) for the rotor-oriented d-q frame PMSM system with the linearization feedback in (7·10). First the Eigen matrix E_l comprising three eigenvalues is assigned as shown in (7·13).

$$E_l = \begin{bmatrix} -800 & 0 & 0 \\ 0 & -1600 & 0 \\ 0 & 0 & -3200 \end{bmatrix} \tag{7·13}$$

Secondly, the basic feedback matrix L is chosen through MATLAB simulation based on (7·2) and (7·14) as

$$L = \begin{bmatrix} -182 & 3.8 \\ 0 & 19600 \\ L31 & -6540000 \end{bmatrix} \tag{7·14}$$

L31 is tuned through trial and error from 16.5 to 400 to adapt the offset between the estimated rotor position profile and the actual locus. It is found that the shaft position estimation offset was affected by tuning the element L31 in the Luenberger matrix.

After the element L31 of the Luenberger matrix is tuned, the Eigen values of the sensorless Luenberger observer are inevitably changed. The desirable offset to actual shaft position locus should show symmetry and evenly encircle the actual locus in polarity. Figs.7·2-7·4 illustrate that the varying parameters L31 from the Luenberger matrix result in a different, unsymmetrical estimated shaft position offset pattern relative to the actual locus. The corresponding magnitude of the PI regulation is chosen to be 0.015.

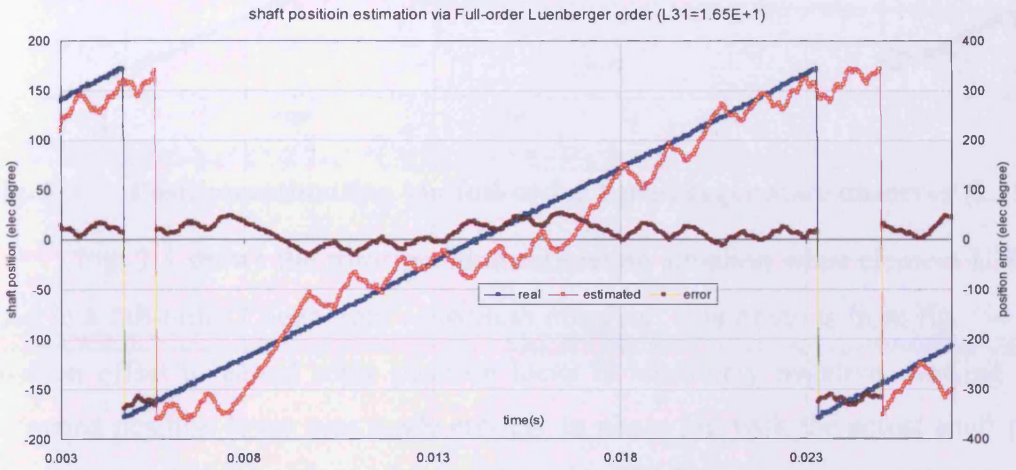

Fig. 7·2 Shaft position estimation via full-order Luenberger observer (L31=16.5)

Fig. 7·2 shows the shaft position estimation characteristics via full-order Luenberger observer in an electrical cycle when element L31=16.5, where the triangle-shaped locus profile represents an actual rotor trace encircled by the saw-tooth-shaped curve representing the estimated shaft position trace while the position error curve is fluctuating over the o-axis. It was noted that negative position bias existed in the range [-180°, -100°] and [-20°, 180°], while positive position bias existed in the range [100°, -20°]. The period for the negative position estimation bias is much longer than that for positive position estimation bias. The full-order Luenberger observer appeared to correct the positive position estimation bias but the correction is so great that the position bias could not quickly return to a positive value.

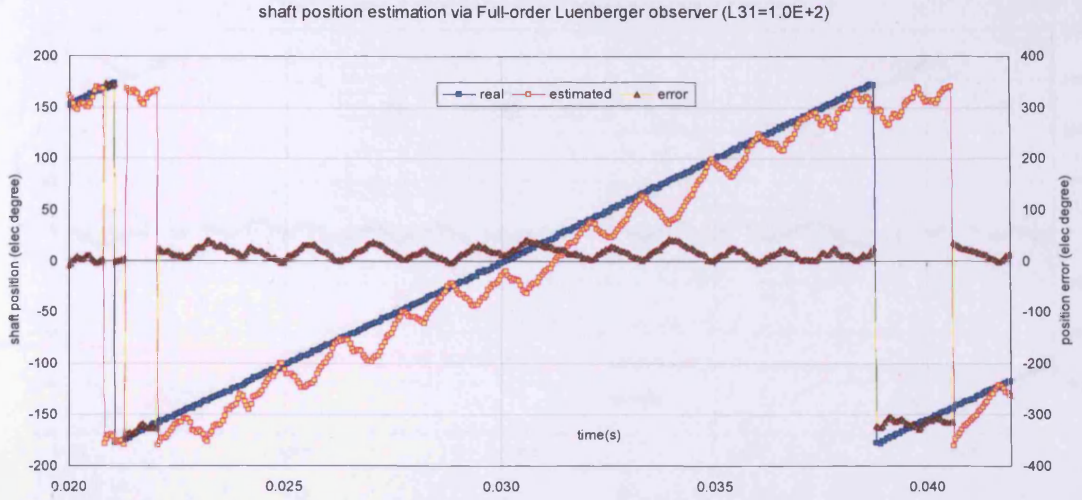

Fig. 7·3 Position estimation via full-order Luenberger state observer (L31=100)

Fig. 7·3 shows the rotor position estimation situation when element L31=100 is used in a full-order Luenberger sensorless observer. It is obvious from fig. 7·4 that the position offset to actual rotor position locus is absolutely negative showing that the estimated position locus was made entirely in phase lag with the actual shaft position. The reason is that the estimated speed from the FOLU observer was unable to generate enough integration for the estimated position to go towards the actual rotor locus, while the correction from PI regulation inversely keeps the estimated position away from the actual rotor position locus.

Generally, the FOLU observer has better response to a faster estimated speed than the actual speed so that the integration for the estimation speed could make the estimated position go beyond the actual value. Next the PI regulation would correct the positive offset into the negative offset. fig. 7·3 illustrates how the integration of the speed estimation is decided by the configuration of Eigen values from the FOLU observer and, indirectly, by the Luenberger matrix L.

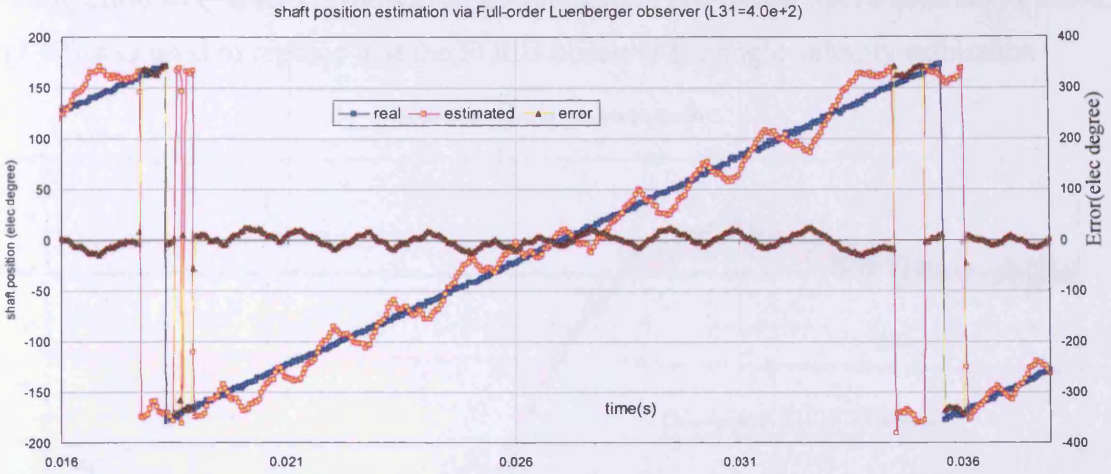

Fig. 7·4 Position estimation via full-order Luenberger state observer (L31=400)

Fig. 7·4 illustrates that ideally, when the tuned element L31 is equal to 400, employing the full-order Luenberger observer could make the corrective position offset swing positively and negatively relative to the actual position locus. It is shown that the actual triangle-shaped position curve is encircled by the estimated shaft position locus. It is obvious that the element L31=400 makes the best Luenberger feedback matrix because the generated speed is convenient to make its integration sufficient to go over the actual position, while PI regulation makes the estimated position drift downwards until the integration of the estimated speed takes dominant action again. Compared with the SD-Luenberger observer, the multiple Eigen value characteristics of the FOLU observer would enforce the effect from the integration of the estimated speed through the multiple Eigen values rather than the single Eigen value for the SDL observer in the rotor position estimation performance.

Terminal oscillation also appears in figs. 7·2-7·4. The reason is similar to that with the SDL observer in that the angle PI regulator produces a maximum magnitude of correction at the start or end of the electrical cycle when the variation of d-axis current reaches its maximum value.

7.3.3.2 Speed Response

The speed response characteristics to a 1000 rpm step unit for the full-order Luenberger observer was tested under the same experimental condition as were the other sensorless observers. Because the speed estimation obtained directly from the full-order Luenberger observer was unstable in the experiment, if the estimated speed was used

for integration to extract position information, back-EMF based speed estimation based on (7·12) was used to replace that the FOLU observer for angle velocity estimation.

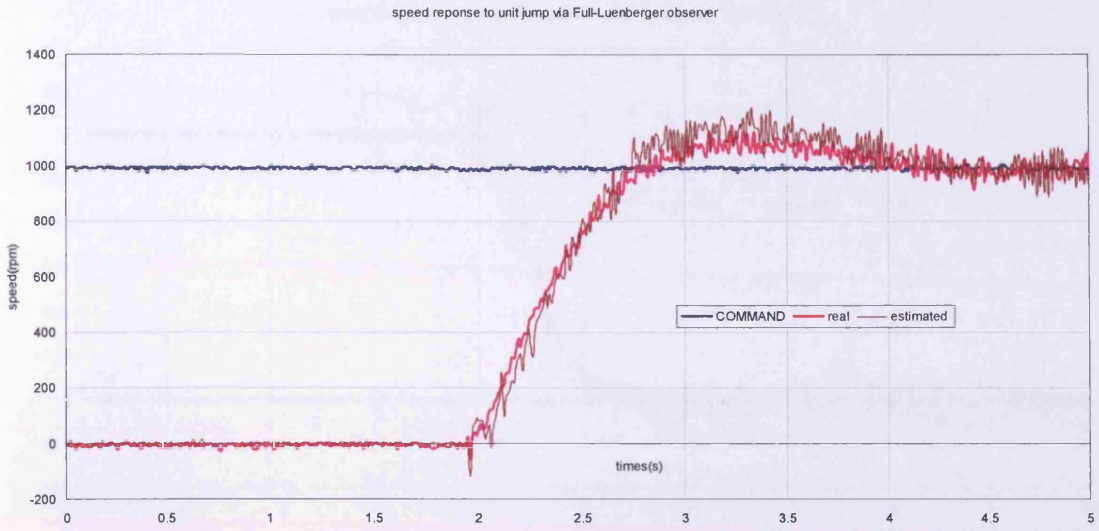

Fig. 7·5 Speed response characteristics via full-order Luenberger observer to unit step command of 1000 rpm

Fig. 7·5 shows good speed response characteristics to a 1000 rpm step unit command under the FOLU observer's sensorless control method. The back-EMF-based estimated speed not only traces the actual speed during the acceleration stage but also the overshoot and steady states. Fig. 7·5 also demonstrates the self-start transient period under the position sensorless control by the FOLU observer. The PMSM is initially kept in the standstill state after the negative movement immediately upon start up due to correction from the PI regulator; the PMSM is induced to accelerate toward the speed command of 1000 rpm until steady state is reached. The negative initial startup speed shows that the rotor was led in the wrong direction because of incorrect position estimation resulting in the following correction command of the PI regulator.

Fig. 7·6 shows the estimated speed response characteristics to the negative speed reference under sensorless control of the full-order Luenberger observer. The speed response characteristic profile in fig. 7·6 demonstrates the reverse speed response capability. Many positive or negative speed glitches appear at the nearby startup point.. This obviously implies that the rotor was started after many positive or negative swings of the rotor movement. These rotor swings represent an incorrect position estimation from the FOLU observer and the corresponding correction by the PI regulation actions. Although these frequent incorrect estimations and corrections from the sensorless

observer are not desirable at start up, it significantly shows the Luenberger observer to have stronger robust capability for self-startup. The PMSM motor occasionally has

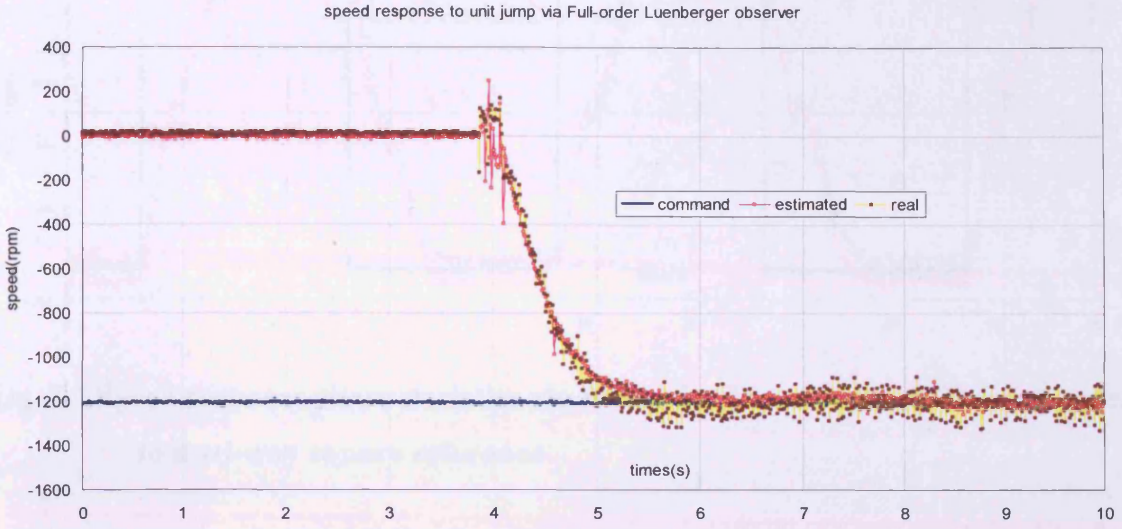

Fig. 7·6 Speed response characteristics via full-order Luenberger observer to unit step command of 1200 rpm

some dead-area points for start-up or on high load. The angle PI regulator with the Luenberger observer would be able to pull the rotor away from those dead-area points in balance so as to start the rotor despite the incorrect estimation and following correction action. Actually PI regulation with Luenberger observer can move the rotor in the wrong direction and then correct the wrong position to move the rotor in the right direction, such trial and error procedure is actually the reason that Luenberger observer can start up at arbitrary position.

7.3.3.2.1 Speed response to square command:

Fig. 7·7 shows the speed response characteristics under a dual-way square reference via the full-order Luenberger-based sensorless observer for position through the pure flux-linkage angle velocity estimation in (7·12). The dual-way square speed reference changes the output speed command between 1000 rpm and -1000 rpm every 4 seconds. The PMSM rotor is successfully controlled by the FOLU-based sensorless observer and a pure flux-linkage speed estimation scheme to trace the actual speed. Due to the estimated position bias generated by the angle PI regulator, the estimated speed trace profile in fig. 7·7 stayed behind the actual speed trace so there is a subsequent phase lag in the time domain. The estimated position error generates the steady estimated speed glitches shown in fig. 7·7.

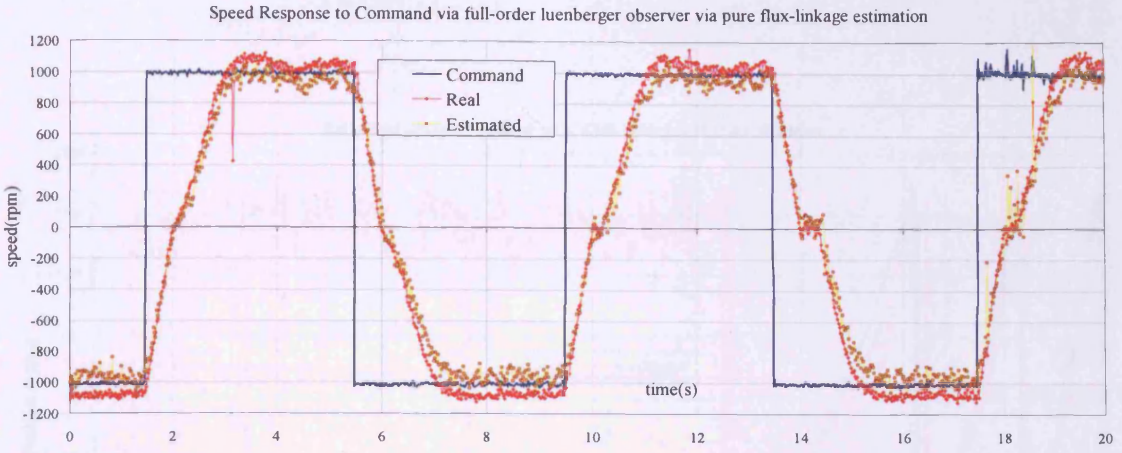

Fig. 7·7 Speed response characteristics via full-order Luenberger (FOLU) observer to dual-way square reference

It can be clearly observed that the existing speed oscillation, implying low electrical signals create more measurement error and that the PI regulator attempts to correct the wrong estimation when the speed crosses zero. Such trial-and-error intermission shows the FOLU with angle PI regulator is able to overcome the electrical signal noise through signal injection even if the estimation is wrong.

7.3.3.2.2 Self-Startup /zero-speed startup characteristics

A self-startup experiment is used to verify if a full-Luenberger-based sensorless controlled PMSM is able to self startup. Fig. 7·8 illustrates the estimated position dynamics locus profile during the step unit speed response period. It includes three stages: a standstill oscillating stage, a steady converging stage and a startup stage. During the standstill oscillating stage, the FOLU observer makes the trial-and-error action to correct any incorrectly estimated position with a magnitude of up to electrical 360°; during the steady converging stage, the FOLU observer stabilizes the estimation error, which becomes constant due to the errors attempting to converge.

During the start-up stage, the FOLU observer rapidly decreases the error of estimated position through the PI regulator and eventually makes the rotor start up. Fig. 7·8 shows the extreme case in which the initial position bias reaches almost 360 elec °, but the FOLU observer still successfully uses the angle PI regulation to finally correct the generated position bias and make the rotor start up at the arbitrary initial position under the proper load, as long as the generated torque is sufficient to overcome the start-up load.

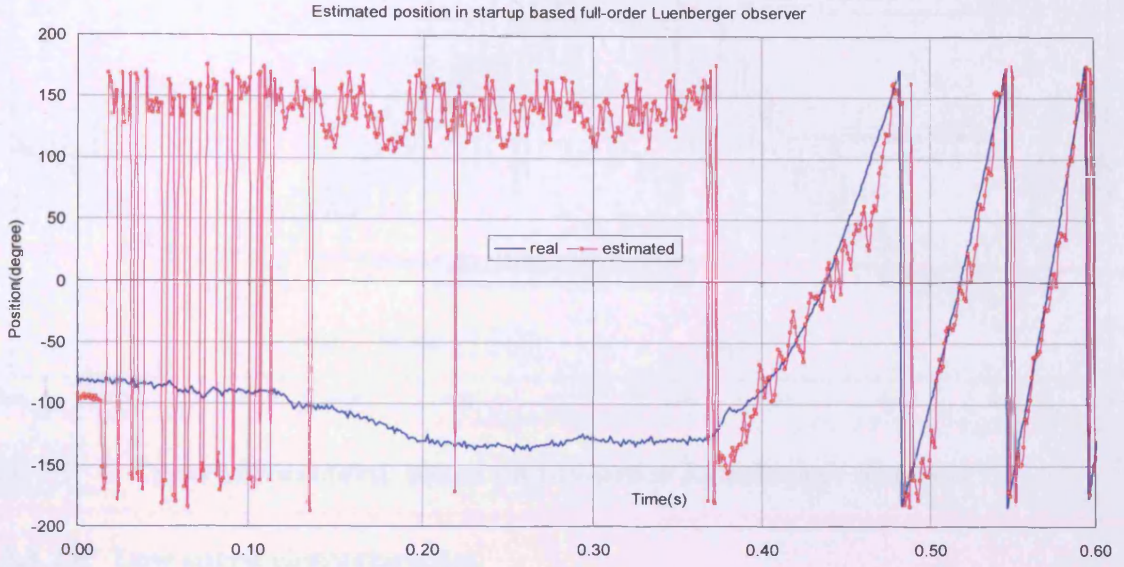

Fig. 7·8 Estimated position trace during startup period based on full-order Luenberger observer

7.3.3.2.3 Load operation characteristics

Fig. 7·9 shows the phase current waveform generated through the estimated position/angle by the full-order Luenberger observer which reflects the load operation characteristics under sensorless control. Experimentally, a low load implemented by keeping a shunt generator stator closed loop with the highest power resistance while switching on the excited field through shunt armature connected in parallel with the stator winding. Fig. 7·9 shows that the phase current reference produced by the FOLU observer gives highest noise and most glitches compared to the actual ideal reference produced based on actual position. This noise is caused by inappropriately selected Eigen vectors of the full-order Luenberger matrix and correction by PI regulation.

Due to a sensorless-generated current reference with high ripple, the actual current waveform brings severe distortion, which is determined by the angle PI regulation correction mechanism and the Eigen characteristics of the Luenberger observer.

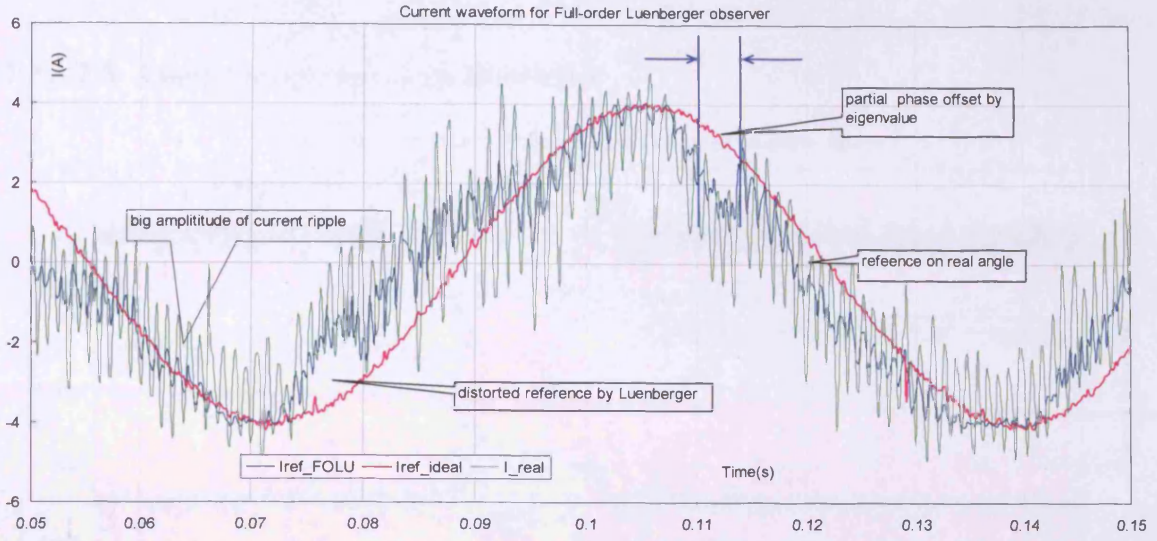

Fig. 7·9 Current waveform based on full-order Luenberger observer

7.3.3.2.4 Low speed characteristics

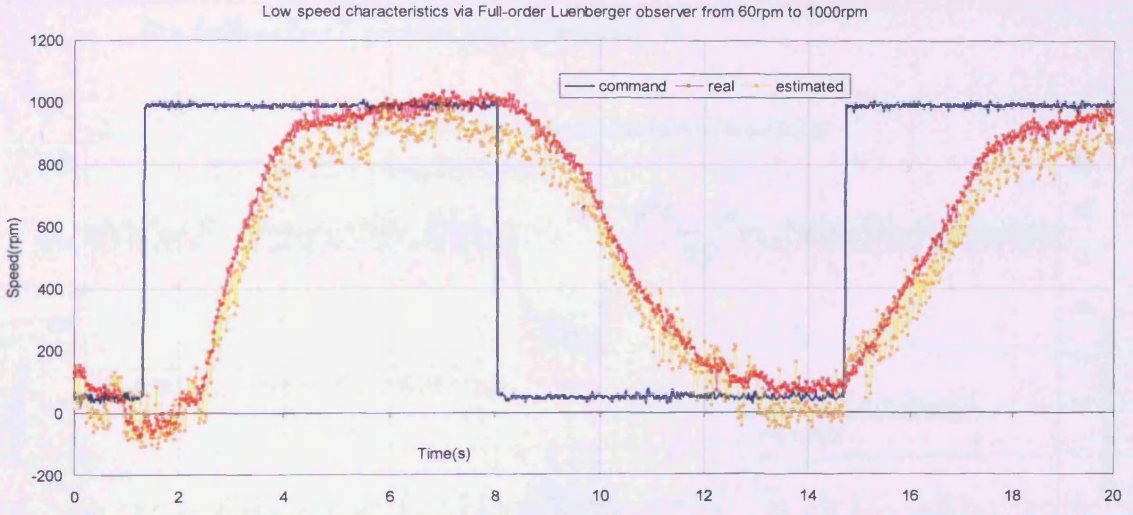

Fig. 7·10 Low speed (100rpm to 1000 rpm) characteristics via full-order Luenberger observer based on full-order Luenberger observer

Fig. 7·10 illustrates that the lowest speed the FOLU-based sensorless control PMSM can reach is 100 rpm, while the speed square reference changes the speed command between 1000 rpm and -1000 rpm every 7 s. The minimum speed for the FOLU-based sensorless control is obviously less than that of the other sensorless methods investigated. This is because such rough precision is caused by the angle PI regulation mechanism from the FOLU-based sensorless control so that the low electrical signals at low speed can give higher measurement errors to drive the FOLU observer with PI regulator.

7.3.3.2.5 Load disturbance characteristics

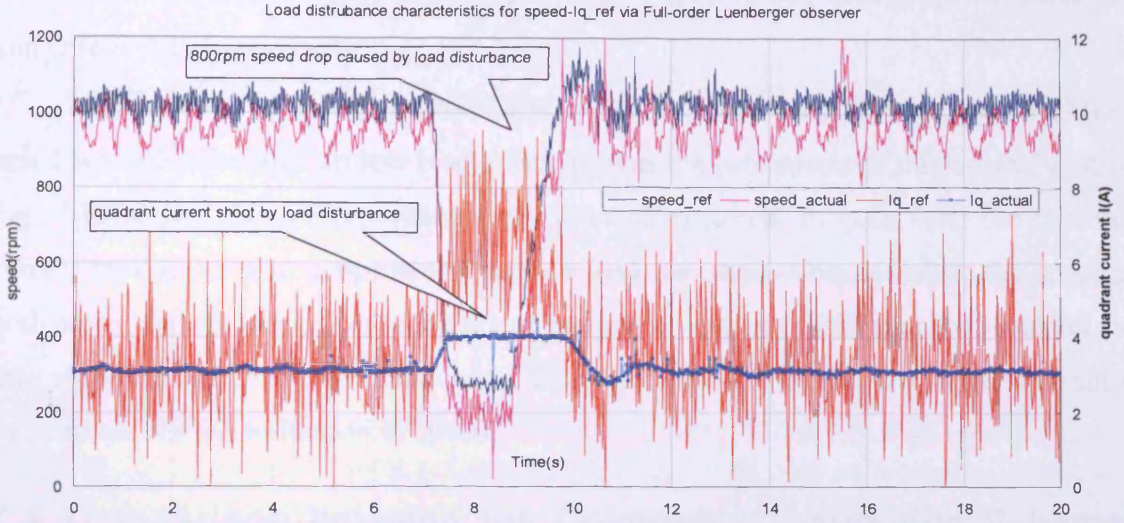

Fig. 7·11 High load disturbance effect on speed and Iq response characteristics via the full-order Luenberger observer

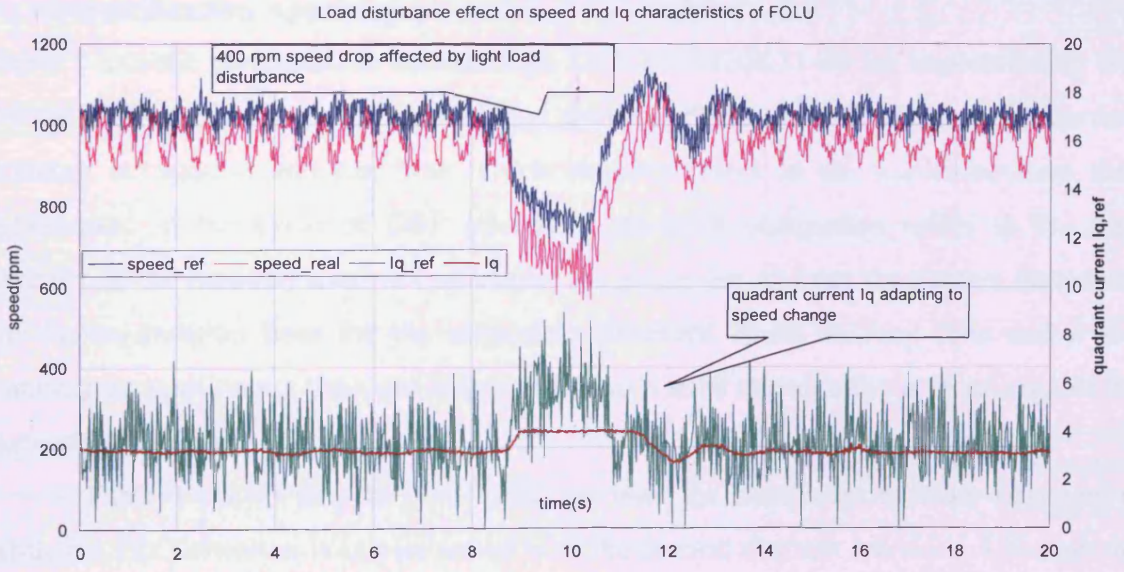

Fig. 7·12 Low load disturbance effect on speed and Iq response characteristics via the full-order Luenberger observer

The load disturbance results shown in figs. 7·11-7·12 shows the speed and quadrant current response to a step change of load torque. The series resistor connected with armature winding of the generator is tuned with great value so that small load torque is generated by the armature winding, this is the reason that the torque applied to the shaft of PMSM is so low in Fig. 7·11 and Fig. 7·12. The lower part of figs.7·11-7·12 reflects

the disturbed behaviour of the DC shunt generator armature current through the quadrant current Iq, which increases at a 5 A (Fig. 7·11)and 3 A (Fig. 7·12) steps while the imposed load disturbance causes the speed to drop to 800 rpm (Fig. 7·11) and 400 rpm (Fig. 7·12) respectively.

Fig. 7·11 shows the speed and Iq response to heavy load disturbance for FOLU-based sensorless control on low load which proves the robustness of this control system. Fig. 7·12 shows the corresponding light load disturbance. In each case the quadrant current rapidly rises to adapt to the sudden load variation. Consequently, the speed of both actual and reference dropped and stayed at a low level of 300 rpm for 1 second and then recovered to rise to normal due to the delay caused by quadrant torque current to compensate for the reduction in speed.

7.4 Comparison between the Covariance Correction Schemes for the EKF/LKF-based State Observer and Single-variable PI Regulation for the Luenberger State Observer

7.4.1 Comparison of Position Estimation Precision between Two Bias-rectification Approaches

Table 1 lists the computation load through DSP TMS320C31-50 for implementing five sensorless methods. The computation load shown includes three features: cycle number, memory occupation and run time. Cycle number refers to the implementation time represented in the cycle of DSP operation, memory occupation refers to the total quantity of the memory used to implement the algorithm and run time refers directly to the implementation time for the sensorless observer. Short running time and a low memory occupation are the most important factors used to judge the performance of the sensorless observer.

Table 1 shows that the EKF observer uses the maximum memory occupation, while the FLO observer is implemented with the second shortest run time. Although the SDL observer is implemented with the lowest memory occupation, the run time required is up to 20.32 us, which is the third longest among all the sensorless observers. The FOLU observer only occupies 153 instruction words of memory, which is even less than that of the FLO observer, but needs the maximum time to be implemented. In terms of memory occupation, the remarkable point is that the memory needed to implement the EKF observer is much higher than for any other observers due to online matrix calculation. The run time for implementing the EKF, SDL and FOLU observers is almost twice that for implementing the FLO and LKF observers. From a cost and

benefit standpoint, the proposed novel LKF is no doubt the best scheme because it is implemented with the shortest run time and a fairly small memory.

Type	Cycle number	Memory Occupation(instruct number)	Run Time(μs)
FLO	265	170	10.6
EKF	513	393	20.5
LKF	211	118	8.4
SDL	508	116	20.32
FOLU	540	153	21.6

Table 7.1 The computation load for five sensorless control methods

Table 7.2 shows the mean error between the estimated and actual rotor position of all the sensorless observers included in the comparison The position bias computation excludes the error value generated by phase shift at the start/end-point of each cycle, since the phase lead or lag always makes the error up to ±360 elec °, which would reduce the precision of error calculation. Furthermore, considering the bipolar error in the position estimation characteristics of the Luenberger observer, only absolute values of the position error are used in the average position error calculation. The result in table 7.2 reveals that the FLO and LKF observers for sensorless control of the PMSM would obtain less mean error for the estimated position than would the EKF, SDL and FOLU observers. The LKF-based sensorless control PMSM even gives the least mean error for the estimated position which proves that the Kalman filter applied in a flux-linkage-based linear model could improve the precision of position estimation.

Table 7.3 summarises the sensorless observer specifications and shows that EKF and LKF implement the correction by variance, while SDL and FOLU realise the correction through single variable PI regulation. The data in table 7.2 prove that position estimation precision is decided by correction for the state-estimation observer-based sensorless control and that variance correction would be more precise in position estimation than would a single variable PI regulator.

SENSORLESS TYPE	Mean Error (elec deg)
Flux Linkage Observer(FLO)	8.1
Extended Kalman Filter(EKF)	12.4
Linear Kalman Filter(LKF)	7.5
Single Dimension Luenberger(SDL)	13.9
Full-Order Luenberger(FOLU)	10.0

Table 7.2 The position estimation mean error for five sensorless control methods

Table7.3 includes the specifications for all the sensorless methods with these aspects: state order, co-ordinate frame and position correction type. The FLO observer belongs to the back-EMF estimation type with a low pass filter for integration compensation. The FLO observer is not a state estimation sensorless observer. EKF and LKF can be categorised as a multi-order state estimation observers in a stationary co-ordinate frame with variance correction, while the FOLU observer is a multi-order state estimation sensorless observer in a rotational co-ordinate frame with single variable PI regulation. The SDL observer is a single-order state estimation sensorless observer in a rotational co-ordinate frame with single variable PI regulation.

TYPE	Order	Co-ordinate frame	Position Correction
FLO	1	α-β	no
EKF	4	α-β	Variance
LKF	3	α-β	Variance
SDL	1	d-q	Angle PI by ΔId
FOLU	3	d-q	Angle PI by ΔId

Table 7.3 Specifications for the five sensorless control methods

Fig. 7·13 (a)-(e) shows the triangle-shaped estimated position profile in one electrical cycle of 360° for all the sensorless observers. They are captured when the PMSM runs at the rated speed. The estimated position profile comprises the estimated and actual rotor position profiles and the error between them. Fig. 7·13 (f) uses a histogram to represent the comparison of the error generated by the sensorless observers.

The estimated position error profile in fig. 7·13 (a)-(e) classifies the error correction of the observers. The error profiles of the FLO, EKF and LKF observers in show almost positive above 0° [elec deg] except for the 360° phase shift at the start/end of the electrical cycle. The positive estimated position error profile in fig. 7·13 (a)-(c) shows that the estimated position consistently leads the actual value or follows it with phase lag. The position error profile of the LKF observer has a similar pattern to that of the FLO observer: the LKF observer uses variance correction to correct the estimated bias of flux linkage in a stationary co-ordinate frame. Compared with the error profile of the EKF observer which has a high ripple, and the noise of FLO, the position error profile of the LKF observer has a reduced noise and ripple due to variance correction.

The position error profile in fig. 7·13 (d)-(e) shows single variable PI regulation as another type of error correction and features an bipolar position offset, including both the positive and negative offset. The only difference between the SDL observer in and the FOLU observer is that the SDL observer could not generate the same amount of

positive and negative offset. The ripple in position error with PI regulation in fig. 7·13 (d)-(e) is higher in amplitude than that with variance correction in fig. 7·13 (b)-(c),

In summary, FLO and two Kalman filters produce unidirectional offset while the two Luenberger observers create a bidirectional offset. Apparently the error profiles of the Luenberger observers is made of random large offsets plus high ripple while that of the Kalman filter seems to comprise regularly limited offset plus minor noise. This point strongly implies that the covariance correction could make a sensorless control appropriately limit the estimated position error.

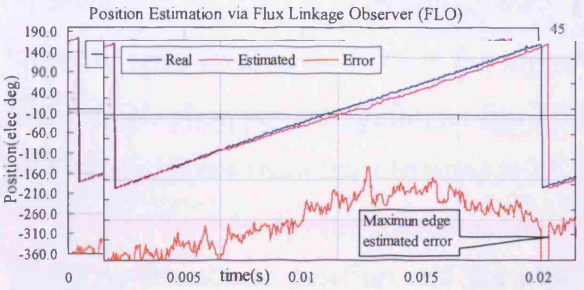

(a) position estimation via FLO

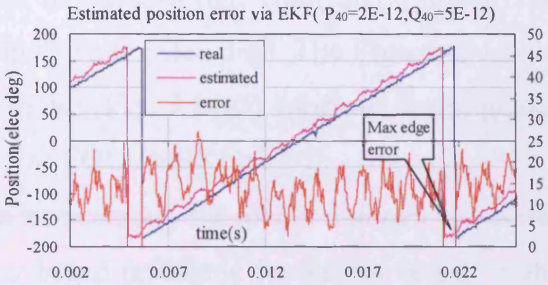

(b) position estimation via EKF

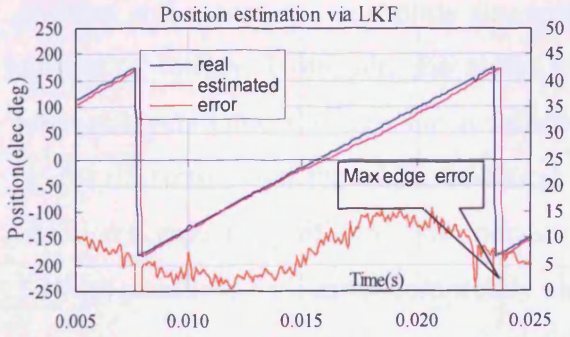

(c) position estimation via LKF

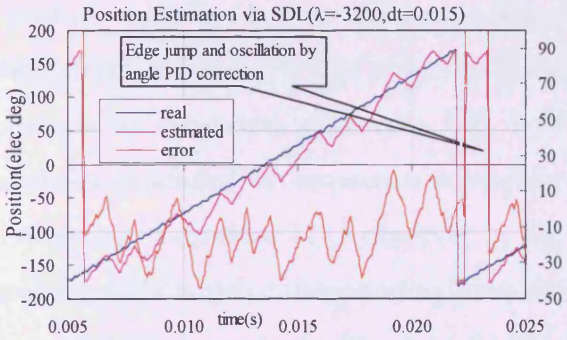

(d) position estimation via SDL

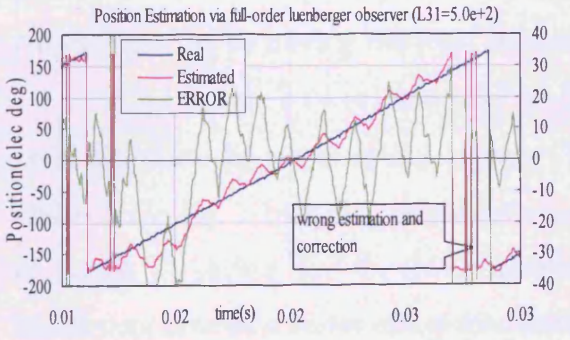

(e) position estimation via FOLU

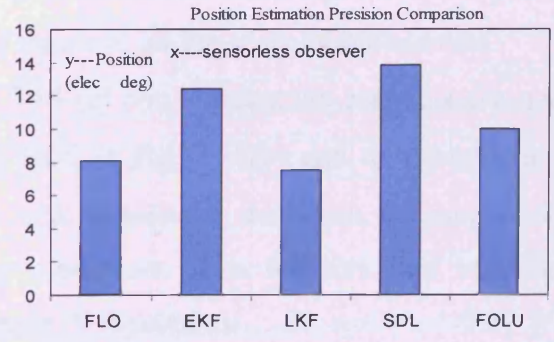

(f)

Fig. 7·13 Position estimation performance of (a) FLO, (b) EKF, (c) LKF, (d) SDL and (e) FOLU. (f) comparison of estimation precision

It is concluded in Fig. 7·13 that the estimated position error generated by FLO and LKF is smaller than EKF and two Luenberger observers, but the peak estimated

position error by FLO and LKF is greater than EKF but less than two Luenberger observers.

The lowest tolerance of 7.5° [elec deg] by LKF is close to the 8.1° [elec deg] by FLO [7·4]-[7·5] which is due to the fact that the LKF is based on orthogonal flux-linkage components. EKF could create a 12.4° [elec deg] mean angle error, while initial variance P_{40} and covariance Q_{40}, representing the fourth matrix element, could affect estimation precision [7·6]-[7·7], where P_{40} = 2E-12, Q_{40} = 5E-12. The full-order Luenberger observer can secure a 10.0° [elec deg] tolerance, close to that of EKF. The element L_{31} (expresses "column1, row3") can be used to tune rotor angle offset. The mean error created by SDL is the highest at up to 13.9° [elec deg]. The Eigen values for the SDL observer are -3200, as fig. 7·13 (d) shows. Fig. 7·13 (f) confirms the sequence of error values from least to most is LKF> FLO> FOLU> EKF> SDL.

Fig. 7·14 (a)-(e) compares the actual phase current, the ideal reference waveform based on the actual position and the observer-based reference waveform based on the estimated position. It shows the ideal current reference waveform based on the actual position and shows the complete sinusoidal profile which is ideal for the actual phase current to follow. However, the actual phase current reference is the observer-based reference generated through the estimated position by sensorless observers. Fig. 7·14 (a)-(e) illustrates that the observer-based references generated by respective sensorless observers appear significant. The non-state-estimation sensorless FLO observer in fig. 7·14 (a) produces an almost completely sinusoidal profile which correspondingly results in nearly the best actual phase current waveform with the least ripple. Fig. 7·14 (b) also creates a similar, completely sinusoidal, profile to that of the FLO, and the actual phase current benefits by having the least amount of ripple of all the sensorless observers.

FLO in fig. 7·14 (a) and LKF in fig. 7·14 (c) could create the current reference perfectly close to a sinusoidal signal. The EKF in fig. 7·14(b) and the Luenberger observers in fig. 7·14(d)-(e) create references with undesirable distortion, the magnitude of which is severe for the two Luenberger observers. It is intuitive that variance adjustment creates a better effect than does angle PI regulation.

The phase lag between real current and its reference is found only in FLO and LKF in fig. 7·14 (a) &(c). The low pass filter has been used for the calculation of flux linkage in both observers. Large peak loss is shown in fig. 7·14 (b) for EKF, which implies heavy computation time due to variance matrices. High partial distortion of the reference is also found for the Luenberger observers as shown in fig. 7·14 (d) and (e)

due to the double impact of a large Eigen value and large angle PI regulation. This point proves why partial phase excursion will not occur with FLO and Kalman filters. The peak loss, phase lag and offsets of all the observers are compared in fig 7.14 (f).

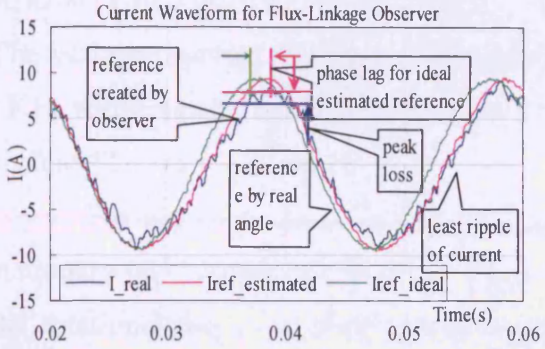

(a) current waveform by FLO

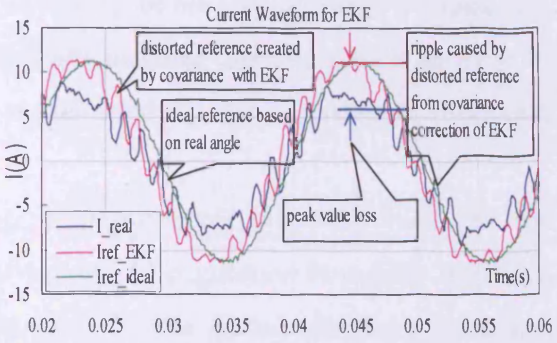

(b)) current waveform by EKF

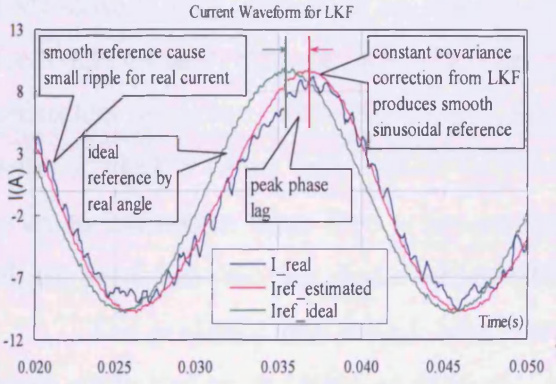

(c)) current waveform by LKF

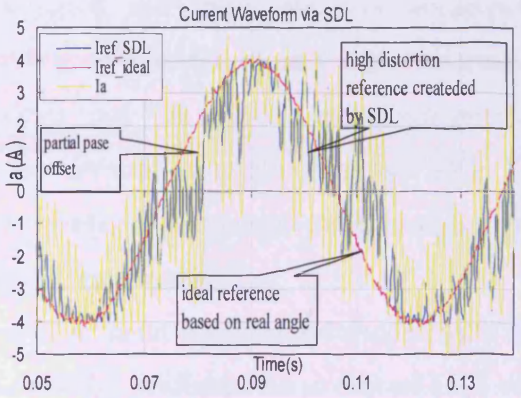

(d)) current waveform by SDL

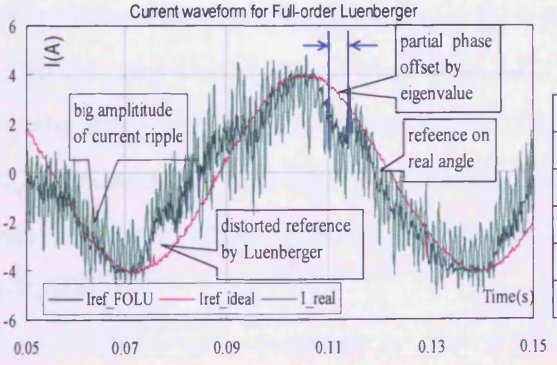

(e)) current waveform by FOLU

Type	Phase lag	Phase Offset	Peak Loss
FLO	YES	NO	YES
EKF	NO	NO	YES
LKF	YES	NO	YES
SDL	NO	YES	NO
FOLU	NO	YES	NO

(f)

Fig. 7·14 Current waveforms for (a) FLO (b), EKF (c), LKF (d) SDL and (e) FOLU. (f) performance comparison

Fig. 7·14(f) shows that the EKF observer generates a phase current without phase lag due to its reference leading the ideal references while FLO and LKF give a phase current with phase lag.

It can be concluded from the position estimation and current reference waveforms shown in figs. 7·13-7·14, that the decisive factor for the position estimation precision in the state estimation sensorless method is the position error correction scheme. This falls into two categories, variance tuning or single-variable PI regulation. The variance tuning scheme is represented by Kalman filter observers such as EKF or LKF, while single variable PI regulation is represented by the Luenberger observers such as SDL or FOLU observers.

For the co-ordinate frame, the variance tuning scheme is mainly based on the stationary α-β co-ordinate frame while single variable PI regulation is mainly based on the rotational d-q co-ordinate frame shown in table 3. The state-estimation sensorless methods, apart from LKF, have a lower estimation precision than do the classic back-EMF-based FLO observer, as the state estimation sensorless observer implements feedback control through the state error, which is present in any state estimation sensorless observer. The experiment also proves that the average estimated position error of FLO is lower than that of the other state estimation methods except LKF. The average estimation error further proves that the variance correction scheme could give higher precision than the single-variable PI regulation scheme.

The proposed novel LKF observer creates a linear speed-noise model with flux input controlled by the Kalman filter and gives similar performance to that of EKF with low implementation cost and the best estimation precision. The position and error estimation waveform explains the difference between two error correction schemes: the position error waveform of FLO with LPF compensation contains only the offset caused by the integration drift. The error waveform of EKF contains the offset caused by the differential effect and ripples caused by covariance correction, while the LKF waveform has the same offset through the integration drift and ripples caused by covariance correction.

The error waveform of the two Luenberger observers contains ripples caused only by differential effect and PI regulation. The phase current and its reference waveforms eventually could make a confirmative comparison. FLO and LKF observers could make a similar reference to the sinusoidal reference, while the EKF observer could make a sinusoidal reference with a small, acceptable triangle-shaped ripple. However, the two Luenberger observers could make the distorted sinusoidal reference have severe noise. Such a distorted reference could make the peak load current too low.

7.4.2 Analysis of Speed Response for Two Position Correction Schemes

Fig.7·15 shows that LKF have the slowest acceleration than any other observers, and it is explained that constant covariance perform worst in the error correction of speed response.

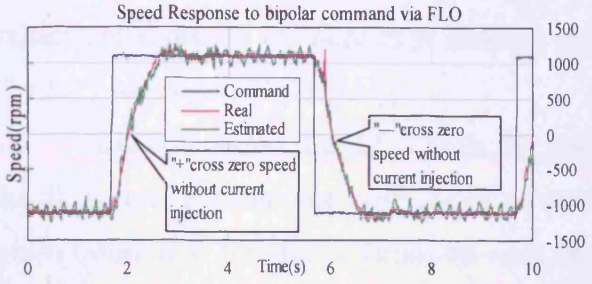

(a) speed response based on FLO

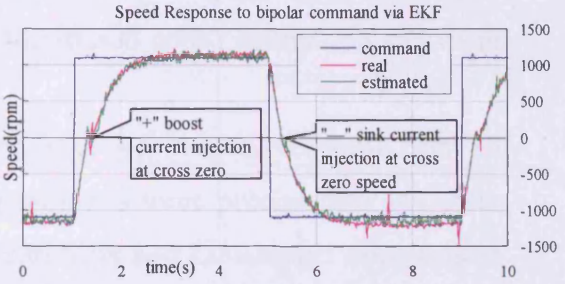

(b) speed response by EKF

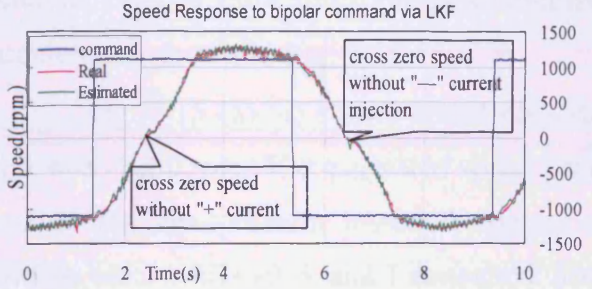

(c) speed response by LKF

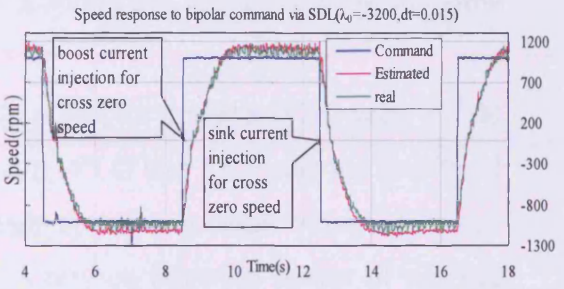

(d) speed response based on SDL

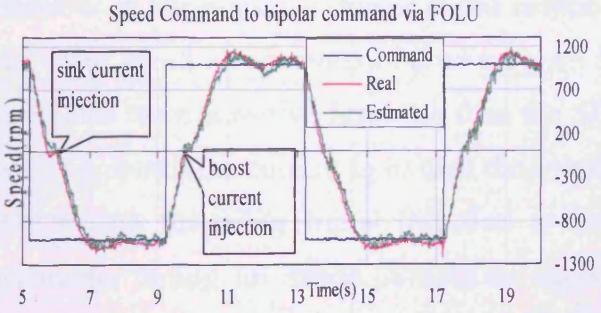

(e) speed response based on FOLU

Sensorless	Speed estimation	Current injection via cross zero
FLO	Position increment	no
EKF	Direct differential	yes
LKF	Direct differential	no
SDL	q-axis back-EMF via pure flux-linkage	yes
FOLU	q-axis back-EMF via pure flux-linkage	yes

(f)

Fig. 7·15 Speed response comparison for (a) FLO, (b) EKF, (c)LKF, (d) SDL and (e) FOLU. and (f) speed-measure list

The PMSM used its shaft coupled to that of the shunt DC generator equivalent to about 0.8~1 Nm measured load. Speed-estimation methods are listed in fig. 7·15(f) as follows: the speed estimation based on FLO is implemented only by estimated angle increment, while the state estimation techniques such as EKF and LKF can directly obtain the speed information through one of the estimated states. The other state estimations such as SDL and FOLU with large Eigen values can also estimate speed at start up; however,

shortly afterwards, the estimated speed turns unstable [7·8-7·10]. The problem here is solved by speed measurement based on the pure d-q flux linkage described in (7·12).

Because of the estimated position curve with high distortion and the oscillation or pulses in the edge of cycle shown in fig. 7·15 (d-e), it is difficult to use the angle increment approach with the Luenberger methods to calculate speed. Sine and cosine values are replaced by pure flux linkage in the flux-based speed estimation shown in (7·12) [7·4-7·5 and 7·11].

It is concluded that FLO have the fastest acceleration in speed response from all the observers, because the derivate of estimated position is more precise than any other speed estimation for state estimation such as Kalman filter and Luenberger observers as long as estimated position has the enough high precision. The speed estimation by Kalman filter or pure flux linkage estimation by Luenberger proves to have the slow acceleration shown in Fig. 7·15.

Fig. 7·15 (a)-(e) shows speed responses to a bipolar command between +1000 rpm and -1000 rpm. The estimated speed produced by FLO and LKF past the zero level and do not need current injection applied through speed command when the speed crosses zero, while EKF and Luenberger observers rely on injection (boost or sink) to realize smooth zero-passing, The double integration of measured noise from the LKF observer is attributed to slower speed response than the other approaches. Even under the same speed measurement based on pure flux linkage in (7·12), the FOLU observer generates more sensitive response than the SDL observer The higher position precision would enhance the current Iq to tune the speed response behaviour via the PI regulator. The reason for using signal injection at zero-pass for EKF is to overcome precise parameter tuning for speed covariance adjustment at low speed. However, the signal injection used at zero-cross in Luenberger observers is to avoid a slow speed boost from zero speed or a sink crossing zero speed. The acceleration ability for the flux-linkage approach in fig. 7·15 (d) based on SDL is close to that from EKF in fig. 7·15 (b). This shows that the flux-based speed estimation in the Luenberger observer can give a similar performance to that of EKF.

Fig. 7·15 (f) lists aspect of usage of current injection at cross-zero speed for the observers all of which, apart from FLO and LKF, need current injection to improve cross-zero speed. If the estimated position has enough precision, as for FLO and LKF, the sensorless observer could accelerate rapidly to pass the near-zero speed area. This is why EKF and the two Luenberger observers need to inject current at zero-cross speed for acceleration.

7.5 References

[7•1] B. Bhangu, C. Williams, C. Bingham and J. Coles, "EKF and other nonlinear state-estimation techniques for sensorless control of automotive PMSMs", *Int. Symp. on Power Electronics, Electrical Drives, Automation and Motion, Proceedings of the SPEEDAM 2002,* Ravello, Italy, C5.33-38,

[7•2] P. Snary, B. Bhangu, C.M. Bingham, D.A. Stone and N. Schofield, "Matrix converters for sensorless control of PMSMs and other auxiliaries on deep-sea ROVs ", *IEE Proceeding on Electric Power Application, 2005,* Vol.1152, No.2, 382-392

[7•3] B. S. Bhangu and C. M. Bingham, "GA-based tuning of nonlinear observers for sensorless control of IPMSMs", *Power Electronics, Machines and Drives, 2004,*April 2004, Vol.1, 93 - 97

[7•4] M. C. Huang, A. J. Moses, F. Anayi and X. G. Yao, "Linear Kalman filter (LKF) sensorless control for permanent magnet synchronous motor based on orthogonal output linear model", *Int. Symp. on Power Electronics, Electrical Drives, Automation and Motion, SPEEDAM 2006,* Taormina, Italy, 1381 – 1386

[7•5] M. C. Huang, A. J. Moses, F. Anayi and J Sagarduy, "Two Reduced-order Stochastic State Observer Comparison &Investigation based on LKF and SDL", *37th IEEE Power Electronics Specialists Conference(PESC2006)*, Jeju, South Korea June 18~22, 2006, 1484-1489

[7•6] S. Bolognani, R. Oboe, and M. Zigliotto, "Sensorless Full-Digital PMSM Drive With EKF Estimation of Speed and Rotor Position", *IEEE Transaction on Industrial Electronics*, February 1999, Vol. 46 (1), 184-191

[7•7] S. Bolognani, M. Zigliotto and M. Zordan, "Extended-range PMSM sensorless speed drive based on stochastic filtering", *IEEE Transaction on Power Electronics*, Jan 2001, Vol.16, 110 – 117

[7•8] D. Hamada, "Stability analysis of sensorless permanent magnet synchronous motor drive with a reduced order observer", *Proceedings of the International Conference of Electric Machines and Drives*, Seattle, USA, 1999, 95 – 97

[7•9] K. Tatematsu, D. Hamada, K. Uchida, S. Wakao and T. Onuki, "Sensorless control for permanent magnet synchronous motor with reduced order observer",

Proceeding of the 29th Annual IEEE Power Electronics Specialists Conference, Fukuoka, Japan, 1998, 125-131

[7•10] K. Tatematsu, D. Hamada, K. Uchida, S. Wakao and T. Onuki, "Sensorless permanent magnet synchronous motor drive with reduced order observer", *Proceedings of the 13th Annual Applied Power Electronics Conference and Exposition*, Anaheim, USA,1998, 75-80

[7•11] Y. F. Shi, Z. Q. Zhu and D. Howe, "EKF-based Hybrid Controller for Permanent Magnet Brushless Motors Combining Hall Sensors and a Flux-Observer-based Sensorless Technique", *Proceedings of the IEEE Int. Conf. on Electric Machines and Drives*, San Antonio, TX, 2005 , 1466 – 1472

[7•12] N. Matsui, and M. Shigyo, "Brushless DC motor control without position and speed sensors", *IEEE Transaction on Industrial Application*, Jan.-Feb1992, Vol.28 (1),120 – 127

[7•13] J. X. Shen and Z. Q. Zhu, "Improved speed estimation in sensorless PM brushless AC Drives", *IEEE Transaction on Industrial Application*, Vol.38 (4), July/August 2002, 1072 – 1080

[7•14] http://usdigital.com/products/interfaces/encoder/converters/

CHAPTER 8, CONCLUSION AND FURTHER RESEARCH OPPORTUNITIES

8.1 Conclusions

(1) The invariant-variance LKF-based sensorless technique and Flux linkage observer can obtain the higher average precision position estimation than other methods under no load mode and LKF observer has high self-start-up capability at almost any arbitrary position on load. In generator mode, LKF observers can secure most close to sinusoidal current waveform with lower ripple and distortion than other observers.

(2) The comparison of sensorless methods shows that the position correction plays the dominant role in state estimation sensorless controlled PMSMs. The variance-corrected state estimation technique not only gives high estimation precision but also generates more rapid response to load disturbance from external environment than single-variable PI regulation schemes.

(3) Investigation of SDL/ FOLU observer methods prove the position PI regulation scheme lacks the high precision position correction capability of FLO and Kalman filters with covariance correction. The PI regulation scheme can not make estimated position stabilise at the terminal of estimated position cycle. Due to high offset to actual position trace, SDL/FOLU-based sensorless control of a PMSM can not operate in the mode of high load like a generator.

(4) The novel constant Variance correction in LKF is proved to be the best on-line correction approach with respect to the average position estimation for state-estimation sensorless control than classic invariable correction in EKF. The constant variance correction LKF-based sensorless estimation is the optimal effective position estimator for the same computation cost and precision, full-range power operation as EKF. However, the constant variance correction in LKF gives the poorest speed response of the five observers investigated. Considering comprehensive performance and neglecting arbitrary self start, FLO is the best sensorless method.

(5) Neglecting the self start-up at the arbitrary initial position, the experiment proves that flux linkage observer is surprisingly the best sensorless estimation method of five shaft position estimation methods on the aspects of the average/peak estimated position

error and rapid speed response under the no electromagnetic load. The other position estimation methods can't make the satisfactory performance on the aspects of both position error and speed response, the heavy computation load from on-line matrix calculation causes EKF to generate the great position estimation error; the invariant covariance correction causes LKF to make the slowest speed response of five sensorless methods; two types of Luenberger observers are hard to find the appropriate eigenvalues for the stabilised system, and single variable PI regulation further increase the estimated position error, therefore two types of Luenberger observers prove to be the worst sensorless observer.

(6) Essentially all five sensorless methods are based on back-emf/flux linkage extraction, only the approaches of back-emf/flux linkage extraction used by five sensorless methods are different. Flux linkage observer is based on the integration; EKF and two Luenberger observers is based on the differential way; LKF is based on both the integral and differential way. This point can be used to explain why the five sensorless methods make poor performance at zero or near zero speed.

(7) The Luenberger observer are proved to easily unstable for the speed estimation due to choice of eigenvalues, furthermore, shaft position estimation is inevitably affected to cause the greatest estimated position error, therefore, Luenberger-based sensorless control PMSM is limited to be used in heavy load application.

(8) Position correction scheme is the key for the self start-up of sensorless control PMSM, covariance correction scheme proves to make the estimated position converge to the real position more precisely than single variable PI regulation; single variable PI regulation demonstrates the stronger correction than covariance correction under the heavy load at the initial start-up period.

(9) The experiment reports that FLO can obtains the lowest operational speed of 60 rpm. It is concluded that all the state estimation methods have the poorer performance than FLO with aspect on lowest operational speed.

8.2 Future Research Opportunities

(1) The next research highlight should be high frequency signal injection method at ultra low speed [0, ±60 rpm], since the high frequency signal injection method can overcome the drawback of the state observer not being able to generate the precise position estimation in the low signal area. The high frequency injection signal method is to detect the rotor spatial saliency due to structure or magnetic saturation. Instead of a parameter-sensitive observer, the position/speed information is extracted from the response of the high frequency excitation applied to the PM motor. Rotor position detection techniques based on phase inductance evaluation, allow for reliable low- and zero- speed operation in machines showing self or induced anisotropy.

(2) The high frequency signal injection method techniques is advised to be complemented by a state observer or a Kalman filter, also requiring a shift to other sensorless methods as the speed increases. Usually, a special signal is injected to the motor with extra hardware and signal processing to obtain the position information. The Kalman filter observer combined with high frequency signal injection should be considered.

Appendix A Coding for DSP and Host PC

The coding used in the DSP for the sensorless control PMSM is PMSM.asm, and the code complied on the host PC as a front-end user program is PMSM.exe. The code scripts are written in assembly language and given below.

A.1 PMSM.asm

A.1.1 Definition of variables

R0~7 and AR0~AR7 are used for main register variables. The RAM from 0X809CB0 to 0X809CF8 and 0x809E00 are for 14 matrix calculation. The RAM from 0X809E00 to 0X809E07 is 8 space vector switch control words. Table for the ARCTG function start from 0x809E70, Table for the SIN function start from 0x809E80. The rest of RAM are used for EKF varables.

```
; BLAC strategy.
; AR0: 0x809E00  voltage vectors, variables and reserves
; AR1: 0x809E80  table for sin(x)
; AR2: 0x808000  address for timers
; AR3: 0x809E70  table for arctan(x)
; AR4: 0x809D00  rule base for fuzzy control
; IR0: current voltage vector
; IR1: for SIN, COS, ARCTG, etc.
; R0: temperary results, such as those of SIN, COS, INVF, etc..
; R1: temperary usage
; R2: reference of Id
; R3: reference of Iq
; R4: old voltage vector
; R5: current encoder value or motor speed
; R6: temperary usage
; R7: temperary usage

; ***************************
;     RESERVED SPACE
; ***************************
;matrix area1
;
;for 14 matrix calculation
;THIS AREA IS LIMITED IN 0X809CB0 TO 0X809CF8
```

```
        .START  "MATRIX1", 0x809CB0
        .SECT "MATRIX1"

; STACK
; Space from 0x809DA3 to 0x809DFF is reserved for
; the stack.
;
; Switching Table
; Truth Table for the gate signals of inverter.
; Look up the gate signals from the table according
; to the voltage vector.
;
      .START  "TRUTH", 0x809E00
      .SECT "TRUTH"
; BLAC switching table vs. voltage vector
      .WORD 0x0EA          ; ABC=000--------11101010
      .WORD 0x0DA          ; ABC=001--------11011010
      .WORD 0x0E6          ; ABC=010 --------11100110
      .WORD 0x0D6          ; ABC=011--------11010110
      .WORD 0x0E9          ; ABC=100--------11101001
      .WORD 0x0D9          ; ABC=101--------11011001
      .WORD 0x0E5          ; ABC=110--------11100101
      .WORD 0x0D5          ; ABC=111--------11010101
 ;
; Reservation of some RAM.
      .WORD 0x000000FFF     ; reserved              (0x809E08)
      .WORD 0x0FFFFF000     ; reserved              (0x809E09)

; Table for the ARCTG function.
; One-eigth cycle is devided into 10 steps.
;
      .START  "ARCTAN", 0x809E70
      .SECT "ARCTAN"

;
; Table for the SIN function. A cycle is devided into 125 grids.
;
      .START  "SINE", 0x809E80
      .SECT "SINE"

; Interruption vector of Timers
;
      .start  "TIMERS", 0X809FC9
      .sect   "TIMERS"
      B TINT0
      B TINT1
```

A.1.2 main loop:

The main loop includes initialization and PID calculation.

```
;*****************************************************************
;File Name      :EKF.asm
;Project        :PMSM Drive Based on TMS320C31-50
;Originator     :Ming Chuan Huang (Cardiff University, UK)
;*****************************************************************
; (1) encoder-based rotor position detection and speed measurement;
; (2) calibration of current transducers;
; (3) sensorless estimation of rotor position and speed;
; (4) both encoder-based and sensorless BLAC vector control;
```

```
; (5) PID, speed controls;
; (6) numerours subroutines, such as sin, cos, arctan, inversion, frame conversions.
; ***************************
;     MAIN PROGRAM
; ***************************
;
; SET START ADDRESS
      .start  "smpmsm", 0x809802   ; Start assembling here
      .sect   "smpmsm"
;
; SETTING THE PARAMETERS OF PID, FUZZY ALGORITHM AND OTHER REGULATORS
KP:    .SET 3.15E-3 ; PROPORTION
KI:    .SET 3.15E-3   ; INTEGRATION
KD:    .SET 0       ; DERIVATION
TS:    .SET 3.E-3           ; SAMPLING CYCLE
IMAXP:  .SET 4.0             ; POSITIVE MAXIMUM CURRENT
IMAXN:  .SET -4.0            ; NEGATIVE MAXIMUM CURRENT
ICHNLMT:.SET 0.01              ; LIMIT OF CURRENT CHANGE, FOR PID ONLY
ICHNMAX:.SET 1.5             ; MAXIMUM CURRENT CHANGE, FOR DECREASING
ICHNFCT:.SET 1.2             ; ICHNMAX / ICHNFCT, FOR INCREASING
ICHNFCT2:.SET 8.             ; ICHNMAX / ICHNFCT2, SMALLER ICHNMAX
SPEEDR: .SET -1100.0           ; SPEED COMMAND(1100RPM)
SPERBD1:.SET 4990.           ; SPEED ERROR BAND #1
SPERBD2:.SET 4980.           ; SPEED ERROR BAND #2
SPERBD3:.SET 6.              ; SPEED ERROR BAND #3, USELESS IN SLAC5
SPERBD4:.SET 300.            ; SPEED ERROR BAND #4, USELESS IN SLAC5
HYST:  .SET 625.0            ; CONSTANT FOR HYSTE. CONTR. FREQ.
THYST:  .SET 50.0e-6           ; CYCLE OF HYETE. CONTR. (s)
SPDMEAS:.SET 60              ; RATIAO OF HYST (20KHz) & SPEED MEASUR. FREQ.
SPDEST: .SET 0.9997          ; FACTOR FOR COMBINED SPEED ESTIMATION
;
; END OF SETTING THE PARAMETERS OF REGULATORS
;
; SETTING THE PARAMETERS OF BLAC MOTOR
R:     .SET 0.6             ; RESISTANCE IN ALFA-BETA FRAME (ohm)
L:     .SET 5.5e-3          ; INDUCTANCE IN ALFA-BETA FRAME (H)
FL:    .SET 71.501679e-3          ; FLUX LINKAGE EXCITED BY MAGNETS (Wb)
NFL:   .SET 9.549/92.8e-3     ; 60/(2*Pi)/FL
W0:    .SET 1.5*2*3.141592654  ; CUT-OFF FREQUENCY OF FLUX OBSERVER
; END OF SETTING THE PARAMETERS OF BLAC MOTOR
;
; SETTING ENCODER CONSTANTS
; ENCBS1: .SET 2116            ; BIAS OF ENCODER VALUE
; ENCBS2: .SET 1883
; END OF SETTING ENCODER CONSTANTS
;
;
; SETTING THE CURRENT ERROR BAND FOR HYSTERISIS CONTROL
DELT_I: .SET 0.02            ; ERROR BAND FOR HYSTERISIS CONTROL
KIQ:   .SET -1.0           ; GAIN OF Iq REFERENCE, NEGATIVE
INVKIQ: .SET 1.0           ; INVERSION OF THE GAIN
; END OF SETTING THE CURRENT ERROR BAND FOR HYSTERISIS CONTROL
;
; Initialization
START:  LDP @AD_DA           ; load data pointer;
      AND 0, R1
      STI R1, @DA_P          ; switch off the inverter
      LDI 0, IR0           ; clear IR0
      LSH 16, IR0
      LDI 0x404F, AR0        ; set AR0 as 0x809E00
      LSH 9, AR0
      LDI 0x404F, AR1        ; set AR1 as 0x809E80
```

```
        LSH 9, AR1
        OR 0x80, AR1
        LDI 0x808, AR2          ; set AR2 as 0x808000
        LSH 12, AR2
        LDI 0x404F, AR3         ; set AR3 as 0x809E70
        LSH 9, AR3
        OR 0x70, AR3
        LDI 0x2027, SP          ; set SP as 0x809DA3
        LSH 10, SP
        OR 0x1A3, SP
        LDI 0x2027, AR4         ; set AR4 as 0x809D00
        LSH 10, AR4
        OR 0x100, AR4
        LDI 0x2027, AR5         ; set AR5 as 0x809C00
        LSH 10, AR5
; initializing the timers and interruptions
        AND 0x1FFF, ST          ; global interruption OFF
        AND 0, IF               ; reset register IF
        AND 0, IE
        LSH 16, IE
        OR 0x300, IE            ; Timer 0 & 1 interruption ON
        LDI 0, R1
        LSH 16, R1
        STI R1, *+AR0(0x44)
        STI R1, *+AR2(0x20)     ; reset the Timer0
        STI R1, *+AR2(0x24)     ; set the Timer0 counter register
        STI R1, *+AR2(0x30)     ; reset the Timer1
        STI R1, *+AR2(0x34)     ; set the Timer1 counter register
        LDI 0x2FAF, R1          ; 4s
        LSH 12, R1
        OR 0x80, R1
        STI R1, *+AR2(0x28)     ; set the Timer0 period register
        LDI HYST, R1            ; 50us
        STI R1, *+AR2(0x38)     ; set the Timer1 period register
        OR 0x2000, ST           ; global interruption ON
        LDI SPDMEAS, R1
        STI R1, *+AR0(0x45)
; getting the offset of current measurement

        ldi @AD1_S, r0
        CALL CURR
        ldf *+ar0(0x0b), r0     ;A current measured
        addf *+ar0(0x54), r0    ;add offset (when Ia=0)
        stf r0, *+ar0(0x54)
        ldf *+ar0(0x0d), r0     ;B current measured
        addf *+ar0(0x55), r0    ;add offset (when Ib=0)
        stf r0, *+ar0(0x55)
        ldf *+ar0(0x0f), r0     ;C current measured
        addf *+ar0(0x56), r0    ;add offset(when Ic=0)
        stf r0, *+ar0(0x56)
        ldf *+ar0(0x54), r0
        mpyf 7.8125e-3, r0
        stf r0, *+ar0(0x54)
        ldf *+ar0(0x55), r0
        mpyf 7.8125e-3, r0
        stf r0, *+ar0(0x55)
        ldf *+ar0(0x56), r0
        mpyf 7.8125e-3, r0
        stf r0, *+ar0(0x56)
BLAC:   LDF 0., R0
        STF R0, *+AR0(0x4A)             ; set the original
        STF R0, *+AR0(0x4B)             ; currents being zero
        STF R0, *+AR0(0x4C)
```

```
      LDF SPEEDR,R0
      CMPF 0.0,R0
      BNN PRUN
      LDF IMAXN,R3
      B SVIQ
PRUN   LDF IMAXP, R3          ; setting the original Iq reference
SVIQ   STF R3, *+AR0(0x43)    ; save current Iq reference
      LDF 0., R2              ; setting original Id reference
     ; LDI R4, IR0            ; setting original voltage vector
     ; LDI *+AR0(IR0), R0
     ; STI R0, @DA_P
      LDI 0x2C1, R0
      STI R0, *+AR2(0x20)     ; start the Timer0
      STI R0, *+AR2(0x30)     ; start the Timer1
      LDI @AD1_S, R0          ; starting A/D converters to measure
;GH     B   GH
; normal operation begins. since the flag ST is used in the following
; program, it must not be changed by any ISR. in other words, in an ISR,
; the first instruction must be PUSH ST, and the second last be POP ST.
BLAC2:  LDI *+AR0(0x44), R0     ; if speed is not measured since last
      B BLAC2                 ; regulation of Iq ref., no more action
;
; the following six instructions are used to choose BLAC operation
; either with or without current regulation. keeping them means to
; choose the operation without current regulation; deleting them with
; semi-colons, to choose the operation with current regulation.
;       ldf *+ar0(0x26), r0
;       cmpf 600., r0
;       bn BLAC2
;       ldf .9, r3              ; setting the Iq reference without regulation
;       stf r3, *+ar0(0x43)
;       b BLAC2                 ; for temperary use, no regulation of Iq
;
; the following is to regulate the Iq reference. Id reference is zero.
IQRREG: LDF *+AR0(0x25), R0     ; calculating the current speed error,speed command
      SUBF *+AR0(0x26), R0      ; current speed error is in R0
      STF R0, *+AR0(0x27)       ; current error
; saving the speed errors
      LDF *+AR0(0x28), R6
      STF R6, *+AR0(0x29)       ; last 2nd error
      LDF *+AR0(0x27), R6
      STF R6, *+AR0(0x28)       ; last error
     ; STF R0, *+AR0(0x27)      ; current error
; current error is in R0, last error is in R6, old Iq is in R3
;
; the following two instructions are temperarily used
; to skip the hybrid (PID+fuzzy) control, but to use
; only one control (either PID or fuzzy)
      CALL PID
IQRREG2:CALL IQLMT              ; limiting Iq reference
      STF R3, *+AR0(0x43)       ; save new Iq reference
; Iq regulation is finished
      MPYI 0, R0                ; set flag showing Iq has been regulated
      STI R0, *+AR0(0x44)       ; since last speed measurement. no more
    ;  B BLAC2                  ; regulation before next measurement
      RETS
;
; PID algorithm
PID:   LDF *+AR0(0x27), R0
      LDF *+AR0(0x28), R6
      MPYF *+AR0(0x30), R0      ; PID or PI algorithm
      MPYF *+AR0(0x31), R6
      SUBF R6, R0
```

```
      LDF *+AR0(0x29), R6
      MPYF *+AR0(0x32), R6
      ADDF R0, R6          ; the calculated change of Iq is in R6
      stf r6,*+ar0(0x67)
      LDF *+AR0(0x2A), R0
      CMPF R0, R6          ; limiting the change of Iq
      BNN IQRREG4            ; R6 must be ranged as:
      MPYF -1., R0         ; -R0 <= R6 <= R0
      CMPF R0, R6
      BNN IQRREG3
IQRREG4:LDF R0, R6
IQRREG3:ADDF R6, R3          ; new Iq reference is in R3
      RETS
;
; switching between fuzzy logic and PID algorithm
;FnPID:  LDF *+AR0(0x27), R0     ; current error
;       ABSF R0, R0
;       SUBF *+AR0(0x36), R0
;       MPYF *+AR0(0x3C), R0
;       MPYF R0, R1
;       SUBF 1., R0
;       MPYF R0, R3
;       SUBF3 R3, R1, R3
;       RETS
;
; limiting the new Iq
IQLMT:  CMPF IMAXP, R3         ; limit of new Iq reference
      BN IQRREG1
      LDF IMAXP, R3
      RETS
IQRREG1:CMPF IMAXN, R3
      BNN IQRREG0
      LDF IMAXN, R3
IQRREG0:RETS
;subroutine POSTIDG deal with +-2pi jump on the edge of position triangle wave
;input is float register R5:POSITION ERROR
;OUTPUT IS FLOAT register R5:POSITION ERROR
POSTIDG: CMPI 0,R5
      BNN FLPO ;IF DELTA>=0,FLPO (CLOCKWISE or jump in anti-clockwise)
  ;IF DELTA<0,
      CMPI -2000,R5
      BN PLGP  ;IF DELTA<=-3000,4000+DELTA
      B OTDG
  ;IF DELTA>=0
FLPO    CMPI 2000,R5
      BNN PLGN  ;IF DELTA>=3000,4000-DELTA (2pi of jump in anticlockwise)
      B OTDG    ;or so clockwise if delta<3000 or >=0
  ;JUMP of -2pi
PLGP    ADDI 4000,R5
      B OTDG
  ;jump of 2pi
PLGN    LDI 4000,R0
      SUBI R0,R5
    ;  LDI R0,R5
OTDG    FLOAT R5,R5
      RETS
;
```

A.1.3 Interrupt Service Routine List

The start and end of the ISR including Timer1 and Timer0 is presented here, . At the start of the ISR, the status register (ST) and Interrupt Enable (IE) register are stored in the system stack, using the PUSH command. They are returned at the end using the POP command, thereby setting the DSP's conditional flags to the state from where the interrupt occurred.

```
; ************************
;    SUBROUTINES
; ************************
;
;
; INDEX for subroutines
; ABCDQ:      a, d, c --> d, q, 0
; ALIGN:      aligning the rotor at a certain position
; ARCTG:      ARCTAN(R1/R0)
; ARCTG1:     ARCTAN(R0)
; COS:        COS(theta)
; COSM:       COS(theta-120degrees)
; COSP:       COS(theta+120degrees)
; CURR:       3-phase current measurement
; DELAY:      delay
; DISCURR:    display actual current and current reference
; DQABC:      d, q --> a, b, c
; INVF:       inversion of a floating-point number, 1/R0
; IREFD0:     a,b,c current references while Id=0
; IREG:       current regulation, obtaining voltage vector
; POST:       reading encode value and compensating
; SIN:        SIN(theta)
; SINM:       SIN(theta-120degrees)
; SINP:       SIN(theta+120degrees)
; TINT0:      Timer0 ISR
; TINT1:      Timer1 ISR, calculate speed, regulate current reference
; VOLT:       DC voltage measurement
;
; Notes:
; (1) Since the flag ST is used in the main program, it must not be
; changed by any ISR, in other words, it should be saved with PUSH
; and POP in the ISR.
; (2) If any register of R0 to R7 is saved in any subroutine as
; both fixed-point data and float-point data, it should be saved
; like: PUSH R0, PUSHF R0, ... ..., POPF R0, POP R0. It must not be
; saved like: PUSHF R0, PUSH R0, ... ..., POP R0, POPF R0. An example
; is in the subroutine INVF.
;
;*************************************************************************
```

A.1.3.1 Control Interrupt Timer1

Timer1 interrupt subroutine will be executed in the frequency of 20khz, conducting voltage&current measurement and position read-in, sensorless algorithm, space vector hysteresis control.

```
;*****************************************
; Interruption Service Subroutine TINT1.
; The ISR is for Timer 1.
; (1) Hysterisis control every 50us.
; (2) Speed measurement every 3ms.
; Speed (0x5B): ne=LPF(EMF/flux), fast response
; Speed (0x57): nd=LPF(dTheta_est/dt), high accuracy at steady state
; Speed (0x60): nc=nd/(Ts+1)+ne*Ts/(Ts+1), fast & accurate
; Speed (0x5F): na=dTheta_enc/dt, correct, using encoder
; Speed (0x26): speed feed back, selected from above
; USED BUT NOT CHANGED:
;  R0, R1, R3, R5, R6, R7
; CHANGED: none
; CALLED SUBROUTINE(S):
;  ARCTG, COS, CURR, IREFD0, IREG, POST, SIN, VOLT
;
TINT1:  PUSH ST
      PUSH R5
      PUSHF R5
      PUSH R3
      PUSHF R3
      PUSH R1
      PUSHF R1
      PUSH R0
      PUSHF R0
      PUSH R6
      PUSHF R6
      PUSH R7
      PUSHF R7
      AND 0x0FDFF, IE       ; disable interuption of Timer 1
      LDF *+AR5(0xF9),R0
      STF R0,*+AR0(0X7C)  ;U_Alfa K-1
      LDF *+AR5(0xFA),R0
      STF R0,*+AR0(0X7D)  ;U_BETA K-1
      CALL CURR             ; measure the real current
      LDI @AD1_S, R0        ; starting A/D converters
      CALL VOLT
; estimating rotor position
;*******************************
ITHRE:  PUSH R4
      ASH -1, R4            ; voltage vector
      BC VVECT1
      LDF 0., R0
      LDF 0., R1
      B VVECT2
VVECT1: LDF *+AR0(0x4D), R0
      LDF *+AR0(0x4F), R1
VVECT2: ASH -1, R4
      BNC VVECT3
      ADDF *+AR0(0x4D), R0
      SUBF *+AR0(0x4F), R1
VVECT3: ASH -1, R4
      BNC VVECT4
```

```
    ADDF *+AR0(0x4E), R0
VVECT4: POP R4
    LDF *+AR0(0x11), R5
    MPYF R5, R0          ; U_Alfa in R0
    STF R0,*+AR5(0xF9)    ;SAVE U_Alfa
    MPYF R5, R1          ; U_Beta in R1
    STF R1,*+AR5(0xFA)    ;SAVE U_BETA
    PUSHF R0
    PUSHF R1
    LDF *+AR0(0x4B), R0    ; current vector (Ib)
    ADDF *+AR0(0x4C), R0   ;Ib+Ic
    MPYF -0.5, R0         ;(Ib+Ic)/2
    ADDF *+AR0(0x4A), R0   ;Ia+(Ib+Ic)/2
    MPYF *+AR0(0x4E), R0   ; [Ia+(Ib+Ic)/2]*2/3 =I_Alfa in R0
    STF R0, *+AR0(0x1F)    ; save I_Alfa
    MPYF *+AR0(0x50), R0   ; R*I_Alfa in R0
    LDF *+AR0(0x4C), R1
    SUBF *+AR0(0x4B), R1
    MPYF *+AR0(0x4F), R1   ; I_Beta in R1
    STF R1, *+AR0(0x20)    ; save I_Beta
    MPYF *+AR0(0x50), R1   ; R*I_Beta in R1
    POPF R5
    SUBF3 R1, R5, R1       ; U_Beta-R*I_Beta in R1
    stf r1, *+ar0(0x5a)    ; save U_Beta-R*I_Beta
    MPYF *+AR0(0x53), R1   ; LPF replacing pure integration
    POPF R5
    SUBF3 R0, R5, R0       ; U_Alfa-R*I_Alfa in R0
    stf r0, *+ar0(0x59)    ; save U_Alfa-R*I_Alfa
    MPYF *+AR0(0x53), R0   ; LPF replacing pure integration
    LDF *+AR0(0x52), R5    ; LPF replacing pure integration
    MPYF *+AR0(0x46), R5   ; LPF replacing pure integration
    ADDF R5, R0          ; flux-linkage_Alfa in R0
    STF R0, *+AR0(0x46)    ; save flux_linkage_Alfa
    LDF *+AR0(0x52), R5    ; LPF replacing pure integration
    MPYF *+AR0(0x47), R5   ; LPF replacing pure integration
    ADDF R5, R1          ; flux-linkage_Beta in R1
    STF R1, *+AR0(0x47)    ; save flux_linkage_Beta
    LDF *+AR0(0x51), R5
    MPYF *+AR0(0x1F), R5   ; I_Alfa*L in R5
    SUBF R5, R0          ; flux(by magnet)_Alfa in R0
    LDF *+AR0(0x51), R5
    MPYF *+AR0(0x20), R5   ; I_Beta*L in R5
    SUBF R5, R1          ; flux(by magnet)_Beta in R1
   LDF 102.4, R5        ; the following 12 instructions are
   MPYF R0, R5          ; .flux(by magnet)_Alfa-------->DA2_1
   MPYF 80., R5         ; .
   FIX R5, R5           ; .
   ADDI 0x800, R5       ; .flux(by magnet)_Beta-------->DA2_2
   LDF 102.4, R5        ; .
    MPYF R1, R5          ; .
    MPYF 80., R5         ; .
    FIX R5, R5           ; used to display the vector (R0+jR1)
    ADDI 0x800, R5       ; via D/A2_1 and D/A2_2.

    CALL POST            ; read the real rotor position
    STI R5, @DA2_1
;*************************************************************************
 ;innovation
    LDF *+AR0(0x1F),R0
    STF R0,*+AR5(0xE7) ;I_Alfa --->Y(1)
    LDF *+AR0(0x20),R0
    STF R0,*+AR5(0xE8) ;I_Beta --->Y(2)
```

```
    CALL FILTER
    CALL FRSQER
    LDI 0XE9,IR0      ;
LPKK16 LDF *+AR5(IR0),R0   ;Pk-1|k-1---->P0
    SUBI 0X2B,IR0     ;
    STF R0,*+AR5(IR0)  ;
    ADDI 0X2C,IR0     ;
    CMPI 0XF9,IR0     ;
    BNE LPKK16        ;
;prediction
    LDF *+AR5(0XFB),R0
    STF R0,*+AR5(0XB2)  ;Xk|k(0)-->x0(0)
    LDF *+AR5(0XFC),R0
    STF R0,*+AR5(0XB3)  ;Xk|k(1)-->x0(1)
    LDF *+AR5(0XFD),R0
    STF R0,*+AR5(0XB4)  ;Xk|k(2)-->x0(2)
    LDF *+AR5(0xFE),R0
    STF R0,*+AR5(0xB5)  ;Xk|k(3)-->x0(3)
    CALL PRDTX
    CALL PKKP
    CALL FEEDBACK
    LDI *+AR0(0X23),R5  ;SAVE estimated
; hysterisis control
ITHRED: LDF *+AR0(0x43), R3    ; load the current Iq reference
   ;  LDF 3.0,R3
     CALL IREFD0          ; calculating current references
   ;  CALL RVSEF
     call DISCURR         ; display currents
     CALL IREG
     LDI IR0, R4          ; generating the voltage vector
     LDI *+AR0(IR0), R0     ; loading new switching status for inverter
     STI R0, @DA_P        ; output switching status

; end of hysterisis control
; (4) Measurement: differential of EKF estimated-obtained position
; na=dTheta_actual/dt
     LDI *+AR0(0X45),R0  ; times of hysterisis control
     ADDI -1,R0        ;COUNT-1
     BZ TINT12
     STI R0,*+AR0(0X45)  ;save times of hysterisis control
     B TINT13
TINT12  LDI SPDMEAS,R0
     STI R0,*+AR0(0X45)  ; save times of hysterisis control
     STI R0, *+AR0(0x44) ; times of hysterisis control
     LDI *+AR0(0X23),R5  ;SAVE estimated EKF position
     LDI R5, R6        ;SAVE estimated EKF position for next step
     SUBI *+AR0(0x5E), R5 ;CURRENT position- old rotor position
     call POSTIDG
     MPYF 1.67, R5         ;w(2pi/4000/3/2/pi/50us/60)

; display the actual speed and reference speed
     MPYF 0.4096, R5    ; these four instructions are used to,4096/5000/2
     FIX R5, R5         ; display the estimated speed based Theta of EKFvia D/A2_4
     ADDI 0x800, R5     ; the scale is:1V per 1000rpm
     STI R6,*+AR0(0x5E)
     LDF *+AR0(0X25),R5    ;speed reference
     MPYF 0.4096, R5    ; these four instructions are used to,4096/5000/2
     FIX R5, R5         ; display the estimated speed based Theta of EKFvia D/A2_4
     ADDI 0x800, R5     ; the scale is:1V per 1000rpm
     STI R5, @DA_1      ; speed reference display in DA_1
     LDF *+AR5(0XB4),R0 ;directly from EKF
     MPYF 0.5,R0
     MPYF 9.55,R0       ;1/2/PI/(1/60)
```

```
      STF R0, *+AR0(0x5F)     ;speed DIRECTLY obtained from EKF
      MPYF 0.4096, R0    ; these four instructions are used to,4096/5000/2
      FIX R0, R0         ; display the estimated speed based EKF
      ADDI 0x800, R0     ; the scale is:1V per 1000rpm
      STI R0, @DA_3      ; DIRECTLY EKF speed display in DA_3

;*************************************************************
      CALL POST
     ; STI R5, @DA2_1
      LDI R5, R6
      SUBI *+AR0(0x58), R5 ;CURRENT position- old rotor position
      call POSTIDG
      MPYF 1.67, R5          ;w(2pi/4000/3/2/pi/50us/60)
      STF R5, *+AR0(0x57)     ;speed obtained from ENCODER
      STI R6, *+AR0(0x58)     ; store rotor position
      MPYF 0.4096, R5    ; these four instructions are used to,4096/5000/2
      FIX R5, R5         ; display the estimated speed based Theta of EKFvia D/A_2
      ADDI 0x800, R5     ; the scale is:1V per 1000rpm
      STI R5, @DA_2      ; Real speed display in DA_2
; select a speed estimation or measurement as speed feed-back
; in (0x57) is the speed obtained from the estimated position, nd
; in (0x5B) is the speed calculated using approximate EMF and flux, ne
; in (0x5F) is the speed measured using the encoder value, na
; in (0x60) is the speed combination, nc
      ldf *+ar0(0x5F), r0     ; select from 0x57, 0x5B, 0x5F & 0x60
      stf r0, *+ar0(0x26)     ; temperary use as speed feed back
      CALL IQRREG
TINT13  NOP
; end of (4)
; end of speed estimations and measurement
;

      OR 0x0200, IE          ; enable interuption of Timer 1
      POPF R7
      POP R7
      POPF R6
      POP R6
      POPF R0
      POP R0
      POPF R1
      POP R1
      POPF R3
      POP R3
      POPF R5
      POP R5
      POP ST
      RETI
;
```

A.1.3.2 Timer0 interrupt:

Timer0 interrupt is for speed tuning.

```
;*******************************************
; Interruption Service Subroutine TINT0.
TINT0:  PUSH ST
      PUSH R0
      PUSHF R0
      LDI SPEEDR*0.7, R0
      FLOAT R0, R0
      CMPF *+AR0(0x25), R0 ;speed command
```

```
      BN TINT01
      LDI SPEEDR, R0
      FLOAT R0, R0
      MPYF -1.0,R0
      STF R0, *+AR0(0x25)
      LDF 0.2,R3
      STF R3,*+AR0(0X43)
      POPF R0
      POP R0
      POP ST
      RETI
;**********************************
TINT01: LDI SPEEDR, R0
      FLOAT R0, R0
      STF R0, *+AR0(0x25)
      LDF -0.3,R3
      STF R3,*+AR0(0X43)
      POPF R0
      POP R0
      POP ST
      RETI
```

A.1.4 Loading peripheral acquisition data into the DSP

The data page is set to the external memory address $00c0_h$.

```
; SETTING ADDRESS FOR EACH BOARD.
AD_DA: .SET 0x0C00000        ; MSB OF ALL THE ADRESSES
```

The addressing of $00D9_h$ and $00FF_h$ starts the ADC conversion process, see below for details.

```
;
DA2_1: .SET 0x0D9          ; D/A CONVERTER #2-1
DA2_2: .SET 0x0DA          ; D/A CONVERTER #2-2
DA2_3: .SET 0x0DB          ; D/A CONVERTER #2-3
DA2_4: .SET 0x0DC          ; D/A CONVERTER #2-4
DA2_P: .SET 0x0DD          ; DIGITAL OUTPUT PORT #2
DA_1:  .SET 0x0E1          ; D/A CONVERTER #1
DA_2:  .SET 0x0E2          ; D/A CONVERTER #2
DA_3:  .SET 0x0E3          ; D/A CONVERTER #3
DA_4:  .SET 0x0E4          ; D/A CONVERTER #4
DA_P:  .SET 0x0E5          ; DIGITAL OUTPUT PORT #1
AD1_S: .SET 0x0E8          ; START OF A/D BOARDER #1
AD1_1: .SET 0x0E9          ; A/D CONVERTER #1-1
AD1_2: .SET 0x0EA          ; A/D CONVERTER #1-2
AD1_3: .SET 0x0EB          ; A/D CONVERTER #1-3
AD1_4: .SET 0x0EC          ; A/D CONVERTER #1-4
AD1_P: .SET 0x0ED          ; DIGITAL INPUT PORT #1
AD2_S: .SET 0x0F0          ; START OF A/D BOARDER #2
AD2_1: .SET 0x0F1          ; A/D CONVERTER #2-1
AD2_2: .SET 0x0F2          ; A/D CONVERTER #2-2
AD2_3: .SET 0x0F3          ; A/D CONVERTER #2-3
AD2_4: .SET 0x0F4          ; A/D CONVERTER #2-4
AD2_P: .SET 0x0F5          ; DIGITAL INPUT PORT #2
EN_PST: .SET 0x0FF         ; ROTOR POSITION INPUT FROM ENCODER
```

```
; END OF SETTING ADDRESS
```

A.1.5 Voltage Measurement

This section of code is used for voltage measurement.

```
; Subroutine VOLT.
; Measure the DC voltage of inverter.
; Transform the data into floating-point number.
; Both data are stored in RAM 0x809E10 & 0x809E11.
; The A/D converter must be started long time enough perior to
; running this subroutine. This subroutine does not include the
; instructions to start the A/D converter.
; INPUT: none
; OUTPUT:
;  dc voltage integer is in 0x809E10
;  dc voltage floating-point is in 0x809E11
; USED BUT NOT CHANGED: none
; CHANGED: R0
; CALLED SUBROUTINE(S): none
;
VOLT:  LDI @AD1_4, R0              ; measure DC voltage via AD1_4
     AND *+AR0(0x08), R0          ; reset the 20 MSBs
VOLTD:  STI R0, *+AR0(0x10)          ; store integer in 0x809E10
     LDI @AD1_4, R0
     AND *+AR0(0x08), R0
     CMPI *+AR0(0x10), R0
     BNZ VOLTD
     ASH 20, R0                ; same as Subroutine I12S32
     ASH -20, R0
     FLOAT R0, R0               ;store DC VOLTAGE floating-point in 0X67
     MPYF -1.0, R0
     STF R0,*+AR0(0x67)
     MPYF *+AR0(0x13), R0          ; scaling to the real value in Volts
     ADDF *+AR0(0x11), R0          ; average
     MPYF 0.5, R0              ;measured voltage signal is negative
     STF R0, *+AR0(0x11)          ; store floating-point in 0x809E11
     STF R0,*+AR0(0x67)           ;store DC VOLTAGE floating-point in 0X67
     RETS
;
```

A.1.6 Current Measurement:

Such section of code is used for current measurement:

```
;*****************************************************************
; Subroutine CURR.
; Measure the three phases of currents.
; Transform those data into floating-point numbers.
; All the data are stored in RAM from 0x809E0A to
; 0x809E0F. Filtered currents are stored in RAM from
; 0x809E4A to 0x809E4C.
; The A/D converters must be started long time enough prior to
; running this subroutine. This subroutine does not include the
; instructions to start the A/D converters.
```

```
;
; INPUT: none
; OUTPUT:
;  a current integer is in 0x809E0A
;  a current floating-point is in 0X809E0B
;  b current integer is in 0x809E0C
;  b current floating-point is in 0x809E0D
;  c current integer is in 0x809E0E
;  c current floating-point is in 0x809E0F
; USED BUT NOT CHANGED: none
; CHANGED: R0
; CALLED SUBROUTINE(S): none
;
CURR:  LDI @AD1_1, R0              ; measure A-current via AD1_1
       AND *+AR0(0x08), R0         ; reset the 20 MSBs
CURRA: STI R0, *+AR0(0x0A)         ; store integer in 0x809E0A
       LDI @AD1_1, R0
       AND *+AR0(0x08), R0
       CMPI *+AR0(0x0A), R0
       BNZ CURRA
       ASH 20, R0                  ; same as Subroutine I12S32
       ASH -20, R0
       FLOAT R0, R0
       MPYF *+AR0(0x12), R0        ; scaling to the real value in Amps
       mpyf KIQ,r0
       subf *+ar0(0x54), r0        ; deducting offset, little influence
       STF R0, *+AR0(0x0B)         ; store floating-point in 0x809E0B
       STF R0, *+AR0(0x4A)
;
       LDI @AD1_2, R0              ; measure B-current via AD1_2
       AND *+AR0(0x08), R0         ; reset the 20 MSBs
CURRB: STI R0, *+AR0(0x0C)         ; store integer in 0x809E0C
       LDI @AD1_2, R0
       AND *+AR0(0x08), R0
       CMPI *+AR0(0x0C), R0
       BNZ CURRB
       ASH 20, R0                  ; same as Subroutine I12S32
       ASH -20, R0
       FLOAT R0, R0
       MPYF *+AR0(0x12), R0        ; scaling to the real value in Amps
       mpyf KIQ,r0
       subf *+ar0(0x55), r0        ; deducting offset, little influence
       STF R0, *+AR0(0x0D)         ; store floating-point in 0x809E0D
       STF R0, *+AR0(0x4B)
;
       LDI @AD1_3, R0              ; measure C-current via AD1_3
       AND *+AR0(0x08), R0         ; reset the 20 MSBs
CURRC: STI R0, *+AR0(0x0E)         ; store integer in 0x809E0E
       LDI @AD1_3, R0
       AND *+AR0(0x08), R0
       CMPI *+AR0(0x0E), R0
       BNZ CURRC
       ASH 20, R0                  ; same as Subroutine I12S32
       ASH -20, R0
       FLOAT R0, R0
       MPYF *+AR0(0x12), R0        ; scaling to the real value in Amps
       mpyf KIQ,r0
       subf *+ar0(0x56), r0        ; deducting offset, little influence
       STF R0, *+AR0(0x0F)         ; store floating-point in 0x809E0F
       STF R0, *+AR0(0x4C)
       RETS
;
```

A.1.7 Outputting data with DAC:

The subroutine "DISCURR" can be used to display any variable in the code.

```
;*****************************************************************
; Subroutine DISCURR.
; Display an actual current and a current reference
; via DA2_3 and DA2_4. To be called after CURR and IREFD0
; so that all necessary input data are ready.
; INPUT:
;  rotor position is in R5,
;  d-axis current reference is in R2,
;  q-axis current reference is in R3,
;  a-phase current reference is in 0x16,
;  a-, b- and c- phase actual current are in 0x0b, 0x0d, 0x0f.
; OUTPUT: D/A converters DA2_3, DA2_4
; USED BUT NOT CHANGED: none
; CHANGED: R0
; CALLED SUBROUTINE(S): ABCDQ
;
DISCURR:nop
;
; (1) display an actual current via DA2_3
; choose 1-1 or 1-2
; 1-1: display d- or q- axis current
; 1-2: display a-phase current
; 1-1:
;  choose 0x1c or 0x1d in the next instruction
;  0x1c: d-axis current, 0x1d: q-axis current.
    ; ldf *+ar0(0x1d), r0
; end of 1-1
; 1-2:

    ldf *+ar0(0x0B), r0
    mpyf *+ar0(0x14), r0

    fix r0, r0
    addi 0x800, r0
     ldf *+ar0(0x25),r0

    ldf *+ar0(0x43), r3
    ldf r3,r0          ;  display Iq in DA_3
    mpyf INVKIQ, r0
    mpyf 409.6, r0      ;409.6=2048/5a

    fix r0, r0
    addi 0x800, r0
; end of (1)
;
; (2) display a current reference via DA2_1
; choose 2-1 or 2-2
; 2-1: display d- or q- axis current
; 2-2: display a-phase current
; 2-1:
;  choose R2 or R3 in the next instruction
;  R2: d-axis current, R3: q-axis current
    ldf r3, r0
; end of 2-1
; 2-2:
    ldf *+ar0(0x16), r0
    mpyf INVKIQ, r0
; end of 2-2
```

```
      mpyf *+ar0(0x14), r0
      fix r0, r0
      addi 0x800, r0
     ; sti r0, @DA2_1        ; output current reference via DA2_1
      ldf *+ar0(0x17), r0
      mpyf INVKIQ, r0
; end of 2-2
      mpyf *+ar0(0x14), r0
      fix r0, r0
      addi 0x800, r0
      sti r0, @DA2_2         ; output current reference via DA2_2
; end of (2)
      ldf *+ar0(0x18), r0
      mpyf INVKIQ, r0
; end of 2-2
      mpyf *+ar0(0x14), r0
      fix r0, r0
      addi 0x800, r0
      sti r0, @DA2_3         ; output current reference via DA2_3
      rets
;
```

A.1.8 Encoder measurement:

The subroutine "ENCODER" is used to read in converted binary value of encoder, the subroutine "POST" would transform the absolute encoder position binary value into the equivalent normalised electrical angle value for sinusoidal function.

```
;
;************************************************************
; Subroutine ENCODER.
ENCODER:LDI @AD1_P,R5
      and 0x1fff,R5
      LSH 0XFFFFFFFF,R5
      RETS
;*****************************************************************
; Subroutine POST.
; Read the accurate rotor position generated
; by encoder twice. If the two values are same, store
; them in R5 and return, otherwise go on reading and
; comparing.
; The measured encoder value is compensated considering its bias.
; INPUT: none
; OUTPUT:
;  compensated encoder value is in R5.
; USED BUT NOT CHANGED: R0
; CHANGED: none
; CALLED SUBROUTINE(S): ENCBS
;
POST:  PUSH R0
      LDI @AD1_P,R5
      and 0x1fff,R5
      CMPI 1071,R5  ;<32.7
      BNN OFFSETEMF
      ADDI 7121,R5
      B CYCLE1
```

```
OFFSETEMF SUBI 1071,R5
CYCLE1  CMPI 5461,R5        ;COMP 720DEG
     BNN RECLT1
COMPE   CMPI 2731,R5
     BNN OUT2
   ;  LDI 3096,R0
   ;  addi R0,R5       ;R5+3096-->R5
     B OUT
OUT2    SUBI 2731,R5
     B OUT
RECLT1  SUBI 5461,R5
     B COMPE
OUT  STI R5, *+AR0(0X64)
     float r5,r5
     MPYF 1.4652,R5
     FIX R5,R5
     POP R0
     RETS
```

A.1.9 d-q transformation:

The subroutine "DQABC" is to transform current in d-q axis coordinate frame to three phase current. It is used by the subroutine "IREFD0" to calculate three phase current reference.

```
;***********************************************************************
; Subroutine DQABC.
; Transformation from d, q to a, b, c.
; a=COS(theta)*d-SIN(theta)*q
; b=COS(theta-120degrees)*d-SIN(theta-120degrees)*q
; c=COS(theta+120degrees)*d-SIN(theta+120degrees)*q
; INPUT:
;  The rotor position is stored in R5.
;  The d variable is stored in 0x809E1C.
;  The q variable is stored in 0x809E1D.
;  The 0 variable occupying 0x809E1E is assumed to be zero.
; OUTPUT:
;  The a variable is stored in 0x809E19.
;  The b variable is stored in 0x809E1A.
;  The c variable is stored in 0x809E1B.
; USED BUT NOT CHANGED: none
; CHANGED: R0
; CALLED SUBROUTINE(S):
;  SIN, SINM, SINP, COS, COSM, COSP
;
DQABC:  CALL SIN
     MPYF *+AR0(0x1D), R0    ; q*SIN
     STF R0, *+AR0(0x19)
        CALL COS
     MPYF *+AR0(0x1C), R0    ; d*COS
     SUBF *+AR0(0x19), R0    ; d*COS-q*SIN
     STF R0, *+AR0(0x19)     ; a obtained
;
     CALL SINM
     MPYF *+AR0(0x1D), R0    ; q*SINM
     STF R0, *+AR0(0x1A)
     CALL COSM
     MPYF *+AR0(0x1C), R0    ; d*COSM
     SUBF *+AR0(0x1A), R0    ; d*COSM-q*SINM
```

```
    STF R0, *+AR0(0x1A)    ; b obtained
;
    CALL SINP
    MPYF *+AR0(0x1D), R0   ; q*SINP
    STF R0, *+AR0(0x1B)
    CALL COSP
    MPYF *+AR0(0x1C), R0   ; d*COSP
    SUBF *+AR0(0x1B), R0   ; d*COS-q*SIN
    STF R0, *+AR0(0x1B)    ; c obtained
;
    RETS
;
;*********************************************************************
; Subroutine IREFD0.
; Calculating the reference of each phase of current.
; The calculation is based on the rotor position (stored in R5) and
; the references of Id and Iq. Let Idref=0, and I0ref=0. Iqref is
; stored in R3. The reference of each phase of current is thus:
; IAref=-SIN(theta)*Iqref
; IBref=-SIN(theta-120degrees)*Iqref
; ICref=-SIN(theta+120degrees)*Iqref
; INPUT:
;  Id reference is in R2,
;  Iq reference is in R3,
;  Rotor position is in R5.
; OUTPUT:
;  IAref, IBref and ICref are stored in 0x809E16, 0x809E17 AND
;  0x809E18 respectively.
; USED BUT NOT CHANGED: none
; CHANGED: R0
; CALLED SUBROUTINE(S):
;  SIN, SINM, SINP, COS, COSM, COSP, DQABC
;
IREFD0: CALL SIN            ; KIQ is applied.
    MPYF R3, R0
    MPYF KIQ, R0
    STF R0, *+AR0(0x16)
    CALL SINM
    MPYF R3, R0
    MPYF KIQ, R0
    STF R0, *+AR0(0x17)
    CALL SINP
    MPYF R3, R0
    MPYF KIQ, R0
    STF R0, *+AR0(0x18)
    RETS
```

A.1.10 space vector current control:

The subroutine "IREG" is to generate three phase switch control signal by space vector current law.

```
;*********************************************************************
; Subroutine IREG.
; Regulating the current of each phase with hysteresis
; control according to the measured current value and the
; required current value. A voltage vector is generated.
; INPUT:
;  The measured current values are sotred in 0x809E0B,
;  0x809E0D and 0x809E0F respectively.
```

```
; The current references are stored in 0x809E16, 0x809E17
; and 0x809E18 respectively.
; OUTPUT:
; The generated voltage vector is stored in IR0.
; USED BUT NOT CHANGED: none
; CHANGED: R0
; CALLED SUBROUTINE(S): none
;
; chose one of the following two instrucitons
IREG:  NOP            ; band of hysteresis = 0
     LDF *+AR0(0x0B), R0    ; measurement
     SUBF *+AR0(0x16), R0   ; measurement - reference
     ABSF R0, R0            ; error (absolute value)
     CMPF DELT_I, R0        ; comparing error with hysterisis band
     BN IREG1               ; if error is smaller than band, pass!
     LDF *+AR0(0x0B), R0    ; otherwise regulating voltage vector.
     CMPF *+AR0(0x16), R0
     BN IREGA
     AND 3, IR0             ; measurement > reference
     BR IREG1
IREGA:  OR 4, IR0           ; measurement < reference
IREG1:  LDF *+AR0(0x0D), R0    ; measurement
     SUBF *+AR0(0x17), R0   ; measurement - reference
     ABSF R0, R0            ; error (absolute value)
     CMPF DELT_I, R0        ; comparing error with hysterisis band
     BN IREG2               ; if error is smaller than band, pass!
     LDF *+AR0(0x0D), R0    ; otherwise regulating voltage vector.
     CMPF *+AR0(0x17), R0
     BN IREGB
     AND 5, IR0             ; measurement > reference
     BR IREG2
IREGB:  OR 2, IR0           ; measurement < reference
IREG2:  LDF *+AR0(0x0F), R0    ; measurement
     SUBF *+AR0(0x18), R0   ; measurement - reference
     ABSF R0, R0            ; error (absolute value)
     CMPF DELT_I, R0        ; comparing error with hysterisis band
     BN IREG3               ; if error is smaller than band, pass!
     LDF *+AR0(0x0F), R0    ; otherwise regulating voltage vector.
     CMPF *+AR0(0x18), R0
     BN IREGC
     AND 6, IR0             ; measurement > reference
     BR IREG3
IREGC:  OR 1, IR0           ; measurement < reference
IREG3:  AND *+AR0(0x24), IR0
          RETS
```

A.1.11 EKF subroutine:

EKF algorithm includes 5 subroutines "PRDTX", "PKKP", "FEEDBACK", "FILTER" and "FRSQER". The subroutine "PRDTX" represents the prediction, the subroutine "PKKP" represents the predicted covariance, the subroutine "FEEDBACK" represent Kalman gain feedback, the subroutine "FRSQER" represent the filtered covariance .

```
;subroutine PRDTX
;calculating the x vector(Ialpha, Ibeta, omega, theta);
;input of Ialpha, Ibeta, omega, theta are stored in 0x809cB2/B3/B4/B5;
;      Xk|k-1 4*1 are stored in 0x809C(BA-BD),F(13,14,23,24) in 0x809c(B6-B9)
```

```
;THIS SUBROUTINE OCCUPY 35 WORD
PRDTX:   LDF *+AR5(0XB5),R5
      MPYF 0.4776,R5   ;THETA/2.094--->TIMES
      ABSF R5,R5       ;|TIMES|
      FIX R5,R0        ;INT(TIMES)
      FLOAT R0,R0
      MPYF 2.094,R0    ;INT(THETA/2.094)*2.094
      LDF *+AR5(0XB5),R5
      ABSF R5,R5       ;|theta|
      SUBF R0,R5       ;THETA-INT(THETA/2.094)*2.094
      STF R5,*+AR5(0XB5)
      MPYF *+AR0(0x6D),R5 ;convert the unit rad into div   convert rate 4000/(2pi)=1910.22
      FIX R5,R5
      STI R5,*+AR0(0X23) ;SAVE ROTOR POSITION FOR SENSORLESS
      STI R5,@DA_4
      CALL SIN
      STF R0,*+AR5(0XB0)
      CALL COS
      STF R0,*+AR5(0XB1)
      LDF *+AR5(0XB2),R1   ;x0(1) Ialpha
      MPYF *+AR0(0x6E),R1      ;(1-Tc*R/L)Ialpha ----->*+AR0(0X6E)
      LDF *+AR5(0XB0),R2   ;sin(THETA)
      MPYF *+AR0(0X69),R2      ;(Psi*Tc/L)sin(THETA)
      STF R2,*+AR5(0xB6)   ;(Tc*PSI/L)*sin(THETA)------------->F(13)
      LDF *+AR5(0XB4),R3   ;OMIGA
      MPYF R3,R2           ; (Psi*Tc*omiga/L)sin(THETA)
      STF R2,*+AR5(0XB9)   ;(Tc*PSI/L)*omiga*SIN(THETA)------->F(24)
      LDF *+AR0(0X7C),R3   ;Valphav k-1
      MPYF *+AR0(0x6C),R3      ;Tc*Va/Ls--->*+AR0(0x6C)
      ADDF R3,R2           ;(Psi*Tc/L)sin(THETA)+Tc*Va/Ls
      ADDF3 R1,R2,R3       ;(1-Tc*R/L)Ialpha+(Psi*Tc/L)*omiga*sin(THETA)+Tc*Va/L
      STF R3,*+AR5(0XBA)    ;(1-Tc*R/L)Ialpha+(Psi*Tc/L)*omiga*sin(THETA)+Tc*Va/L---->Xk|k-
1(1)
      LDF *+AR5(0XB3),R1   ;x0(2) Ibeta
      MPYF *+AR0(0x6E),R1      ;(1-Tc*R/L)Ibeta
      LDF *+AR5(0XB1),R2   ;COS(THETA)
      MPYF *+AR0(0X6A),R2  ;(-Tc*PSI/L)*COS(THETA)
      STF R2,*+AR5(0XB8)   ;(-Tc*PSI/L)*COS(THETA)------------->F(23)
      LDF *+AR0(0X7D),R3   ;Vbeta k-1
      MPYF *+AR0(0x6C),R3      ;Tc*Vb/Ls
      ADDF R3,R1           ;(1-Tc*R/L)Ibeta+Tc*Vb/Ls
      MPYF *+AR5(0XB4),R2  ;(-Tc*PSI/L)*omiga*COS(THETA)
      ADDF3 R1,R2,R3       ;(1-Tc*R/L)Ibeta-(Tc*PSI/L)*omiga*COS(THETA)+Tc*Vb/Ls
   STF  R3,*+AR5(0XBB)      ;(1-Tc*R/L)Ibeta-(Tc*PSI/L)*omiga*COS(THETA)+Tc*Vb/Ls--->Xk|k-
1(2)
      MPYF -1.0,R2         ;(Tc*PSI/L)*omiga*COS(THETA)
      STF R2,*+AR5(0XB7)   ;(Tc*PSI/L)*omiga*COS(THETA)-->F(14)
      LDF *+AR5(0XB4),R0   ;OMIGA0
      STF R0,*+AR5(0XBC)   ;OMIGA0------>Xk|k-1(3)
      MPYF *+AR0(0X6B),R0  ;OMIGA0*Tc
      ADDF *+AR5(0XB5),R0  ;OMIGA0*Tc+THETA
      CMPF 0.0,R0
      BNN JMPPK
      ADDF 2.094,R0
JMPPK    STF R0,*+AR5(0XBD)   ;OMIGA0------>Xk|k-1(4)

      RETS
;
;
;subroutine PKK-1
;INPUT IS matrice P0 4*4
;output is matrice Pk|k-1: 4*4 are stored in 0x809c(CE-DD)
; THIS SUBROUTINE OCCUPY 152 WORD
```

```
PKKP:   LDF *+AR5(0xBE),R0          ;P11
        MPYF *+AR0(0x6F),R0         ;(1+2F11)P11 (1+2F11)---->*+AR0(0x6F)
       LDF *+AR5(0XC0),R1 ;P13
        LDF *+AR5(0XC6),R3 ;P31
        ADDF R3,R1 ;P13+P31
        LDF *+AR5(0XB6),R4          ;F(13)--->R4
        MPYF R4,R1                  ;F(13)*(P13+P31)
        LDF *+AR5(0XC1),R2          ;P14
        LDF *+AR5(0XCA),R3          ;P41
        ADDF R3,R2                  ;P14+P41
        LDF *+AR5(0XB7),R5;F(14)---->R5
        MPYF R5,R2        ;F14*(P14+P41)
        ADDF R0,R1        ;(1+2F11)P11+F(13)*(P13+P31)
        ADDF3 R1,R2,R3        ;(1+2F11)P11+F(13)*(P13+P31)+F14*(P14+P41)
        ADDF 0.04,R3        ;(1+2F11)P11+F(13)*(P13+P31)+F14*(P14+P41)+Q1
 STF R3,*+AR5(0xCE);(1+2F11)P11+F(13)*(P13+P31)+F14*(P14+P41)+Q1------>Pk|k-1(11),Q1=0.4
        LDF *+AR5(0XC0),R0 ;P13
        MPYF *+AR0(0x6E),R0    ;(1+F11)P13  1+F11--->*+AR0(0x6E)
        ADDF R0,R2        ;(1+F11)P13+F14*(P14+P41)
        LDF *+AR5(0XC8),R0 ;P(33)
        MPYF R4,R0        ;F(13)*P(33)
        ADDF R0,R2        ;(1+F11)P13+F14*(P14+P41)+F(13)*P(33)
 STF R2,*+AR5(0XD0) ;(1+F11)P13+F14*(P14+P41)+F(13)*P(33)---->Pk|k-1(13)
        LDF *+AR5(0XC6),R1 ;P(31)
        MPYF *+AR0(0x6E),R1     ;(1+F11)*P(31)
        ADDF R0,R1        ;(1+F11)*P(31)+F(13)*P(33)
        LDF *+AR5(0XC9),R0 ;P34
        MPYF R5,R0        ;F(14)*P(34)
        ADDF R0,R1        ;(1+F11)*P(31)+F(13)*P(33)+F(14)*P(34)
 STF R1,*+AR5(0XD6) ;(1+F11)*P(31)+F(13)*P(33)+F(14)*P(34)--->Pk|k-1(31)
        LDF *+AR5(0XBF),R0              ;P12
        MPYF *+AR0(0x6F),R0             ;(1+2F11)P12
        LDF *+AR5(0XB8),R6              ;F(23)------>R6
        LDF *+AR5(0XB9),R7              ;F(24)------>R7
        LDF *+AR5(0XC0),R1          ;P(13)
        LDF *+AR5(0XC1),R2          ;P(14)
        MPYF R6,R1                  ;F(23)*P(13)
        MPYF R7,R2                  ;F(24)*P(14)
        ADDF R2,R1                  ;F(23)*P(13)+F(24)*P(14)
        ADDF R1,R0                  ;(1+2F11)P12+F(23)*P(13)+F(24)*P(14)
        LDF *+AR5(0XC7),R1              ;P(32)
        LDF *+AR5(0XCB),R2              ;P(42)
        MPYF R4,R1                  ;F(13)*P(32)
        MPYF R5,R2                  ;F(14)*P(42)
        ADDF R2,R1                  ;F(13)*P(32)+F(14)*P(42)
        ADDF R1,R0                  ;(1+2F11)P12+F(23)*P(13)+F(24)*P(14)+F(13)*P(32)+F(14)*P(42)
 STF  R0,*+AR5(0XCF) ;(1+2F11)P12+F(23)*P(13)+F(24)*P(14)+F(13)*P(32)+F(14)*P(42)----->Pk|k-
1(12)
        LDF *+AR5(0XC1),R0 ;P(14)
        MPYF *+AR0(0x6E),R0     ;(1+F11)*P(14)
        LDF *+AR5(0XC9),R1 ;P(34)
        MPYF R4,R1        ;F(13)*P(34)
        ADDF R1,R0        ;(1+F11)*P(14)+F(13)*P(34)
        LDF *+AR5(0XCD),R1 ;P(44)
        LDF *+AR5(0XC4),R2 ;P(23)
        MPYF R5,R1        ;F(14)*P(44)
        MPYF *+AR0(0X6B),R2     ;F(43)*P(23)
        ADDF R1,R2        ;F(14)*P(44)+F(43)*P(23)
        ADDF R0,R2        ;(1+F11)*P(14)+F(13)*P(34)+F(14)*P(44)+F(43)*P(23)
 STF R2,*+AR5(0XD1) ;(1+F11)*P(14)+F(13)*P(34)+F(14)*P(44)+F(43)*P(23)--->PK|K-1(14)
        LDF *+AR5(0XC4),R0 ;P23
        LDF *+AR5(0XC5),R1 ;P24
        LDF *+AR5(0XC6),R2 ;P31
```

```
    LDF *+AR5(0XCA),R3 ;P41
    MPYF R4,R0      ;F13*P23
    MPYF R5,R1      ;F14*P24
    MPYF R6,R2      ;F23*P31
    MPYF R7,R3      ;F24*P41
    ADDF R1,R0 ;F13*P23+F14*P24
    ADDF R3,R2 ;F23*P31+F24*P41
    ADDF R2,R0 ;F13*P23+F14*P24+F24*P41
    LDF *+AR5(0XC2),R1 ;P21
    MPYF *+AR0(0x6F),R1    ;(1+2F11)P21
    ADDF R1,R0      ;(1+2F11)*P21+F13*P23+F14*P24+F24*P41
STF R0,*+AR5(0XD2) ;(1+2F11)*P21+F13*P23+F14*P24+F24*P41---->PK|K-1(21)
    LDF *+AR5(0XC3),R0 ;P22
    MPYF *+AR0(0x6F),R0    ;(1+2F11)P22
    LDF *+AR5(0XC4),R1 ;P23
    LDF *+AR5(0XC7),R2 ;P32
    ADDF R2,R1      ;P23+P32
    MPYF R6,R1      ;F23(P23+P32)
    ADDF R1,R0      ;(1+2F11)P22+F23(P23+P32)
    LDF *+AR5(0XC5),R1 ;P24
    LDF *+AR5(0XCB),R2 ;P42
    ADDF R2,R1      ;P24+P42
    MPYF R7,R1      ;F24*(P24+P42)
    ADDF R1,R0      ;(1+2F11)P22+F23(P23+P32)+F24*(P24+P42)
    ADDF 0.04,R0      ;(1+2F11)P22+F23(P23+P32)+F24*(P24+P42)+Q1, Q1=0.4
STF R0,*+AR5(0XD3) ;(1+2F11)P22+F23(P23+P32)+F24*(P24+P42)+Q1-->PK|K-1(22)
    LDF *+AR5(0XC4),R0 ;P23
    MPYF *+AR0(0x6E),R0    ;(1+F11)P23
    LDF *+AR5(0XC8),R1 ;P33
    LDF *+AR5(0XCC),R2 ;P43
    MPYF R6,R1      ;F23*P33
    MPYF R7,R2      ;F24*P43
    ADDF R1,R0      ;(1+F11)P23+F23*P33
    ADDF R2,R0      ;(1+F11)P23+F23*P33+F24*P43
STF R0,*+AR5(0XD4)      ;(1+F11)P23+F23*P33+F24*P43--->PK|K-1(23)
    LDF *+AR5(0XC7),R0 ;P32
    MPYF *+AR0(0x6E),R0    ;(1+F11)P32
    ADDF R1,R0      ;(1+F11)P32+F23*P33
    LDF *+AR5(0XC9),R2 ;P34
    MPYF R7,R2      ;F24*P34
    ADDF R2,R0      ;(1+F11)P32+F23*P33+F24*P34
STF R0,*+AR5(0XD7)      ;(1+F11)P32+F23*P33+F24*P34--->PK|K-1(32)
    LDF *+AR5(0XC5),R3 ;P24
    LDF *+AR5(0XC9),R0 ;P34
    LDF *+AR5(0XCD),R1 ;P44
    LDF *+AR5(0XC4),R2 ;P23
    MPYF R6,R0 ;F23*P34
    MPYF R7,R1 ;F24*P44
    MPYF *+AR0(0X6B),R2 ;F43*P23
    MPYF *+AR0(0x6E),R3 ;(1+F11)*P24
    ADDF R1,R0 ;F23*P34+F24*P44
    ADDF R3,R2 ;F43*P23+(1+F11)*P24
    ADDF R2,R0 ;(1+F11)*P24+F23*P34+F24*P44+F43*P23
STF R0,*+AR5(0XD5);(1+F11)*P24+F23*P34+F24*P44+F43*P23--->PK|K-1(24)
    LDF *+AR5(0XC8),R0 ;P33
    LDF 0.07,R2
    ADDF3 R2,R0,R1 ;P33+Q3 Q3<----------5.07
STF R1,*+AR5(0XD8)      ;P33+Q3--->Pk|k-1(33)
    MPYF *+AR0(0X6B),R0  ;F43*P33
    LDF *+AR5(0XC9),R1 ;P34
    ADDF3 R0,R1,R2      ;F43*P33+P34
STF R2,*+AR5(0XD9) ;F43*P33+P34--->pK|K-1(34)
    LDF *+AR5(0XCC),R2 ;P43
```

```
        ADDF R2,R0     ;F43*P33+P43
    STF R0,*+AR5(0XDC) ;F43*P33+P43--->PK|K-1(43)
        ADDF3 R2,R1,R3  ;P34+P43
        MPYF *+AR0(0X6B),R3    ;F43*(P34+P43)
        LDF *+AR5(0XCD),R0 ;P44
        ADDF3 R3,R0,R1      ;F43*(P34+P43)+P44
        ADDF 0.00005,R1     ;F43*(P34+P43)+P44+Q4 Q4<----------0.0005
    STF R1,*+AR5(0XDD)    ;F43*(P34+P43)+P44+Q4--->PK|K-1(44)
        MPYF3 R4,R2,R1  ;F13*P43
        MPYF3 R5,R0,R3  ;F14*P44
        ADDF R3,R1      ;F13*P43+F14*P44
        LDF *+AR5(0XCA),R3 ;P41
        MPYF *+AR0(0x6E),R3    ;(1+F11)P41
        ADDF R3,R1      ;(1+F11)P41+F13*P43+F14*P44
        LDF *+AR5(0XC6),R3 ;P31
        MPYF *+AR0(0X6B),R3     ;F43*P31
        ADDF R3,R1    ;(1+F11)P41+F13*P43+F14*P44+F43*P31
    STF R1,*+AR5(0XDA)  ;(1+F11)P41+F13*P43+F14*P44+F43*P31--->PK|K-1(41)
        MPYF R6,R2    ;F23*P43
        MPYF R7,R0    ;F24*P44
        ADDF R2,R0    ;F23*P43+F24*P44
        LDF *+AR5(0XCB),R1 ;P42
        LDF *+AR5(0XC7),R2 ;P32
        MPYF *+AR0(0x6E),R1 ;(1+F11)P42
        MPYF *+AR0(0X6B),R2  ;F43*P32
        ADDF R2,R1    ;(1+F11)P42+F43*P32
        ADDF R1,R0 ;(1+F11)P42+F23*P43+F24*P44+F43*P32
    STF R0,*+AR5(0XDB) ;(1+F11)P42+F23*P43+F24*P44+F43*P32--->PK|K-1(42)
        RETS
;subroutine FEEDBACK
;input is P 4*4 , R 2*2 ,
;output is K 4*4 are stored in 0x809c(D6-DD)
; THIS SUBROUTINE OCCUPY 60 LINE
FEEDBACK: LDF *+AR5(0xCE),R1 ;P(11)--->
        ADDF 0.75,R1       ;P(11)+R(11) (0.5 ---------->R1)
        LDF *+AR5(0xD3),R2 ;P(22)
        ADDF 0.75,R2       ;P(22)+R(22) (0.5 ---------->R2)
        MPYF3 R2,R1,R5       ;[P(11)+R(11)]*[P(22)+R(22)]
        LDF *+AR5(0XCF),R6 ;P(12)---------->R6
        LDF *+AR5(0XD2),R7 ;P(21)---------->R7
        MPYF3 R6,R7,R3     ;P(12)*P(21)
        SUBF3 R3,R5,R0     ;[P(11)+R(11)]*[P(22)+R(22)]-P(12)*P(21)
        call INVF
    STF R0,*+AR5(0xDE)     ;R0------->DELTA
        MPYF R0,R3       ;DELTA*P(12)*P(21)
        MPYF3 R0,R2,R4     ;DELTA*[P(22)+R(22)]
        LDF *+AR5(0xCE),R5 ;P(11)
        MPYF R4,R5       ;DELTA*P(11)*[P(22)+R(22)]
        SUBF R3,R5     ;DELTA*P(11)*[P(22)+R(22)]-DELTA*P(12)*P(21)
    STF R5,*+AR5(0XDF)    ;DELTA*P(11)*[P(22)+R(22)]-DELTA*P(12)*P(21)--->K(11)
        LDF *+AR5(0XD3),R5 ;P(22)
        MPYF R0,R5 ;DELTA*P(22)
        MPYF R1,R5     ;DELTA*P(22)*[P(11)+R(11)]
        SUBF R3,R5     ;DELTA*P(22)*[P(11)+R(11)]-DELTA*P(12)*P(21)
    STF R5,*+AR5(0XE2)    ;DELTA*P(22)*[P(11)+R(11)]-DELTA*P(12)*P(21)--->K(22)
        MPYF3 R6,R0,R5 ;DELTA*P(12)
        MPYF 0.5,R5    ;DELTA*P(12)*R1
    STF R5,*+AR5(0XE0)     ;DELTA*P(12)*R1--->K(12)
        MPYF3 R7,R0,R5 ;DELTA*P(21)
        MPYF 0.5,R5    ;DELTA*P(21)*R1
    STF R5,*+AR5(0XE1) ;DELTA*P(21)*R1--->K(21)
        LDF *+AR5(0XD6),R3 ;P(31)
        MPYF R2,R3     ;P(31)*[P(22)+R(22)]
```

```
      MPYF R0,R3       ;DELTA*P(31)*[P(22)+R(22)]
      LDF *+AR5(0XD7),R5 ;P(32)
      MPYF R7,R5       ;P(21)*P(32)
      MPYF R0,R5       ;DELTA*P(21)*P(32)
      SUBF R5,R3       ;DELTA*P(31)*[P(22)+R(22)]-DELTA*P(21)*P(32)
STF R3,*+AR5(0XE3) ;DELTA*P(31)*[P(22)+R(22)]-DELTA*P(21)*P(32)--->K(31)
      LDF *+AR5(0XDA),R3 ;P(41)
      MPYF R2,R3       ;P(41)*[P(22)+R(22)]
      MPYF R0,R3       ;DELTA*P(41)*[P(22)+R(22)]
      LDF *+AR5(0XDB),R5 ;P(42)
      MPYF R7,R5       ;P(21)*P(42)
      MPYF R0,R5       ;DELTA*P(21)*P(42)
      SUBF R5,R3 ;DELTA*P(41)*[P(22)+R(22)]-DELTA*P(21)*P(42)
STF R3,*+AR5(0XE5) ;DELTA*P(41)*[P(22)+R(22)]-DELTA*P(21)*P(42)--->K(41)
      MPYF3 R0,R1,R4    ;DELTA*[P(11)+R(11)]
      LDF *+AR5(0XDB),R3 ;P(42)
      MPYF3 R3,R4,R5    ;DELTA*P(42)*[P(11)+R(11)]
      LDF *+AR5(0XDA),R2 ;P(41)
      MPYF R0,R2       ;DELTA*P(41)
      MPYF R6,R2       ;DELTA*P(41)*P(12)
      SUBF R2,R5       ;DELTA*P(42)*[P(11)+R(11)]-DELTA*P(41)*P(12)
STF R5,*+AR5(0XE6) ;-DELTA*P(41)*P(12)+DELTA*P(42)*[P(11)+R(11)]--->K(42)
      LDF *+AR5(0XD7),R5 ;P(32)
      MPYF R4,R5 ;DELTA*P(32)*[P(11)+R(11)]
      LDF *+AR5(0XD6),R2 ;P(31)
      MPYF R0,R2 ;DELTA*P(31)
      MPYF R6,R2 ;DELTA*P(31)*P(12)
      SUBF R2,R5 ;DELTA*P(32)*[P(11)+R(11)]-DELTA*P(31)*P(12)
STF R5,*+AR5(0XE4)  ;DELTA*P(32)*[P(11)+R(11)]-DELTA*P(31)*P(12)--->K(32)
      RETS
;SUBROUTINE FILTER
;INPUT IS vector y 2*1 ,Xk|k-1 4*1 ,matrice K 4*4
;OUTPUT IS FILTERED Vector Xk|k 4*1
;THIS SUBROUTINE OCCUPY 36 WORD
FILTER:  LDF *+AR5(0XE7),R0 ;y(1)
      LDF *+AR5(0XBA),R1 ;x(1)---R1
      SUBF R1,R0       ;y(1)-x(1)---R0
      LDF *+AR5(0XE8),R2 ;y(2)
      LDF *+AR5(0XBB),R3 ;x(2)---R3
      SUBF R3,R2       ;y(2)-x(2)---R2
      LDF *+AR5(0XDF),R4 ;K(11)
      MPYF R0,R4       ;K(11)*[yK(1)-x(1)]
      LDF *+AR5(0XE0),R5 ;K(12)
      MPYF R2,R5       ;K(12)*[y(2)-x(2)]
      ADDF R5,R4       ;K(11)*[y(1)-x(1)]+K(12)*[y(2)-x(2)]
      ADDF R1,R4 ;xK|K-1(1)+K(11)*[y(1)-x(1)]+K(12)*[y(2)-x(2)]
STF R4,*+AR5(0XFB);xK|K-1(1)+K(11)*[y(1)-x(1)]+K(12)*[y(2)-x(2)]-->XF(1)
      LDF *+AR5(0XE1),R4 ;K(21)
      MPYF R0,R4       ;K(21)*[y(1)-x(1)]
      LDF *+AR5(0XE2),R5 ;K(22)
      MPYF R2,R5       ;K(22)*[y(2)-x(2)]
      ADDF R5,R4       ;K(21)*[y(1)-x(1)]+K(22)*[y(2)-x(2)]
      ADDF R3,R4 ;x(2)+K(21)*[y(1)-x(1)]+K(22)*[y(2)-x(2)]
STF R4,*+AR5(0XFC) ;x(2)+K(21)*[y(1)-x(1)]+K(22)*[y(2)-x(2)]--->XF(2)
      LDF *+AR5(0XE3),R4 ;K(31)
      MPYF R0,R4       ;K(31)*[yK(1)-x(1)]
      LDF *+AR5(0XE4),R5 ;K(32)
      MPYF R2,R5       ;K(32)*[y(2)-x(2)]
      ADDF R5,R4       ;K(31)*[y(1)-x(1)]+K(32)*[y(2)-x(2)]
      LDF *+AR5(0XBC),R5 ;X(3)
      ADDF R5,R4       ;X(3)+K(31)*[y(1)-x(1)]+K(32)*[y(2)-x(2)]
STF R4,*+AR5(0XFD) ;K(31)*[y(1)-x(1)]+K(32)*[y(2)-x(2)]--->XF(3)
      LDF *+AR5(0XE5),R4 ;K(41)
```

```
        MPYF R0,R4      ;K(41)*[y(1)-x(1)]
        LDF *+AR5(0XE6),R5 ;K(42)
        MPYF R2,R5      ;K(42)*[y(2)-x(2)]
        ADDF R5,R4      ;K(42)*[y(1)-x(1)]+K(42)*[y(2)-x(2)]
        LDF *+AR5(0XBD),R5 ;X(4)
        ADDF R5,R4      ;X(4)+K(41)*[y(1)-x(1)]+K(42)*[y(2)-x(2)]
        STF R4,*+AR5(0xFE) ;X(4)+K(41)*[y(1)-x(1)]+K(42)*[y(2)-x(2)]--->XF(4)
        RETS
;subroutine FRSQER
;INPUT IS MATRICE K 4*4 , Pk|k-1 4*4
;output is matrice KHP 4*4
;THIS SUBROUTINE OCCUPY 110 WORD
FRSQER:  LDF *+AR5(0XDF),R0 ;K11
        MPYF -1.0,R0 ;-K11
        ADDF 1.0,R0 ;1-K11
        LDF *+AR5(0XE0),R1 ;K12
        MPYF -1.0,R1 ;-K12
        LDF *+AR5(0xCE),R2 ;P11
        LDF *+AR5(0XD2),R3 ;P21
        MPYF R0,R2 ;(1-K11)*P11
        MPYF R1,R3 ;-K12*P21
        ADDF R3,R2 ;(1-K11)*P11+-K12*P21
  STF R2,*+AR5(0XE9) ;(1-K11)*P11+-K12*P21--->P(11)
        LDF *+AR5(0XCF),R2 ;P12
        LDF *+AR5(0XD3),R3 ;P22
        MPYF R0,R2 ;(1-K11)*P12
        MPYF R1,R3 ;-K12*P22
        ADDF R3,R2 ;(1-K11)*P12+-K12*P22
  STF R2,*+AR5(0XEA) ;(1-K11)*P11+-K12*P21--->P(12)
        LDF *+AR5(0XD0),R2 ;P13
        LDF *+AR5(0XD4),R3 ;P23
        MPYF R0,R2 ;(1-K11)*P13
        MPYF R1,R3 ;-K12*P23
        ADDF R3,R2 ;(1-K11)*P13+-K12*P23
   STF R2,*+AR5(0XEB) ;(1-K11)*P13+-K12*P23--->P(13)
        LDF *+AR5(0XD1),R2 ;P14
        LDF *+AR5(0XD5),R3 ;P24
        MPYF R0,R2 ;(1-K11)*P14
        MPYF R1,R3 ;-K12*P24
        ADDF R3,R2 ;(1-K11)*P14+-K12*P24
   STF R2,*+AR5(0XEC) ;(1-K11)*P14+-K12*P24--->P(14)
        LDF *+AR5(0XE2),R0 ;K22
        MPYF -1.0,R0 ;-K22
        ADDF 1.0,R0 ;1-K22
        LDF *+AR5(0XE1),R1 ;K21
        MPYF -1.0,R1 ;-K21
        LDF *+AR5(0XD2),R4 ;P21
        LDF *+AR5(0xCE),R5 ;P11
        MPYF3 R4,R0,R2 ;(1-K22)*P21
        MPYF3 R5,R1,R3 ;-K21*P11
        ADDF R3,R2 ;(1-K22)*P21+-K21*P11
  STF R2,*+AR5(0XED) ;(1-K22)*P21+-K21*P11--->P(21)
        LDF *+AR5(0XCF),R6 ;P12
        LDF *+AR5(0xD3),R7 ;P22
        MPYF3 R1,R6,R2 ;-K21*P12
        MPYF3 R0,R7,R3 ;(1-K22)*P22
        ADDF R3,R2 ;-K21*P12+(1-K22)*P22
 STF R2,*+AR5(0xEE) ;-K21*P12+(1-K22)*P22--->P(22)
        LDF *+AR5(0XD0),R2 ;P13
        LDF *+AR5(0XD4),R3 ;P23
        MPYF R1,R2 ;-K21*P13
        MPYF R0,R3 ;(1-K22)*P23
        ADDF R3,R2 ;(1-K22)*P23+-K21*P13
```

```
  STF R2,*+AR5(0XEF) ;(1-K22)*P13+-K21*P23--->PF(23)
      LDF *+AR5(0XD1),R2 ;P14
      LDF *+AR5(0XD5),R3 ;P24
      MPYF R1,R2 ;-K21*P14
      MPYF R0,R3 ;(1-K22)*P24
      ADDF R3,R2 ;(1-K22)*P24+-K21*P14
  STF R2,*+AR5(0XF0) ;(1-K22)*P24+-K21*P14--->PF(24)
      LDF *+AR5(0XE3),R0 ;K31
      MPYF -1.0,R0 ;-K31
      LDF *+AR5(0XE4),R1 ;K32
      MPYF -1.0,R1 ;-K32
      MPYF3 R5,R0,R2 ;-K31*P11
      MPYF3 R4,R1,R3 ;-K32*P21
      ADDF R3,R2 ;-K31*P11-K32*P21
      ADDF *+AR5(0XD6),R2 ;-K31*P11-K32*P21+P31
  STF R2,*+AR5(0XF1);-K31*P11-K32*P21+P31--->PF(31)
      MPYF3 R6,R0,R2 ;-K31*P12
      MPYF3 R7,R1,R3 ;-K32*P22
      ADDF R3,R2 ;-K31*P12-K32*P22
      ADDF *+AR5(0XD7),R2;-K31*P12-K32*P22+P32
  STF R2,*+AR5(0XF2);-K31*P11-K32*P21+P32--->PF(32)
      LDF *+AR5(0XD0),R2 ;P13
      LDF *+AR5(0XD4),R3 ;P23
      MPYF R0,R2 ;-K31*P13
      MPYF R1,R3 ;-K32*P23
      ADDF R3,R2 ;-K31*P13-K32*P23
      ADDF *+AR5(0XD8),R2 ;-K31*P13-K32*P23+P33
  STF R2,*+AR5(0XF3) ;K31*P13-K32*P23+P33--->PF(33)
      MPYF *+AR5(0XD1),R0 ;-K31*P14
      MPYF *+AR5(0XD5),R1 ;-K32*P24
      ADDF R0,R1 ;-K31*P14-K32*P24
      ADDF *+AR5(0XD9),R1 ;-K31*P14-K32*P24+P34
 STF R1,*+AR5(0XF4) ;-K31*P14-K32*P24+P34---->PF(34)
      LDF *+AR5(0XE5),R0 ;K41
      MPYF -1.0,R0 ;-K41
      LDF *+AR5(0XE6),R1 ;K42
      MPYF -1.0,R1 ;-K42
      MPYF3 R5,R0,R2 ;-K41*P11
      MPYF3 R4,R1,R3 ;-K42*P21
      ADDF R3,R2 ;-K41*P11-K42*P21
      ADDF *+AR5(0XDA),R2;-K41*P11-K42*P21+P41
  STF R2,*+AR5(0XF5) ;-K41*P11-K42*P21+P41--->PF(41)
      MPYF3 R0,R6,R2 ;-K41*P12
      MPYF3 R1,R7,R3 ;-K42*P22
      ADDF R3,R2 ;-K41*P12-K42*P22
      ADDF *+AR5(0XDB),R2 ;-K41*P12-K42*P22+P42
 STF R2,*+AR5(0XF6) ;-K41*P12-K42*P22+P42--->PF(42)
     LDF *+AR5(0XD0),R2 ;P13
     LDF *+AR5(0XD4),R3 ;P23
     MPYF R0,R2 ;-K41*P13
     MPYF R1,R3 ;-K42*P23
     ADDF R3,R2 ;-K41*P13-K42*P23
     ADDF *+AR5(0XDC),R2 ;-K41*P13-K42*P23+P43
STF R2,*+AR5(0XF7) ;-K41*P13-K42*P23+P43--->PF(43)
     MPYF *+AR5(0XD1),R0 ;-K41*P14
     MPYF *+AR5(0XD5),R1 ;-K42*P24
     ADDF R1,R0 ;-K41*P14-K42*P24
     ADDF *+AR5(0XDD),R0 ;-K41*P14-K42*P24+P44
STF R0,*+AR5(0XF8) ;-K41*P14-K42*P24+P44--->PF(44)
     RETS
```

A.1.12 Mathematic subroutine:

The subroutine "ARCTG" is used for arc tangent function;

The subroutine "COS" is used for cosine function;

The subroutine "COSM" is used for cosine function with 120 degree behind;

The subroutine "COSP" is used for cosine function with 120 degree lead;

The subroutine "SIN" is used for sine function;

The subroutine "SINM" is used for sine function with 120 degree behind;;

The subroutine "SINP" is used for cosine function with 120 degree lead;

The subroutine "INVF" is used for inverse function;

```
;*****************************************************
; Subroutine ARCTG.
; Calculating ARCTAN(x/y).
; The x and y must not be both zero.
; One cycle (2Pi) is 4000 grids.
; INPUT: x in R1, y in R0, not changed
; OUTPUT: ARCTAN(x/y) in R5.
; USED BUT NOT CHANGED: none
; CHANGED: none
; CALLED SUBROUTINE(S): INVF, ARCTG1
;
ARCTG:  PUSH R0
        PUSH R1
        PUSHF R0
        PUSHF R1
        ABSF R0, R0
        ABSF R1, R1
        CMPF3 R1, R0
        BN ARCTG2
ARCTG0: CALL INVF       ; ABS(x) <= ABS(y)
        MPYF R1, R0     ; R0 = ABS(x) / ABS(y)
        CALL ARCTG1     ; R5 = ARCTAN(ABS(x)/ABS(y))
        B ARCTG4
ARCTG2: PUSHF R0        ; ABS(x) > ABS(y)
        LDF R1, R0      ; R0 = ABS(x)
        POPF R1         ; R1 = ABS(y)
        CALL INVF
        MPYF R1, R0     ; R0 = ABS(y) / ABS(x)
        CALL ARCTG1     ; R5 = ARCTAN(ABS(y)/ABS(x))
        SUBI 1000, R5
        MPYI -1, R5     ; R5 = ARCTAN(ABS(x)/ABS(y))
```

```
ARCTG4: POPF R1
        BN ARCTG6
ARCTG5: POPF R0
        BNN ARCTG7
ARCTG8: SUBI 2000, R5
        MPYI -1, R5
ARCTG7: POP R1
        POP R0
        RETS
ARCTG6: POPF R0
        BN ARCTG3
ARCTG9: SUBI 4000, R5
        MPYI -1, R5
        B ARCTG7
ARCTG3: ADDI 2000, R5
        B ARCTG7
;
;*************************************************************
; Subroutine ARCTG1.
; Calculating ARCTAN(x) by looking up a table.
; x must be ranged from 0 to 1. result is from 0 to 500.
; INPUT: x in R0, not changed
; OUTPUT: ARCTAN(x) in R5.
; USED BUT NOT CHANGED: R6, R7, IR1
; CHANGED: none
; CALLED SUBROUTINE(S): none
ARCTG1: PUSH R6
        PUSH R7
        PUSH IR1
        PUSHF R6
        PUSHF R7
        LDF R0, R5
        MPYF 10., R5
        FIX R5, IR1
        LDF *+AR3(IR1), R6
        PUSHF R6
        ADDI 1, IR1
        LDF *+AR3(IR1), R7
        SUBF3 R6, R7, R7
        SUBI 1, IR1
        FLOAT IR1, R6
        SUBF R6, R5
        MPYF R7, R5
        POPF R6
        ADDF R6, R5
        FIX R5, R5
        POPF R7
        POPF R6
        POP IR1
        POP R7
        POP R6
        RETS
;
;*************************************************************
; Subroutine COS.
; Calculating the COS of an angle
; theta. Theta is stored in R5, ranging from
; 0 to 8192(2048*4). The unit of theta is 0.1 grad.
; In other words, a cycle is devided into
; 8193 grids. 0 in R5 means theta=0; 4096
; in R5 means theta=3.1415926 rad. The result
; of COS(theta) is stored in R0.
; This subroutine is based on the Subroutine SIN.
```

```
;
; Because the revolusion of encoder is 8192ppr,
; the encoder value can be directly input to
; calculate the COS(theta). The Subroutine SIN
; is used to get the COS result.
; INPUT:
;  the angle theta is in R5.
; OUTPUT:
;  COS(theta) is in R0.
; USED BUT NOT CHANGED: R5
; CHANGED: none
; CALLED SUBROUTINE(S): SIN
;
COS:   PUSH R5
       CMPI 1001, R5        ;cmpi 90.09deg,r5
       BN COS1
       SUBI 5000, R5        ; Theta=Theta-450deg(360deg+90deg)
       BR COS2
COS1:  SUBI 1000, R5        ; Theta=Theta-90deg
COS2:  MPYI -1, R5          ; Theta=-Theta
       CALL SIN
       POP R5
       RETS
;
;*********************************************************
; Subroutine COSM.
; Calculating COS(theta-120degrees).
; Theta is stored in R5, ranging from 0 to 8188.
; The result is stored in R0.
; This subroutine is based on the Subroutine SIN.
; INPUT:
;  the angle theta is in R5.
; OUTPUT:
;  COS(theta-120degrees) is in R0.
; USED BUT NOT CHANGED: R5
; CHANGED: none
; CALLED SUBROUTINE(S): SIN
;
COSM:  PUSH R5
       CMPI 2334, R5        ;cmpi 210.06deg(120.06deg+90deg)
       BN COSM1
       SUBI 6333, R5        ; Theta=Theta-569.97deg(360deg+120deg+89deg)
       BR COSM2
COSM1: SUBI 2333, R5        ; Theta=Theta-209.97deg(120+89.97)
COSM2: MPYI -1, R5          ; Theta=-Theta
       CALL SIN
       POP R5
       RETS
;
;*********************************************************
; Subroutine COSP.
; Calculating COS(theta+120degrees).
; Theta is stored in R5, ranging from 0 to 3999.
; The result is stored in R0.
; This subroutine is based on the Subroutine SIN.
; INPUT:
;  the angle theta is in R5.
; OUTPUT:
;  COS(theta+120degrees) is in R0.
; USED BUT NOT CHANGED: R5
; CHANGED: none
; CALLED SUBROUTINE(S): SIN
;
```

```
COSP:  PUSH R5
       CMPI 3667, R5        ;cmpi 330.03deg(360deg-29.97deg)
       BN COSP1
       SUBI 7666, R5        ; Theta=Theta-689.94deg(720deg-30.06deg)
            BR COSP2
COSP1: SUBI 3666, R5        ; Theta=Theta-329.94deg(360deg-30.06deg)
COSP2: MPYI -1, R5          ; Theta=-Theta
       CALL SIN
       POP R5
       RETS
;
;*********************************************************
; Subroutine DELAY.
DELAY:
       PUSH R0
       PUSH R1
       LDI 0x02fFf,R0
dec    LDI @AD1_P,R1
       and 0x1fff,R1
       STI R1,*+AR0(0X64)
       LSH 0XFFFFFFFF,R1
       sti r1,@DA2_2
       SUBI 0X01,R0
       BNZ dec      ;delay for 20mS
       POP R1
       POP R0
       RETS

;
;*********************************************************************
; Subroutine INVF.
; Calculating the the inverse of a floating-point number.
; The floating-point number v is stored in R0. After the compution is
; completed, 1/v is also stored in R0. Iteration is performed. More
; iterations may lead to higher accuracy. This subroutine performs
; four times of iterations. The error should be less than 0.015%.
; To perform y/v, just multify y by the inverse of v (i.e., 1/v).
; See pp. 3-10 ~ 3-12 of SPRU194
; INPUT:
;  number to be inverted is in R0.
; OUTPUT:
;  result of inversion is in R0.
; USED BUT NOT CHANGED:
;  R1, R6, R7
; CHANGED: none
; CALLED SUBROUTINE(S): none
;
INVF:  PUSH R1
       PUSH R6
       PUSH R7
       PUSHF R1
       PUSHF R6
       PUSHF R7
       LDF R0, R7           ; v is saved for later usage
       ABSF R0, R0          ; the algorithm uses v=|v|
; Extract the exponent of v.
            PUSHF R0
            POP R1                  ; 32 MSBs OF R0 is loaded to 32 LSBs of R1.
            ASH -24, R1             ; the 8 LSBs of R1 contain the exponent of v
; x[0] formation is given the exponent of v.
       NEGI R1, R1          ; -e is in R1
            SUBI 1, R1              ; now having -e-1, the exponent of x[0]
       ASH 24, R1           ; -e-1 is in Bit 24 to Bit 31
```

```
        PUSH R1
        POPF R1                         ; now R1 = x[0] = 1.0 * 2**(-e-1)
    MPYF 1.3333333333, R1   ; now R1 = x[0] = 1.3333 * 2**(-e-1)
; Now the iterations begin.
;
    MPYF3 R1, R0, R6      ; R6 = v * x[i-1]
    SUBRF 2.0, R6         ; R6 = 2.0 - v * x[i-1]
    MPYF R6, R1           ; R1 = x[i] = x[i-1] * (2.0 - v * x[i-1])
;
    MPYF3 R1, R0, R6      ; R6 = v * x[i-1]
    SUBRF 2.0, R6         ; R6 = 2.0 - v * x[i-1]
    MPYF R6, R1           ; R1 = x[i] = x[i-1] * (2.0 - v * x[i-1])
;
    MPYF3 R1, R0, R6      ; R6 = v * x[i-1]
    SUBRF 2.0, R6         ; R6 = 2.0 - v * x[i-1]
    MPYF R6, R1           ; R1 = x[i] = x[i-1] * (2.0 - v * x[i-1])
;
    RND R1, R1            ; this minimizes error in the LSBs
; For the last iteration, using the formulation:
; x[i] = (x[i-1] * (1.0 - (v * x[i-1]))) + x[i-1]
    MPYF3 R1, R0, R6      ; R6 = v * x[i-1] = 1.0..01 => 1
    SUBRF 1.0, R6         ; R6 = 1.0 - v * x[i-1] = 0.0..01 => 0
    MPYF R1, R6           ; R6 = x[i-1] * (1.0 - v * x[i-1])
    ADDF R6, R1           ; R1 = x[i] = x[i-1] * (1.0 - v * x[i-1]) + x[i-1]
;
    RND R1, R0            ; round the result because this subroutine is often followed by MPYF.
; Now the case of V < 0 is handled.
    NEGF R0, R6
    LDF R7, R7            ; this sets condition flags
    LDFN R6, R0           ; if v < 0, then R0 = -R0
;
    POPF R7
    POPF R6
    POPF R1
    POP R7
    POP R6
    POP R1
       RETS
;
;*********************************************************************
;Subroutine RVSEF
;SWAP IBref and ICref
RVSEF:  LDF *+AR0(0X16),R0 ;IAref<----R0
    LDF *+AR0(0X17),R1 ;IBref<----R1
    LDF *+AR0(0X18),R2 ;ICref<----R2
    STF R0,*+AR0(0X17) ;R0--->ICref
    STF R1,*+AR0(0X18) ;R0--->ICref
    STF R2,*+AR0(0X16) ;R1--->IBref
    RETS

;*******************************************************
; Subroutine SIN.
; Calculating the SIN of an angle
; theta. Theta is stored in R5, ranging from
; 0 to 8192. The unit of theta is 0.1 grad.
; In other words, a cycle is devided into
; 8192 grids. 0 in R5 means theta=0; 4096
; in R5 means theta=3.1415926 rad. The result
; of SIN(theta) is stored in R0.
;
; Because the revolusion of encoder is 8192ppr,
; the encoder value can be directly input to
; calculate the SIN(theta). The Table SINE is
```

```
; used to get the result.
; INPUT:
;  the angle theta is in R5.
; OUTPUT:
;  SIN(theta) is in R0.
; USED BUT NOT CHANGED:
;  R6, R7, IR1
; CHANGED: none
; CALLED SUBROUTINE(S): none
;
SIN:   PUSH R6
       PUSH R7
       PUSH IR1
       PUSHF R6
       PUSHF R7
       LDI R5, IR1
       LSH -5, IR1       ;R5/16--->K
       LDF *+AR1(IR1), R6 ; sin(k)--->R6
       ADDI 1, IR1
       LDF *+AR1(IR1), R7 ; sin(k+1)--->R7
       SUBI 1, IR1       ;K-1---->K
       LSH 5, IR1        ;K*32--->K
       SUBI R5, IR1      ;K-R5--->IR1
       SUBF R6, R7       ;sin(k+1)-sin(k)---->sin(k+1)
       FLOAT IR1, R0     ;IR1--->R0
       MPYF R7, R0       ;(SIN(K+1)-SIN(K))(K-R5)--->R0
       MPYF -0.03125, R0  ;R0*(-0.0305)
       ADDF R6, R0       ;SIN(K)+R0
       POPF R7
       POPF R6
       POP IR1
       POP R7
       POP R6
       RETS
;
;*****************************************************
; Subroutine SINM.
; Calculating SIN(theta-120degrees).
; Theta is stored in R5, ranging from 0 to 3999.
; The result is stored in R0.
; This subroutine is based on the Subroutine SIN.
; INPUT:
;  the angle theta is in R5.
; OUTPUT:
;  SIN(theta-120degrees) is in R0.
; USED BUT NOT CHANGED: R5
; CHANGED: none
; CALLED SUBROUTINE(S): SIN
;
SINM:  PUSH R5
       CMPI 1333, R5
       BN SINM1
       SUBI 1333, R5          ; Theta=Theta-1365
       BR SINM2
SINM1: SUBI -2666, R5         ; Theta=Theta+2729
SINM2: CALL SIN
       POP R5
       RETS
;
;*****************************************************
; Subroutine SINP.
; Calculating SIN(theta+120degrees).
; Theta is stored in R5, ranging from 0 to 3999.
```

```
; The result is stored in R0.
; This subroutine is based on the Subroutine SIN.
; INPUT:
;  the angle theta is in R5.
; OUTPUT:
;  SIN(theta+120degrees) is in R0.
; USED BUT NOT CHANGED: R5
; CHANGED: none
; CALLED SUBROUTINE(S): SIN
;
SINP:  PUSH R5
       CMPI 2666, R5
       BN SINP1
       SUBI 2666, R5          ; Theta=Theta-2729
       BR SINP2
SINP1: SUBI -1333, R5         ; Theta=Theta+1365
SINP2: CALL SIN
       POP R5
       RETS
```

A.2 Linear Kalman Filter :

The subroutine LKF is to execute linear Kalman filter algorithm.

```
;*************************************************************************
LKF:  LDF *+AR0(0X68),R0  ;(0X68)<-----THETA(0)
      MPYF 0.4776,R0      ;THETA/(2PI/3)
      FIX R0,R0           ;INT[THETA/(2PI/3)]
      FLOAT R0,R0
      MPYF 2.094, R0      ;2.094*INT[THETA/(2PI/3)]
      LDF *+AR0(0X68),R1  ;confine as [0,2pi/3]
      SUBF R0,R1          ;theta'=THETA-2.094*INT[THETA/(2PI/3)] to confine as [0,2pi](electrical)
      CMPF 0.0,R1
      BNN TRA
      ADDF 2.094,R1       ;if theta'<0, 2.094+theta' [2pi+theta'](electrical)
TRA   LDF R1,R0           ;*+AR0(0X6C)<------4000/(2PI/3)=1910.22
      STF R1,*+AR0(0X68)  ;update theta(0)
      MPYF *+AR0(0X6c),R0 ;1910.22*THETA,(0X68)<-----THETA
      FIX R0,R0
      STI R0,@DA_2
;*************************************************************
      LDI R0,R5
      CALL COS
      MPYF *+AR5(0XB6),R0 ;y2*cos(theta), y2 psi(beta)<---(0x47)
      LDF R0,R1           ;y2*cos(theta)<----R1
      CALL SIN
      MPYF *+AR5(0XB5),R0 ;y1*sin(theat)<----R0, y1 psi(alfa)<----(0x46)
      SUBF R0,R1          ;y2*cos(theta)-y1*sin(theat)
      STF R1,*+AR0(0X6B)  ;E=y2*cos(theta)-y1*sin(theat)
```

```
    MPYF *+AR0(0X6D),R1  ;k1*E-->R1, (0x6d)<---k1
    LDF *+AR0(0X69),R0   ;OMIGA(R)
    MPYF *+AR0(0X65),R0  ;T*OMIGA(R) ,(0X65)<---THYST
    ADDF R1,R0           ; T*OMIGA(R)+k1*E
    ADDF *+AR0(0X68),R0  ;THETA(0)+T*OMIGA(R)+k1*E
    STF R0,*+AR5(0XB0)   ;THETA(0)+T*OMIGA(R)+k1*E------>*+AR5(0XB0)
;********** OMIGA(R) ***********************************************
    LDF *+AR0(0X69),R0   ;OMIGA(R)<-----(0X69)
    ADDF *+AR0(0X6A),R0  ;OMIGA'+OMIGA(R)<---R0,OMIGA'<-----(0X6A)
    LDF *+AR0(0X6B),R1   ;E<---(0X6B)
    MPYF *+AR0(0x6E),R1  ;K2*E,k2<---(0x6E)
    ADDF R0,R1           ;OMIGA'+OMIGA(R)+K2*E
    STF R1,*+AR5(0XB1)   ;OMIGA'+OMIGA(R)+K2*E---->*+AR5(0XB1)
;************************ OMIGA'  ***********************************
    LDF *+AR0(0X6B),R1   ;E<---(0X6B)
    MPYF *+AR0(0X6F),R1  ;K3*E
    ADDF *+AR0(0X6A),R1  ;OMIGA'+K3*E
    STF R1,*+AR5(0XB2)   ;OMIGA'+K3*E------>*+AR5(0XB2)
    RETS
;
```

A.3 Single Dimension Luenberger:

The subroutine "TSTR" and "LUENBGR" is to execute SD Luenberger algorithm.

```
;2-phase/2-phase rotationary transformation subroutine 2S/2R
;input is alpha<---R0, Ibeta<---R1
;OUTPUT is d<---R0,q<---R1
TSTR:  LDF *+AR5(0XB9),R0  ;Theta(k+1)<---AR5(0XB9)
       STF R0,*+AR5(0XB8)  ;Theta(k+1)--->Theta(k)<---AR5(0XB8)
       LDF *+AR5(0XB2),R0  ;Omiga(k+1)<---AR5(0XB2)
       STF R0,*+AR0(0X69)  ;Omiga(k)<---AR0(0X69),Omiga(k)<---Omiga(k+1)
       LDF *+AR5(0XB1),R0  ;xi(k+1)<---AR5(0XB1)
       STF R0,*+AR5(0XB0)  ;xi(K)<---AR5(0XB0),xi(k+1)--->xi(k)
       LDF *+AR0(0X1C),R0  ;Id(k)<---*+AR0(0X1C)
       STF R0,*+AR5(0xBE)  ;Id(k-1)<---Id(k),Id(k-1)<---AR5(0xBE)
       LDI *+AR5(0XBD),R5  ;Theta(k) encoderized
       CALL SIN
       STF R0,*+AR5(0XBA)  ;SIN(THETA)
       CALL COS
       STF R0,*+AR5(0XBB)  ;COS(THETA)
       LDF *+AR5(0XBA),R0  ;SIN(THETA)<---R0
       LDF *+AR5(0XBB),R1  ;COS(THETA)<---R1
       LDF *+AR0(0X6A),R2  ;U_AIPHA<---R2
       LDF *+AR0(0X6B),R3  ;U_BETA<---R3
       MPYF3 R0,R3,R4      ;U_beta*sin(theta)
       MPYF3 R1,R2,R5      ;U_alpha*cos(theta)
       ADDF R4,R5          ;U_alpha*cos(theta)+U_beta*sin(theta)<---Vd
       STF R5,*+AR0(0X6C)  ;*+ar0(0x6C)<---Vd
       MPYF3 R0,R2,R4      ;U_AIPHA*SIN(THETA)
       MPYF3 R1,R3,R5      ;U_BETA*COS(THETA)
```

```
      SUBF R4,R5        ;U_BETA*COS(THETA)-U_AIPHA*SIN(THETA)
      STF R5,*+AR0(0X6D)  ;*+ar0(0x6D)<---Vq
      LDI *+AR5(0XBD),R5
      LDF *+AR0(0X0B),R0
      STF R0,*+AR0(0X19)
      LDF *+AR0(0X0D),R0
      STF R0,*+AR0(0X1A)
      LDF *+AR0(0X0F),R0
      STF R0,*+AR0(0X1B)
      CALL ABCDQ
      RETS


;******** Subroutine luenberger observer ********
   ;*****LINEAR INPUT ****
LUENBGR:LDF *+AR0(0X51),R0  ;L<---AR0(0X51)
      MPYF *+AR0(0X69),R0 ;OMIGA(K)*L,AR0(0X69)<---OMIGA(K)
      LDF *+AR0(0X1D),R1  ;Iq<---AR0(0X1D)
      MPYF R0,R1        ;OMIGA(K)*L*Iq
      LDF *+AR0(0X6C),R2  ;Vd<----AR0(0x6C)
      ADDF R1,R2        ;Vd+OMIGA(K)*L*Iq
      STF R2,*+AR0(0x6E)  ;Ud<--AR0(6E)=Vd-OMIGA(K)*L*Iq
      LDF *+AR0(0X1C),R1  ;Id<---AR0(0X1C)
      MPYF R0,R1        ;OMIGA(K)*L*Id
      LDF *+AR0(0X6D),R2  ;Vq<---AR0(0X6D)
      SUBF R1,R2        ;Vq-OMIGA(K)*L*Id
      STF R2,*+AR0(0X6F)  ;Uq<---AR0(0X6F)
   ;Luenberger Observer
      LDF *+AR5(0XB0),R0  ;xi(k)<---AR5(0XB0)
      MPYF *+AR5(0XB3),R0 ;A0*T+1<---AR5(0XB3),(A0*T+1)xi(k)
      LDF *+AR5(0XB4),R1  ;B0*T<---AR5(0XB4)
      MPYF *+AR0(0X6F),R1 ;Uq<---AR0(0X6F),B0*T*Uq
      ADDF R1,R0        ;(A0*T+1)xi(k)+B0*T*Uq
      LDF *+AR5(0XB5),R1  ;K0*T
      MPYF *+AR0(0X1D),R1 ;K0*T*Iq,Iq<---AR0(0X1D)
      ADDF R1,R0        ;(A0*T+1)xi(k)+B0*T*Uq+K0*T*Iq--->xi(K+1)
      STF R0,*+AR5(0XB1)  ;Xi(k+1)<---(A0*T+1)xi(k)+B0*T*Uq+K0*T*Iq
      LDF *+AR5(0XB6),R1  ;H0<---AR5(0XB6)
      MPYF *+AR0(0X1D),R1 ;Iq<---AR0(0X1D),H0*Iq
      ADDF R1,R0        ;Xi(k+1)+H0*Iq=OMIGA(K+1)
      STF R0,*+AR5(0XB2)  ;OMIGA(K+1)
    ;********  Position Integration
      LDF *+AR5(0XB8),R1  ;theta(k)<---AR5(0XB8)
      MPYF *+AR0(0X68),R0 ;AR0(0X68)--->THYST,THYST*OMIGA(k+1)
      ADDF R1,R0        ;THYST*OMIGA(k+1)+theta(k)
      STF R0,*+AR5(0XB9)  ;Theta(k+1)<---AR5(0XB9)
   ;**********  Position correction
       LDF *+AR0(0X1c),R0  ;current Id reference
       MPYF -1.0,R0       ;Iq*-Iq,Iq(k)<--AR0(0x1d)

    ;*********** PI ******
      LDF *+AR5(0XC3),R6
      STF R6,*+AR5(0XC4)  ;Delta1--->Delta2
      LDF *+AR5(0XC2),R6
      STF R6,*+AR5(0XC3)  ;Delta--->Delta1
      STF R0,*+AR5(0XC2)  ;current Delta(k)<---R0
      LDF *+AR5(0XB9),R3 ;R3<---THETA(K+1)
      CALL PI
      CMPF 0.0,R3
      BNN PZ
      ADDF 2.094,R3
PZ    STF R3,*+AR5(0XB9) ;Theta(k+1)<---AR5(0XB9)
      LDF R3,R0
```

```
    ;************  Theta encoderized
      LDF *+AR5(0XB9),R0  ;(0XB9)<-----THETA(k+1)
      MPYF 0.4776,R0      ;THETA/(2PI/3)
      ABSF R0,R0
      FIX R0,R0           ;INT[THETA/(2PI/3)]
      FLOAT R0,R0
      MPYF 2.094, R0      ;2.094*INT[THETA/(2PI/3)]
      LDF *+AR5(0XB9),R1  ;confine as [0,2pi/3]
      ABSF R1,R1
      SUBF R0,R1          ;theta'=THETA-2.094*INT[THETA/(2PI/3)] to confine as [0,2pi](electrical)
    ; LDF *+AR5(0XB9),R2
    ; CMPF 0.0,R2
    ; BNN TRA
    ; LDF 2.094,R0
     ; SUBF R1,R0
     ; B TRA1
TRA   LDF R1,R0           ;*+AR0(0X6C)<------4000/(2PI/3)=1910.22
TRA1  STF R0,*+AR5(0XB9)  ;update theta(0)
      MPYF *+AR5(0XBC),R0 ;1910.22*THETA,(0XB8)<-----THETA
      FIX R0,R0
      STI R0,*+AR5(0XBD)  ;Theta(k)(int encoderized) --->AR0(0x23)

    ; STI R0,@DA_2
      LDI R0,R5           ;Theta(k+1) encoderized<----R5
  ;*************************
      RETS
```

A.4 Full-order Luenberger :

The subroutine "FTSTR" and "FLUENBGR" are for full order Luenberger observer.

```
;2-phase/2-phase rotationary transformation subroutine 2S/2R
;input is alpha<---R0, Ibeta<---R1
;OUTPUT is d<---R0,q<---R1
FTSTR:  LDF *+AR5(0XB9),R0  ;Theta(k+1)<---AR5(0XB9)
    STF R0,*+AR5(0XB8)  ;Theta(k+1)--->Theta(k)<---AR5(0XB8)
    LDF *+AR5(0XB2),R0  ;Omiga(k+1)<---AR5(0XB2)
    STF R0,*+AR0(0X69)  ;Omiga(k)<---AR0(0X69),Omiga(k)<---Omiga(k+1)
    LDF *+AR5(0XB1),R0  ;zeta(k+1)<---AR5(0XB1)
    STF R0,*+AR5(0XB0)  ;zeta(K)<---AR5(0XB0),zeta(k+1)--->zeta(k)
    LDF *+AR5(0XB4),R0  ;eta(k+1)<---AR5(0XB4)
    STF R0,*+AR5(0XB3)  ;eta(K)<---AR5(0XB3),eta(k+1)--->eta(k)
    LDF *+AR5(0XB6),R0  ;gamma(k+1)<---AR5(0XB6)
    STF R0,*+AR5(0XB5)  ;gamma(K)<---AR5(0XB5),gamma(k+1)--->gamma(k)
    LDI *+AR5(0XD3),R5  ;Theta(k) encoderized
    CALL SIN
    STF R0,*+AR5(0XBA)  ;SIN(THETA)
    CALL COS
    STF R0,*+AR5(0XBB)  ;COS(THETA)
    LDF *+AR5(0XBA),R0  ;SIN(THETA)<---R0
    LDF *+AR5(0XBB),R1  ;COS(THETA)<---R1
    LDF *+AR0(0X6A),R2  ;U_AIPHA<---R2
    LDF *+AR0(0X6B),R3  ;U_BETA<---R3
    MPYF3 R0,R3,R4      ;U_beta*sin(theta)
    MPYF3 R1,R2,R5      ;U_alpha*cos(theta)
    ADDF R4,R5          ;U_alpha*cos(theta)+U_beta*sin(theta)<---Vd
    STF R5,*+AR0(0X6C)  ;*+ar0(0x6C)<---Vd
    MPYF3 R0,R2,R4      ;U_AIPHA*SIN(THETA)
    MPYF3 R1,R3,R5      ;U_BETA*COS(THETA)
    SUBF R4,R5          ;U_BETA*COS(THETA)-U_AIPHA*SIN(THETA)
    STF R5,*+AR0(0X6D)  ;*+ar0(0x6D)<---Vq
```

```
      LDI *+AR5(0XD3),R5  ;<--------Theta(k) encoderized
      LDF *+AR0(0X0B),R0
      STF R0,*+AR0(0X19)
      LDF *+AR0(0X0D),R0
      STF R0,*+AR0(0X1A)
      LDF *+AR0(0X0F),R0
      STF R0,*+AR0(0X1B)
      CALL ABCDQ
      RETS


;******** Subroutine luenberger observer ********
   ;*****LINEAR INPUT ****
FLUENBGR:LDF *+AR0(0X51),R0  ;L<---AR0(0X51)
      MPYF *+AR0(0X69),R0 ;OMIGA(K)*L,AR0(0X69)<---OMIGA(K)
      LDF *+AR0(0X1D),R1  ;Iq<---AR0(0X1D)
      MPYF R0,R1          ;OMIGA(K)*L*Iq
      LDF *+AR0(0X6C),R2  ;Vd<----AR0(0x6C)
      ADDF R1,R2          ;Vd+OMIGA(K)*L*Iq
      STF R2,*+AR0(0x6E)  ;Ud<--AR0(6E)=Vd-OMIGA(K)*L*Iq
      LDF *+AR0(0X1C),R1  ;Id<---AR0(0X1C)
      MPYF R0,R1          ;OMIGA(K)*L*Id
      LDF *+AR0(0X6D),R2  ;Vq<---AR0(0X6D)
      SUBF R1,R2          ;Vq-OMIGA(K)*L*Id
      STF R2,*+AR0(0X6F)  ;Uq<---AR0(0X6F)
   ;full_order Luenberger Observer
;*********************************************************
      LDF *+AR5(0XB0),R0  ;AR5(0XB0)--->zeta(k)
      MPYF *+AR5(0XB7),R0 ;AR5(0XB7)--->lug11,lug11*zeta(k)-->R0
      LDF *+AR5(0XB3),R1  ;AR5(0XB3)--->eta(k)
      MPYF *+AR5(0XBD),R1 ;AR5(0XBD)--->lug12,lug12*eta(k)
      ADDF R0,R1          ;lug11*zeta(k)+lug12*eta(k)--->R1 ---1st add result
      LDF *+AR0(0x6E),R0  ;AR0(0X6E)--->Ud(k)
      MPYF *+AR5(0xBE),R0 ;AR5(0xBE)--->B11,B11(k)*Ud(k)--->R0
      ADDF R0,R1          ;lug11*zeta(k)+lug12*eta(k)+B11(k)*Ud(k)----->R1---2nd add result
      LDF *+AR5(0XBF),R0  ;AR5(0XBF)--->C11
      MPYF *+AR0(0X1c),R0 ;AR0(0X1c)--->Id,C11*Id--->R0
      ADDF R0,R1          ;lug11*zeta(k)+lug12*eta(k)+B11(k)*Ud(k)+C11*Id--->R1---3rd add result
      LDF *+AR5(0xC0),R0  ;AR5(0xC0)--->C12
      MPYF *+AR0(0x1d),R0 ;Iq<---AR0(0X1D),C12*Iq
      ADDF R0,R1          ;lug11*zeta(k)+lug12*eta(k)+B11(k)*Ud(k)+C11*Id+C12*Iq---->R1----4th add
result
      STF R1,*+AR5(0xB1)  ;R1--->zeta(k+1),AR5(0XB1)--->zeta(k+1)
      LDF *+AR5(0xB0),R0  ;AR5(0XB0)--->zeta(k)
      MPYF *+AR5(0xC1),R0 ;AR5(0xc1)--->lug21,lug21*zeta(k)
      LDF *+AR5(0XB3),R1  ;AR5(0XB3)--->eta(k)
      MPYF *+AR5(0XC8),R1 ;AR5(0XC8)--->lug22,lug22*eta(k)
      ADDF R0,R1          ;lug21*zeta(k)+lug22*eta(k)---->R1---1st add result
      LDF *+AR5(0XB5),R0  ;AR5(0XB5)--->gamma(k)
      MPYF *+AR5(0XCB),R0 ;AR5(0XCB)--->lug23,lug23*gamma---->R0
      ADDF R0,R1          ;lug21*zeta(k)+lug22*eta(k)+lug23*gamma--->R1---2nd add result
      LDF *+AR0(0X6F),R0  ;AR0(0X6F)--->Uq(k)
      MPYF *+AR5(0xBE),R0 ;AR5(0xbe)--->B11,B11*Uq(k)
      ADDF R0,R1          ;lug21*zeta(k)+lug22*eta(k)+lug23*gamma+B11*Uq(k)--->R1---3rd add result
      LDF *+AR0(0X1C),R0  ;AR0(0X1C)--->Id(k)
      MPYF *+AR5(0XCC),R0 ;AR5(0XCC)--->C21,C21*Id(k)
      ADDF R0,R1          ;lug21*zeta(k)+lug22*eta(k)+lug23*gamma+B11*Uq(k)+C21*Id(k)--->R1---4th
add result
      LDF *+AR0(0X1D),R0  ;AR0(0X1D)---->Iq(k)
      MPYF *+AR5(0XCD),R1 ;AR5(0XCD)---->C22,C22*Iq(k)
      ADDF R0,R1          ;lug21*zeta(k)+lug22*eta(k)+lug23*gamma+B11*Uq(k)+C21*Id(k)+C22*Iq(k)--
->R1----5th add result
      STF R1,*+AR5(0XB4)  ;R1--->eta(k+1),AR5(0XB4)--->eta(K+1)
```

```
      LDF *+AR5(0XB0),R0  ;AR5(0XB0)--->zeta(k)
      MPYF *+AR5(0xCE),R0 ;AR5(0xCE)--->lug31,lug31*zeta(k)
      LDF *+AR5(0XB3),R1  ;AR5(0XB3)--->eta(k)
      MPYF *+AR5(0XCF),R1 ;AR5(0XCF)--->lug32,lug32*eta(k)
      ADDF R0,R1          ;lug31*zeta(k)+lug32*eta(k)--->R1---1st add result
      LDF *+AR5(0XB5),R0  ;AR5(0XB5)--->gamma(k)
      MPYF *+AR5(0XD0),R0 ;AR5(0XD0)--->lug33,lug33*gamma(k)
      ADDF R0,R1          ;lug31*zeta(k)+lug32*eta(k)+lug33*gamma(k)--->R1---2nd add result
      LDF *+AR0(0X1C),R0  ;AR0(0X1C)--->Id
      MPYF *+AR5(0XD1),R0 ;AR5(0XD1)--->C31,C31*Id
      ADDF R0,R1          ;lug31*zeta(k)+lug32*eta(k)+lug33*gamma(k)+C31*Id--->R1---3rd add result
      LDF *+AR0(0X1D),R0  ;AR0(0X1D)--->Iq
      MPYF *+AR5(0XD2),R0 ;AR5(0XD2)--->C32,C32*Iq
      ADDF R0,R1          ;lug31*zeta(k)+lug32*eta(k)+lug33*gamma(k)+C31*Id+C32*Iq--->R1---4th add
result
      STF R1,*+AR5(0XB6)  ;R1--->gamma(k+1)
      STF R1,*+AR5(0XB2)  ;AR5(0XB2)--->omiga(k+1),omiga(k+1)<---R1
;*************************************************************
      MPYF 3.991,R1
      FIX R1,R1
      ADDI 0X800,R1
      STI R1,@DA2_3
;*************************************************************
    ;******** Position Integration
      LDF *+AR5(0XB8),R1  ;theta(k)<---AR5(0XB8)
      LDF *+AR5(0XB5),R0  ;AR5(0XB5)--->omiga(k+1)
      MPYF *+AR0(0X68),R0 ;AR0(0X68)--->THYST,THYST*OMIGA(k+1)
      ADDF R1,R0          ;THYST*OMIGA(k+1)+theta(k)
      STF R0,*+AR5(0XB9)  ;Theta(k+1)<---AR5(0XB9)
   ;********** Position correction
       LDF *+AR0(0X1c),R0  ;current Id reference, AR0(0X1c)<---Id
       MPYF -1.0,R0        ;Iq*-Iq,Iq(k)<--AR0(0x1d)
   ;********** PI ******
      LDF *+AR5(0XC3),R6
      STF R6,*+AR5(0XC4)  ;Delta1--->Delta2
      LDF *+AR5(0XC2),R6
      STF R6,*+AR5(0XC3)  ;Delta--->Delta1
      STF R0,*+AR5(0XC2)  ;current Delta(k)<---R0
      LDF *+AR5(0XB9),R3 ;R3<---THETA(K+1)
      CALL PI
      CMPF 0.0,R3
      BNN PZ
      ADDF 2.094,R3
PZ    STF R3,*+AR5(0XB9) ;Theta(k+1)<---AR5(0XB9)
      LDF R3,R0
    ;************* Theta encoderized
      LDF *+AR5(0XB9),R0  ;(0XB9)<-----THETA(k+1)
      MPYF 0.4776,R0      ;THETA/(2PI/3)
      ABSF R0,R0
      FIX R0,R0           ;INT[THETA/(2PI/3)]
      FLOAT R0,R0
      MPYF 2.094, R0      ;2.094*INT[THETA/(2PI/3)]
      LDF *+AR5(0XB9),R1  ;confine as [0,2pi/3]
      ABSF R1,R1
      SUBF R0,R1          ;theta'=THETA-2.094*INT[THETA/(2PI/3)] to confine as [0,2pi](electrical)
     ; LDF *+AR5(0XB9),R2
     ; CMPF 0.0,R2
     ; BNN TRA
     ; LDF 2.094,R0
      ; SUBF R1,R0
      ; B TRA1
TRA   LDF R1,R0           ;*+AR0(0X6C)<------4000/(2PI/3)=1910.22
TRA1  STF R0,*+AR5(0XB9)  ;update theta(0)
```

```
      MPYF *+AR5(0XBC),R0  ;1910.22*THETA,(0XB8)<-----THETA
      FIX R0,R0
      STI R0,*+AR5(0XD3)   ;Theta(k)(int encoderized) --->AR5(0xD3)

     ; STI R0,@DA_2
      LDI R0,R5          ;Theta(k+1) encoderized<----R5
   ;*************************
      RETS
;
;*******PI***********
;**** OUTPUT:R3
PI:   LDF *+AR5(0XC2),R0  ;AR5(0XC2)--->Delta_theta(K)
      LDF *+AR5(0XC3),R6  ;AR5(0XC3)--->Delta_theta(k-1)
      MPYF *+AR5(0XC5),R0 ;Kpi*Delta_theta(K),Kpi<---AR5(0XC5)
      MPYF *+AR5(0XC6),R6 ;Kp*Delta_theta(k-1),Kp<---AR5(0XC6)
      SUBF R6,R0          ;Kpi*Delta_theta(K)-Kp*Delta_theta(k-1)
      LDF *+AR5(0XC4),R6  ;AR5(0XC4)--->Delta_theta(K-2)
      ADDF R0,R6          ;Kpi*Delta_theta(K)-Kp*Delta_theta(k-1)+Delta_theta(K-2)
     ; LDI *+AR5(0XC9),R2
     ; SUBI 0X1,R2
     ; CMPI 0,R2
     ; BN CHANGD
      LDF *+AR5(0XC7),R0  ;Delta_thetaLIMIT
     ; B LMCP
CHANGD; LDI -1,R2
     ; STI R2,*+AR5(0XC9)
     ; LDF *+AR5(0XCA),R0
LMCP  CMPF R0,R6
      BNN TH4
      MPYF -1.0,R0
      CMPF R0,R6
      BNN TH3
TH4   LDF R0,R6
TH3   LDF *+AR0(0X5B),R0
      CMPF 0.0,R0
      BNN  TH5
      MPYF -1.0,R6  ;SGN(THETA)
TH5   ADDF R6,R3
      RETS
```